Bonding Networks in Intermetallic Systems: Effects of Optimization, Cooperation, and Competition on Properties

By

Anastasiya I. Vinokur

A dissertation submitted in partial fulfillment of

the requirement for the degree of

Doctor Of Philosophy

(Chemistry)

at the

UNIVERSITY OF WISCONSIN-MADISON

2017

Date of final oral examination: May 11, 2017

This dissertation is approved by the following members of the Final Oral Committee:

Daniel C. Fredrickson, Associate Professor, Chemistry
Judith Burstyn, Professor Chemistry
Kyoung-Shin Choi, Professor, Chemistry
Song Jin, Professor, Chemistry
John F. Berry, Professor, Chemistry

Abstract

The field of intermetallic materials offers a wide range of structural diversity as well as a rich bounty of important properties like superconductivity and magnetism. Despite progress made in some systems, particularly thermoelectrics, the structure-property relationships remain largely elusive due to the extensive variety of atomic arrangements and properties that arise. In this dissertation, we aim to understand how form affects function in intermetallics through an approach familiar to inorganic molecular chemists: the analysis of directional bonding.

Despite the impression that their bonding is completely delocalized, intermetallics in fact exhibit a mixture of covalent, ionic and metallic interactions. Bonding in intermetallics can then be considered in terms of its deviation from the Lewis dot-like depictions of fully localized models of the actual electronic structure. The electronic structure can be represented as a bonding scheme for an atom where valence electron pairs are localized between atom pairs (either homoatomic or heteroatomic), which represent the bonding orbitals, or on the atom itself, representing the nonbonding orbitals. As the assigned bonding scheme based on either type of interaction is equivalent in all symmetry related atoms, bonding in intermetallics can be discussed in terms of networks of these homoatomic or heteroatomic bonding schemes. Of course, intermetallics are not limited to a single bonding network as multiple networks may be necessary to depict the full electronic structure of a phase. Bonding analysis, then, in intermetallics can also involve an investigation into the interactions of the various bonding networks.

The research within this dissertation aims to understand how the electronic structure, as represented by the bonding networks, affects the properties of intermetallic materials by studying systems that optimize their networks or allow for various interactions between their networks.

Chapters 2 and 3 explore two possible types of interactions: competing and cooperating. In Chapter 2, the observed competition between the Co-Co and Si-Si bonding networks within a new polymorph of a previously reported $GdCoSi_2$ phase causes an inherent weakness in the Co-Co bonds, which we exploit to trigger a reversible diffusionless phase transition.

Chapter 3 focuses on the cooperative interactions between bonding networks. From calculations of the electronic structures of body centered cubic (bcc) Mo, and its binary isoelectronic variant, ZrRu, a picture emerges of two 18-electron resonance structures, the relative weights of which are determined by the electronegativity differences of the elements in the structure. The resonance formalism connects the work on the transition metal rich CsCl-type phases to the previous studies of bonding in isostructural transition metal poor compounds by presenting a continuum where the prevalence of the second resonance structure changes as a function of the availability of d orbitals to participate in bonding for one of the elements.

In Chapter 4, the structural mechanisms by which a phase can optimize a single dominant bonding network are investigated. The nonstoichiometry of an Al column in a promising thermoelectric material, $FeAl_{2.6}$, is linked to the valence electron count dictated by the Fe-Fe bonding network. The analysis is further supplemented by DFT-Chemical Pressure (CP) calculations, which shed light on the extensive positional disorder within the Al column and possible strategies to induce ordering.

The final chapter departs from the general discussion of bonding, but continues along the topic of disorder, focusing on substitutional disorder. Using CP, a coloration pattern of a new Ru-substituted Y_2Co_{17} ternary variant is explained as a strategy by the structure to optimize its bond distances. The insights gained open a possibility of guiding the synthesis of ternary variants of binary phases through the prediction of possible substitution patterns.

What if Orpheus,
confident in the hard-
found mastery,
should go down into Hell?
Out of the clean light down?
And there, surrounded
by the closing beasts
and readying his lyre,
should notice, suddenly,
they had no ears?
Jack Gilbert

To my grandmother, Maria Tikhenko, for the gift of the unexpected

Acknowledgements

Time flies when you're having fun and the past five years spent in the collaborative environment of the Fredrickson group raced by in a blink of an eye. At times (well, many times), research threw curve balls. There were dead-ends and unanswerable questions. There were broken instruments and failed experiments. Tears, rejection letters, and best of all joys, infinite joys, of successes and new insights that became chapters in this dissertation. Through it all, like Achilles roasted in the flames, I became a better scientist. So I would like to thank my adviser, Prof. Daniel C. Fredrickson, for giving me this chance to grow. The odyssey of the past five years would have had a far different ending if not for his encouragement and optimism, for the knowledge shared and advice given. I hope, for many more years to come, he will impart his passion for intermetallics onto other young scientists and continue turning sugar into cutting edge science (with just a touch of coffee as a catalyst).

The electrifying environment of these past five years was also shaped by the members of the Fredrickson group. Many of them, like Dr. Amelia Hadler, Dr. Veronica Berns and Vince Yannello were amazing teachers. Others, like Dr. Yiming Guo and Katerina Hilleke never failed to answer questions and troubleshoot with me. I'm grateful to all of them for their time and effort. I want to especially thank Dr. Rie Fredrickson who taught me a lot about intricacies of Jana2006, intermetallic synthesis, and always made me feel welcome in the group.

Science, of course, by its very nature is a collaborative process and I had opportunities to work with a number of scientists outside of the Chemistry department. I would like to thank Dr. John Fournelle from the Geology Department for assisting me with Microprobe measurements and also the staff of 11 BM at Argonne National Laboratory for the high quality powder X-ray diffraction experiments.

My last two years in the department, I had an amazing opportunity to work as a crystallography laboratory assistant alongside Dr. Ilia Guzei. I'm grateful for his mentorship, which shaped me as a crystallographer as well as a scientist. I learned a lot about public science outreach and scientific collaborations. One of the numerous collaborative projects that sprung from my work as a crystallographer-in-training is featured in Appendix E.

I met a lot of fantastic people over the course of my stay in Madison. I'm ever grateful for running into two remarkable people in particularly, Matthew Dorris and Rebeca Pinhancos, We made a lot of great memories together, though in retrospect, maybe reading maps was not our strong suite. I also want to thank my Berry group buddies, Brian Dolinar and Jill Chipman, who religiously got tea with me on Tuesdays, through rain or shine. And I would also like to thank Alex Foot, who despite being the busiest graduate student in the world, still found time to watch anime with me every Wednesday. Also a big thank you to one of my oldest friends, Sari, for reminding me every once in a while just how cool my job is.

Of course, this list would not be complete without my family. My sister, Svetlana, had been a fountain of motivation and I also want to thank my nephews, Dennis and Sebastian, for putting up with me while I tried to indoctrinate them into science. Finally, words cannot express my gratitude for the constant, tireless, bottomless source of support and love that came from my mom and dad, Tatyana and Igor. When I was at my lowest, they picked me up. When I was at my highest, they shared my joy. They believed in me even when I was on a brink of losing belief in myself. This journey would have ended far sooner if not for them. Thank you! A million times, thank you!

Table of Contents.

List of Figures

Chapter 1

Chapter 2

Appendix D

Appendix E

List of Tables

Appendix B

Appendix C

Appendix D

Chapter 1.

Introduction

1.1. Structure Property Relationships in Intermetallics

The field of intermetallics, inorganic compounds composed of metallic elements, is a testament to the triumphs of the solid state synthesis. A recent search through the Inorganic Crystal Structure Database (ICSD) for phases that excluded halogens and first row main group elements yielded over 70,000 hits. These structures represent hundreds of variations in atomic arrangements, known as structure types, which range from simple binary variants of closed packed structures[1] to monstrous giants with millions of atoms per unit cell,[2,3] and even further still to structures that require one to invoke higher dimension space to describe their periodicity.[4,5] Along with this cornucopia of structural diversity, intermetallics exhibit a multitude of properties important for future and current economies, including superconductivity,[6,7] magnetism,[8] thermoelectric properties,[9,10] and shape memory.[11-13] Examples of this diversity are shown in Figure 1.1.

Currently, many new materials and their properties are discovered at the whims of goddess Fortuna in part due to a lack of predictive tools available to solid state chemists. A key to being able to design a material, the antidote to serendipity, is an inherent understanding of *how* atomic arrangements influence properties.

When such insights are gained for a type of intermetallic system, they prove to be incredibly powerful in guiding future synthesis. In the case of solid solutions, empirical

observations led Hume-Rothery to connect the stability ranges of different types of brasses to their valence electron concentration (VEC).[14] In this manner, based on the stoichiometry, which dictates the VEC, one could predict whether the solid solution would assume a Cu_5Zn_8 structure type (VEC= 1.62) or a body centered cubic (bcc) structure type (VEC= 1.50).[15] Further theoretical insights by Jones grounded the empirical observation in the relationship between the Fermi energy and first Brillouin zone[16] and opened the way to understanding complex systems like quasicrystalline aluminides.[17]

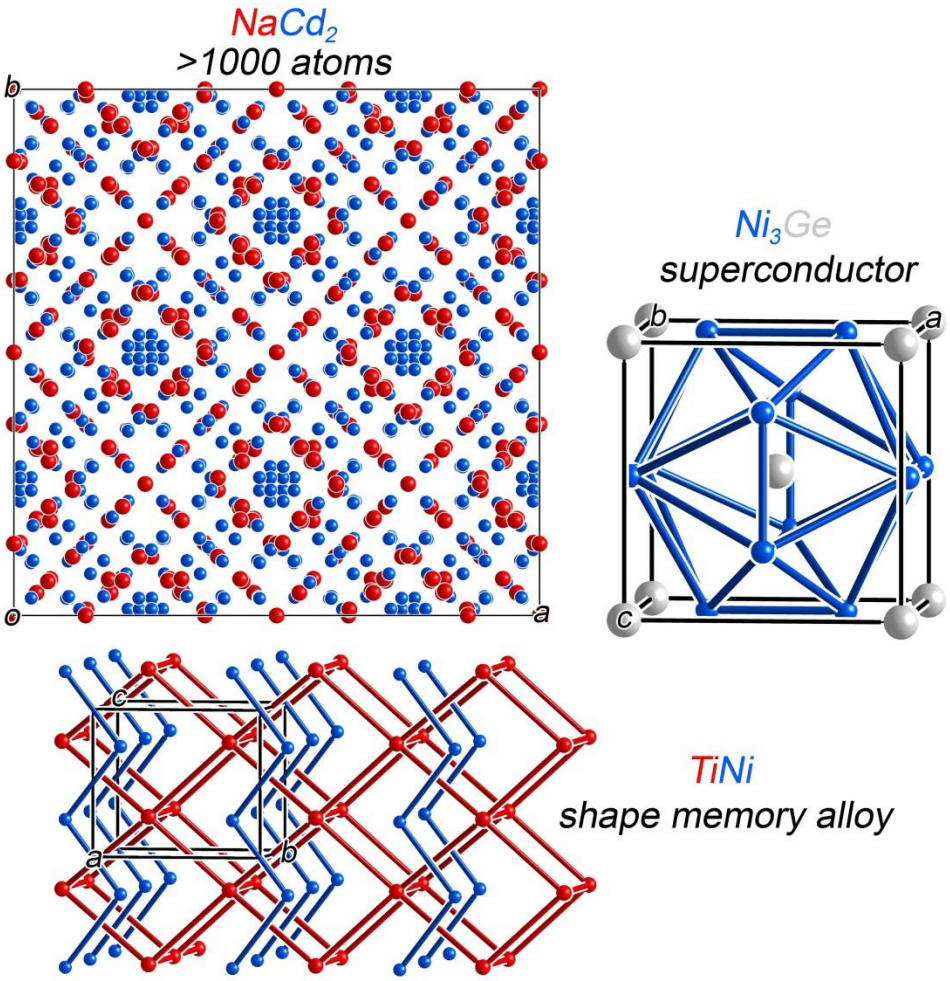

Figure 1.1. Select examples of the far ranging diversity of structural motifs and properties exhibited by intermetallics.

Similarly, an understanding of structure-property relationships for thermal conductivity proved fruitful in the development of new classes of thermoelectric materials. When the thermal conductivities of the skutterudites with atoms trapped within their cavernous cage-like networks were compared to those with empty cages, it was found that the stuffed skutterudites had surprisingly low thermal conductivity.[18] This discovery led to the recognition of the inclusion of "rattling atoms"[19] and, more generally, disorder[9] into the structure of the materials as a synthetic strategy to yield better thermoelectrics.

Yet despite the inroads already made into our understanding of structure property relationships, these advances have been isolated to a limited number of systems. More general concepts of how atomic arrangements affect a material's characteristics and stability remain elusive. In this work, we hope to bring new insights into the structure-property relationship and phase formation for a wider range of intermetallics by using an approach familiar to inorganic chemists: the analysis of bonding.

1.2. Bonding in intermetallics

In the field of molecular chemistry, the analysis of orbital interactions within molecules yields numerous insights into their stability ranges and properties, such as the blue color and paramagnetism of O_2. A similar approach can prove useful for intermetallics, despite their reputation for highly delocalized bonding. The large coordination environments and dense atomic packings of atoms in these materials give

the impression that these compounds bond in the same delocalized manner as pure metals and alloys. Yet, theoretical calculations suggest a more unruly picture where metallic, ionic, and covalent bonding coexist to varying degrees.[20] Calculations of electronic structure have shown the prevalence of HOMO-LUMO like gaps, called pseudogaps, in the density of states (DOS) distributions of many intermetallics. Such gaps suggest the presence of directional, possibly molecular-like, bonding. Furthermore, for many stable systems, the Fermi energy, which represents the level of electron filling within the DOS, falls within the pseudogap. And just as the presence of a HOMO-LUMO gap in molecular systems can be traced to the interactions of atomic orbitals to form molecular orbitals, the presence of pseudogaps in numerous intermetallic phases has been explained by using tight binding methods such as the Hückel method that build up the crystal orbitals based on the atomic orbital interactions. [21]

Within molecules, bonding can be understood in terms of localizing two electrons between a pair of atoms or on one atom as lone pairs, and bonding schemes like a Lewis dot structure can be used to depict a fully localized electronic structure. Of course, one would need to generate molecular orbitals with bonding (either σ or π), nonbonding or antibonding character to capture the actual electronic structure as it could show some degree of delocalization beyond the bonding atomic pairs. Still, fully localized models of electronic structure are useful because they allow one nominally to assign valence electron counts to atoms and they facilitate the creation of electron counting rules like the 18 electron rule for organometallics, which serve as bench marks for stability.

Now what if we apply the same principles of fully localized Lewis dot structure like models of the electronic structure to intermetallics? In this case, the homoatomic and the heteroatomic interactions of atomic pairs would be just further deviations from the total localization of electrons and we can begin nominally assigning electron pairs to these contacts. Also, by extending the ideas of molecular bonding to intermetallics, we can imagine that the electronic structure of intermetallics is also built from bonding, nonbonding or antibonding types of orbitals, albeit more delocalized. The assignment of a fully localized bonding scheme for an atom would detangle the heteroatomic and homoatomic interactions and allow us to assign valence electron counts to atoms. And since atoms in intermetallics can be related by crystal symmetry, by assigning a bonding scheme to one of the atoms, we can build an entire network of the same bonding scheme throughout the whole compound. Thus we can begin thinking about bonding in intermetallics as a deviation from these fully localized bonding networks, which can be built from the perspective of homoatomic or heteroatomic interactions.

The strength of applying this molecular perspective to bonding in intermetallics and assigning valence electron counts is that in addition to giving us bench marks for stability, it can explain preferred stoichiometry in phases. In Chapter 4, our investigation into the bonding within a promising thermoelectric material, $FeAl_{2.6,}$ explains the unusual Al loading as a result of the valence electron count needed to optimize an Fe-Fe based bonding network.

Yet intermetallics are not limited to a single bonding network. With multiple homoatomic and heteroatomic interactions coexisting in a single compound and valence

electron counts that exceed the capacity of a single fully localized bonding network, multiple networks can be necessary to describe the electronic structure. Therefore, an analysis of bonding within intermetallic compounds may also require investigation of interactions between the bonding networks.

What are the possible interactions? As the networks can be thought of as being built from σ and π-type bonds, the strength of the network depends on how many antibonding σ* and π* and nonbonding states are filled. The filling of the states depends on the location of the Fermi energy and so we can imagine that each network would have a preferred Fermi energy. In cases where the ideal Fermi energies are different for the multiple networks, a competition can arise. This competition would manifest as one network being nearly optimized (its ideal Fermi energy achieved) to the detriment of another network, where its antibonding states are filled. Such a competition could have a profound effect on the properties of the resulting phase as the filling of antibonding states in one network introduces an Achilles heel within it. The weakened bonds could be susceptible to breaking under different environmental conditions. In Chapter 2, we explore how competing bonding networks in a ternary Gd-Co-Si system give rise to a reversible phase transition as the Si-Si bonding is optimized to the detriment of the Co-Co network.

On the other hand, if the ideal Fermi energy is similar for both networks, the networks can cooperate. This cooperation would manifest as both networks having similar fraction of bonding and antibonding states being filled and both networks having the potential to be optimized. Whereas the competition between networks could

introduce an inherent structural weakness, cooperation would lend strength and resistance to structural changes. Chapter 3 investigates the cooperative bonding networks of one of the highest melting transition metals, body centered cubic (bcc) Mo, and its binary transition metal rich variant, ZrRu.

As hinted by the analogies to molecular chemistry, an important aspect of the analysis of bonding in intermetallics will be an ability to generate orbitals that are representative of the actual electronic structure as it allows us to determine how accurate our simplified fully localized model is in comparison. For molecular systems, Molecular Orbital (MO) analysis serves this purpose. In the next section, we will present a novel tool, the reversed approximation Molecular Orbital (raMO) analysis that serves to generate orbitals representative of the actual electronic structure and allows us to test the accuracy of our fully localized bonding network schemes.

1.3. Analyzing bonding networks with reversed approximation Molecular Orbitals Analysis

The method of reversed approximation Molecular Orbital (raMO) analysis was developed in the Fredrickson group as a way to analyze local bonding within the transition metal poor intermetallic structures and to bring molecular-like insights into these extended solids.[22] The method utilizes the strength of DFT-calibrated Hückel models, as DFT gives the method the accuracy of the electronic structure calculations and the Hückel method lends ready flexibility to focus on specific fragments of the structure and the participating orbitals.

The analysis involves the production of localized orbitals in a similar spirit to Wannier functions. This is accomplished, as the name "raMO" implies, by reversing a typical MO calculation. Instead of using simple atomic orbitals as a basis set to generate more complex molecular orbitals, the occupied crystal orbitals are used to generate simple localized functions. These simple orbitals that are targeted in the analysis are based on the model of bonding we anticipate in a system under analysis.

For an intermetallic phase, we anticipate that a transition metal would use all nine of the available valence s, p, and d orbitals while a main group element would use the available four valence s and p orbitals to build either homoatomic or heteroatomic bonding networks. For example, in CoAl, a CsCl type intermetallic, our valence electron count is 12 (9 electrons coming from Co and 3 electrons contributed by Al), which we will need to assign to one or more bonding networks. With two elements, three possible networks can exist, built from Co-Co, Co-Al, or Al-Al interactions, which are summarized in Figure 1.2. For a Co-Co bonding network, based on the fact that each Co has six Co neighbors arranged in an octahedron, our simplified bonding scheme would depict six electron pairs. Similar bonding schemes can be drawn up for the Al-Al bonding network as each Al has six Al neighbors, and for the Co-Al bonding network our bonding picture would involve eight electron pairs. Now realistically, since Al only has s and p orbitals to particulate in bonding, we cannot hybridize these atomic orbitals to account for all six localized contacts in the Al-Al bonding scheme. Similarly as the Co-Al network would require eight localized orbitals, the lack of d orbitals on Al would render such

hybridization impossible. That leaves the Co-Co network as the best possible approximation of the electronic structure.

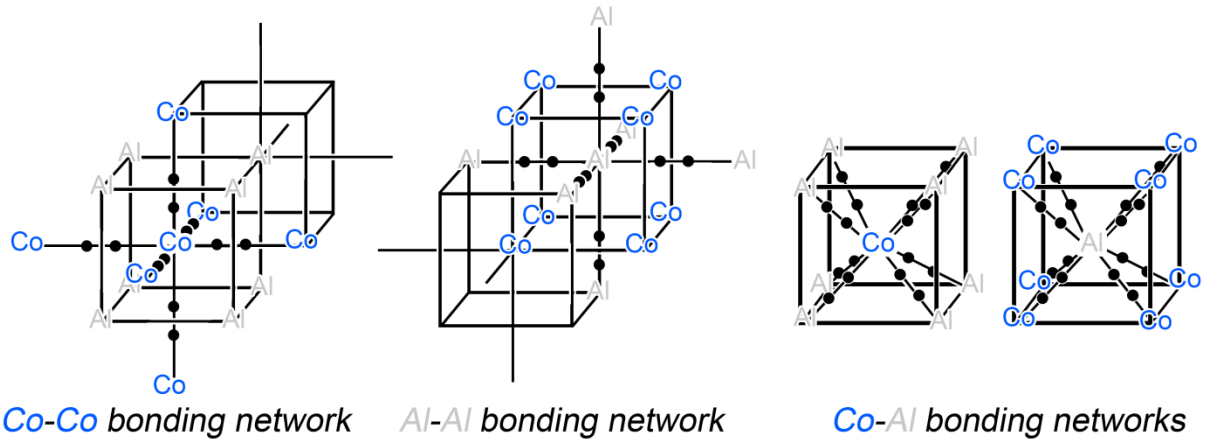

Figure 1.2. Summary of possible bonding networks for CoAl based on stoichiometry and crystal structure.

But just how accurate is our simple fully localized model? To answer this question, we use the raMO analysis to reproduce the nine Co s, p, and d orbitals (Figure1.3a) that serve as potential building blocks of the Co-Co network. If the proposed bonding model is correct, then the generated orbitals, raMOs, will depict localized functions readily identifiable as being based on the nine s, p and d orbitals.

As seen in Figure 1.3b, the resulting raMOs for Co contain densities on the central Co atom and each does correspond to an s, p, or d target function. But now, we also see additional contributions from the neighboring atoms as evidenced by the blue or green densities located at those atoms. In all nine of the generated raMOs there are densities on the neighboring Al, but there are only six orbitals (4s, $4p_x$, $4p_y$, $4p_z$, $3d_{z2}$ and $3d_{x2-y2}$) that

also exhibit densities on the neighboring Co atoms. The densities on the neighboring Al are the manifestations of the

delocalization expected of an intermetallic electronic structure. On the other hand, by taking linear combinations of the six raMOs with densities on the neighboring Co atoms, we can produce six hybrid orbitals that depict densities between one pair of Co atoms at a time and these densities bear a strong resemblance, isolobal, to σ bonds (Figure 1.3c). These six isolobal bonds confirm the simple localized Co-Co bonding model we proposed as they represent functions where a pair of electrons is localized between two bonding atoms.

Can this bonding network account for all of the available valence electrons? Each of the isolobal σ bonding states yields 1 electron per Co, as the electron pairs are shared between two Co atoms, we account for six electrons thus far. But in addition to the six bonding states, there were three orbitals that showed no Co-Co interactions. Applying molecular bonding language, these can be thought of as Co-Co nonbonding states. The three nonbonding states can each provide 2 electrons per Co as the electron pairs are not shared and thus bring the total of electrons that the Co-Co bonding network can accommodate to 12 electrons per Co. The number of accommodated electrons matches the valence electron count determined by stoichiometry of the phase. We can conclude then, that for CoAl, its electronic structure can be approximated with a single bonding network built from six Co-Co fully localized interactions.

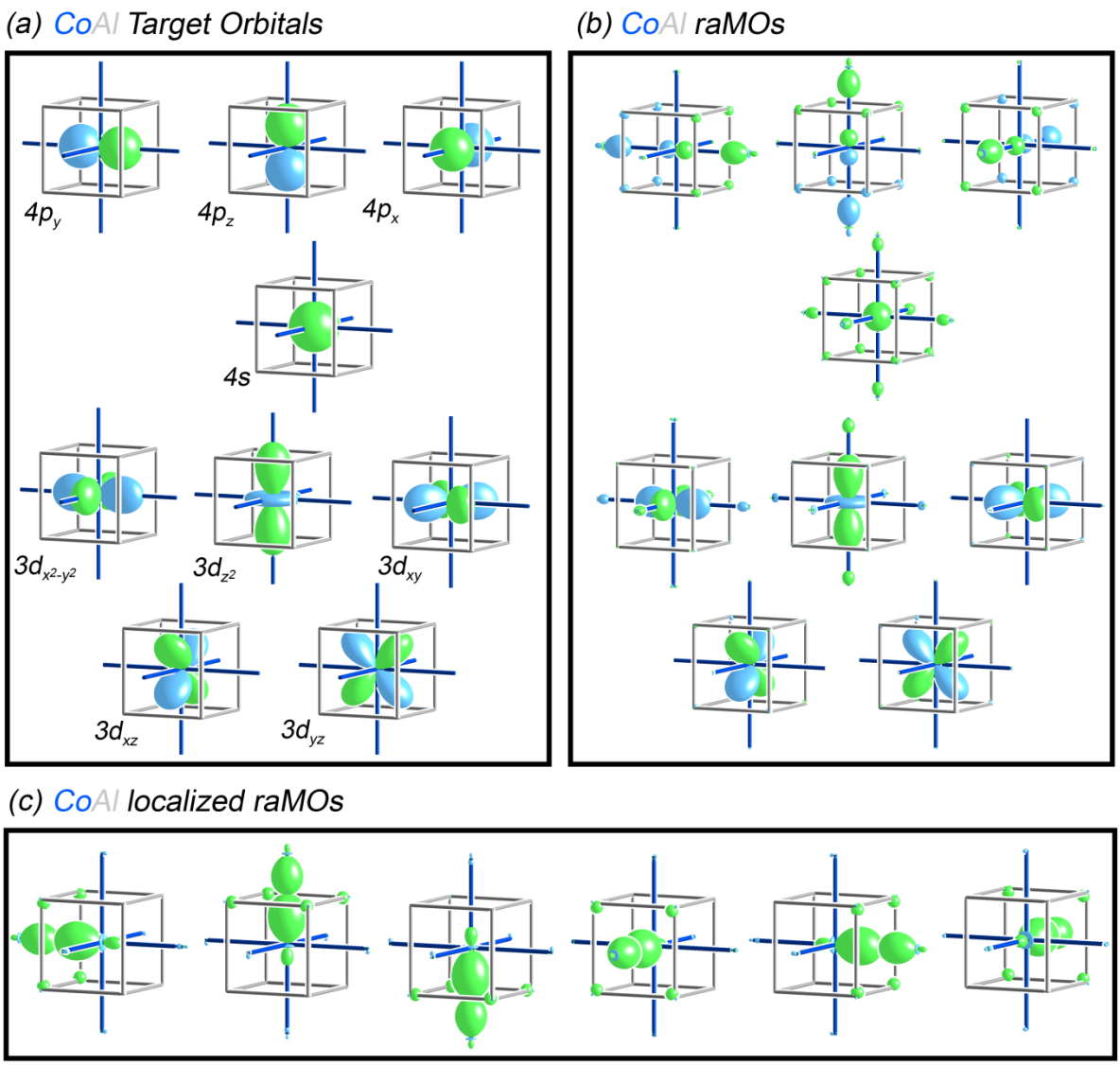

Figure 1.3. Reversed approximation Molecular Orbital analysis of CoAl. (a) The target orbitals for the description of the Co-Co bonding network. (b) The generated raMOs for Co exhibit additional densities on the neighboring Al, while six of them based on 4s, $4p_x$, $4p_y$, $4p_z$, $3d_{z2}$ and $3d_{x2-y2}$ also show interactions with neighboring Co atoms. (c) The six directional interactions that have the same symmetry (isolobal) as σ bonds are generated by taking linear combinations of the 4s, $4p_x$, $4p_y$, $4p_z$, d_{z2} and d_{x2-y2}, orbitals that show signs of Co-Co interaction.

Application of the raMO analysis to a wide range of transition metal poor phases , like CoAl, revealed another connection to molecular chemistry: many structural features can be connected to the attempts by the transition metals to achieve an 18 electron configuration.[23] This observation is summarized in an 18-*n* rule for intermetallics, which states that a transition metal will form *n* number of transition metal-transition metal isolobal bonds if it is *n* number of electrons short of achieving an 18 electron configuration.[23,24] The 18-*n* rule successfully explains a number of structural trends such as the CsCl-structure type of $NiSi_2$ (18 electrons/Ni), which features no Ni-Ni interactions, and the β-$FeSi_2$ structure type of $FeSi_2$ (16 electrons/Fe), which features two Fe-Fe σ isolobal bonds.[24] In the case of CoAl, with a valence electron count of 12, *n*=6 and with the raMO analysis we observed six isolobal Co-Co bonds.

As demonstrated, the raMO method and the 18-*n* rule work well for cases like the transition metal poor phases since they require no more than nine orbitals to generate all of the necessary directional bonds for transition metal based networks. Atoms in intermetallic phases, however, can expand their coordination environment beyond nine contacts. In this dissertation, we make extensive use of the raMO analysis, but as presented in Chapters 2 and 3, we take the method beyond the original scope of binary transition metal poor systems and apply it to ternary and transition metal-rich phases. In Chapter 4, we further enrich our conclusions from raMO analysis regarding the positional disorder in the Al column of $FeAl_{2.6}$ phase with another theoretical technique, DFT-Chemical Pressure (CP), which quantifies size effects. Thus we open a new venue where the two methods provide complementary insights into the same structural features.

1.4. Outline of Thesis

In the tradition of the Fredrickson group, in this work we will pursue the question of structure-property relationship by combining the Edisonian approaches of synthesis and observations with the insights gained from theoretical calculations. Specifically, we will investigate the effects of bonding networks, their optimization and interactions, on atomic arrangements and properties of intermetallic phases.

Chapter 2 focuses on the competition between the transition metal and main group bonding networks within a ternary Gd-Co-Si system as a method for destabilization of a phase to induce a diffusionless phase transition. The chapter begins with experimental work, where a previously reported intermetallic phase $GdCoSi_2$ of the $CeNi_{1-x}Si_2$-structure type was synthetically targeted. This synthesis yielded a novel $CeNi_{1-x}Si_2$ superstructure. The observed $GdCoSi_2$ phase exhibited many of the same features of alternating layers of corner sharing Co centered Si tetrahedra and Gd-Si AlB_2 type slabs, as in the originally reported structure, but the Si tetrahedra appeared distorted, thus changing the Co atomic arrangement from square nets to zig-zag chains. The bonding networks within the parent $CeNi_{1-x}Si_2$ structure and the superstructure were probed by raMO analysis. For both systems, two networks were found: one built for Co-Co interactions and the second from Si-Si interactions. Closer analysis revealed a two electron mismatch between the electron count suggested by the raMOs and the actual valence electron count in the parent $CeNi_{1-x}Si_2$ structure. The superstructure alleviated the discrepancy in the number of electrons between the ideal and the actual electron counts by forming two σ Co-Co isolobal bonds along the Co zig-zag chains. However, the

small size of the observed lobes on the neighboring Co atoms bore signs of competition with the Si bonding network, where Co-Co σ* states were partially filled as a result of optimization of the Si-Si bonding states. The Co-Co bonds proved sufficiently weak that upon heating to 383 K a reversible diffusionless phase transition to the parent structure was observed, thus confirming that the introduction of competition within the bonding networks is a viable strategy to promote phase transitions.

In Chapter 3, we explore cooperation between bonding networks by the application of the raMO analysis to the bcc elemental transition metal and its transition metal rich CsCl isoelectronic variant. The structure of bcc-Mo is imagined as two interpenetrating simple cubic networks, where a Mo atom and its second nearest neighbors arranged in an octahedral geometry belong to one network, while the first nearest neighbors arranged in a cube to a second network. With this arrangement, application of the raMO method reveals six Mo-Mo isolobal σ bonds to the second nearest neighbors and consequent adherence to the 18-*n* rule so long as all of the electrons from the second network are also used and the total valence electron count is 12. Since the two networks within Mo are symmetry equivalent, evoking resonance structures become key to capturing the full picture of the bonding within bcc-Mo. In this way, the electronic structure of bcc-Mo can be described as two resonance structures, each centered on one of the interpenetrating primitive cubic networks. Whereas in the elemental metals the two resonance structures have equal weights, the weights differ in a transition metal rich CsCl isoelectronic variant such as the ZrRu. The features in the reproduced raMOs centered on Ru and Zr share many similarities to the raMOs

reproduced for Mo, but in the case of Zr, the lobes appear smaller and delocalized. Thus ZrRu can also be understood in terms of two resonance structures, but the resonance structure based on the more electronegative Ru network has a higher weight. At the end of the chapter, we connect previous investigations into transition metal-main group CsCl phases to the current work by presenting a continuum from ZrRu to RuSn, showing that RuSn can be understood as eliminating one of the transition metal-based resonance structures as Sn lacks the d orbitals necessary to create six localized isolobal σ bonds.

Chapter 4 focuses on atomic arrangements as a result of the optimization of a single bonding network. We investigate a promising thermoelectric material, $FeAl_x$ ($2.5>x<2.8$). This previously reported phase exhibits extensive positional disorder, which manifests as a continuous column of electron density, and can be modeled with several partially occupied Al sites. The Al content for the reported phase has varied widely depending on the crystallographic model used. We began our investigation by first synthetically targeting this phase, which resulted in confirming the composition as $FeAl_{2.6}$, and also testing the robustness of this structure as a function of temperature within the range of 100 to 400 K. As neither phase transition nor ordering within Al columns were observed, the investigation turned towards an analysis of the transition metal bonding network built from Fe zig-zag chains as the stabilizing factor. With application of raMO, it was discovered that $FeAl_{2.6}$ adheres to the 18-*n* rule and that the nonstoichiometry was essential for reaching the correct electron count of approximately 16 electrons per Fe. The results from DFT-Chemical Pressure (CP) calculations on two types of ordered models, which placed Al atoms at various positions along the column,

revealed that the overall chemical pressure schemes remained predominantly unchanged despite the differences in positions and highlighted the potential for freedom of motion along the channels. This apparent lack of preference for particular atomic positions opens up possibilities for multitudes of ordering patterns coexisting in one crystal structure and is linked to the isolation of the disorder to the channels.

Finally, in Chapter 5, we consider results from a separate line of research aimed at further understanding disorder and substitutions within intermetallic phases. Our specific focus here is on the phenomenon of compositional disorder through the analysis of coloration patterns of a newly discovered Ru-substituted ternary variant of Y_2Co_{17}, $Y_2Ru_{4.85}Co_{12.15}$. The analysis begins by first investigating the origins of Y_2Co_{17} which is derived by substituting within $CaCu_5$-type YCo_5 one third of Y atoms by Co dumbbells to create two layers that repeat along *c*. Through the course of detailed CP analysis, the origin of the Co dumbbell substitutions was traced to the relief of negative CP between the Y atoms. Further CP analysis of the Co sites in Y_2Co_{17} revealed variations in preferences for larger atoms at different atomic sites. These preferences were traced to the experimentally observed substitution patterns in $Y_2Ru_{4.85}Co_{12.15}$ and helped explain the wide range of occupancies exhibited by Ru.

1.5. References

(1) Omori, T.; Oikawa, K.; Sato, J.; Ohnuma, I.; Kattner, U. R.; Kainuma, R.; Ishida, K. *Intermetallics* **2013**, *32*, 274.

(2) Morton, A. J. *phys. stat. sol. a* **1974**, *23*, 275.

(3) Morton, A. J. *phys. stat. sol. a* **1975**, *31*, 661.

(4) Fredrickson, R. T.; Fredrickson, D. C. *Inorg Chem* **2013**, *52*, 3178.

(5) Palatinus, L.; Klementová, M.; Dřínek, V.; Jarošová, M.; Petříček, V. *Inorg Chem* **2011**, *50*, 3743.

(6) Matthias, B. T.; Geballe, T. H.; Willens, R. H.; Corenzwit, E.; Hull, G. W. *Physical Review* **1965**, *139*, A1501.

(7) Han, F.; Malliakas, C. D.; Stoumpos, C. C.; Sturza, M.; Claus, H.; Chung, D. Y.; Kanatzidis, M. G. *Physical Review B* **2013**, *88*.

(8) Mihalik, M.; Svoboda, P.; Mihalik, M.; Vejpravová, J.; Sechovský, V. *Journal of Magnetism and Magnetic Materials* **2005**, *290–291, Part 1*, 606.

(9) Yamada, T.; Yamane, H.; Nagai, H. *Advanced Materials* **2015**, *27*, 4708.

(10) Kanno, M.; Yamada, T.; Ikeda, T.; Nagai, H.; Yamane, H. *Chemistry of Materials* **2017**, *29*, 859.

(11) Nishiyama, Z. *Martensitic Transformations*; Academic Press, 1978.

(12) Van Humbeeck, J. *Advanced Engineering Materials* **2001**, *3*, 837.

(13) Wei, Z. G.; Sandstroröm, R.; Miyazaki, S. *Journal of Materials Science* **1998**, *33*, 3743.

(14) Hume-Rothery, W.; Raynor, G. V. *The structure of metals and Alloys*; 4th ed.; Institute of Metals: London, 1962.

(15) Müller, U. *Inorganic Structural Chemistry*; 2nd ed.; Wiley: Chichester, 2007.

(16) Jones, H. *Proceedings of the Physical Society* **1937**, *49*, 250.

(17) Trambly de Laissardière, G.; Nguyen-Manh, D.; Mayou, D. *Progress in Materials Science* **2005**, *50*, 679.

(18) Sales, B. C.; Mandrus, D.; Williams, R. K. *Science* **1996**, *272*, 1325.

(19) Arčon, D.; Zorko, A.; Jeglič, P.; Xu, J.; Tang, J.; Tanabe, Y.; Heguri, S.; Tanigaki, K. *Journal of the Physical Society of Japan* **2012**, *82*, 014703.

(20) Todorov, E.; Evans, M.; Lee, S.; Rousseau, R. *Chemistry – A European Journal* **2001**, *7*, 2652.

(21) Hoffmann, R. *Angewandte Chemie International Edition in English* **1987**, *26*, 846.

(22) Yannello, V. J.; Kilduff, B. J.; Fredrickson, D. C. *Inorg Chem* **2014**, *53*, 2730.

(23) Yannello, V. J.; Fredrickson, D. C. *Inorg Chem* **2014**, *53*, 10627.

(24) Yannello, V. J.; Fredrickson, D. C. *Inorg Chem* **2015**, *54*, 11385.

Chapter 2.

Toward Design Principles for Diffusionless Transformations: The Frustrated Formation of Co-Co Bonds in a Low-Temperature Polymorph of $GdCoSi_2$

This chapter has been published: Vinokur, A. I.; Fredrickson, D.C., *Inorg. Chem.*, **2016**, 55, 6148-60.

2.1. Abstract

Diffusionless (or displacive) phase transitions allow inorganic materials to show exquisite responsiveness to external stimuli, as is illustrated vividly by the superelasticity, shape memory, and magnetocaloric effects exhibited by martensitic materials. In this Article, we present a new diffusionless transition in the compound $GdCoSi_2$, whose origin in frustrated bonding points toward generalizable design principles for these transformations. We first describe the synthesis of $GdCoSi_2$ and the determination of its structure using single crystal X-ray diffraction. While previous studies based on powder X-ray diffraction assigned this compound to the simple $CeNi_{1-x}Si_2$ structure type (space group *Cmcm*), our structure solution reveals a superstructure variant (space group *Pbcm*) in which the Co sublattice is distorted to create zigzag chains of Co atoms. DFT-calibrated Hückel calculations, coupled with a reversed approximation Molecular Orbital analysis, trace this superstructure to the use of Co-Co isolobal bonds to complete filled 18 electron configurations on the Co atoms, in accordance with the 18-*n* rule. The formation of these

Co-Co bonds is partially impeded, however, by a small degree of electron transfer from Si-based electronic states to those with Co-Co σ* character. The incomplete success of Co-Co bond creation suggests that these interactions are relatively weak, opening the possibility of them being overcome by thermal energy at elevated temperatures. In fact, high temperature powder and single crystal X-ray diffraction, as well as differential scanning calorimetry, indicate that a reversible *Pbcm* to *Cmcm* transition occurs at about 380 K. This transition is diffusionless, and the available data point toward it being first order. We expect that similar cases of frustrated interactions could be staged in other rare-earth-transition metal-main group phases, providing a potentially rich source of compounds exhibiting diffusionless transformations and the unique properties these transitions mediate.

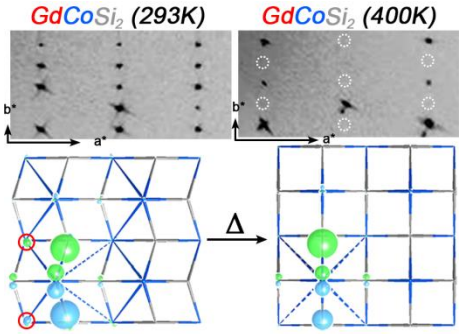

Figure 2.0. The differences in the reciprocal space reconstructions of the *hk*o layers between the high temperature (400 K) and the low temperature (293 K) datasets for $GdCoSi_2$ show a temperature driven phase transition from a *C*-centered parent structure to the *P*-centered superstructure. The raMO reconstructions of Fe based orbitals point to a formation of Fe-Fe σ bonds as the driving force of the superstructure formation, but weakness of the bonds allows for reversibility of the phase transition.

2.2. Introduction

Martensitic transformations provide an unparalleled example of how atomic motions within a solid state material at the Ångstrom length scale can give rise to dramatic macroscopic effects. They are characterized as first-order transitions between phases accomplished by small but highly coordinated shifts in the equilibrium atomic positions, such as the distortion of a square net into a rectangular one.[1] Their name derives from the transition between the malleable fcc-based austerite form of steel to the brittle bcc-based martensite form through simple changes in the c/a ratio of the unit cells,[1,2] perhaps the first example of this type of phase transition characterized. Martensitic transformations have since become the basis for a number of unique physical properties in alloys and intermetallic phases including superelasticity,[3-5] negative thermal expansion,[6] shape memory effects,[7,8] and strong magnetocaloric[9-11] or magnetoelastic effects.[12,13] As these transformations can be triggered through changes in temperature,[1,14] pressure,[15-17] or magnetic field,[18,19] they provide a gateway to materials highly responsive to external stimuli. However, most research into martensitic transformations has focused on derivatives of the bcc structure.[7,8] The ability to design new systems exhibiting such transitions could open vast opportunities for new materials properties.

A prerequisite to this ability to engineer new martensitic systems is more predictive approaches to the more general phenomena of diffusionless phase transitions, of which martensites make up a subset. While numerous diffusionless transitions have been reported for intermetallic compounds, in most cases their origins are unexplained, leaving open the question of how new transition may be targeted.[6,10,11,20-26] In this Article, we pre-

sent a diffusionless transition in the compound $GdCoSi_2$, whose origins in conflicts between Co-Co bonding and Co-Si electron transfer offer clues to more general design principles for these phase transformations.

Our synthetic and structural investigation of $GdCoSi_2$ was inspired by an interest in the competition among multiple interaction types in lanthanide–transition metal–main group element (RE-T-E) systems. This competition can be seen in the bonding modes that predominate in their binary subsystems: T-E binaries tend to be governed by achieving filled 18 electron counts on the T elements. The structures of these compounds can often be rationalized by noting that each T atom will need 18-*n* electrons to reach such a closed shell electron configuration, where *n* is number of T-T bonds (or multicenter functions isolobal to direct T-T bonds) it participates in.[27-29] RE-E binaries, on the other hand, tend to show large enough electronegativity differences that they often adhere to the Zintl concept, in which closed-shell configurations are accomplished through a combination of ionization and E-E bonding.[30,31] Finally, RE-T compounds exhibit a wide diversity of structures, ranging from those that can be interpreted in terms of the Zintl or 18-*n* schemes, to Laves phases and quasicrystals in which atomic packing constraints play a large role.[32-37] An intriguing question is how the structural chemistry of RE-T-E phases prioritizes and reconciles these various bonding schemes.

Phases adopting the $CeNi_{1-x}Si_2$ structure type (space group *Cmcm*) are common fixtures of RE-T-E phase diagrams,[38-42] providing one starting point for investigating this question. This structure type is relatively simple, easily described in terms of an intergrowth of RE-T-E layers of the $BaAl_4$ or $ThCr_2Si_2$ type with RE-E slabs of the AlB_2-type.[39,43-

[45] Another attractive feature is that their division into T-E and RE-E regions could make them amenable to an analysis combining the 18-*n* rule and Zintl concept.

A closer look at their reported crystal structures, however, reveals surprising irregularities: while nominally belonging to the same structure type, the positions assigned to the T atoms vary widely depending on the system.[38,46-49] Many of these assignments were based on powder X-ray diffraction data, without refinements of the crystal structures, raising concerns about their definitiveness. In addition, several of the $CeNi_{1-x}Si_2$-type phases have been reported to be subject to vacancies[43,50] or incommensurate modulations.[44,51]

As we will see in this Article, a richer structural chemistry does indeed lie beneath the putative $CeNi_{1-x}Si_2$ structure type of one such phase: $GdCoSi_2$. Our synthesis and crystallographic investigations of $GdCoSi_2$ yield not the simple $CeNi_{1-x}Si_2$-type phase reported previously,[48,52] but a superstructure derived from a shearing distortion of its Co-Si layers. Through DFT-calibrated Hückel calculations, we will trace this distortion to the attempt to form Co-Co isolobal bonds in accordance with the 18-*n* rule. The full development of these bonds, however, is hindered by a mismatch in the relative energies of the Co- and Si-based states of the system. This weakened driving force suggests the possibility of a diffusionless high-temperature transition to the simpler $CeNi_{1-x}Si_2$ type, which we in fact observe experimentally to occur at ca. 380 K. In this way, the $GdCoSi_2$ offers a window into how phases with the potential for these valuable phase transitions may be identified or designed.

2.3. Experimental

Synthetic procedures. $GdCoSi_2$ was synthesized through the reaction of its component elements (gadolinium pieces, Rare Metall, 99.9%, filed to a powder; cobalt powder, 99.9%, Aldrich; silicon, powder, -100+200 mesh, 99.99%, Alfa Aesar). The elements were weighted out in stoichiometric ratios and pressed into pellets in an Ar-filled glovebox. The pellets then were arc-melted under Ar two times for 10 seconds each (to maximize homogeneity while minimize potential loss by evaporation) and wrapped in Ta foil. The wrapped pellets were sealed in evacuated fused silica ampoules and annealed at 1000°C for 7 days. The annealing process was then ended by either quenching the samples in ice water or allowing the samples to slowly cool to room temperature. All syntheses resulted in hard, gray, shiny, and well-faceted pellets that showed no visible air sensitivity even after weeks in air.

Single Crystal X-ray Diffraction. Crystals picked from the crushed samples were analyzed at room temperature with an Oxford Diffraction Xcalibur E diffractometer with a Mo Kα (λ=0.71069 Å) sealed-tube X-ray source. To examine the possibility of a high temperature phase transition, single crystal X-ray diffraction measurements were also carried out over a range of temperatures accessible with the Oxford Cryojet HT accessory. For the room temperature data set, the run list consisted of ω scans chosen to cover a full sphere of reciprocal space out to a resolution of 0.8 Å. The scans were taken with a 0.8° step width and a 20 sec exposure time. The run list for the full experiment at 400 K was also based on ω scans, this time with a step width of 0.5° and a 35 sec. exposure time, chosen to cover a

full sphere out to 0.8 Å resolution. For all data sets, CrysalisPro ver. 171 was used for the run-list generation and processing of the frame data.[53]

Structure Solution and Refinement. Examination of the data set collected at room temperature yielded an orthorhombic unit cell with *a*=4.25 Å, *b*=15.81 Å, and *c*=3.99 Å (with a small twin component of 8.4% with only minor overlap). The systematic absences observed in reciprocal space reconstructions of the diffraction data were consistent with space group *Pbcm*. This space group assignment was confirmed in the subsequent structure solution and refinement.

During the structure solution process, 4 symmetry-distinct atomic positions were obtained with the charge-flipping algorithm[54,55] as implemented in SUPERFLIP,[56] and the resulting model was refined on F^2 using Jana 2006.[57] All sites were refined anisotropically, with the refinement converging to R(I>3σ)=1.58. The largest peaks in the Fourier difference map corresponded to maximum and minimum densities of 0.78 electrons/$Å^3$ and -0.83 electrons/$Å^3$, respectively.

Table 2.1. Crystal data for $GdCoSi_2$.

Chemical formula	$GdCoSi_2$	
Crystal dim. (mm^3)	0.013 × 0.030 × 0.038	
Crystal color	Metallic gray	
Radiation source, λ (Å)	Mo Kα, (0.71069 Å)	
Absorption correction	Analytical	
Data collection temp.	Room temp.	400K
Pearson symbol	*oP*16	*oC*16
Space group	*Pbcm* (no. 57)	*Cmcm* (no. 63)
a (Å)	4.25926(18)	4.08012(13)

b (Å)	15.8053(8)	16.2545(6)
c (Å)	3.9900(2)	4.00172(12)
Cell volume (Å^3)	268.60(2)	264.990(12)
Calc. density (g/cm^3)	6.7349	6.8245
Absorption coef. (mm^{-1})	31.168	31.594
θ_{min}, θ_{max}	4.79 , 28.7	5.02, 28.55
Number of reflections	1793	965
R_{int} (I> 3σ, all)	2.06, 2.08	2.00, 2.00
Unique refl. (I > 3σ, all)	351, 378	200,210
Number of parameters	27	18
R (I > 3σ), R_w (I > 3σ)	1.58, 3.99	1.22, 2.56
R(all), R_w(all)	1.86, 4.16	1.30, 2.61
S (I >3σ), S (all)	1.27, 1.27	1.26, 1.25
$\Delta\rho_{max}$, $\Delta\rho_{min}$ (e^-/Å^3)	0.78, -0.83	0.26, -0.35

In contrast to the data collected at room temperature, the data collected at 400 K were well-indexed with an orthorhombic *C*-centered cell of dimensions *a*=4.08 Å, *b*=16.25 Å and *c*= 4.00 Å. The systematic absences were consistent with *C*-centered cell , and the following steps of the analysis confirmed the assignment of the space group *Cmcm*. Applying the charge-flipping procedure to these data yielded the four symmetry-distinct atomic positions of the $CeNi_{1-x}Si_2$ structure type. As with the room temperature data set, the resulting model was refined on F^2 using Jana 2006, with all sites modeled anisotropically. The solution converged to R((I>3σ)=1.22, with the largest features in the Fourier difference map corresponding to a maximum density peak of 0.26 electrons/Å^3 and minimum desnity hole of -0.35 electrons/Å^3.

Details concerning both the room temperature and high-temperature crystal structure refinements are given in Table 2.1, while the refined atomic coordinates, atomic displacement parameters, and selected interatomic distances are provided in the Appendix A.

Powder X-ray Diffraction. For phase analysis with powder X-ray diffraction, fragments of the samples were crushed and manually ground into a fine powder, which was mounted onto a glass fiber with vacuum grease. Diffraction data on the powders were collected on a Rigaku Rapid II diffractometer with Mo Kα radiation (λ=0.7107 Å) equipped with a curved image plate detector. RINT RAPID was used to collect the data, while the averaging over the frames to create I vs. 2θ profiles was performed with the 2DP Pattern Integration software for the 2θ range 2° to 45° with a step size 0.02°. For the samples quenched from 1000 °C , the strongest peaks in the diffraction pattern appeared to agree with those previously reported for $GdCoSi_2$ in the $CeNi_{1-x}Si_2$ type (space group *Cmcm*), with $GdCo_2Si_2$ occurring as an impurity. Slow-cooled samples contained additional impurities.

X-ray diffraction data with better resolved peaks were collected on the quenched samples at synchrotron beamline 11-BM at the Advanced Photon Source, Argonne National Laboratory using a calibrated wavelength of 0.459264 Å. The strongest peaks in the pattern were in close agreement with *Pbcm* $GdCoSi_2$ polymorph, and the presence of a $GdCo_2Si_2$ impurity was also confirmed. Additional weaker peaks appeared to correspond to the *Cmcm* $GdCoSi_2$ polymorph. The powder patterns of the quenched samples were also collected at 380 K, 400 K, and 360 K (the order chosen based on the results of differential scanning calorimetry data described below). In the data collected at 380 K, the peaks as-

signed to the high temperature $GdCoSi_2$ polymorph became enhanced in intensity relative to the room temperature pattern, while the majority of the peaks for low temperature phase decreased and shifted to the left due to thermal expansion. The trend continued at 400 K, where the pattern was dominated by the *Cmcm* phase. The transition reversed upon cooling the sample down: in the pattern collected at 360 K, the *Pbcm* phase prevailed again.

Elemental Analysis with Energy Dispersive X-ray Spectroscopy (EDS). Samples were prepared for energy dispersive X-ray spectroscopy (EDS) measurements by suspending fragments of the reaction products in epoxy, allowing the epoxy to harden, then hand-polishing the samples against a diamond lapping film to create flat surfaces. A final polishing step was then performed on a polishing wheel with 0.25 micrometer diamond suspension. The samples were carbon coated, and elemental analysis was performed with a Hitachi S-3100N Scanning Electron Microscope equipped with an EDS probe (Voltage=10 keV). Most samples exhibited three distinct phases as revealed by the Back Scattered Electron (BSE) imaging. EDS measurements identified $Gd_{1.07(2)}Co_{1.07(4)}Si_{1.85(2)}$ as the composition of the major phase (corresponding well to $GdCoSi_2$), with the remaining phases being $Gd_{1.10(2)}Co_{2.01(4)}Si_{1.88(1)}$ (which is assigned to $GdCo_2Si_2$) and $Gd_{1.03(2)}Co_{0.58(3)}Si_{1.37(1)}$, which is most likely a ternary variant of the $GdSi_2$ phase. No substantial quantities of elements other than Gd, Fe, Si, C (as expected for a carbon coated sample) and O (as a minor gadolinium oxide impurity in some samples) were detected.

Differential Scanning Calorimetry. Differential scanning calorimetry (DSC) data were collected on a TA Differential Scanning Calorimeter Q2000. The heating rate was 5

K/min under a nitrogen gas flow of 50 mL/min. The sample was cycled twice between 300 K and 430 K, with additional cycle then being carried out between 323 K and 430 K. The data were analyzed with the TA Universal Analysis software.

Electronic Structure Calculations. First principles GGA-DFT calculations were performed on both the *Pbcm* and *Cmcm* versions of $GdCoSi_2$ using the Vienna Ab Initio Simulation Package (VASP).[58,59] The calculations employed the generalized gradient approximation (GGA) and the projector augmented wave (PAW) potentials provided with the package.[60,61] The calculations were carried out in the high precision mode (corresponding to an energy cutoff of 335.0 eV) with Γ-centered 16×16×4 k-point grids. Both structures were geometrically optimized using a two-step procedure: first the atomic parameters were relaxed while the unit cell was held constant then all of the structural parameters were released. In terms of total energy, the two forms of $GdCoSi_2$ were calculated to be extremely similar, with the *Cmcm* form being 0.008 eV/atom lower in energy. The inability to predict the preference for the *Pbcm* structure at low temperatures may be due to our approximation of the Gd 4f electrons as part of the ion cores (which should not affect our qualitative bonding analysis of the two structures).

The GGA-DFT band energies and density of states distributions were then used for the refinement of the Hückel parameters with the program eHtuner.[62] Once the parametrization was completed, Hückel calculations were performed with YAeHMOP[63] to obtain the Hamiltonian matrix at the Γ point for a 4×4×2 supercell. Using this matrix, the raMO analysis[64] was carried out with the in-house Matlab programs figuretool2 and mak-

eraMO. Additional computational details, including the DFT-calibrated Hückel parameters used, are provided in the Appendix A.

2.4. Synthetic results for the room temperature structure of $GdCoSi_2$.

The preparation of $GdCoSi_2$ as the principal phase via solid state synthesis required an iterative approach. In our initial attempts, we used near stoichiometric ratios of the elements, and tried terminating the annealing step of the synthesis with both quenching and slow-cooling. In the quenched sample, the strongest peaks in the collected powder X-ray diffraction pattern matched well with the pattern expected for the reported $CeNi_{1-x}Si_2$-type $GdCoSi_2$ phase, with weaker peaks being attributable to a $GdCo_2Si_2$ impurity or simply background noise. The slow cooled samples also contained strong peaks that matched $GdCoSi_2$, but with a wider variety of weaker peaks potentially matching the expected patterns of Gd_6Co_5 and $Gd_6Co_3Si_2$. The cleaner results obtained from the quenched sample led us to adopt this procedure in our subsequent syntheses.

SEM-Back Scattered Electron (BSE) investigations of the quenched sample provided greater detail into its multiphasic character. As is illustrated in Figure 2.1a, the BSE images of the sample exhibit a striped appearance, with domains of at least three different shades of grey (dark, medium, and light) being present. Energy Dispersive X-ray Spectroscopy (EDS) identified the dark phase $GdCo_2Si_2$, while the medium phase corresponded to the elemental composition $GdCoSi_2$expected for as our target phase. The domains appearing as lighter were found to have the approximate composition $Gd(CoSi)_2$, presumably

a colored variant of $GdSi_2$, though such a phase did not appear in the powder diffraction data. Altogether, the X-ray diffraction and EDS confirmed that we had obtained the targeted $GdCoSi_2$ phase, albeit in a mixture with other Gd-Co-Si phases.

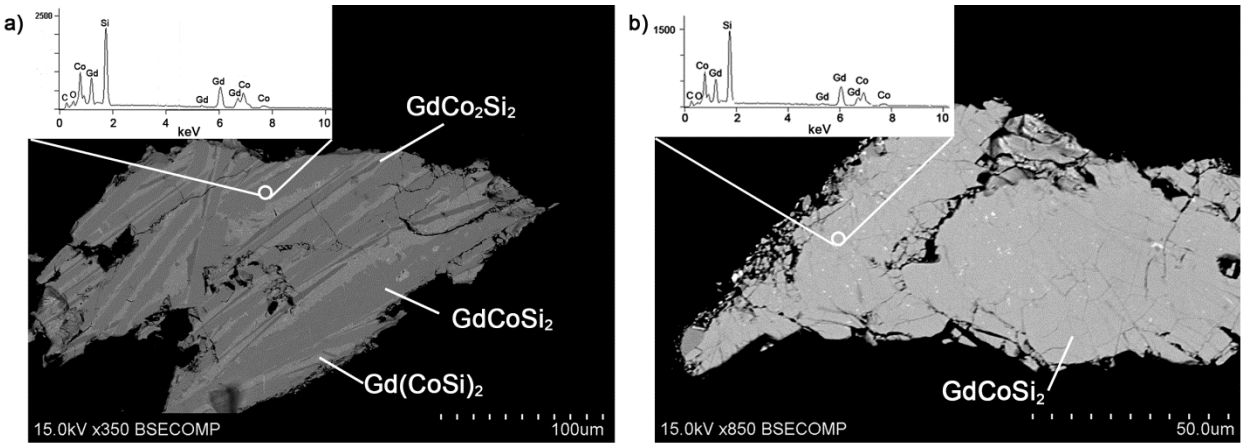

Figure 2.1. Back Scattered Electron images of two samples of $GdCoSi_2$ from (a) the initial synthesis terminated by quenching, and (b) a subsequent synthesis with improved accuracy in the stoichiometric loading.

Based on these results, we carried out additional rounds of syntheses of $GdCoSi_2$ with additional care being taken to ensure a precise stoichiometric loading, and the samples were quenched after annealing. The new strategy yielded a sample that showed minimal impurities according to powder X-ray diffraction (with $GdCo_2Si_2$ being again chief among the side products). SEM-BSE images and EDS measurements confirmed the higher phase purity of this sample (Figure 2.1b).

2.5. Structure determination and description room temperature structure of $GdCoSi_2$.

To explore the structural details of the $GdCoSi_2$, we screened suitably-sized fragments selected from our crushed reaction products using single crystal X-ray diffraction. A promising crystal was found from our first quenched sample, whose diffraction pattern could be indexed with an orthorhombic cell of dimensions a = 4.25 Å, b = 15.79 Å, and c = 3.98 Å. These dimensions correspond well to the 4.07 Å × 16.30 Å × 4.00 Å orthorhombic cell previously reported for $GdCoSi_2$,[48,52] but with noticeably shorter b and longer a-axis lengths.

A closer inspection of the diffraction pattern of this crystal (and others taken from this and other samples) revealed more significant differences from the literature structure of $GdCoSi_2$. The $CeNi_{1-x}Si_2$ structure type originally assigned to $GdCoSi_2$ adopts the space group *Cmcm*, whose *C*-centering leads to the reflection condition (*hkl*): $h+k=2n$. Reflections with indices such that $h+k$= odd are then expected to be systematically absent. As can be seen in the *hk*o layer of the diffraction pattern (Figure 2.2), however, relatively strong reflections are found throughout reciprocal space that violate this condition. In light of these clear violations, the structure must then be assigned a primitive centering, with the highest possible space group symmetry consistent with the remaining systematic absences then being *Pbcm*. With the space group thus assigned, the structure solution and refinement proceeded smoothly.

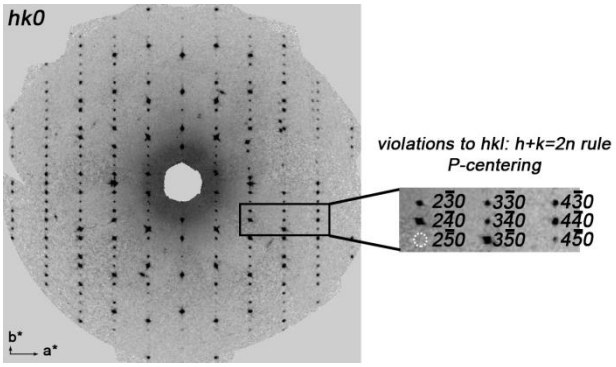

Figure 2.2. Reciprocal space reconstruction of the *hk*o layer of the diffraction data collected on $GdCoSi_2$ at room temperature. Note the violations of the *hkl*: $h+k = 2n$ reflection condition expected for a *C*-centered structure.

As hinted by the cell dimensions and lower symmetry, the resulting structure represents a superstructure of the $CeNi_{1-x}Si_2$ type. In our structural description it is then informative to begin with the parent structure. The crystal structure of the previously reported $CeNi_{1-x}Si_2$-type $GdCoSi_2$ structure is shown in Figure 2.3a. Here, somewhat flattened $Si@Co_4$ tetrahedra link together through shared edges into layers, reminiscent of similar layers that occur in the $ThCr_2Si_2$-type $GdCo_2Si_2$ (though with the Co and Si site occupancies swapped).[65] The Co atoms of these layers are capped by Si atoms, with the capping atoms of neighboring layers interdigitating to create Si zigzag chains running along the *c* axis. The Gd atoms fill spaces in the resulting framework in coordination environments that locally resemble those of the Al atom sites of the AlB_2 type. Two symmetry-distinct Si sites emerge from this arrangement: those in the Co-Si layers, and those in the Si zigzag chains.

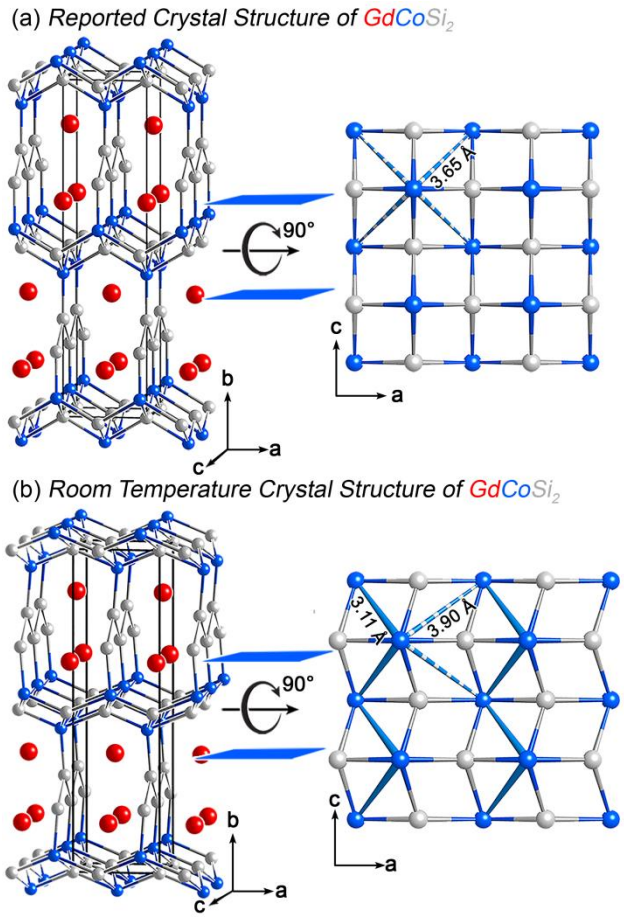

Figure 2.3. The room temperature crystal structures $GdCoSi_2$, illustrated by comparison with the parent $CeNi_{1-x}Si_2$ structure type. (a) The $CeNi_{1-x}Si_2$-type structure reported by Pelizzone *et al.* for $GdCoSi_2$.[48] (b) The room temperature *Pbcm* structure of $GdCoSi_2$ determined here.

When the refined *Pbcm* structure, the major differences occur in the layers of $Si@Co_4$ tetrahedra, as is most easily visualized from a top-down view (right sides of Figures 2.3a and 2.3b). From this view, the layer in the original *Cmcm* structure appears as highly symmetrical. The Si atoms trace out a square net, with the Co atoms lying alternatively above and below these squares. In this arrangement, each Co atom has four Co-Si contacts within the layer all at a distance of 2.36 Å. For each Co atom, the closest Co neighbors are

the four Co atoms on the other side of the layer, at 3.65 Å (dotted blue lines). These long Co-Co distances suggest little interaction between the Co atoms.

In the *Pbcm* structure, however, much of this symmetry is broken. The Co atoms have shifted along the *a*-axis to condense into chains (blue cylinders in Figure 2.3b), with each Co atom now having two much closer Co neighbors at 3.11 Å (as well as two Co-Co contacts that are now much more distant). Similar displacements occur for the Si atoms to maintain similar Co-Si distances to those of the parent structure. Overall, the edge-sharing connectivity of the $Si@Co_4$ tetrahedra is maintained, but their shapes have become distorted through flattening and elongation.

The loss of the *C*-centering during this distortion can be perceived by comparing the tetrahedral layers centered at $y=0$ and $y=1/2$ along their edges (left panels of Figure 2.3). For the $y=0$ layer, the opposing motions creating of the Co-Co chains appear from the side as a shearing distortion. The Co atoms at the top of the layer ($y>0$) have shifted toward the left relative to the Si atoms, while those at the bottom of the layer ($y<0$) have moved to the right. In the $y=1/2$ layer, a similar shearing distortion is present, but this time the directionality is opposite. Now the top set of Co atoms moves to the right rather than to the left, and the lower Co atoms move to the left rather than to the right. The distortions in the two layers are mirror images of each other (related, strictly speaking, through a *c*-glide operation perpendicular to *b*) but not translationally equivalent.

In summary, our structural solution for $GdCoSi_2$ shows both similarities and differences to that reported previously. The overall site occupancies and topology match well with the $CeNi_{1-x}Si_2$ type. However, when we zoom-in on the more detailed features of the

structure, greater complexity comes into focus. The $Si@Co_4$ tetrahedral layers exhibit a shearing distortion which groups the Co atoms into zigzag chains.

How should we account for these differences from the previously reported $GdCoSi_2$ structure? The earlier studies of $GdCoSi_2$ based their conclusions on powder X-ray diffraction data, from which small distortions within the unit cell would be difficult to detect. Indeed, based on our simulated powder patterns for the *Pbcm* $GdCoSi_2$ phase, the violations to the *C*-centering reflection condition would not be expected to be discernable using a laboratory powder diffractometer. It could then be tempting to consider the *Pbcm* $GdCoSi_2$ model as a revision to the earlier structure.

A comparison of the unit cell parameters between the current and previous models, however, suggests that such a conclusion is hasty. While powder diffraction does not have a high sensitivity to small displacements within a unit cell, it is exquisitely accurate in the determination of unit cell dimensions. The significant differences in the cell parameters could then suggest that the *Cmcm* structure is phase distinct from that described here. Indeed, the shorter *b*-axis and longer *a*-axis of the *Pbcm* structure could be attributed to the flattening and lengthening of the tetrahedral layers on going to the superstructure. As we will see below, an electronic structure analysis highlights how a phase transition to its *Cmcm* parent structure should be facile, setting the stage for the experimental investigations of the high-temperature behavior of $GdCoSi_2$.

2.6. Clues to chemical origins of the superstructure in the density of states (DOS) distribution of $GdCoSi_2$.

In the previous section, we saw that $GdCoSi_2$ appears to adopt a superstructure of the $CeNi_{1-x}Si_2$ type previously assigned to it. The details of this superstructure are focused in the structure's layers of edge-sharing $Si@Co_4$ tetrahedra running perpendicular to the *b*-axis, with distortions leading to the formation of the Co zig-zag chains and significant displacements in the Si square nets. What drives these structural changes relative to the original $CeNi_{1-x}Si_2$ structure type? Here, we will see that electronic structure calculations can provide a simple account for these structural observations in terms of the electron counts on the Co atoms.

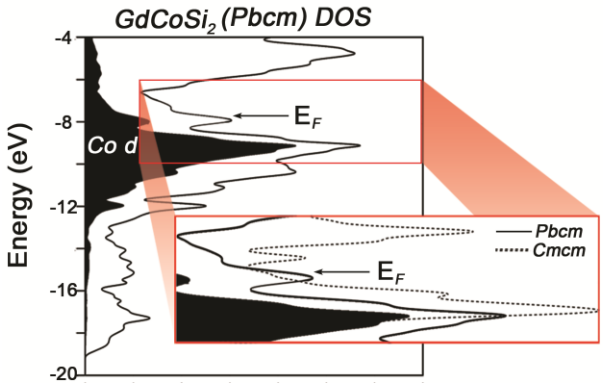

Figure 2.4. The electronic density of states (DOS) distribution of $GdCoSi_2$, calculated using a DFT-calibrated Hückel model. The main panel shows the DOS curve for the *Pbcm* structure described in this Article, while the inset compares this DOS distribution near the Fermi energy (E_F) with that of the phase's *Cmcm* parent structure. The contributions from the Co 3d orbitals are shaded in black.

In investigating the origins of the *P*-centered variant, we calculated its electronic DOS distribution using a DFT-calibrated Hückel model (Figure 2.4). Here the generic features of an intermetallic based on a late transition metal can be seen: a dense block of Co d states (with contributions from the Si 3p) occurs between about -8 and -12 eV. Below this block of d-based levels broader features are found corresponding to Si 3s-rich bands from ca. -19 to -13. The Fermi energy (E_F) lies just at the top of the Co d levels, corresponding to a nearly filled set of d orbitals. Rather than coinciding with DOS minimum, as might be expected from the complete filling of the 3d subshell of the Co atoms, however, the E_F crosses a sharp peak in the DOS—not an obvious sign of electronic stability. From the DOS distribution of the *Pbcm* structure alone, then, it is difficult to see how the observed structure leads to enhanced stability.

Given that Co is a 3d metal, it is conceivable that the superstructure could be coupled with magnetic ordering to open up a more pronounced pseudogap at the E_F. However, the Co d contribution to the DOS is in fact relatively small at the E_F. Indeed, the only magnetic phenomena observed in earlier magnetic susceptibility measurements on $GdCoSi_2$ was the antiferromagnetic ordering of the Gd 4f electrons at 7.5 K.[6]

The role of the superstructure becomes clearer when we compare these results to the DOS distribution that would occur for an idealized $GdCoSi_2$ phase in the originally reported *Cmcm* geometry, shown in the inset to Figure 2.4 as a dotted curve. Near the E_F (which differs by only 0.157 eV between the *Pbcm* and *Cmcm* structures), the DOS curves for the structures have similar magnitudes. A bigger difference occurs in the features just below the E_F: for the *Cmcm* structure, the DOS distribution grows in a very large peak of

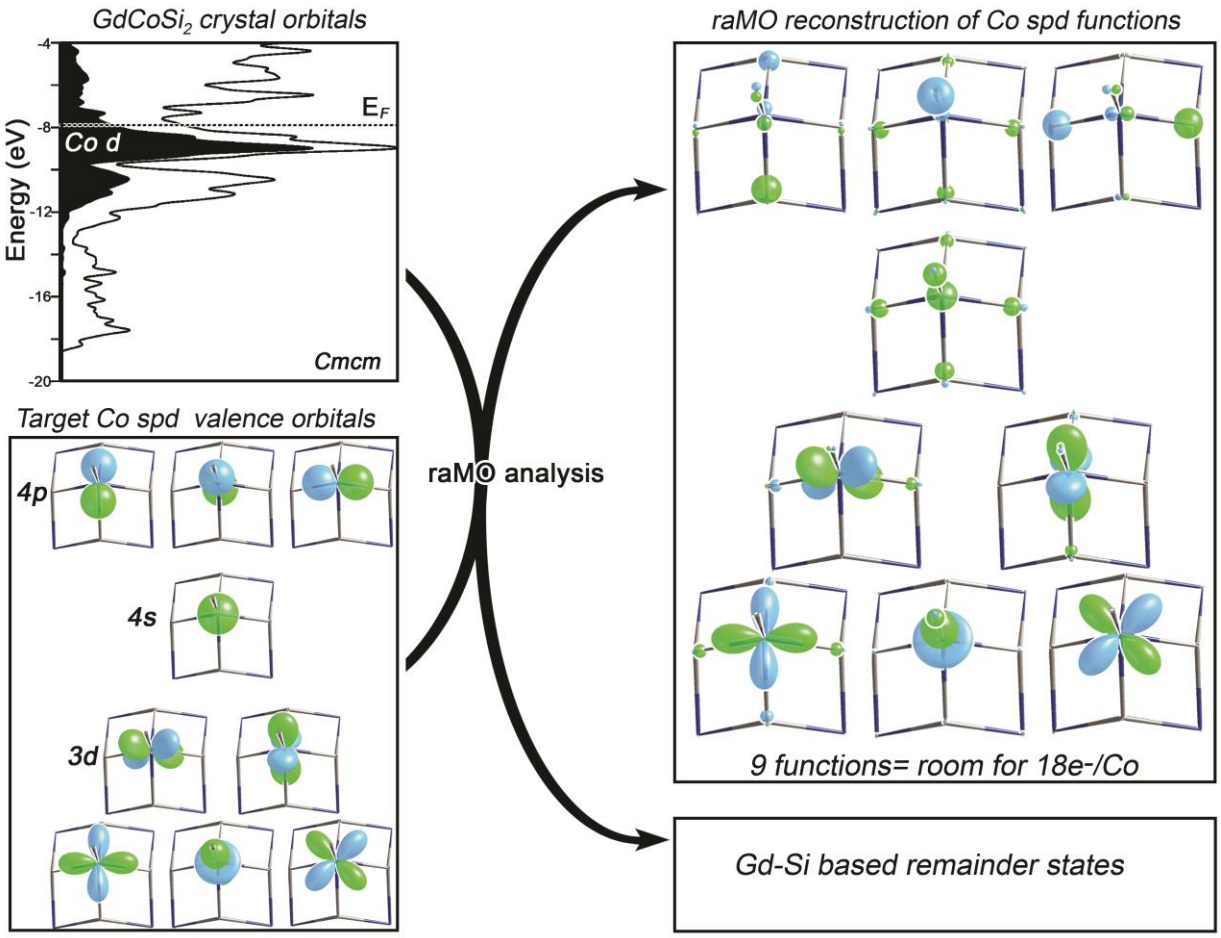

Figure 2.5. Schematic illustration of the application of the reversed approximation Molecular Orbital (raMO) method to a *Cmcm* version of $GdCoSi_2$. The occupied crystal orbitals are used to reconstruct the 9 spd valence atomic orbitals of the transition metal (T) atoms. The reconstructions correspond to electron pairs associated with the nodal characters of the T valence orbitals. Electrons not mapped to the T centers are grouped in wavefunctions associated with the Gd-Si sublattice. These remainder states can then be used for investigation of bonding subsystems that are orthogonal to the T atomic orbitals.

Co 3d-rich states as we move down by about 1 eV. In the *Pbcm* structure, on the other hand, the corresponding peak is shifted downwards. The sharp spike at the E_F in the *Pbcm*

structure's DOS then appears as being based on states that are left behind during the stabilization of states further down in energy during the structural transformation.

These results suggest that the formation of the *Pbcm* superstructure in $GdCoSi_2$ does not result from the familiar Peierls distortion or Fermi surface nesting mechanisms.[66] The outcomes of either of these mechanisms would be the opening of a pseudogap at the E_F, via interactions focused on specific segments of k-space. Instead, the superstructure seems to lie in the stabilization of the large number of states spread throughout the Brillouin zone, all collected under a large peak in the DOS.

2.7. Electron counting in $GdCoSi_2$, guided by the reversed approximation MO approach.

From a comparison of the DOS distributions of *Pbcm* and *Cmcm* versions of the $GdCoSi_2$ structure, the formation of the superstructure appears to be connected to the stabilization of a large number of Co 3d-based crystal orbitals just below the E_F. We now turn to the question of how the observed superstructure provides this stability.

A productive approach to examining how the distortions of the crystal structure lead to changes in bonding is offered by the reverse approximation Molecular Orbital (raMO) analysis. In this method, a model MO diagram hypothesized to describe the bonding at one point of the structure is chosen, then the occupied crystal orbitals of the system are used as a basis set for the reproduction of these target MOs.[64] The resulting raMO functions provide the best approximation to the proposed MO diagram possible from the

electronic structure of the full compound. In this way, the raMO approach allows us to quickly test analogies between molecular and intermetallic chemistry.

For transition metal-containing intermetallics, we have found that analogies to the 18 electron rule of molecular transition metal complexes are especially productive. Through the examination of a large number of structure types, this connection has been formalized in the 18-*n* rule: each transition metal (T) atom in these compounds will require 18-*n* valence electrons to achieve a closed shell configuration, where *n* is the number of electron pairs it shares covalently with other T atoms (often in multicenter functions isolobal to classical σ bonds).[27-29] Much like the Zintl concept, this rule can be applied by simply counting the number of T-T contacts in a compound to obtain a prediction of the ideal electron count (while keeping a look-out for bonds between main group atoms that do not interact with the T atoms). However, the applicability of the 18-*n* rule is best verified through raMO analysis.

To begin our raMO analysis, we take our model MO diagram as consisting of a Co atom's nine s, p, and d valence orbitals that would form the basis of an 18-electron configuration, and then attempt to reconstruct these functions using the occupied crystal orbitals of $GdCoSi_2$.

This process is illustrated for an idealized *Cmcm* version of $GdCoSi_2$ in Figure 2.5. The filled crystal orbitals are represented by the states below the E_F in the DOS curve (top, left). These states are then analyzed in terms of how well they can reproduce the valence orbitals of the Co atoms (bottom, left). The output of the raMO calculation consists of the raMO reconstructions of the Co orbitals (top, right), and additional functions orthogonal

to the Co-based raMOs (bottom, right). These remainder functions contain all of system's electrons that are not associated with the Co atoms in question.

In the top right panel of Figure 2.5, we show the raMO reconstructions of a Co atom's s, p, and d valence orbitals. The nodal character of each of these valence orbitals is well-represented by their corresponding functions, with the original atomic orbital being delocalized to various degrees through bonding to the surrounding Si atoms. This result indicates that each of the Co s, p, and d orbitals can be associated with an electron pair, corresponding to a filled 18 electron configuration. As none of the raMO functions show significant overlap with the neighboring Co atoms, the Co atoms have filled close-shells independently of each other. This scheme would account for 18 of $GdCoSi_2$'s 1×3+1×9+2×4 = 20 valence electrons per formula unit (assuming that the Gd atoms contribute 3 valence electrons each).

We thus have two electrons/formula unit unaccounted for, which would belong to some bonding subsystem orthogonal to the Co orbitals. These additional electrons are accounted for in the raMO analysis with the Gd-Si-based functions that appear as left over when we attempted to reproduce all of the structure's Co s, p, and d valence orbitals (Figure 2.5, bottom right). Given the larger electronegativity of Si over Gd, it is likely that these extra electrons are more strongly associated with the Si atoms. The bonding in the remainder functions can be probed by using them in a second round of raMO analysis in which we attempt to reproduce filled octets on the Si atoms.

As noted previously in the structural description, there are two symmetry-distinct Si sites in the structure. One Si site forms the central positions of the edge-sharing $Si@Co_4$

tetrahedra and lies in layers perpendicular to *b* forming square nets. Due to the high degree of involvement of these Si atoms in bonding to the Co atoms, a raMO analysis of the non-Co-based raMOs leads to no significant population of these Si atoms' valence s and p orbitals.

The other Si position, however, gives a very different result. These Si atoms create zig-zag chains that pass between the layers of tetrahedra, and have only one contact each to Co atoms. Their other near-neighbor interactions are along Gd-Si and Si-Si contacts that trace out slabs of an AlB_2-type $GdSi_2$ structure. In Figure 2.6, we show the raMO reconstructions of the s and p valence orbitals for one of the Si atoms in these slabs, using the remainder functions from the earlier raMO step. The s-orbital and the two p orbitals lying within the $GdSi_2$-type slab show strong contributions to their raMO reconstructions, indicating that Si-based electron pairs can be associated with each of these orbitals. The third p orbital, however, appears to be very poorly reproduced in this analysis, suggesting that it has essentially no involvement in the remainder states. This result is easily understood from this orbital's orientation: as it points directly along a Co-Si contact, this p-orbital's contribution to the electronic structure was already accounted for in the Co-based raMOs.

The Si-based raMOs obtained through this analysis can be simply interpreted in terms of bonding along the Si zig-zag chains. Two of these raMOs, those centered by the Si s orbital and the Si p orbital oriented along the chain, show strong bonding contributions from the neighboring Si atoms. Taking linear combinations of these two raMOs produces two localized Si-Si σ bonding functions, with some support from the surround-

ing Gd atoms. The electron pairs in these functions should then be considered as shared covalently between Si atoms along the chain.

The third raMO is based on the Si p orbital that is oriented perpendicular to the plane of the Si zigzag chain. The main bonding interactions for this function occur between the central Si atom and nearby Gd atoms. This function can thus be viewed as a Si lone-pair that engages in Lewis acid/base interactions with the Gd.

Altogether, this Gd-Si remainder analysis has revealed raMOs with room for 4 electrons per Si atom in the $GdSi_2$ slabs of the structure: 2 electrons from the two σ Si-Si bonds and 2 electrons from the lone pair. The Si atoms in the zigzag chains account for half of the Si in the structure. These Si-based raMOs then contribute 4 electrons per formula unit (f.u.) to the predicted ideal electron count for the phase. When we add these to the 18 electrons/Co atom in the Co-based states, we obtain 22 electrons per formula unit as the correct count for a closed shell configuration.

This predicted electron count is in fact 2 electrons/f.u. above that given by the structure's stoichiometry, hinting that a *Cmcm* polymorph would be electron deficient. Some confirmation of this mismatch is evident in the finer details of some of the raMO functions. For example, the Si lone-pair function shows a small degree of Si-Si π bonding. Also, the Si-Si σ bonding raMOs show small contributions of Si-Si bonding further down the chain, indicating that there are not quite enough electrons for completely independent Si-Si bonds to be reconstructed.

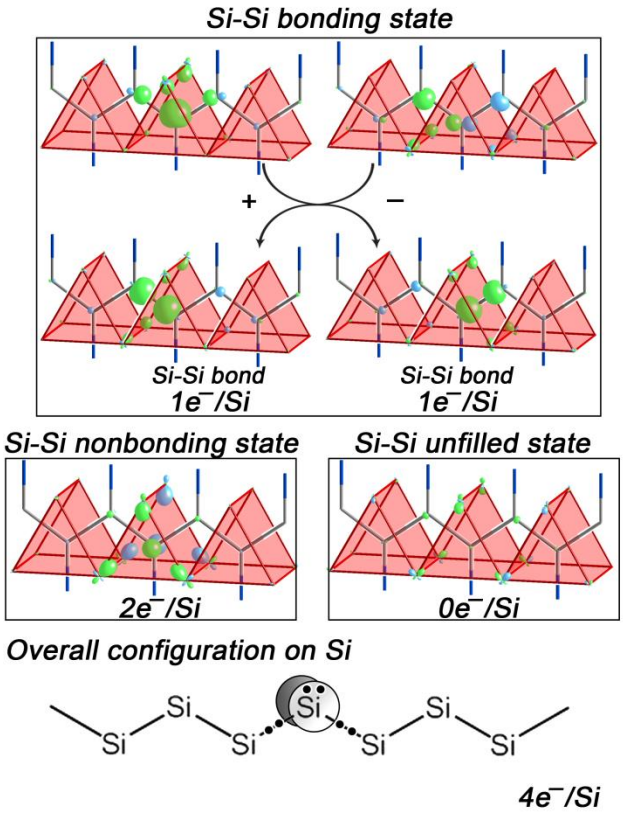

Figure 2.6. raMO reconstructions of a Si atom's 3s and 3p orbitals in $GdCoSi_2$ in the idealized *Cmcm* form, derived from the remainder functions of the previous raMO step (see Figure 2.5). The resulting Si-based functions can be interpreted roughly in terms of two Si-Si σ bonds and a Si lone pair, although the delocalization of the functions along the Si zigzag chains suggests that the system is electron deficient.

Such an electron deficiency could provide a powerful driving force for superstructure formation. As the structure is two electrons/f.u. short of the count needed to complete 18 electron configurations on the Co atoms and a Zintl-like scheme for the Si chains, this deficiency could be remedied in two simple ways. First, additional Si-Si bonds could be created to lower the preferred electron count for the Si sublattice. Alternatively, Co-Co

bonds could be formed to reduce the electrons needed for their filled octadecets, in-line with the 18-*n* rule for transition metal (T)-main group (E) intermetallics.

Our earlier description of the *Pbcm* superstructure points toward the latter mechanism. The geometries of the Si zigzag chains are largely unchanged relative to the simpler *Cmcm* structure. Instead the symmetry-breaking is concentrated in the layers of $Si@Co_4$ tetrahedra (Figure 2.3b), with the Co atoms condensing into their own zigzag chains. The formation of two Co-Co bonds at each Co atom would lower the number of electrons needed for a 18-electron configuration by two, exactly the number by which the original *Cmcm* structure is deficient.

This hypothesis can be tested through a raMO analysis of the *Pbcm* $GdCoSi_2$ structure. The reconstruction of the Co 4s, 4p, and 3d orbitals proceeds essentially as before, with the major differences being found in the raMOs centered by the Co s and p orbitals (Figure 2.7a). Whereas in the *Cmcm* structure no significant contributions were seen in the s and p raMOs from the neighboring Co atoms, this changes in the *Pbcm* structure. Small but noticeable bonding lobes are now present from the central atom's Co neighbors along the zigzag chain, particularly for the p_x and p_y raMOs. Co-Co interactions have begun to appear.

This Co-Co bonding can be better visualized by localizing the raMOs through taking linear combinations of them (Figure 2.7b). In this process, two bonding functions directed along Co-Co contacts emerge (with strong bridging contributions from nearby Si atoms), one for each of the central atom's Co neighbors along the chain. The Co atom's sharing of two electron pairs in functions isolobal to classical Co-Co σ bonds would allow

it to achieve an 18 electron configuration with only 16 electrons, solving the electron deficiency of the *Cmcm* structure.

However, the degree of Co-Co overlap in these functions is substantially poorer here than in other T-E compounds that use such T-T bonds to satisfy the 18 electron rule. In particular, the lobes on the neighboring Co atoms are strikingly small compared to those of central Co atom and the bridging Si atoms. This relatively small contribution from the Co neighbors would be consistent with some functions with Co-Co antibonding character being occupied, as could be expected from the E_F for the *Pbcm* structure being in a peak above a pseudogap.

Other indications of a not-quite-achieved electron precise configuration are found in the Si-based functions obtained in the remainder analysis. Similar hints of delocalization in the Si raMOs to those in Figure 2.6 are found for the *Pbcm* structure, indicating that the Si-sublattice remains slightly electron deficient. One possible explanation for these trends would be that the E_F's that optimize the Co-Co and Si-Si interactions do not quite line up. If the gap separating Co-Co σ and σ* were to lie somewhat below that for the filling of the Si-based functions, a small population of Co-Co σ* would occur before the Si-Si bonds and Si lone-pairs were fully occupied.

Some confirmation of this picture is provided by a look at how the Co-Co bonding functions change as electrons are added or removed from the structure (Figure 2.8). Adding one electron/Co atom (filling the band structure past the peak at the structure's original E_F) leads to the bonding contributions from the Co neighbors being weakened further.

On the other hand, removing one electron/Co (so that the E_F is lowered into a pseudogap) strengthens the Co-Co bonding to levels more typical of T-T isolobal bonds.

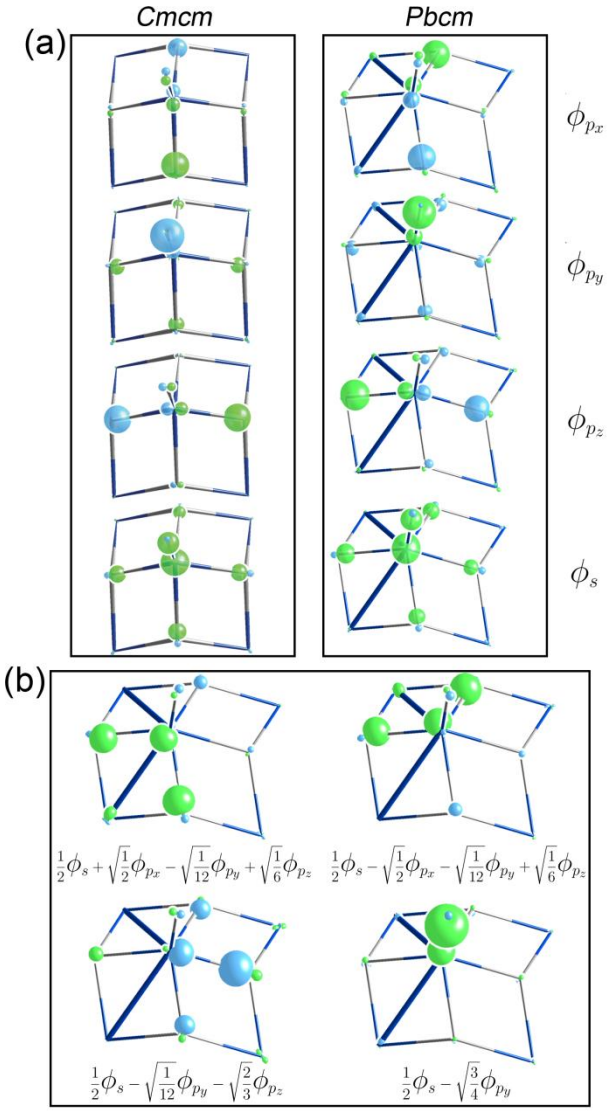

Figure 2.7. The formation of Co-Co bonding on going from the idealized *Cmcm* structure of $GdCoSi_2$ to the *Pbcm* structure observed at room temperature. (a) Comparison of the raMO reconstructions of the 4s and 4p atomic orbitals of a Co atom. (b) Linear combinations of the Co raMOs for the *Pbcm* structure chosen to create maximally localized Co-Co bonding functions (top pair), with two Co-Co nonbonding orbitals also resulting (bottom pair).

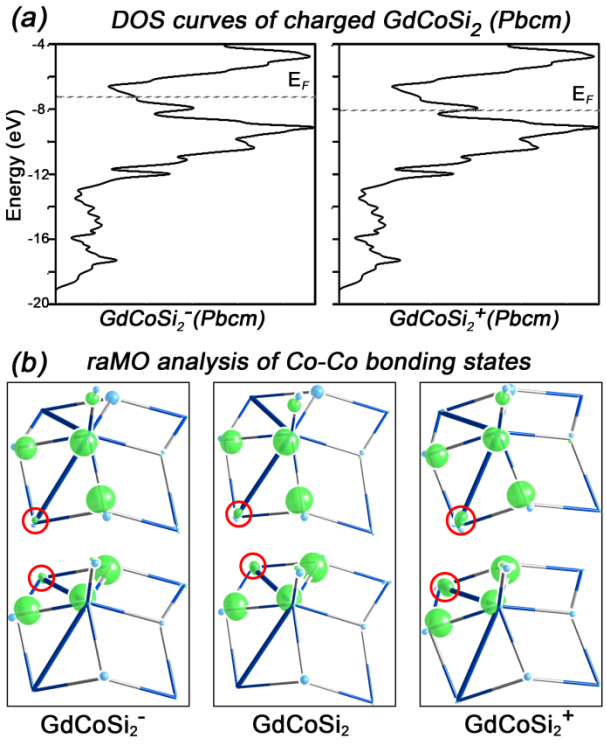

Figure 2.8. The dependence of the Co-Co bonding in the *Pbcm* structure of $GdCoSi_2$ on valence electron count. (a) Electronic DOS distributions showing the placement of the E_F for $GdCoSi_2$ with one additional or one less electron/Co atom (assuming a rigid band model). Both changes move the E_F off of the peak encountered for the neutral electron count. (b) Evolution of the Co-Co bonding functions derived in Figure 2.7 with electron count. The localized raMOs show increasing Co-Co bonding character upon removal of electrons from the system.

In summary, the *Pbcm* superstructure of $GdCoSi_2$ appears, from the structural point of view, to correspond to an electron precise phase: its 20 electrons/formula unit coincides nicely with the 16 electrons necessary to fill 18 electron configurations on the Co atoms linked into chains and the 4 needed for the Si-Si bonds and Si lone-pair. This model is confirmed loosely by the electronic structure calculations of the compound, but the ex-

pected bonding optimization appears to be frustrated by electron transfer from the Si-based states to Co-Co antibonding functions.

In this sense, the superstructure has only partially achieved its apparent purpose of providing the Co atoms with closed-shell electron configurations. The result leads us to wonder how strongly this superstructure is favored. As we demonstrate in the next section, the answer is not so strongly. In fact, moderate heating can overcome its Co-Co bonds to induce a reversible phase transformation to the *Cmcm* parent structure.

2.8. Diffusionless transition in $GdCoSi_2$.

Our theoretical analysis of the previous section suggests that $GdCoSi_2$'s formation of the *Pbcm* superstructure is driven by the need for Co-Co bonds to complete 18-electron configurations on the Co atoms. However, the superstructure appears to only be partially successful in reaching this goal, as electron transfer between the Si and Co sublattices leads to the population of some of the anti-bonding levels of the newly formed Co-Co bonds. This incomplete success suggests that the *Cmcm* parent structure may be stable at higher temperatures, i.e. the $GdCoSi_2$ structure described in previous reports may represent the high-temperature polymorph of a diffusionless phase transition.

To test this hypothesis, we carried out variable temperature single crystal X-ray diffraction experiments on a crystal taken from our highest purity $GdCoSi_2$ sample. A data set collected on the crystal at room temperature again exhibited the strong reflections vio-

lating the systematic absence law for a *C*-centered cell (Figure 2.9a). The refinement of the structure from this data led to the same *Pbcm* superstructure we described above (Figure 2.10a).

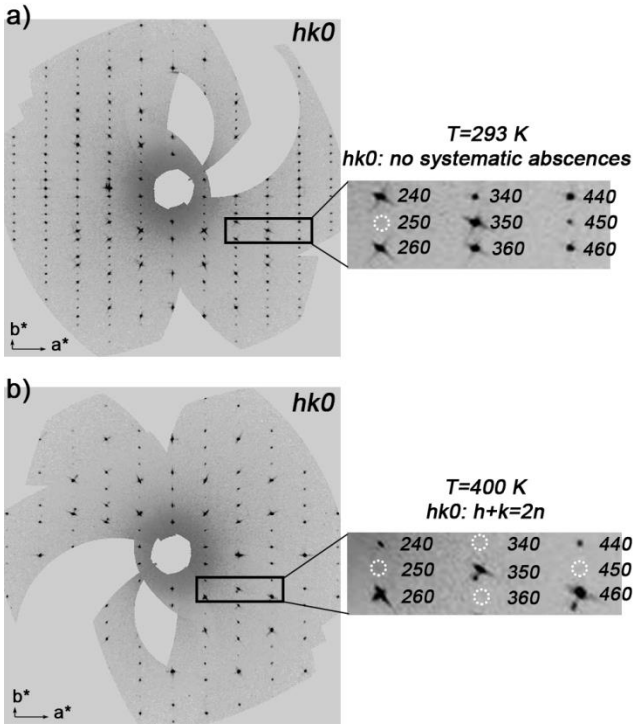

Figure 2.9. A *Pbcm* to *Cmcm* transition observed in single crystal X-ray diffraction data for $GdCoSi_2$. Reciprocal space reconstructions of the *hk*o layer derived from the frame data are shown for the data sets collected at (a) 293 K and (b) 400 K. The room temperature data set features strong reflections that violate the *C*-centering of the *Cmcm* space group. (b) These violators essentially disappear at 400 K.

Upon heating the crystal to 400 K, the unit cell showed a noticeable change in dimensions: the *a*-parameter contracted from 4.26 to 4.08 Å, and the *b*-parameter expanded from 15.81 to 16.25 Å, while the *c*-parameter remained essentially constant. These changes

are clearly not the result of a typical lattice expansion that accompanies the heating of a material, as these changes in fact lead to a smaller overall cell volume for the higher-temperature structure. In fact, the new parameters are quite consistent with the previously reported cell for *Cmcm* $GdCoSi_2$.

Inspection of the full dataset collected at 400 K confirms this interpretation. As is clear for the *hk*o layer in Figure 2.9b, the reflections violating the *C*-centering reflection condition have essentially vanished. The structure solution and refinement of the structure in *Cmcm* symmetry proceeded smoothly, yielding a parent $CeNi_{1-x}Si_2$ type structure (Figure 2.10b). A comparison of the layers of the $Si@Co_4$ tetrahedra between the two structures reveals that the shearing distortion present in the low-temperature *Pbcm* superstructure has vanished in the high-temperature *Cmcm* form.

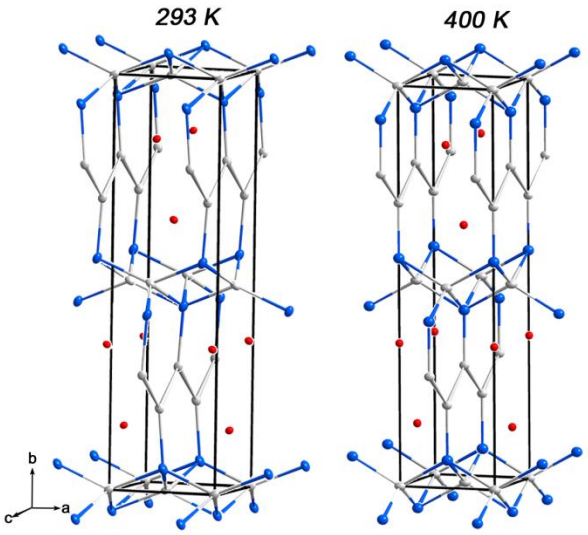

Figure 2.10. The crystal structures of $GdCoSi_2$ at room temperature (*Pbcm*) and 400 K (*Cmcm*) refined from single crystal X-ray diffraction data. The atoms are shown with 50% probability ellipsoids.

The elongation and contraction of the *b* and *a* axis lengths, respectively, during this transformation can then be traced to corresponding changes in the shapes of the $Si@Co_4$ tetrahedra: as the need for close contacts between Co atoms on opposite sides of the layer is relaxed, the tetrahedra become less flattened, leading to both an increased thickness (expansion along *b*) and a shorter repeat period in the layer along the direction of alternation of short and long Co-Co contacts (contraction along *a*). The relative changes in the cell parameters that result are anisotropic as the *a* parameter is equal to the repeat period of the layer of $Si@Co_4$ tetrahedra along that direction, while the *b* parameter accounts not only for the thickness of these layers but also for that of the AlB_2-type slabs between the layers. An interesting outcome of this disparity is that the unit cell volume actually decreases on going from the low-temperature polymorph to the high-temperature one (see Table 2.1).

Is this transformation reversible? To answer this question, we began cooling the crystal, while collecting unit cell runs every 10 K. The unit cells from 390 to 370 K were quite similar to that of the *C*-centered cell at 400 K. At 360 K, however, the cell dimensions of the *Pbcm* structure were recovered, suggesting that the reverse transition occurred somewhere between 370 and 360 K upon cooling. This cell remained essentially unchanged when we cooled the sample further down to 300 K.

To gain a qualitative sense of the temperature for the *Pbcm* to *Cmcm* transition, we then heated the sample in 10 K increments. The parameters for the *Pbcm* cell remained up until 380 K. Then at 390 K, the dimensions switched to those of the *Cmcm* cell. The tran-

sition temperature in the heating direction is then somewhere between 380 and 390 K. Similar results were obtained for a crystal taken from one of our earlier syntheses.

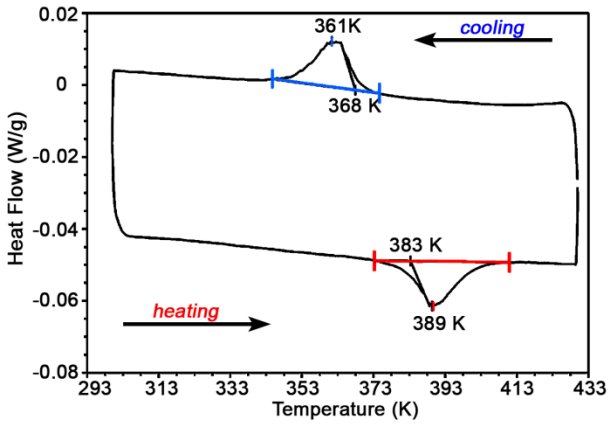

Figure 2.11. Differential scanning calorimetry (DSC) data for $GdCoSi_2$. Upon heating, an endothermic transition occurs with an onset temperature of 383 K. The cooling curve exhibits an exothermic transition at the onset of 368 K. These two features are interpreted as corresponding to the *Pbcm-Cmcm* transition of $GdCoSi_2$ upon heating, and its reversal on cooling. The persistence of these features over several cycles confirms the reversible nature of this transition. The hysteresis in the transition temperatures suggests that the transformation is a first-order process. See Appendix A for additional DSC scans.

These single crystal experiments suggest that the *Pbcm* and *Cmcm* forms of $GdCoSi_2$ are related through a martensitic transition. To better determine the transition temperature, we carried out differential scanning calorimetry experiments on a ground portion of the same sample from which the single crystal analyzed in Figures 2.9 and 2.10 was taken. In these measurements the sample was cycled between room temperature and about 433 K. During heating of the sample, the onset of an endothermic transition is ob-

served at 383 K (Figure 2.11). On the cooling side of the temperature cycle, an exothermic transition is observed at 371 K.[67] These onset temperatures of 383 K and 371 K for the transition upon heating and cooling, respectively, lie within the temperature ranges suggested by the single crystal X-ray diffraction experiments.

As we described earlier, the difference in cell-parameters of the *Pbcm* and *Cmcm* forms of $GdCoSi_2$ should be clearly evident in the powder X-ray diffraction patterns of the two phases. In order to also maximize the resolution between the peaks of the two phases, powder diffraction patterns were measured at various temperatures using the 11-BM beamline at the Advanced Phonon Source (Argonne National Laboratory). At room temperature, the pattern could be indexed with *Pbcm* $GdCoSi_2$ polymorph and a $GdCo_2Si_2$ impurity (Figure 2.12, bottom patterns). The weak peaks remaining were identified as belonging to a small amount of the *Cmcm* form of $GdCoSi_2$ phase, perhaps stabilized at room temperature by epitaxial matching with the $ThCr_2Si_2$-type $GdCo_2Si_2$ impurity.

Heating the powder sample from room temperature to 380 K showed a growth of peaks initially assigned to the *C*-centered polymorph and the decrease in intensity of *P*-centered phase's peaks. At 400 K, the *Cmcm* peaks dominated the pattern (Figure 2.12, top patterns). Cooling down to 360 K reversed the trend, with the peaks for the *Pbcm* polymorph reemerging (see Appendix A).

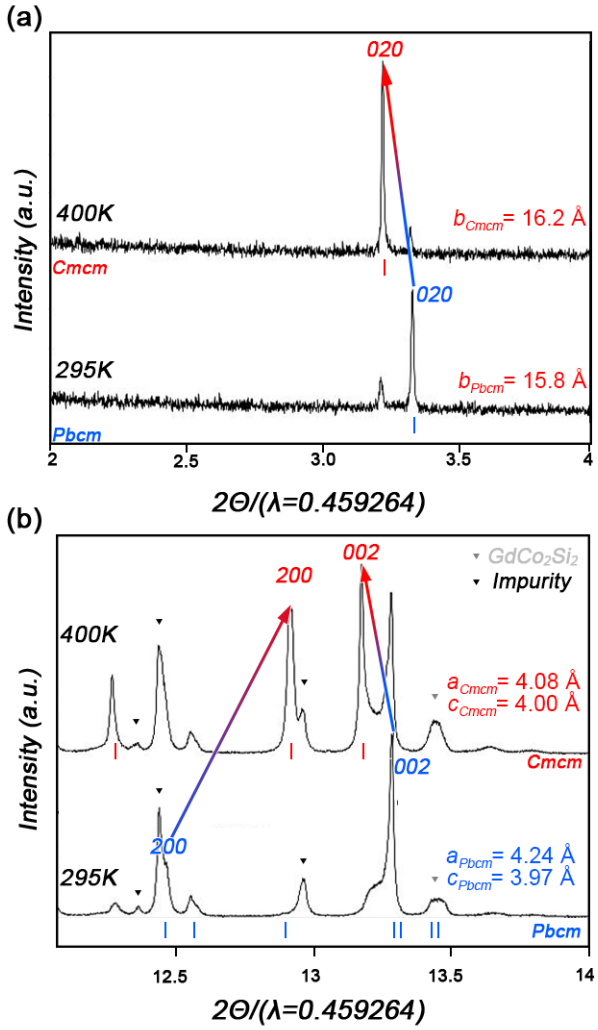

Figure 2.12. Selected regions of the synchrotron powder X-ray diffraction patterns of $GdCoSi_2$ collected at room temperature and 400K. (a) (020) peak of *Pbcm* $GdCoSi_2$ gives way to a new peak to the left upon heating, indicating the shortening of the *b*-axis. (b) The (200) and (202) peaks move to the right and left of their original positions, respectively, on going from 295 to 400 K, signaling a dramatic shortening of the *a*-axis and minute lengthening of the *c*-axis upon heating. These shifts are consistent with a transition to the *Cmcm* form $GdCoSi_2$ observed in the variable temperature single crystal X-ray diffraction experiments.

Altogether, the results of single crystal X-ray diffraction, synchrotron powder X-ray diffraction, and DSC measurements point toward the *Pbcm* and *Cmcm* polymorphs being stable at different temperature ranges, confirming the expectations derived from the theoretical analysis of the previous section. Below about 380 K, the *Pbcm* structure is adopted, while at higher temperatures, the higher symmetry *Cmcm* structure becomes preferred. The abrupt, as opposed to gradual, changes in the cell parameters as a function of temperature and the observed hysteresis are suggestive of a first order transition

2.9. Conclusions

Our original interest in the Gd-Co-Si system was based on the question of how competing interaction types are resolved in ternary compounds. In this Article's exploration of the compound $GdCoSi_2$, we see that one possible outcome is the frustrated formation of bonds that can form the basis of temperature-induced phase transitions. We observed that the room temperature crystal structure of $GdCoSi_2$ is actually a *Pbcm* superstructure of the *Cmcm* $CeNi_{1-x}Si_2$ type previously assigned to it. Using DFT-calibrated Hückel theory and the reversed approximation MO analysis, we were able to trace this superstructure to the partially successful formation of the Co-Co bonds needed for the completion of 18 electron configurations on these atoms. The complete formation of these bonds, however, is impeded by electron transfer from Si-based orbitals to the Co-Co σ^* levels, allowing for the *Cmcm* basic structure to be stabilized by entropic effects at the moderate temperature of ca. 380 K.

The bonding model explaining the facile nature of this transition offers predictions for how the transition temperature can be adjusted through elemental substitution. Changes in the composition that tend to strengthen the transition metal-transition metal (T-T) bonding in the low-temperature form should stabilize the superstructure to higher temperatures. Such stabilization could be achieved by partial replacement of Co by a transition metal with a lower valence electron count or d orbitals with a greater radial extent, e.g. Fe, Ru, Rh, or Ir.

Conversely, substitutions aimed at destabilizing the T-T bonding could lower the transition temperature. Examples here could include the substitution of Gd with a larger lanthanide (RE) element or main group element (E) with a larger group 14 element, forcing the T atoms to approach each other from a longer distance when making T-T bonds. The substitution of Si by a less electronegative element from its column would also enhance the electron transfer from the main group sublattice, weakening the T-T bonds. A challenge in testing these predictions will be the prevalence of T vacancies and variations in the T-E occupation patterns that can arise in $CeNi_{1-x}Si_2$ type phases.

The origin of $GdCoSi_2$'s *Pbcm-Cmcm* transition also points toward a possible design principle for diffusionless transformations: the presence of such transitions can be promoted by frustrated bonding in which electronically-driven distortions from a simple structure type are dampened by competition from other interactions.

Building on the specific mechanism in $GdCoSi_2$, we could scan the crystal structure databases for T-containing phases whose structures nominally violate the 18-*n* rule, but also contain a competing bonding type, such as E-E or RE-E bonding. These structures

can then be investigated for previously unnoticed superstructures and phase transitions. Such studies would not only provide a rigorous test of the limits of our current bonding concepts for RE-T-E compounds, but also likely will uncover new diffusionless (and perhaps even martensitic) transitions needed for the creation of new advanced materials responsive to their environments.

Acknowledgement

We thank Vincent Yannello, Katerina Hilleke, and Yiming Guo for valuable discussions on the application of the raMO method, as well as one of the reviewers for insights into the nature of the phase transition presented. We thank Men Zhu for assistance and guidance with the DSC measurements. In addition, we are grateful to Dr. Lynn Ribaud at the APS 11-BM beamline for the collection of the synchrotron diffraction data. Use of the Advanced Photon Source at Argonne National Laboratory was supported by the U. S. Department of Energy, Office of Science, Office of Basic Energy Sciences, under Contract No. DE-AC02-06CH11357. We gratefully acknowledge the financial support of the Wisconsin Alumni Research Foundation. The research involved calculations using computer resources supported by National Science Foundation Grant CHE-0840494.

2.10. References

(1) Nishiyama, Z. *Martensitic Transformations*; Academic Press: New York, 1978.

(2) Tammann, G.; Scheil, E. *Z. Anorg. Allg. Chem.* **1926**, *157*, 1-21.

(3) Kim, H. Y.; Hashimoto, S.; Kim, J. I.; Hosoda, H.; Miyazaki, S. *Mater. Trans., JIM* **2004**, *45*, 2443-2448.

(4) Kim, H. Y.; Oshika, N.; Kim, J. I.; Inamura, T.; Hosoda, H.; Miyazaki, S. *Mater. Trans., JIM* **2007**, *48*, 400-406.

(5) Kokorin, V. V.; Konoplyuk, S. M.; Dalinger, A.; Thürer, S.; Gerstein, G.; Maier, H. J. *Appl. Phys. Lett.* **2015**, *106*, 131908.

(6) Zhao, Y.-Y.; Hu, F.-X.; Bao, L.-F.; Wang, J.; Wu, H.; Huang, Q.-Z.; Wu, R.-R.; Liu, Y.; Shen, F.-R.; Kuang, H.; Zhang, M.; Zuo, W.-L.; Zheng, X.-Q.; Sun, J.-R.; Shen, B.-G. *J. Am. Chem. Soc.* **2015**, *137*, 1746-1749.

(7) Wei, Z. G.; Sandstroröm, R.; Miyazaki, S. *J. Mater. Sci,* **1998**, *33*, 3743-3762.

(8) Van Humbeeck, J. *Adv. Eng. Mater.* **2001**, *3*, 837-850.

(9) Tegus, O.; Brück, E.; Zhang, L.; Dagula; Buschow, K. H. J.; de Boer, F. R. *Physica B: Condens. Matter* **2002**, *319*, 174-192.

(10) Brück, E.; Ilyn, M.; Tishin, A. M.; Tegus, O. *J. Magn. Magn. Mater.* **2005**, *290–291, Part 1*, 8-13.

(11) Li, B.; Ren, W. J.; Zhang, Q. *Appl. Phys. Lett.* **2009**, *95*, 172506-172506.

(12) Magen, C.; Morellon, L.; Algarabel, P. A.; Marquina, C.; Ibarra, M. R. *J. Phys.: Condens. Matter* **2003**, *15*, 2389.

(13) Antoni, P.; Lluís, M.; Mehmet, A. *J. Phys.: Condens. Matter* **2009**, *21*, 233201.

(14) Spiridon, I. P.; Lohan, N. M.; Suru, M. G.; Mihalache, E.; Bujoreanu, L. G.; Pricop, B. *Met. Sci. Heat Treat.* **2016**, *57*, 548-552.

(15) Bowden, H. G.; Kelly, P. M. *Acta Metall.* **1967**, *15*, 1489-1500.

(16) Xie, Z. L.; Sundqvist, B.; Hänninen, H.; Pietikäinen, J. *Acta Metall. Mater.* **1993**, *41*, 2283-2290.

(17) Jona, F.; Marcus, P. M. *J. Phys.: Condens. Matter* **2003**, *15*, 7727.

(18) Kainuma, R.; Imano, Y.; Ito, W.; Sutou, Y.; Morito, H.; Okamoto, S.; Kitakami, O.; Oikawa, K.; Fujita, A.; Kanomata, T.; Ishida, K. *Nature* **2006**, *439*, 957.

(19) Wang, Z.; Xiu, P.; Huang, L.; Nie, Z.; Zeng, J.; Brown, D. E.; Ren, Y.; Wang, Y. *J. Magn. Magn. Mater.* **2016**, *406*, 179-183.

(20) Poutcharovsky, D. J.; Yvon, K.; Parthé, E. *J. Less Common Met.* **1975**, *40*, 139-144.

(21) Borshchevsky, A.; Fleurial, J.-P. *J. Cryst. Growth* **1994**, *137*, 283-288.

(22) Rochnia, M.; Deiseroth, H.-J. *Croat. Chem. Acta* **1995**, *68*, 701-708.

(23) Choe, W.; Pecharsky, V. K.; Pecharsky, A. O.; Gschneidner, K. A.; Young, V. G.; Miller, G. J. *Physical Review Letters* **2000**, *84*, 4617-4620.

(24) Audebrand, N.; Ellner, M.; Mittemeijer, E. J. *J. Alloys Compd.* **2003**, *353*, 228-232.

(25) Muñoz-Perez, S.; Cobas, R.; Susilo, R. A.; Cadogan, J. M. *Journal of Physics: Conference Series* **2011**, *286*, 012018.

(26) Mazzone, D. G.; Gerber, S.; Gavilano, J. L.; Sibille, R.; Medarde, M.; Delley, B.; Ramakrishnan, M.; Neugebauer, M.; Regnault, L. P.; Chernyshov, D.; Piovano, A.; Fernández-Díaz, T. M.; Keller, L.; Cervellino, A.; Pomjakushina, E.; Conder, K.; Kenzelmann, M. *Phys. Rev. B* **2015**, *92*, 024101.

(27) Yannello, V. J.; Fredrickson, D. C. *Inorg. Chem.* **2014**, *53*, 10627-10631.

(28) Kilduff, B. J.; Yannello, V. J.; Fredrickson, D. C. *Inorg. Chem.* **2015**, *54*, 8103-8110.

(29) Yannello, V. J.; Fredrickson, D. C. *Inorg. Chem.* **2015**, *54*, 11385-11398.

(30) Schäfer, H.; Eisenmann, B.; Müller, W. *Angew. Chem. Int. Ed.* **1973**, *12*, 694-712.

(31) Chemistry, structure, and bonding of Zintl phases and ions; Kauzlarich, S. M., Ed.; VCH: New York, 1996.

(32) Pearson, W. B. *Acta Crystallogr. B* **1968**, *24*, 1415-22.

(33) Simon, A. *Angew. Chem. Int. Ed.* **1983**, *22*, 95-113.

(34) Tsai, A. P. *J. Non-Cryst. Solids* **2004**, *334-335*, 317-322.

(35) Berns, V. M.; Fredrickson, D. C. *Inorg. Chem.* **2013**, *52*, 12875-12877.

(36) Berns, V. M.; Engelkemier, J.; Guo, Y.; Kilduff, B. J.; Fredrickson, D. C. *J. Chem. Theory Comput.* **2014**, *10*, 3380-3392.

(37) Berns, V. M.; Fredrickson, D. C. *Inorg. Chem.* **2014**, *53*, 10762-10771.

(38) Dörrscheidt, W.; Savelsberg, G.; Stöhr, J.; Schäfer, H. *J. Less Common Met.* **1982**, *83*, 269-278.

(39) Chabot, B.; Parthé, E.; Steinmetz, J. *J. Less Common Met.* **1986**, *125*, 147-156.

(40) Szytuła, A.; Ptasiewicz-Bak, H.; Leciejewicz, J.; BaŻela, W. *J. Magn. Magn. Mater.* **1989**, *80*, 189-194.

(41) Johrendt, D.; Lux, C.; Mewis, A. *Z. Naturforsch., B: Chem. Sci.* **1996**, *51*, 1213-1214.

(42) Penc, B.; Szytuła, A.; Wawrzyńska, E.; Hernandez-Velasco, J. *J. Alloys Compd.* **2004**, *366*, 120-123.

(43) Norlidah, N. M.; Venturini, G.; Malaman, B.; Ressouche, E. *J. Alloys Compd.* **1998**, *265*, 77-80.

(44) Esmailzadeh, S.; Hoffmann, R.-D.; Pöttgen, R. *Z. Naturforsch., B: Chem. Sci.* **2004**, *59*, 1451-1457.

(45) Peter, S. C.; Pöttgen, R. *Monatsh. Chem.* **2007**, *138*, 381-388.

(46) Bodak, O. I.; Gladyshevskii, E. I. *Kristollagrafiya* **1969**, *14*, 6.

(47) May, N.; Schaefer, H. *Z. Naturforsch., B: Chem. Sci.* **1974**, *29*, 20-23.

(48) Pelizzone, M.; Braun, H. F.; Muller, J. *J. Magn. Magn. Mater.* **1982**, *30*, 33-36.

(49) Norlidah, N. M.; Venturini, G.; Malaman, B. *J. Alloys Compd.* **1998**, *268*, 193-198.

(50) Sun, Z.-M.; Pan, D.-C.; Lei, X.-W.; Mao, J.-G. *J. Solid State Chem.* **2006**, *179*, 3378-3384.

(51) Zhuravleva, M. A.; Bilc, D.; Pcionek, R. J.; Mahanti, S. D.; Kanatzidis, M. G. *Inorg. Chem.* **2005**, *44*, 2177-2188.

(52) Wu, S.; Yan, J.; Zhang, L.; Qin, W.; Zeng, L.; Zhuang, Y. *Z. Metallkd.* **2000**, *91*, 373-374.

(53) *CrysAlisPro Software System, Version 171.37.35*; Rigaku Oxford Diffraction: Yarnton, UK, 2015.

(54) Oszlányi, G.; Sütő, A. Acta Crystallogr. Sect. A: Found. Crystallogr. **2004**, 60, 134-141.

(55) Oszlányi, G.; Sütő, A. Acta Crystallogr. Sect. A: Found. Crystallogr. **2005**, 61, 147-152.

(56) Katrych, S.; Weber, T.; Kobas, M.; Massüger, L.; Palatinus, L.; Chapuis, G.; Steurer, W. *J. Alloys Compd.* **2007**, *428*, 164-172.

(57) Petříček, V.; Dušek, M.; Palatinus, L. *Jana2006. The Crystallographic Computing System*; Institute of Physics: Praha, Czech Republic, 2006.

(58) Kresse, G.; Furthmüller, J. *Phys. Rev. B* **1996**, *54*, 11169-11186.

(59) Kresse, G.; Furthmüller, J. *Comput. Mater. Sci.* **1996**, *6*, 15-50.

(60) Blöchl, P. E. *Phys. Rev. B* **1994**, *50*, 17953-79.

(61) Kresse, G.; Joubert, D. *Phys. Rev. B* **1999**, *59*, 1758-1775.

(62) Stacey, T. E.; Fredrickson, D. C. *Dalton Trans.* **2012**, *41*, 7801-7813.

(63) Landrum, G. A.; Glassey, W. V. YAeHMOP: Yet Another extended Hückel Molecular Orbital Package. YAeHMOP is freely available via the Internet at http://sourceforge.net/projects/yaehmop/. Last accessed: Mar. 20, 2016.

(64) Yannello, V. J.; Kilduff, B. J.; Fredrickson, D. C. *Inorganic Chemistry* **2014**, *53*, 2730-2741.

(65) Rieger, W.; Parthé, E. *Monatsh. Chem.*, *100*, 444-454.

(66) Canadell, E.; Whangbo, M. H. *Chem. Rev.* **1991**, *91*, 965-1034.

Chapter 3.

18-electron resonance structures in the BCC transition metals and their CsCl-type derivatives

This chapter has been published: Vinokur, A. I.; Fredrickson, D.C., *Inorg. Chem.*, **2017**, 56, 2834-42.

3.1. Abstract

Bonding in elemental metals and simple alloys has long been thought of as involving intense delocalization, with little connection to the localized bonds of covalent systems. In this Article, we show that the bonding in bcc structures of the Group 6 transition metals can in fact be represented, via the concepts of the 18-*n* rule and isolobal bonding, in terms of two balanced resonance structures. We begin with a reversed approximation Molecular Orbital (raMO) analysis of elemental Mo in its bcc structure. The raMO analysis indicates that, despite the low electron count (6 valence electrons/Mo atom), 9 electron pairs can be associated with any given Mo atom, corresponding to a filled 18-electron configuration. Six of these electron pairs take part in isolobal bonds along the second-nearest neighbor contacts, with the remaining three (based on the t_{2g} d orbitals) interacting almost exclusively with first-nearest neighbors. In this way, each primitive cubic network defined by the second-nearest neighbor contacts comprises an 18-*n* electron system with $n = 6$, which essentially describes the full electronic structure of the phase. Of course, either of the two interpenetrating primitive cubic frameworks of the bcc structure can act as a basis for this discussion, leading us to write two resonance structures with equal weights for bcc-

Mo. The electronic structures of CsCl-type variants with the same electron count can then be interpreted in terms of changing the relative weights of these two resonance structures, as is qualitatively confirmed with raMO analysis. This combination of raMO analysis with the resonance concept offers an avenue to extend the 18-*n* rule into other transition metal-rich structures.

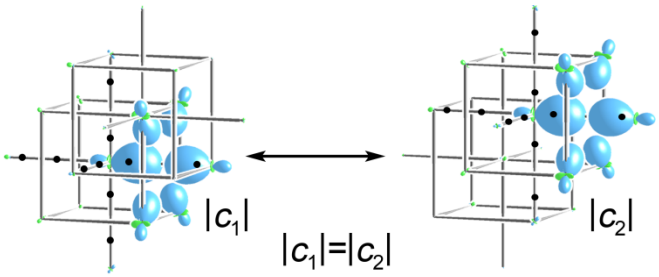

Figure 3.0. The bonding molybdenum metal (bcc) can be represented in terms of two resonance structures of equal weights, where each structure adheres to principles of the 18-*n* rule and isolobal bonding..

3.2. Introduction

It would be difficult to find a family of inorganic substances that have been subjected to more electronic structure calculations than the elemental metals. Historically, the pure metals have served as a benchmark for theoretical methods that would be applied to a wider range of materials.[1-4] The band structures of sp metals such as Na and Al provided some of the early successes of the nearly-free electron model, which, through the concept of the Jones Zone,[5,6] is one of the most powerful approaches to rationalizing the stability of Hume-Rothery phases[7] and many complex intermetallics related to icosahedral quasicrys-

tals.[8,9] Similarly, reproducing the crystal structures of the metallic elements has been a traditional test for electronic structure models, including two of the central foundations of modern quantum mechanical calculations on materials: the tight-binding (either on its own or in combination with a NFE picture to capture the different behavior of the d and sp electrons in transition metals) and the pseudopotential methods.[10-17] Even now, the elemental metals are some of the first examples considered by students learning band theory.

Given this near constant interrogation of the electronic structure of the metallic elements, it is perhaps surprising how new chemical bonding phenomena continue to be recognized in them. Consider the transition metals. Burdett and Lee traced the structural preferences of the d-block to the topology of the orbital overlaps through the method of moments (where the fourth moment of the d-only density of states is found to be the determining factor),[15] while Lee and Hoffmann connected the transition in the relative stabilities of the bcc and fcc structures in the mid-d-block to a Jahn-Teller effect breaking the degeneracy between k-points related by rotational symmetry (rather than connected through a nesting vector, as in the Peierls distortion) on the Fermi surface.[18] The correlation between the non-bonding vs. antibonding character at the Fermi Energy and the type of magnetic ordering exhibited by a metallic system was first noted in the elemental phases of the 3d metals.[19,20] Furthermore, the maximum in melting points of the d-block metals at or near group 6 can be rationalized in terms of Cr, Mo, and W being at the neutral point on a moments-derived acidity scale.[21]

Recently, our interest in the high-melting group 6 transition metals was renewed by our recognition of the importance of the 18-electron rule of molecular chemistry in a varie-

ty of intermetallic compounds. Using the reversed approximation Molecular Orbital (raMO) approach, we determined that the crystal orbitals of transition metal-main group (T-E) intermetallics can be interpreted in terms of electron pairs associated with the nodal properties of each of the T atoms' s, p, and d orbitals (in functions delocalized through bonding across the T atom's coordination environment). Bonding often arises between the T atoms when an insufficient number of electrons are present for each T atom to have an 18-electron configuration independently, leading to the 18-*n* rule: each transition metal will require 18-*n* electrons to achieve a closed shell, where *n* is the number of electrons that atom gains through the covalent sharing of electrons between T atoms in multicenter functions isolobal to classic σ or π T-T bonds.[22-24] raMO analyses have shown the applicability of this scheme to over 30 transition metal-main group binary structure types.[24]

Some of these successes involved structures closely related to the fcc and bcc structures adopted by many elemental transition metals. For example, the CsCl-type phase CoAl is derived by placing different atom types on the positions at the corner and center of the bcc unit cell,[24] while the structures of $MoCuGa_5$,[25] $ScAl_3$, $ZrAl_3$, and VAl_3 are similarly colored variants of the fcc structure.[24] The 18-electron concept thus appeared to be encompassing compounds increasingly similar to the T elements, and we were eager to test whether it could indeed apply to the elemental phases.

Toward that end, we present here a raMO analysis of elemental Mo, showing how electronic pseudogaps near the Fermi energy for group 6 metals, as well as their bcc geometry and high-melting points, can be understood in a surprisingly simple way. The 18-electron bonding scheme will again come to the forefront, but this time with an intriguing

variation: two different 18-electron schemes can be drawn, which are envisioned as resonance structures that together represent the metal's bonding. With this picture in place, the electronic structures of CsCl-type variants (both transition metal-transition metal and transition metal-main group) can be derived by simply changing the relative weights of the two resonance structures in the bonding. The resulting synergy between the 18-*n* and resonance structure concepts hints at a broader approach to electron counting in the diverse family of transition metal-rich intermetallic compounds.

3.3. Experimental Section

To provide a reference for the calibration of simple Hückel models of bcc-Mo, ZrRu, and a hypothetical CsCl-type RuSn compound, the GGA-DFT electronic structures of these phases were calculated with the Vienna Ab Initio Simulation Package (VASP),[26,27] in the high precision mode and using the projector augmented wave (PAW) potentials[28,29] provided with the program. The calculations employed Γ-centered k-point grids of sufficient fineness to converge the total energy to 1 meV/atom: 20×20×20 for Mo (primitive cell), 15×15×15 for RuSn, and 10×10×10 for ZrRu. The energy cutoffs used were 280.7 eV for Mo, and 266.6 eV for both ZrRu and RuSn. All three structures were geometrically optimized, with single point calculations then yielding the band energies and density of states (DOS) distributions.

GGA-DFT band energies and DOS distributions were used for refinement of the parameters of simple Hückel models with the program eHtuner,[30] with the actual Hückel calculations being carried out with YAeHMOP.[31] Once these parameters were finalized,

supercells (results obtained for 3 × 3 × 3 supercells of the conventional cell for Mo and ZrRu, and 6 × 6 × 6 supercells for RuSn and the ZrRu-RuSn intermediates are featured in the figures) were constructed to fold multiple k-points of the primitive cell onto the Γ point.[32] The Γ point Hückel Hamiltonian matrices for the supercells were then calculated with YAeHMOP. These matrices served as the main input for the reversed approximation Molecular Orbital (raMO) analyses,[22] as performed with our in-house Matlab programs figuretool2 and makeraMO. Additional computational details are provided in the Appendix B.

3.4. Bonding analysis of bcc-Mo

In this Article, we will explore how the 18-*n* bonding scheme recently developed for transition metal-main group (T-E) intermetallic phases can be extended to the main group-free cases, e.g. an elemental transition metal. The applicability of such bonding schemes to new materials is simply tested by the reversed approximation Molecular Orbital (raMO) method, which may be viewed as a generalization of the Wannier-based approaches that have yielded many insights into the bonding of inorganic materials.[33-37] Here, one begins by proposing a simple MO diagram that is expected to capture the bonding in a local region of the structure. A model Hamiltonian operator is then constructed whose eigenfunctions are the MOs of this diagram. Next, matrix elements of this operator are calculated using the full compound's occupied crystal orbitals as a basis set. The diagonalization of this matrix to produce eigenvectors then yields the best approximations to

the proposed MO diagram that can be constructed from the true electronic structure of the compound as well as a set of additional functions that represent electrons not involved in the proposed bonding scheme.

As a first step in building a raMO-based bonding picture of group 6 metals, we calculated the DFT electronic structure of elemental Mo, as a representative of the column free from the complex spin-density waves observed in Cr.[38] The electronic density of states (DOS) distribution obtained exhibits features common to the transition metal elements (Figure 3.1a). A pair of large peaks corresponding to the relatively localized Mo d orbitals dominates the DOS curve, as is confirmed from the large d-orbital contributions in the projected DOS (shaded area). In addition, a small tail of states stretches downwards below the d-bands, corresponding to the nearly-free-electron-like bands constructed from the Mo s and p orbitals. The Mo d-rich region of the DOS has a largely bimodal character with two major groups of states separated by a deep well from -7.2 eV to -8.5 eV. The Fermi energy (E_F) lies within this DOS valley. Often such placement of the E_F in a pseudogap is associated with a near half-filling of the d-orbitals, with the states below the E_F being bonding and those above being antibonding—a situation analogous to a large HOMO-LUMO gap in a molecule.

In our earlier investigations of transition metal-based intermetallics, we found that the raMO analysis often traced such pseudogaps to the filling of the 18-electron configurations around the T atoms, in which electron pairs occupy functions with the same nodal properties as the s, p, and d orbitals of the central T atom. To see whether a similar scheme may apply here, we construct a model Hamiltonian operator for elemental Mo for which

the eigenfunctions are simply a Mo atom's one 5s, three 5p, and five 4d orbitals (Figure 3.2). From the orientations of these orbitals relative to the Mo coordination environment in bcc-Mo, we can already see several connections to molecular T chemistry. The five d orbitals are divided by the octahedral symmetry of the environment into two sets, as noted earlier by Goodenough.[39] The t_{2g} set (d_{xy}, d_{xz}, and d_{yz}) is well-oriented for interactions with the first-nearest neighbors (1NNs) defining a cube at a distance of 2.72 Å. The lobes of the e_g orbitals (d_{z2} and d_{x2-y2}), on the other hand, point directly to the second nearest neighbors (2NNs) that trace out an octahedron at 3.14 Å, with the 1NNs in fact lying on the nodal surfaces of the atomic orbitals.[18]

These differences align with the view of the bcc structure as consisting of two interpenetrating primitive cubic (*cP*) lattices: the e_g d orbitals have strong interactions along the edges of the individual primitive cubic sublattices, while the t_{2g} orbitals represent interactions between the sublattices. As we proceed with our analysis, this distinction will take on a larger significance.

Once we have set up the model Hamiltonian based on a Mo atom's s, p, and d valence orbitals, we next use the occupied crystal orbitals of Mo metal as an approximate basis set for solving for eigenfunctions of this operator. This is accomplished by constructing matrix elements of the operator between the crystal orbitals of Mo metal, and then diagonalizing the resulting matrix to obtain eigenvectors. Those eigenvectors with non-zero eigenvalues are the raMO functions, the best possible reconstructions of the original s, p, and d atomic orbitals that can be made from the wavefunctions of the full compound. As the raMO functions form an orthogonal set derived from a unitary transformation of the

occupied crystal orbitals, they are each occupied by a pair of electrons, and sum to the same total Hückel energy as the original wavefunctions.

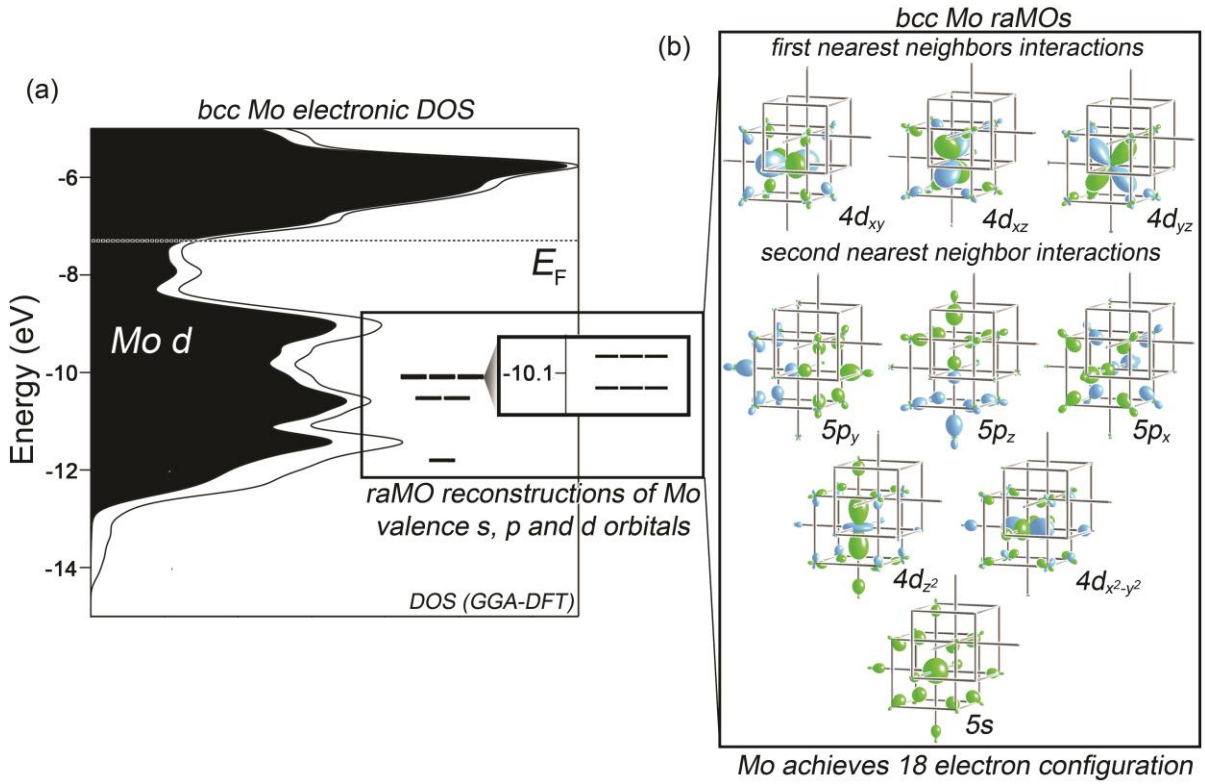

Figure 3.1. Interpretation of the bonding in elemental bcc-Mo in terms of the filling of 18-electron configurations on its atoms. (a) Electron density of states (DOS) distribution of Mo metal, with the contributions from the Mo d shaded. (b) Reconstructions of the 9 s, p, and d valence atomic orbitals of one of the Mo atoms using the reversed approximation MO (raMO) method. The resulting raMOs can be interpreted as comprising 6 bonding states and 3 non-bonding states, corresponding to an 18-electron configuration on the Mo center.

The resulting raMOs for elemental Mo are shown in Figure 3.1b. Each of the nine functions shares its symmetry properties with one of the original Mo atomic orbitals, but

now rather than being focused specifically on the central atom they are spread out through bonding contributions from the neighboring Mo atoms.

As anticipated by our earlier discussion of the distinct overlaps of the e_g and t_{2g} d orbitals, the raMO functions can be divided into two sets. The first group (those centered by the $4d_{xy}$, $4d_{yz}$, and $4d_{xz}$ orbitals) exhibit bonding interactions primarily between the central Mo and its 1NNs. The remaining six raMOs (centered by the 5s, $4p_x$, $4p_y$, $4p_z$, $4d_{z2}$, and 4_{dx2-y2} orbitals) have a significant presence of bonding character on the 2NNs. Aside from the 5s-based raMO, the contributions of the 1NNs are smaller here, or even of π rather than σ character.

Such strong interactions of the a_{1g} 5s, t_{1u} 5p, and e_g 4d orbitals with the 2NNs is quite familiar from molecular chemistry, as these follow the same irreducible representations as an octahedral set of σ-ligands. Indeed, this combination of atomic orbitals is the basis of the Pauling's sp^3d^2 hybrid orbitals that point toward the corners of an octahedron.[40] On the left panel of Figure 3.3, we show the bonding functions that result from taking the appropriate linear combinations to create these sp^3d^2 hybrid functions. Six functions result, the largest components of which are lobes directed along one of the edges of the *cP* sublattice, stemming both from the central atom and from the corresponding vertex of the octahedron formed by the 2NNs. The bonding interaction along each contact is supported by contributions from the four Mo atoms from the 1NN environment. The overall appearance of each function is of a six-center bonding function with the same symmetry properties as a classical Mo-Mo σ bond, a type of function we refer to for brevity as an isolobal bonding function.[24,41] As these six isolobal bonding functions form an or-

thonormal set created from linear combinations of occupied crystal orbitals, they can each be considered as filled with an electron pair.

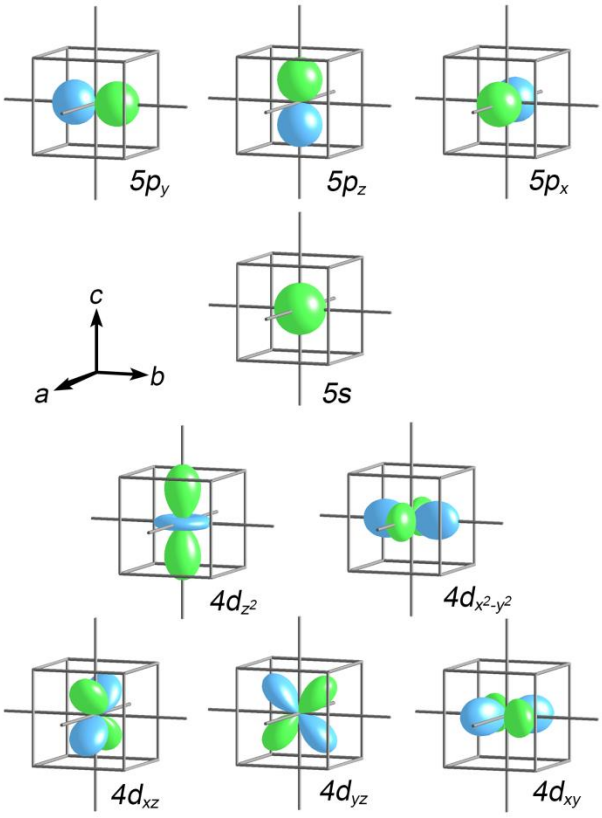

Figure 3.2. The valence s, p, and d atomic orbitals of Mo drawn in the crystal structure of bcc-Mo.

In summary, the edges of the *cP* network can be viewed as isolobal Mo-Mo bonds constructed from the Mo 5s, 5p, $4d_{z2}$ and $4d_{x2-y2}$ orbitals of the corners of the network. The remaining atomic orbitals of the network, the $4d_{xy}$, $4d_{xz}$, and $4d_{yz}$, are nonbonding with respect to the cube edges, and instead contribute to the bonding between the two *cP* networks in the bcc structure.

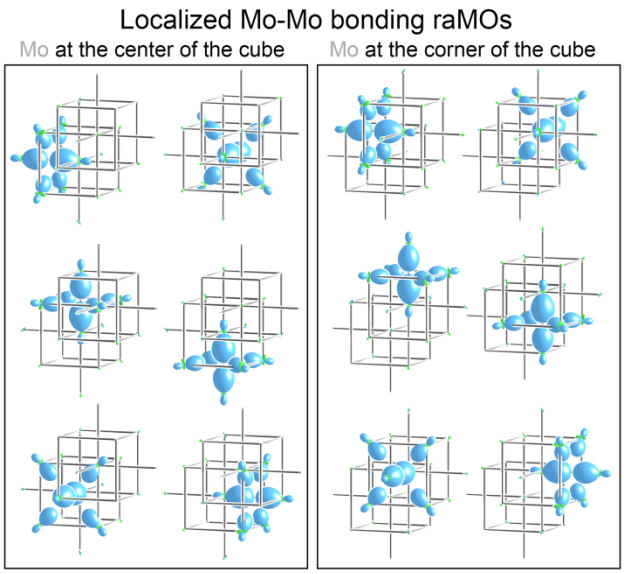

Figure 3.3. Linear combinations of raMOs (LC-raMOs) with bonding along the second nearest neighbors reveal six isolobal Mo-Mo σ bonds. The identical LC-raMOs are obtained for Mo atoms at the unit cell center or unit cell corner.

The use of all of the Mo atomic orbitals in interatomic interactions suggests that the 18-electron rule should play a role in the bonding in some way. In fact, if we continue to focus our attention on just one of the two primitive cubic lattices in the structure, the ra-MO results can be simply interpreted in terms of the 18-*n* rule applicable to T-E intermetallics. Filling the $4d_{xy}$, $4d_{xz}$, and $4d_{yz}$ orbitals with electron pairs and providing each of the six sp^3d^2 hybrid orbitals with one electron to share covalently with its neighbor would require 3×2 + 6×1 = 12 electrons, i.e. given the 6 isolobal bonds that the Mo participates in, it only needs 18-6 = 12 electrons for a closed shell. This is exactly the number of electrons that a single unit cell of the primitive cubic network contains (6 from the *cP* network being considered, 6 from the second network that interpenetrates it). The deep pseudogap just

below the E_F of bcc-Mo can then be connected to the completion of these 18-electron configurations on half of the Mo atoms. The near completeness of this picture—somewhat surprising, given the metallic nature of the material—is discussed in more detail in the Appendix B.

Identical results would be obtained, of course, if we started with the Mo atoms of the other *cP* network in the structure (Figure 3.3, right), with all 12 electrons of the conventional unit cell filling the 18-electron configurations on the second set of atoms. Either representation, however, is sufficient to account for all of the electrons in the structure—in much the same way that the two resonance structures of benzene both satisfy the octet rule but neither captures the full bonding situation or 6-fold symmetry of the molecule on its own. Pursuing this analogy, we can propose two resonance structures for bcc-Mo (Figure 3.4), in each of which half of the Mo atoms achieve a filled octadecet with the support of the other half. The full electronic structure is then represented by a resonance hybrid of these two configurations whose weights, c_1 and c_2, are equal in magnitude. Just as in benzene, the creation of the hybrid restores symmetry elements that are missed by the individual resonance structures (in this case, the body-centering of the lattice).

The ability to write a closed-shell electron configuration for a bcc structure at 12 electrons/cell = 6 electrons/atom helps explain several features of the periodic table's d-block. The bcc structure and high melting points of the group 6 metals mirror this favorable bonding scheme. The tendencies for the hcp and fcc structures (which either show a shallower pseudogap or no pseudogap at all at 6 electrons/atom; see the Appendix B) to be adopted by groups with higher or lower electron counts can then be interpreted as struc-

tural responses to deviations from the bcc structure's preferred 6 valence electrons/atom count (particularly in the 4d and 5d rows, where magnetic ordering is absent). Such a view is consistent with Lee and Hoffmann's attribution of fcc-like structures in more electron-rich transition metal alloys to Jahn-Teller distortions away from the bcc structure.[18]

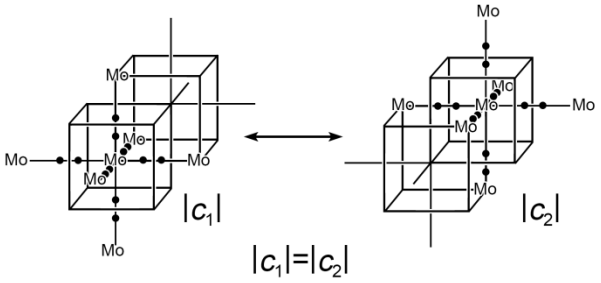

Figure 3.4. 18-electron resonance structures for bcc-Mo. In addition to the six shared electron pairs shown, each 18-electron Mo center also has six electrons in a filled t_{2g} set of d orbitals.

The perseverance of the bcc structure at 5 electrons/atom in V, Nb, and Ta but its near absence at higher electron counts mirrors a general trend in the application of the 18-*n* rule: the 18-*n* electron bonding scheme tends to be much more forgiving of electron deficiencies than of excess electrons.[24] This tendency has a simple explanation. An electron deficiency generally leads to the depopulation of the least stable electrons in the 18-*n* scheme. The result of these electrons being removed can be stronger net bonding, as can be seen by noting that the E_F for Mo metal lies at the very top of a DOS pseudogap, rather than in the middle of it. Excess electrons, on the other hand, will almost invariably occupy antibonding states, increasing the driving force for a structural response to the non-ideal electron configuration.

3.5. Bonding analysis of ZrRu

One advantage of this resonance picture is that it can easily be generalized from elemental phases like Mo to a broad range of CsCl-type derivatives of the bcc structure. To see this, we can follow a strategy used earlier to isolate the covalent and ionic components of the bonding in the bcc structure,[42] and consider an intermetallic phase obtained by replacing Mo with a 1:1 mixture of its neighbors at equal distance to its left and right in the 4d row to maintain the same average electron count. One example of such a CsCl-type compound is ZrRu, where rather than two Mo atoms each bringing 6 electrons to the conventional unit cell, the Ru atom in the cell contributes 8 electrons with the Zr atom adding 4 more. While the overall electron count is the same, however, the landscape the electrons inhabit in the lattice is different. The two interpenetrating primitive cubic lattices in the structure are now populated by different atom types, one by Ru and one by Zr..

A general picture of how this move to a binary compound affects the electronic structure is provided by the GGA-DFT DOS distribution (Figure 3.5). As with elemental Mo, the DOS shows a bi-modal character about the E_F, with large groups of states based on transition metal d orbitals occurring above and below. The same DOS pseudogap and the electronic stabilization it affords are apparent here. Now, though, the d-states in the upper and lower mounds of the states are segregated between the two different atom types. The largely bonding states below the E_F are dominated by Ru d contributions, while the more antibonding levels above the pseudogap are rich in Zr d character.

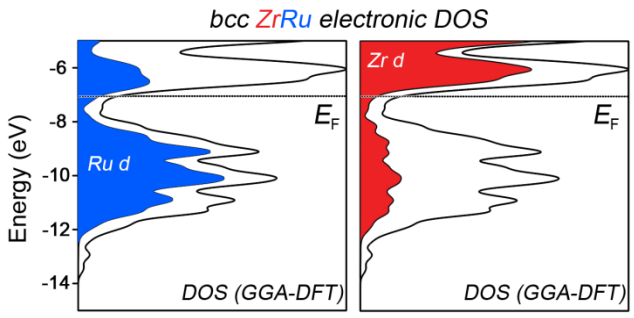

Figure 3.5. The electronic density of state (DOS) distribution of ZrRu (CsCl-type). The d orbitals of the Ru (blue) and Zr (red) d dominate the DOS below and above the Fermi Energy (E_F), respectively.

The asymmetry in the compositions of the bonding and antibonding states is in close accord with the electronegativity considerations, as we recently discussed in the development of the μ_3-acidity model.[21,43] As Ru is significantly more electronegative than Zr, the bonding levels are stabilized by being polarized toward the Ru atoms. To maintain orthogonality with these bonding states, the antibonding functions above the pseudogap are concentrated on the Zr atoms.

This electronegativity difference could also be expected to influence the formation of the 18-electron configurations on the Ru and Zr atoms. To explore this effect, we show in Figure 3.6 the Ru-Ru and Zr-Zr isolobal bonds that are constructed from raMO analyses focusing on the Ru and Zr sublattices, respectively. A quick glance at the two sets of bonding functions suggests that the shared electron pairs needed for 18-electron configurations can be made for both sublattices. The details of the orbitals in the two cases, however, reveal chemically meaningful differences. In particular, compared with Mo metal, the

isolobal bonding functions for the Ru sublattice are much more weighted on the terminal Ru atoms on opposite sides of each bond, with smaller contributions appearing from the bridging Zr atoms. When referring to isolobal bonds constructed for the Zr sublattice, the situation is reversed: the bridging atoms (Ru) now show larger contributions than their counterparts in Mo, with the terminal atoms (Zr) exhibiting smaller lobes. The increased presence of the Ru orbitals in both pictures is consistent with its higher electronegativity.

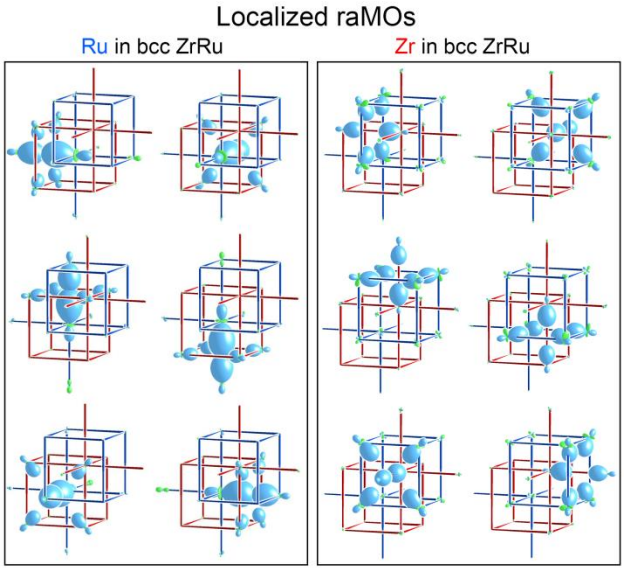

Figure 3.6. Localization of bonding states for Ru and Zr. In the case of Ru, 6 σ Ru-Ru bonding states are observed, reminiscent of Mo. In the case of Zr, although 6 σ isolobal bonding states can be constructed, they are more polarized toward the bridging Ru atoms.

Overall, we can construct 18-electron configurations for either the Ru or Zr sublattices, but those made for the Ru are more tightly localized to the Ru centers, with the Zr showing a higher degree of delocalization into Ru orbitals. The applicability of both bonding descriptions, as well as their unequal importance, can be succinctly summarized with a

pair of resonance structures analogous to those we drew for elemental Mo above (Figure 3.7). The main difference now is that we indicate that the coefficient (c_1) for the Ru-centric picture should be larger than for the Zr-based one (c_2). In this way, the ionicity of the CsCl type structure is accounted for by shifting the balance in the two resonance structures.[44]

3.6. Generalizing the bonding scheme to transition metal-main group CsCl-type phases.

These conclusions suggest a link between the bonding in the seemingly separate classes of intermetallic compounds formed between two different transition metals and those between a transition metal and a main group element. In the 18-*n* bonding scheme that we derived earlier for transition metal (T)-main group (E) CsCl-type phases, such as CoAl, the transition metal atoms are again connected through isolobal bonds into a primitive cubic framework, resulting in an electronic structure with a pseudogap at 18-6 = 12 electrons/T atom, but only a single 18-*n* resonance structure is required.[24] In this final section, we will link these T-T' and T-E CsCl-type phases into a single bonding picture.

The potential for a unified bonding scheme for these two classes of CsCl-type compounds is highlighted by a comparison of the electronic DOS curves. On the left and right sides of Figure 8, we compare the DOS curves calculated for ZrRu with an isoelectronic T-E CsCl-type phase, RuSn (a hypothetical compound based on the experimentally observed CsCl-type RuSi phase, with Sn in place of Si so that principal quantum numbers of the valence s and p orbitals match those of Zr and Ru).

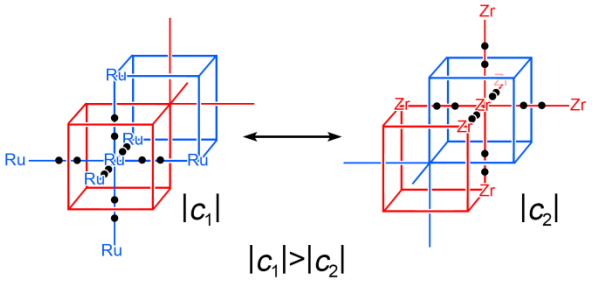

Figure 3.7. Two 18-electron resonance structures for the CsCl-type phase ZrRu, one for the primitive cubic sublattice formed from the Ru atoms, the other for its Zr counterpart. The two resonance structures have different weights reflecting the different electronegativites of Zr and Ru.

The most obvious difference in the two distributions is that the small tail of s-based states at low energies in ZrRu has grown into a separate mound of states between ca. -13 to -18 eV in RuSn, reflecting the inert-pair-like nature of the Sn 5s whose ionization energy is much higher than that of either the Ru or Zr 5s. Beyond this understandable difference, the similarities are striking: in both plots, the E_F lies at the upper end of a deep pseudogap separating a large block for Ru d-rich states at lower energies from a narrower block at higher energies. In both cases, this band-filling corresponds to 12 electrons per formula unit, the 18-*n* count for the Ru sublattice.

The notion that the pseudogaps of these two compounds share a common origin is supported by the raMO analysis. Below the DOS curves in Figure 3.8, we illustrate the LC-raMOs for a Ru-Ru isolobal bond in each of the two structures (for a full set of raMO reconstructions of the Ru s, p, and d valence orbitals, see the Appendix B). In both, the familiar motif of σ-oriented hybrid orbitals emanating along the Ru-Ru contact is visible, along with the bridging contributions from the square of Zr or Sn orbitals that the contact

passes through. The isolobal bonds of the 18-*n* bonding scheme are thus present for both phases.

On moving from ZrRu to RuSn, it seems then that the role of the Zr 4d orbitals in the Ru's 18-*n* bonding scheme is taken over by the Sn 5s (with 5p orbitals adding in both cases further directionality to the bridging orbitals). With the extreme flexibility of the Hückel approach, we can test this idea by attempting to gradually replace the 4d orbitals with low energy 5s orbitals through changes in the atomic orbital parameters. To do this, we simply shift the H_{ii} value of the Zr 5s downwards to that of the Sn 5s, in concert with moving the Zr 4d upwards towards 0 eV to bring it out of the bonding picture (correlating with Sn's empty 5d orbitals rather than its filled and core-like 4d shell). To help simulate the transition between Zr and Sn we also raise the ζ exponential decay coefficient on the 5s Slater-type orbital at each step, to capture more and more of its inert pair character.

In Figure 3.8, we show three steps along this progression with both DOS distributions and the Ru-Ru isolobal bonds from the raMO analysis. At each step, the DOS pseudogap remains essentially fixed in place (though with some widening into a band gap at times, with the E_F lying within it). The presence of the Ru-Ru isolobal bonds is also largely unchanged. Changes are seen, however, in the low energy s-based DOS features and the nature of the bridging contributions in the isolobal bonds. The Zr/Sn 5s gradually drops down to form the distinct group of states calculated for RuSn, while the Zr/Sn bridging orbitals lose their d-contributions in favor of s character.

In summary, we have linked the bonding schemes of ZrRu and RuSn (and by extension, the 12 electron/cell T-T' and T-E CsCl-type phases more generally) through a contin-

uum in which the role of d orbitals on the more electropositive T atoms is taken over by low energy E s orbitals. As these d orbitals on the second T element are removed, of course, the role of the second 18-*n* resonance structure becomes increasingly small, with $|c_1| > |c_2|$ in Figure 3.7. Their complete removal in RuSn then corresponds to the limiting case of $c_2 = 0$. Here, the ionicity of the structure is determined not by the balance between competing resonance structures, but the degree to which the Ru-centered raMOs (within a single resonance structure) are localized on the Ru centers versus spread over their Sn neighbors.

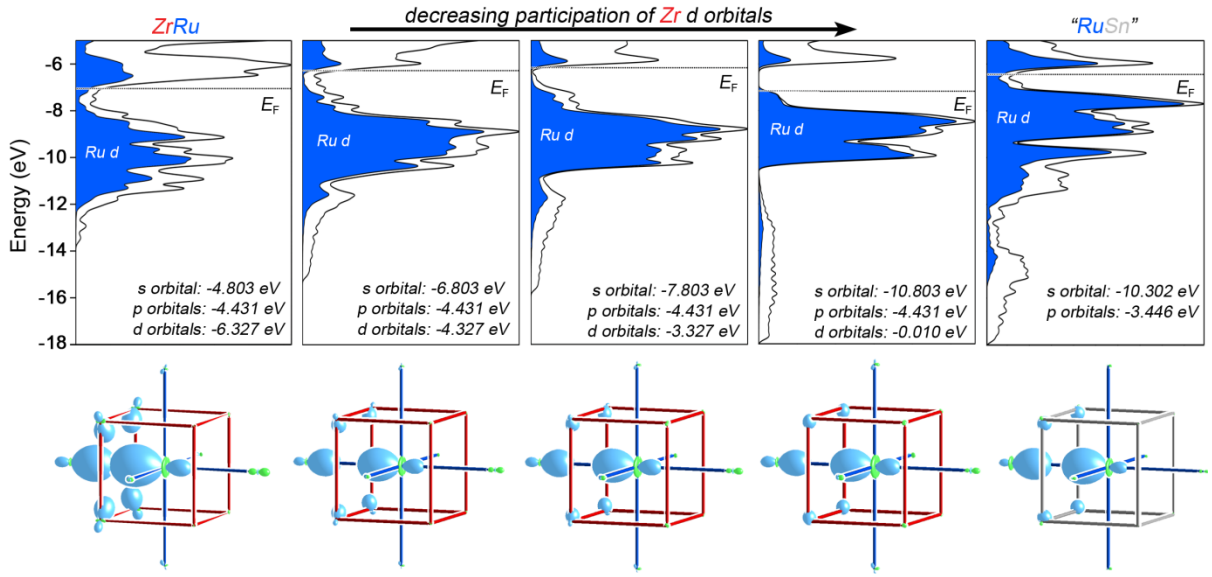

Figure 3.8. The continuity between the 18-*n* bonding schemes for T-T' and T-E CsCl-type phases (T,T'=transition metals, E=main group element). The DFT-calibrated Hückel density of states (DOS) distributions and the LC-raMO-derived Ru-Ru isolobal bonds for ZrRu and RuSn, joined by a series of intermediate phases created by raising the Zr 4d energy while lowering and contracting the Zr 5s orbitals (simulating the replacement of Zr with Sn).

3.7. Conclusions

The 18-electron rule of molecular complexes has an origin that hints at broad applicability: the association of electron pairs with functions surrounding a transition metal center sharing the symmetry properties of each of its nine valence s, p, and d orbitals. While this rule is known to be only loosely followed by the organometallic and coordination compounds for which it was first envisioned, it appears to be remarkably powerful in rationalizing the structures of transition metal (T)-based intermetallic phases once the concept of isolobal bonds along T-T contacts is embraced. The 18-*n* bonding scheme derived for these cases has thus far been limited to the transition metal-main group (T-E) compounds in which the T:E ratio is 50% or less, due to the large number of T-T contacts that arise for more T-rich phases. Beyond six such contacts to any given T atom, it becomes difficult to produce orthogonal hybrid orbitals pointing along each of the contacts separately using its s, p, and d valence orbital manifold.

In this Article, we have seen how the resonance concept provides a route past this difficulty with the development of an 18-*n* bonding scheme for the bcc structures of the group 6 transition metals and isoelectronic binary variants adopting the CsCl type. Using the reversed approximation Molecular Orbital (raMO) analysis on a DFT-calibrated Hückel model of bcc-Mo, we saw that filled 18-electron configurations can be drawn for either of the two primitive *cP* sublattices interpenetrating to form the bcc structure. In each case, Mo atoms of one sublattice achieve an 18-*n* count through sharing electron pairs in isolobal Mo-Mo σ bonds along its edges, with further stabilization by bonding contributions from the Mo atoms of the other *cP* sublattice. The ability to draw 18-*n* electron configurations

on either *cP* sublattice and the substantial overlap between the two bonding pictures that result are captured with their interpretation as two resonance structures with equal weights which together represent the electronic structure of the phase better than either one individually.

The 18-*n* bonding scheme is easily extended to binary variants of the bcc structure. Our raMO analysis of ZrRu, a CsCl-type phase isoelectronic to Mo, revealed that 18-*n* resonance structures can again be drawn for either *cP* sublattice. Now, however, the binary coloring of the lattice results in a shift in the balance between the two resonance structures, with the Ru-based one gaining a heavier weight. This picture is consistent with the DOS distributions that show strong commonalities between Mo and ZrRu, the chief difference being that the Zr and Ru contribute unevenly to the states above and below the Fermi energy (E_F). In the occupied states below the E_F, Ru 4d orbitals predominate, while the unoccupied states just above the E_F are rich in Zr 4d character. Upon substituting the T atoms on one sublattice with a main group element, as in the isoelectronic RuSn, the weaker resonance structure simply vanishes for lack of the d orbitals needed for sp^3d^2 hybridization.

This scheme is, of course, not the first time that the idea of resonance structures has been applied to metals. Goodenough briefly described the conduction band of the bcc transition metals in terms of two sp^3-hybridized diamond networks in resonance.[39] Pauling, on the other hand, constructed a much more comprehensive view of resonance in the metallic state. He enumerated resonance structures for elemental Li in the bcc structure with different configurations of classical 2 center/2 electron bonds among the vast array of

Li-Li contacts,[40] and in fact viewed the bonding in Mo and other transition metals in terms of resonating bonding and non-bonding electron pairs.[45,46] However, due to the large number of resonance structures that result, the structural stability becomes connected with a statistical evaluation of the number of allowed resonance structures, a long way away from the goal of associating stability with specific, local structural features.

A major advantage provided by the 18-*n* scheme is in the relaxation of the degree of localization of the electron pairs—a must for a metallic phase: here we focus on electron pairs contained within the first 8+6 coordination shell of the atoms of the structure generated using the raMO approach, and only localize them further when suitable linear combinations can be identified among the resulting raMO functions. In our case, the concept of resonance enters through the interpenetration of the 18-electron bonding schemes on neighboring sublattices, rather than a desire to identify electron pairs with specific pairs of atoms.

In this 18-*n* bonding picture, however, we can still see something of Pauling's language of bonding electron pairs enter back into the discussion of simple metals. This viewpoint highlights many questions. So far, we have not considered the role that magnetism plays in the bonding of the 3d metals. How do the spin-density waves detected in Cr metal at low temperatures modulate the 18-*n* scheme we described here? Additionally, how does ferromagnetic order stabilize the bcc allotrope of Fe at ambient conditions relative to the hcp structure observed for Ru and Os?

One might also wonder whether similar closed shell electron configurations could be derived for the other classic metallic packings, such as the fcc or hcp structures. For the

transition metals at least, our earlier d-only based models (using only the 0th through 4th moments of the DOS) show the key DOS pseudogaps for the fcc, bcc, and hcp structures all near the same electron count.[21,47] From this viewpoint, the preference of the fcc and hcp structures away from group 6 may arise from their better ability to accommodate non-ideal electron counts. The shallower pseudogaps of the fcc and hcp structures (due to their larger kurtosis values[48]) offer one reason for their increased favorability toward the ends of the d-block, as does the Jahn-Teller instability above 6 electrons/atom for the bcc structure.[18] It is still possible, however, that closed-shell configurations may also be identifiable in the simple fcc and hcp structures when we go beyond low-order moment, d-only models for their electronic structures.

Finally, while our focus in this Article has been on the group 6 transition metals and closely related compounds, the resulting bonding scheme has the potential to introduce new insights into a much broader range of intermetallic phases. While T-rich intermetallics generally have too many T-T contacts at each T atom to be described with a single 18-*n* scheme, the incorporation of the resonance concept suggests the possibility of dissecting the complex web of T-T contacts into several manageable subsystems. We are looking forward to exploring how this approach might be applied to the study of other T-rich structures, such as the α- and β-Mn structures[49,50] and the tetrahedral close packed Frank-Kasper phases.[51,52]

Acknowledgements

This article is dedicated to Prof. Stephen Lee on the occasion of his 60th birthday; the depth of his scientific vision and the vividness with which he shares it continually inspire us to recognize new chemistry in both the seemingly familiar and reputedly unknowable. We thank Vincent Yannello and Katerina Hilleke for the insightful discussions of the raMO procedure and results. We also gratefully acknowledge the financial support of the National Science Foundation (NSF) through grant DMR-1508496. This research involved calculations carried out using computer resources supported by NSF grant CHE-0840494.

3.8. References

(1) Harrison, W. A. *Electronic Structure and the Properties of Solids: The Physics of the Chemical Bond*; Dover Publications: New York, 1989.

(2) Nesper, R. Bonding Patterns in Intermetallic Compounds. *Angew. Chem. Int. Ed.* **1991**, *30*, 789-817.

(3) Pettifor, D. G. *Bonding and Structure of Molecules and Solids*; Oxford University Press: Oxford, 1995.

(4) Burdett, J. K. *Chemical Bonding in Solids*; Oxford University Press: New York, 1995.

(5) Mott, N. F.; Jones, H. *Theory of the Properties of Metals and Alloys*; Clarendon Press: Oxford, 1936.

(6) Berger, R. F.; Walters, P. L.; Lee, S.; Hoffmann, R. Connecting the Chemical and Physical Viewpoints of What Determines Structure: From 1-D Chains to γ-brasses. *Chem. Rev.* **2011**, *111*, 4522-45.

(7) Hume-Rothery, W.; Raynor, G. V. *The Structure of Metals and Alloys*; 4th ed.; Institute of Metals: London, 1962.

(8) Carlsson, A. E. Band-gap Creation by Icosahedral Symmetry in Nearly-free-electron Materials. *Phys. Rev. B* **1993**, *47*, 2515-2521.

(9) Mizutani, U.; Takeuchi, T.; Sato, H. Interpretation of the Hume-Rothery rule in Quasicrystals and their Approximants. *J. Non-Cryst. Solids* **2004**, *334-335*, 331-335.

(10) Heine, V. *s-d* Interaction in Transition Metals. *Phys. Rev.* **1967**, *153*, 673-682.

(11) Deegan, R. A. Structure of the Transition Metals. *J.Phys. C: Solid State* **1968**, 763-766.

(12) Pettifor, D. G. Theory of the Crystal Structures of Transition Metals. *J. Phys. C: Solid State Phys.* **1970**, *3*, 367.

(13) Marvin, L. C. Pseudopotentials and Total Energy Calculations. *Phys. Scr.* **1982**, *1982*, 5.

(14) Hafner, J.; Heine, V. The Crystal Structures of the Elements: Pseudopotential Theory Revisited. *J. Phys. F: Met. Phys.* **1983**, *13*, 2479.

(15) Burdett, J. K.; Lee, S. Moments Method and Elemental Structures. *J. Am. Chem. Soc.* **1985**, *107*, 3063-82.

(16) Skriver, H. L. Crystal Structure from One-electron Theory. *Phys. Rev. B* **1985**, *31*, 1909-1923.

(17) Lee, S. Elemental Structures of the Heavy Main Group Atoms and the Second Moment Scaling Hypothesis. *J. Am. Chem. Soc.* **1991**, *113*, 8611-14.

(18) Lee, S.; Hoffmann, R. Bcc and Fcc Transition Metals and Alloys: A Central Role for the Jahn-Teller Effect in Explaining Their Ideal and Distorted Structures. *J. Am. Chem. Soc.* **2002**, *124*, 4811-4823.

(19) Landrum, G. A.; Dronskowski, R. Ferromagnetism in Transition Metals: A Chemical Bonding Approach. *Angew. Chem. Int. Ed.* **1999**, *38*, 1389-1393.

(20) Dronskowski, R. Itinerant Ferromagnetism and Antiferromagnetism from the Perspective of Chemical Bonding. *Int. J. Quantum Chem.* **2004**, *96*, 89-94.

(21) Stacey, T. E.; Fredrickson, D. C. The μ_3-Model of Acids and Bases: Extending the Lewis Theory to Intermetallics. *Inorg. Chem.* **2012**, *51*, 4250-4264.

(22) Yannello, V. J.; Kilduff, B. J.; Fredrickson, D. C. Isolobal Analogies in Intermetallics: The Reversed Approximation MO Approach and Applications to $CrGa_4$- and Ir_3Ge_7-Type Phases. *Inorg. Chem.* **2014**, *53*, 2730-2741.

(23) Hadler, A. B.; Yannello, V. J.; Bi, W.; Alp, E. E.; Fredrickson, D. C. π-Conjugation in $Gd_{13}Fe_{10}C_{13}$ and Its Oxycarbide: Unexpected Connections between Complex Carbides and Simple Organic Molecules. *J. Am. Chem. Soc.* **2014**, *136*, 12073-12084.

(24) Yannello, V. J.; Fredrickson, D. C. Generality of the 18-*n* Rule: Intermetallic Structural Chemistry Explained through Isolobal Analogies to Transition Metal Complexes. *Inorg. Chem.* **2015**, *54*, 11385-11398.

(25) Kilduff, B. J.; Yannello, V. J.; Fredrickson, D. C. Defusing Complexity in Intermetallics: How Covalently Shared Electron Pairs Stabilize the FCC Variant $Mo_2Cu_xGa_{6-x}$ ($x \approx 0.9$). *Inorg. Chem.* **2015**, *54*, 8103-8110.

(26) Kresse, G.; Furthmüller, J. Efficient Iterative Schemes for Ab Initio Total-Energy Calculations using a Plane-Wave Basis Set. *Phys. Rev. B* **1996**, *54*, 11169-11186.

(27) Kresse, G.; Furthmüller, J. Efficiency of Ab-Initio Total Energy Calculations for Metals and Semiconductors using a Plane-Wave Basis Set. *Comput. Mater. Sci.* **1996**, *6*, 15-50.

(28) Blöchl, P. E. Projector Augmented-wave Method. *Phys. Rev. B* **1994**, *50*, 17953-79.

(29) Kresse, G.; Joubert, D. From Ultrasoft Pseudopotentials to the Projector Augmented-wave Method. *Phys. Rev. B* **1999**, *59*, 1758-1775.

(30) Stacey, T. E.; Fredrickson, D. C. Perceiving Molecular Themes in the Structures and Bonding of Intermetallic Phases: The Role of Hückel Theory in an *ab initio* Era. *Dalton Trans.* **2012**, *41*, 7801-7813.

(31) Landrum, G.A.; Glassey, W. V. YAeHMOP: Yet Another extended Hückel Molecular Orbital Program. YAeHMOP is available free of charge via the WWW at URL: https://sourceforge.net/projects/yaehmop/ [Last accessed: 12/5/2016].

(32) Hoffmann, R. *Solids and Surfaces: A Chemist's View of Bonding in Extended Structures*; VCH Publishers: New York, NY, 1988.

(33) Zurek, E.; Jepsen, O.; Andersen, O. K. Muffin-tin orbital Wannier-like functions for insulators and metals. *ChemPhysChem* **2005**, *6*, 1934-1942.

(34) Zurek, E.; Jepsen, O.; Andersen, O. K. Searching for the Interlayer Band and Unravelling the Bonding in β-$ThSi_2$ and α-$ThSi_2$ with NMTO Wannier-like Functions. *Inorg. Chem.* **2010**, *49*, 1384-1396.

(35) Hooper, J.; Zurek, E. Rubidium Polyhydrides Under Pressure: Emergence of the Linear H_3^- Species. *Chem. Eur. J.* **2012**, *18*, 5013-5021.

(36) Marzari, N.; Mostofi, A. A.; Yates, J. R.; Souza, I.; Vanderbilt, D. Maximally localized Wannier functions: Theory and applications. *Rev. Mod. Phys.* **2012**, *84*, 1419-1475.

(37) Botana, A. S.; Quan, Y.; Pickett, W. E. Disturbing the Dimers: Electron and Hole Doping in the Intermetallic Insulator $FeGa_3$. *Phys. Rev. B* **2015**, *92*, 155134.

(38) *Magnetic Properties of Metals: d-Elements, Alloys and Compounds*; Wijin, H. P. J., Ed.; Spring-Verlag: Berlin, 1991.

(39) Goodenough, J. B. Suggestion Concerning the Role of Wave-Function Symmetry in Transition Metals and Their Alloys. *J. Appl. Phys.* **1958**, *29*, 513-515.

(40) Pauling, L. *The Nature of the Chemical Bond and the Structure of Molecules and Crystals; An Introduction to Modern Structural Chemistry*; 3rd ed.; Cornell University Press: Ithaca, N.Y., 1960.

(41) Fredrickson, R. T.; Fredrickson, D. C. The Modulated Structure of $Co_3Al_4Si_2$: Incommensurability and Co–Co Interactions in Search of Filled Octadecets. *Inorg. Chem.* **2013**, *52*, 3178-3189.

(42) Todorov, E.; Evans, M.; Lee, S.; Rousseau, R. Energy Isosbestic Points in Third-row Transition Metal Alloys. *Chem. Eur. J.* **2001**, *7*, 2652-2662.

(43) Stacey, T. E.; Fredrickson, D. C. Structural Acid–Base Chemistry in the Metallic State: How μ_3-Neutralization Drives Interfaces and Helices in $Ti_{21}Mn_{25}$. *Inorg. Chem.* **2013**, *52*, 8349-8359.

(44) The relative weights of the resonance structures can be estimated from the charges on the Zr and Ru atoms in the Hückel calculation. In the calculation, each Ru atom ends up with 8.56 of the 12 valence electrons per formula unit, with the Zr atoms having the

remaining 3.44 electrons. The Ru- and Zr-centered resonance structures would then have relative contributions of 79 and 21%, respectively.

(45) Pauling, L. The Nature of the Interatomic Forces in Metals. *Phys. Rev.* **1938**, *54*, 899-904.

(46) Pauling, L. The Metallic Orbital and the Nature of Metals. *J. Solid State Chem.* **1984**, *54*, 297-307.

(47) Guo, Y.; Stacey, T. E.; Fredrickson, D. C. Acid–Base Chemistry in the Formation of Mackay-Type Icosahedral Clusters: μ_3-Acidity Analysis of Sc-Rich Phases of the Sc–Ir System. *Inorg. Chem.* **2014**, *53*, 5280-5293.

(48) Clark, P. M.; Lee, S.; Fredrickson, D. C. Transition Metal AB_3 Intermetallics: Structure Maps Based on Quantum Mechanical Stability. *J. Solid State Chem.* **2005**, *178*, 1269-1283.

(49) Bradley, A. J.; Thewlis, J. The Crystal Structure of α-Manganese. *Proc. R. Soc. Lond. A* **1927**, *115*, 456-471.

(50) Preston, G. D. CXXV. The Crystal Structure of β-Manganese. *The London, Edinburgh, and Dublin Philosophical Magazine and Journal of Science* **1928**, *5*, 1207-1225.

(51) Frank, F. C.; Kasper, J. S. Complex Alloy Structures Regarded as Sphere Packings. I. Definitions and Basic Principles. *Acta Crystallogr.* **1958**, *11*, 184-90.

(52) Frank, F. C.; Kasper, J. S. Complex Alloy Structures Regarded as Sphere Packings. II. Analysis and Classification of Representative Structures. *Acta Crystallogr.* **1959**, *12*, 483-99.

Chapter 4.

Principles of Channel Formation in Intermetallics: Structure-Property Relationships for Fe_2Al_5 Rooted in the 18-*n* Bonding Scheme and Chemical Pressure Quadrupoles

4.1. Abstract

Stuffed channels are often key to understanding structure-property relationships in solid state materials. Their appearance in densely packed compounds like intermetallics provides a source of great structural diversity as the channels can be epicenters of disorder and modulation, yet the general forces that guide the formation of such channels remain elusive. In this Article, we explore the basic principles leading to these features through experimental and theoretical investigations of the extensive positional disorder of Al-stuffed channels in Fe_2Al_5. We begin by experimentally confirming the earlier crystallographic model of Grin and coworkers (while introducing some slight modifications), and showing that the behavior of the column of disordered Al is essentially temperature independent over the temperature range of 100 to 400 K. Once this structural picture is established, we compare the electronic structure results for two ordered models of Fe_2Al_5. Both ordered structures show electronic pseudogaps near 16 electrons/Fe atom, very close to the electron concentration given by the phase's composition of $FeAl_{2.62}$, as measured by electron microprobe analysis. Using a reversed approximation Molecular Orbital (raMO) analysis of DFT-calibrated Hückel models, we

interpret the pseudogap in terms of the 18-*n* bonding scheme, with 18 electron configurations being achieved by each Fe atom with the support of $n = 2$ isolobal σ Fe-Fe bonds. Finally, the localization of the Al nonstoichiometry to the disordered Al columns is elucidated with a DFT-Chemical Pressure (CP) analysis. The CP schemes of several models show that unlike the remainder of the structure, the Al atoms in the disordered columns show strong CP quadrupoles suggestive of soft atomic motions along the undulating column of electron density observed in the Fourier map. This scheme hints that the atoms of the column should easily adapt to vacant neighbors along the channel, as well as exhibit soft vibrations that could support phonon scattering. Through this analysis, a generalizable picture emerges for how electronic pseudogaps and soft phonon modes can conspire to create channel structures in intermetallics.

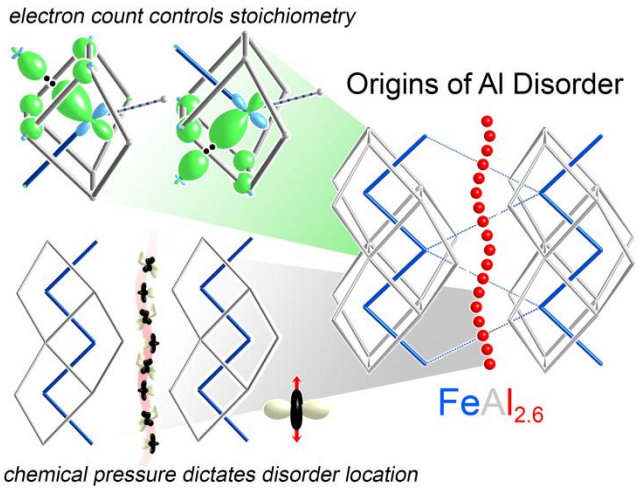

Figure 4.0. The nonstoichiometry and the isolation of the positional disorder to the stuffed channels in Fe_2Al_5 can be understood in terms of the preferred electron count, as dictates by the Fe bonding network, and the chemical pressure scheme, where atoms at any position along the column experience similar chemical pressures.

4.2. Introduction

The identification of channels within crystal structures is one of the fundamental ways in which structure and properties can be linked in solid state materials. In some materials, the presence of such channels is a clear outcome of the building blocks used in the construction of the compound (as in the metal organic frameworks[1]) or the use of a template molecule (as in zeolites[2] or gas clathrates[3]). Conversely, such features would seem to be unlikely in densely packed materials, such as metals. It is perhaps very curious, then, that host channels filled with guest atoms are common motif in the structures of intermetallic phases, the extensive family of compounds formed between metallic elements.[4-6] These features have been observed in quasicrystal approximants,[7] Zintl phases[8-11] and present a central feature in the Nowotny Chimney Ladder phases.[12,13] The filling of the channels varies widely from ordered helices (as in the case of some NCL phases[14] and Zintl phases[15]) to incommensurate modulation of atomic positions[7,16] to complete positional disorder that manifests as a continuous column of electron density.[17,18] In certain cases, the appearance of ordering or disordering of the atoms within channels has been linked to the preferred electron counts as in the case of incommensurately modulated $Co_3Al_4Si_2$[19] and preferred coordination environments as observed in K_8Sn_{25}.[15] Yet despite the prevalence of stuffed channels and their importance to properties of materials, the general forces that drive the stability of these columns, as well as the ordering of the atoms they contain, remain mainly unknown. In this Article, we see how a combined theoretical and experimental investigation of one structure with disordered channels, Fe_2Al_5, can lead to a general scheme for the origin of such features.

As with many other non-trivial intermetallic compounds, the structure of Fe_2Al_5 or $FeAl_{2.5}$, as we occasionally refer to it, has gradually emerged over successive investigations over many decades. After an initial report of an $FeAl_2$ phase in 1933,[20] the stoichiometry of the phase was revised in 1953 to $FeAl_{2.5}$, and the compound was described in passing as being structurally similar to the hexagonal phase Co_2Al_5.[21] Subsequent structural investigations recognized that in fact it adopts its own structure type with little relation to that of Co_2Al_5,[22,23] and the crystal structure determination by Grin et al. in 1994 revealed that a column of Al atoms disordered to such a degree that in the Fourier map, it appeared as a nearly continuous column of electron density.[24] Modeling of this region with a series of fractionally occupied Al positions highlighted the compound's nonstoichiometric Al content, with the crystallographically refined composition being $FeAl_{2.8}$.[24]

The extensive positional disorder inspired numerous theoretical investigations into the properties and stability of this phase. $FeAl_{2.8}$ was discovered to act as a dilute magnet,[25,26] while phonon band structure calculations of the disordered Al columns revealed liquid-like motions along the length of the entire channel.[27] The soft phonon motions due to the extensive disorder suggested that the phase should exhibit low thermal conductivity, highlighting its potential as a thermoelectric material that was just realized experimentally by Kimura et al.[28]

While the relevance of the channels of disordered Al atoms to the properties of this compound has been clearly established, deeper questions remain unresolved: how is the disorder in this channel set-up by the remainder of the structure, and how could

similar situations be staged in other intermetallic compounds? Toward developing answers to these questions, we set out here to reinvestigate the crystal structure of Fe_2Al_5 and correlate its structural features to bonding schemes and chemical pressure (CP) distributions. We will see that the disorder of the Al column is a consistent feature of the compound over a large temperature range. Using the reversed approximation Molecular Orbital analysis, the nonstoichiometry of the Al content will then be linked to the preferred electron count of the Fe bonding network, as the Fe atoms strive to achieve an 18 electron configuration. The localization of the Al nonstoichiometry to the observed channels will then be connected to the emergence of CP quadrupoles on atoms appearing between the zigzag chains of Fe atoms in the structure. This theme of nonstoichiometry driven by electron count and disordering structurally directed by CP is anticipated to play a general role in the chemistry of intermetallic phases.

4.3 Experimental Section

Synthetic procedures. Fe_2Al_5 was synthesized by first grinding together powders of the pure elements (Fe powder, 99.9%, Strem; Aluminum powder -100+325 mesh, 99.97%, Alfa Aesar) in a ratio of 1:2.7 with an agate mortar and pestle, in an Ar-filled glovebox. The mixtures were then pressed into pellets and arc-melted under Ar two times for 10 seconds each (to maximize homogeneity while minimizing the loss of Al by evaporation). The pellets were sealed in evacuated fused silica ampoules and annealed first at 600°C for 4 days, then at 400°C for 6 additional days, and finally quenched in ice water. All syntheses

resulted in hard, gray, and shiny pellets that showed no visible signs of air sensitivity even after weeks in air.

Single Crystal X-ray Diffraction. Crystals were picked from the crushed samples and were first analyzed at room temperature with an Oxford Diffraction Xcalibur E diffractometer with a Mo Kα (λ=0.70930Å) sealed-tube X-ray source. Additional single crystal datasets were collected with the Oxford Cryojet HT accessory at 105 K, 150 K, and 400 K to examine the possibility of superstructure formation resulting from the changes in the disordered Al positions. For the room temperature data set, the run list consisted of ω scans chosen to cover a full sphere of reciprocal space out to a resolution of 0.8 Å. The scans were taken with a 0.6° step width and a 120 second exposure time at a crystal-to-detector distance of 70 mm. The run list for the full experiment at 105 K was also based on ω scans, this time with the same step width but an 80 second exposure time and detector distance of 50mm, chosen to cover a full sphere out to 0.8 Å resolution. A step width of 0.5° and exposure time of 80 seconds were used for additional data collections at 150 K and 400 K. The creation of the run lists and the processing of the frame data were performed with the CrysalisPro ver. 171 software.[29]

For the final variable temperature datasets, the data were collected with a Bruker Quazar APEX2 diffractometer with a Mo Kα IμS microfocus X-ray source (λ=0.71073 Å). The datasets were collected at 100 K, 150 K, 300 K, and 400 K. The run list consisted of ω and φ scans with 0.7° step size and exposure time of 40 seconds, designed to cover a full sphere to a resolution of 0.7 Å. The Apex III software package[30] was used for data

collection and integration. For absorption correction and data reduction SADABS[31] and XPREP were used, respectively.

Structure Solution and Refinement. Analysis of the room temperature dataset revealed an orthorhombic unit cell with unit cell parameters of a=7.5660(3) Å, b=6.4117(2) Å, and c=4.22350(18) Å. The observed systematic absences in the reciprocal space reconstructions were consistent with space group *Cmcm* and the subsequent structure solution and refinement confirmed the correct assignment of the space group symmetry.

An intrinsic phasing algorithm as implemented in ShelXT[32] was used to solve the single crystal structure, yielding 2 symmetry distinct atomic positions. The three positions to model the disordered Al site were obtained from the Fourier difference map. The occupancies of the three disordered Al sites were refined freely, while their thermal displacement parameters were constrained to be the same. The resulting combined occupancy was less than 100%, indicating that the electron density column is only partially occupied. The structure was refined on F^2 using ShelXL.[33] Atoms Fe1 and Al1 were refined anisotropically, while Al2a, Al2b, and Al2c were refined isotropically. The final refinement converged to R(I>3σ)=1.32 for the 300 K dataset. The largest peaks in the Fourier difference map corresponded to maximum and minimum densities of 0.36 electrons/$Å^3$ and -0.27 electrons/$Å^3$, respectively. The formula refined to $FeAl_{2.75}$. Maps of the Fourier electron density were constructed with the Jana2006 program.[34]

The data collected at 100 K, 150 K and 400 K could also be indexed with an orthorhombic unit cell with similar parameters to the room temperature data, with the trends being interpretable in terms of thermal expansion. The systematic absences in the

three datasets were consistent with the *Cmcm* space group. The solutions and refinements yielded structures similar to the room temperature results. The same model was applied to the solution and refinement of the 100 K, 150 K, and 400 K data sets.

The crystal structure refinement details for the four datasets are given in Table 4.1. The refined atomic coordinates, atomic displacement parameters, and selected interatomic distances are provided in Appendix C.

Table 4.1. Crystallographic data for Fe_2Al_5

Chemical formula		$FeAl_{2.75}$		
WDS composition		$Fe_{1.0(2)}Al_{2.62(11)}$		
Crystal dim. (mm^3)		0.106× 0.093 × 0.033		
Crystal color		Metallic gray		
Radiation source, λ (Å)		Mo Kα, (0.71073 Å)		
Absorption correction		Multi-scan		
Data collection temp.	100K	150K	300K	400K
Pearson symbol		*oC*15		
Space group		*Cmcm* (No. 63)		
a (Å)	7.638(2)	7.642(2)	7.651(2)	7.660(2)
b (Å)	6.3949(18)	6.3978(18)	6.4087(18)	6.4183(18)
c (Å)	4.2098(14)	4.2111(14)	4.2173(14)	4.2224(14)
Cell volume ($Å^3$)	205.64(11)	205.88(11)	206.78(11)	207.59(11)
Calc. density (g/cm^3)	4.205	4.1980	4.179	4.163
Absorption coef. (mm^{-1})	8.016	8.005	7.970	7.939
θ_{min}, θ_{max}	4.16, 30.62	4.15, 30.62	4.15, 30.43	4.14, 30.53
Number of reflections	1862	1872	1864	1860
R_{int} (I> 3σ)	1.91	2.12	1.95	1.90
Unique refl. (I > 3σ)	188	189	187	189
Number of parameters	18	18	18	18
R (I > 3σ), R_w (I > 3σ)	1.18, 3.17	1.32, 3.44	1.32, 3.47	1.33, 3.43
R(all), R_w(all)	1.20, 3.17	1.33, 3.44	1.33, 3.47	1.36, 3.44
S (I >3σ)	1.156	1.101	1.183	1.158
$\Delta\rho_{max}$, $\Delta\rho_{min}$ ($e^-/Å^3$)	0.35, -0.30	0.43, -0.31	0.36, -0.27	0.26, -0.27

Powder X-ray Diffraction. The phase analysis with powder X-ray diffraction was performed on manually ground powder of the crushed sample that was then mounted onto a glass fiber with vacuum grease. A Rigaku Rapid II diffractometer with Mo Kα radiation (λ=0.70930 Å) equipped with a curved image plate detector was used for all powder X-ray diffraction data sets. The averaging over the frames to create *I* vs. 2θ profiles was performed with the 2DP Pattern Integration software for the 2θ range 2° to 45° with a step size 0.02°. All major peaks agreed well with the calculated pattern for the previously reported Fe_2Al_5 structure, as is shown in Appendix C.

Elemental Analysis with Energy Dispersive X-ray Spectroscopy (EDS). The energy dispersive X-ray spectroscopy (EDS) measurements were performed on samples prepared by suspending crushed pieces of the reaction product in epoxy. The sample was hand-polished with a diamond lapping film to create a flat surface and was then carbon coated. The elemental analysis was carried out with a Hitachi S-3100N Scanning Electron Microscope equipped with an EDS probe (Voltage=15 keV). The sample appeared homogeneous with the single phase whose composition was measured to be $Fe_{2.069(19)}Al_{4.930(18)}$ (average of 10 points). No elemental impurities other than O and C (from the coating) were observed.

Elemental Analysis with Wavelength Dispersive X-ray Spectroscopy (WDS). Due to the key role that the Al content plays in our electronic structure discussion, the elemental composition was further investigated using Wavelength Dispersive X-ray Spectroscopy (WDS). To prepare the sample, powder of the reaction product was suspended in conducting epoxy. The surface was polished using polycrystalline diamond suspension

spread over a polishing wheel and carbon coated. CAMECA SX51 Electron Probe Microanalyzer (Voltage=15 eV, Current=20 nA) was used for the elemental analysis. An $FeAl_{3.10}$ standard was used. One phase was observed in the sample with a composition of $Fe_{1.0(2)}Al_{2.62(11)}$ (average of 10 measurement points).

Electronic Structure Calculations. Two models were generated for the reversed approximation Molecular Orbital (raMO) analysis. One model was built from a 1×1×2 supercell, with only every fifth atom along the Al2 Al columns being kept. Finally, to generate the appropriate $FeAl_{2.6}$ stoichiometry, one additional Al atom was deleted at random from one of the columns. The second model was also built from a 1×1×2 supercell, but now all Al2b and Al2c atoms were removed as well as half of the Al2a atoms, yielding a final stoichiometry of $FeAl_{2.5}$. The GGA-DFT electronic structures of the two models were calculated with the Vienna Ab Initio Simulation Package (VASP)[35,36] in the high precision mode, using the projector augmented wave (PAW) potentials provided with the program.[37,38] The calculations on both structures were carried out with a 3×3×3 Γ-centered k-point grid and an energy cutoff of 334.9 eV. Both structures were geometrically optimized with a two-step procedure: the relaxation of the atomic coordinates within a fixed unit cell, followed by a step where all structural parameters were released. After the geometry optimization, single point calculations were carried out to obtain band energies and density of states distributions.

The resulting GGA-DFT output was used as a reference point in refinement of the parameters of simple Hückel models with the program eHtuner. [39] The actual Hückel calculations were carried out with YAeHMOP.[40] From the finalized Hückel parameters,

Hamiltonian matrices were calculated with YAeHMOP for the Γ points of 4 × 4 × 4 supercells, which were directly input into our in-house Matlab programs figuretool2 and makeraMO for the reversed approximation Molecular Orbital (raMO) analyses.[41] Further computational details such as the tables of the DFT-calibrated Hückel parameters and comparisons of the GGA-DFT and Hückel DOS curves are provided in Appendix C.

DFT-Chemical Pressure Calculations. DFT-CP analyses were performed on two versions of a model compound with stoichiometry $FeAl_{2.5}$; one in which every other Al2a site was occupied and one in which every other Al2b site was occupied. Prior to the DFT-CP calculations, VASP[35,36] was used to carry out a two-step geometry optimization using ultrasoft LDA pseudopotentials.[42] This optimized geometry was used as an input for the ABINIT program[43,44] to perform electronic structure calculations using Hartwigsen-Goedecker-Hutter norm-conserving pseudopotentials[45] at the equilibrium volume as well as at slightly expanded and contracted volumes. Output from these calculations were spatially-resolved 3D voxel grids of kinetic energy, electron density, and local components of the Kohn-Sham potential. Further details, including energy cutoffs and k-point grids, may be found in Appendix C.

Chemical pressure maps were produced from the ABINIT output using the CPmap module of the CP package (including core unwarping and tricubic interpolation procedures).[46] These maps were divided among contact volumes between pairs of atoms using the binary Hirshfeld-inspired scheme in the CPintegrate module, averaging the CP values within the contact volumes to obtain interatomic pressures. Hirshfeld charges for all atoms were obtained from the output of the CPpackage calculations using neutral

atomic electron density profiles. The resulting charges were used to generate ionic profiles for all atoms using the Atomic Pseudopotentials Engine (APE),[47] with which the CPpackage program was run again to generate the final schemes. The averaged interatomic pressures with the contact volumes were then projected onto real spherical harmonics ($l \leq 6$) centered on the atomic positions. All CP schemes were visualized using figuretool2, an in-house MATLAB application.

Phonon Frequency Calculations. The phonon band structures of both model structures of Fe_2Al_5 used for the CP analyses were calculated using the linear response method in the ABINIT program.[48] A series of calculations were carried out, beginning with the production of a wave function file using a Γ-centered k-point grid. Subsequent non-self-consistent calculations were performed at all q-points corresponding to the k-points used in the reference calculation to obtain linear responses for all atoms in each direction. The interatomic force constants were then determined from these linear responses using the ABINIT utilities *mrgddb* and *anaddb*, with the resulting phonon modes, band structures, and densities of state being visualized using figuretool2.

4.4. Structural Studies using Single Crystal X-ray Diffraction

Synthetic results. The continuous column of electron density previously described for Fe_2Al_5 looked quite consistent with the average cell of an incommensurately modulated phase. As the satellite reflections corresponding to such a modulation would have been very difficult to identify with the point-detector used in the earlier crystallographic

investigation, we decided to carry out single crystal X-ray diffraction experiments on this phase using a CCD area detector to check for such satellites. The synthesis of Fe_2Al_5 for our structural analysis required an iterative process. Initial attempts targeting the $FeAl_{2.8}$ stoichiometry from the prior single crystal refinement[24] resulted in nearly phase pure samples of the neighboring Al-rich phase, Fe_4Al_{13}.[49] In our consecutive experiments, the Al content was lowered until a nearly phase pure sample of the target phase was observed for a loading ratio of 1 Fe:2.7 Al. The purity and the identity of the sample were confirmed by comparing the experimental powder X-ray diffraction with the calculated peak positions for the Fe_2Al_5 structure. All of the major peaks matched the previously reported structure, while some of the minor peaks were attributed to a small amount of an $FeAl_3$ impurity. The homogeneity of the sample was verified by Back Scattered Electron (BSE) images, which showed a single phase in the sample.

Since the reports of Al content have varied over the years, and the phase diagram shows a homogeneity range for the phase of about 70-73 at% Al concentration,[50] it was imperative to determine the Fe:Al ratio independently of the single crystal experiments. Energy Dispersive X-ray Spectroscopy (EDS) measurements confirmed that the synthesized sample was free from elemental impurities and the qualitative Fe:Al ratio of ~2:5. Wavelength Dispersive X-ray Spectroscopy (WDS) was used to more quantitatively determine the stoichiometry, as its use of standards helps eliminate environmental factors that could influence the amount of Al detected. From WDS, the phase was measured to have a composition of $Fe_{1.0(2)}Al_{2.62(11)}$

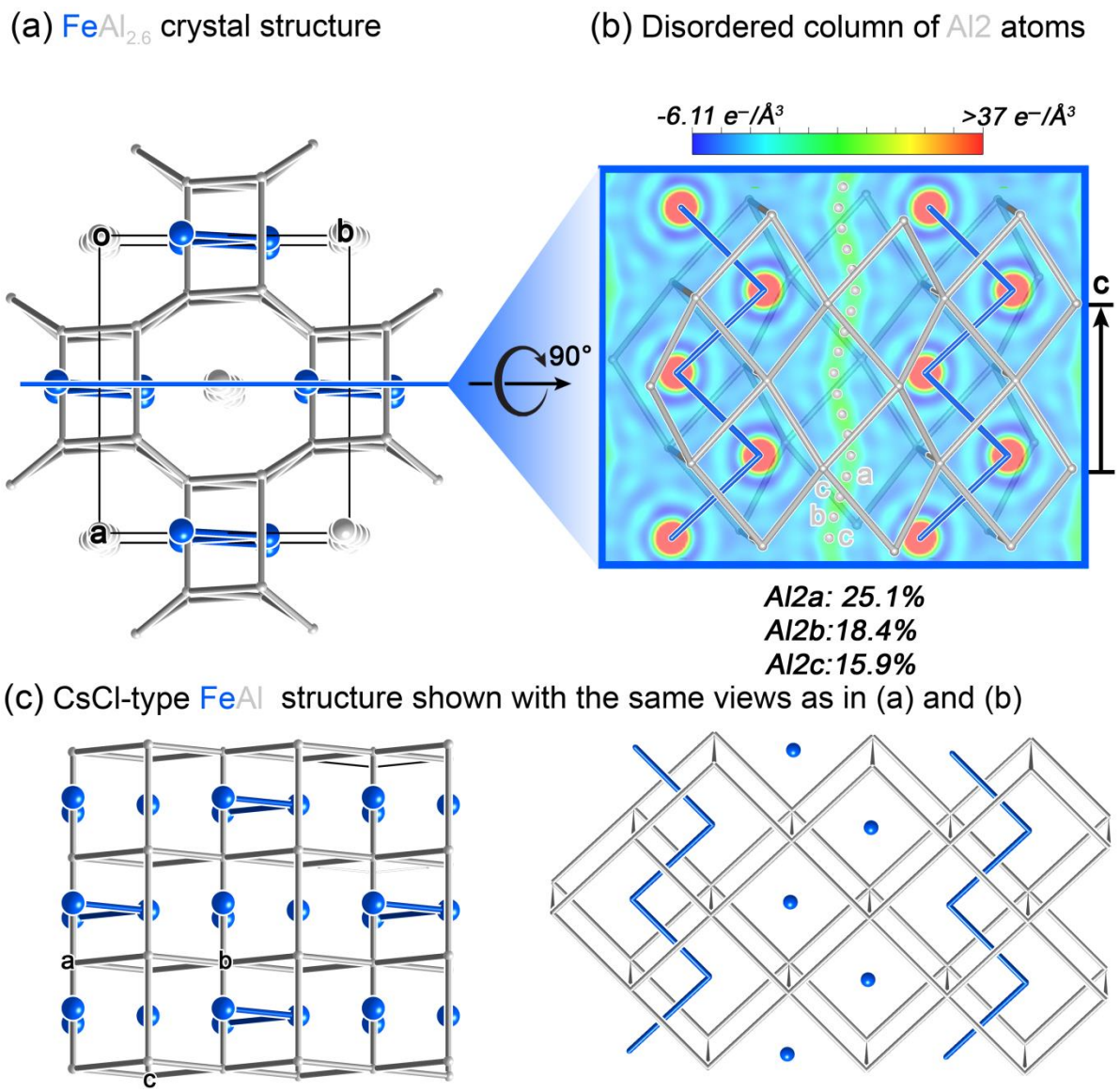

Figure 4.1. The disordered structure of the aluminide Fe_2Al_5. (a) View of the crystal structure tilted approximately down the *c*-axis. (b) The channel of electron density along the c-axis modeled with three partially occupied aluminum sites: Al2a, Al2b, and Al2c. A cross section of the Fourier electron density is shown in the context of the framework. (c) The corresponding views of the CsCl-type structure of FeAl, illustrating how Fe_2Al_5 can be derived from it by the replacement of a zigzag chain of Fe atoms by the disordered aluminum column.

Structure determination and description. Single crystals were picked from the crushed reaction mixture for single crystal X-ray diffraction experiments. The diffraction data were indexed with an orthorhombic unit cell with a=7.5660(3) Å, b=6.4117(2) Å, and c=4.22350(18) Å, parameters that agree closely with those reported previously. No superstructure or satellite reflections were observed for the room temperature data collection and all of the observed systematic absences were consistent with the *C*-centering and *Cmcm* space group assigned earlier. The structure solution similarly showed features consistent with those described by Grin et al., including the presence of the continuous column of electron density corresponding to the disordered Al sites.

A simple way to visualize the arrangement of atoms in Fe_2Al_5 is through its relationship to the CsCl-type structure of FeAl (Figure 4.1). By comparing the views down of the *c* direction of Fe_2Al_5 and the [110] direction of FeAl, a one-to-one correspondence can be detected between the ordered framework of the former and the simple lattice of the latter. In particular, the zigzag chains of Fe atoms running along *c* in Fe_2Al_5 correspond to half of the Fe atoms in FeAl. In place of the other half of the Fe atoms in FeAl, the disordered Al column appears in Fe_2Al_5. In other words, the structure of Fe_2Al_5 can be derived by dividing the Fe sublattice of FeAl into zigzag chains, and replacing every other chain with a column of Al atoms. The Fe atoms now have two Fe neighbors instead of the six that each had in the CsCl type. The other differences between the structures can then be understood as the result of the FeAl host framework bulging around the newly inserted Al columns.

Modelling this disordered region atomistically is challenging, and somewhat arbitrary given the continuous nature of the electron density distribution. We found that it was convenient to model it with three partially occupied Al positions as shown in Figure 4.1b, with two of the sites (Al2a and Al2b) corresponding to maxima in the density, and the third (Al2c) serving as a bridge between these peaks. Curiously, the Al content of the column consistently refined to yield a final formula of $FeAl_{2.75}$ for a wide range of models of partially occupied sites. Since we have independently established the Al stoichiometry to be 2.62 from the WDS experiments, we attempted to constrain the Al occupancies in our crystallographic model accordingly. However, such constraints led to the atomic displacement parameters on the least occupied Al atom positions to become nonpositive definite. The overestimation of Al content in the crystallographic model was also reported by Grin et al, which they attributed to the incomplete absorption correction or possible mixing of Fe onto the disordered Al sites. The presence of a small amount of Fe in this disordered region would easily explain the discrepancy between the WDS and single crystal compositions.

As stated above, neither superstructure or satellite reflections were observed for room temperature data collections, but we were curious to see if this might change at different temperatures. To further investigate possible ordering transitions, we carried out variable temperature single crystal X-ray diffraction experiments. Full data sets were collected at 100 K, 150 K, and 400 K. In all three cases, no additional reflections appeared (see Appendix C), and solving the crystal structures at the three temperature points showed the same continuous column of electron density, which was still well-modelled

with a triad of partially occupied Al positions. As shown is in Figure 4.2, minimal shifts in atom positions are observed; the continuous column of electron density is a robust feature of the compound, at least for the $FeAl_{2.62}$ composition of this crystal.

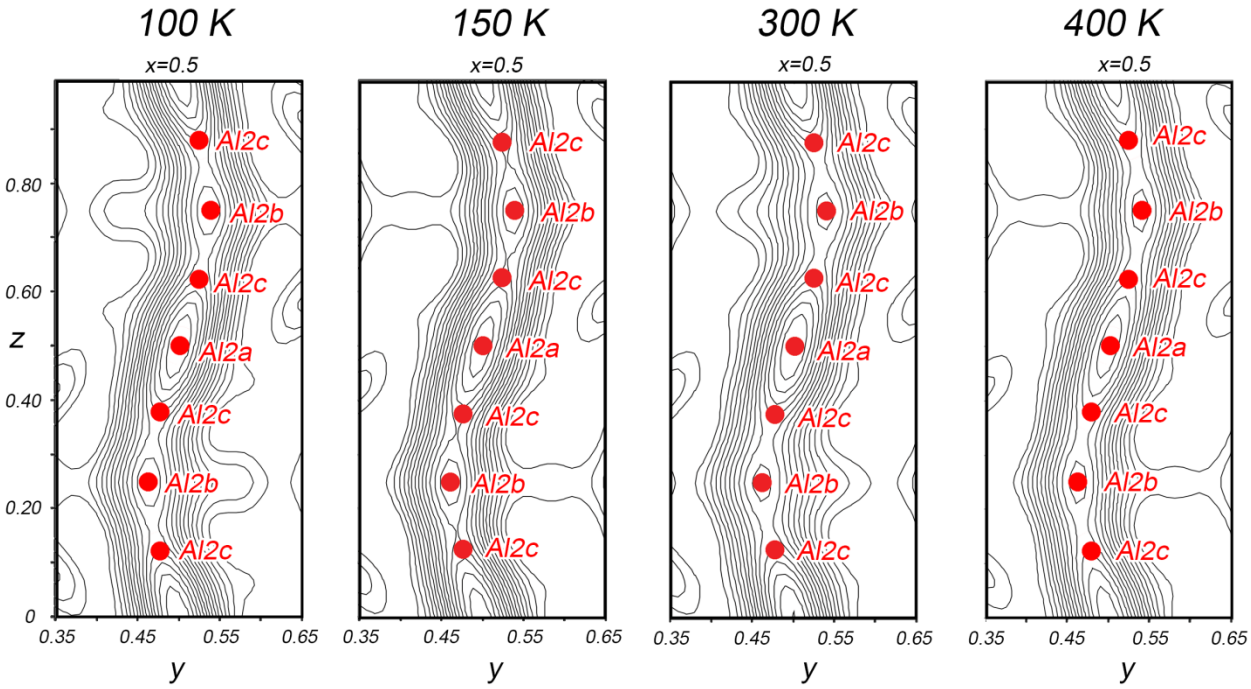

Figure 4.2. Evolution of the X-ray diffraction pattern and Al2a, Al2b and Al2c channel electron density as a function of temperature. The cross sections of the Fourier electron density through the Al2a, Al2b, and Al3 channels obtained for data sets collected at 100 K, 150 K, 300 K, and 400 K.

In this section, we have confirmed the general model of Grin et al. for Fe_2Al_5, and seen how its disordered Al columns form an integral feature of this compound, independent of temperature. The overall structure can be viewed in host-guest type fashion, in which an FeAl host structure accommodates a column of guest Al atoms. The question we will turn to next is what drives this arrangement of atoms. We will answer this question in two steps using electronic structure calculations which focus on the different roles of electron count and atomic size.

4.5. Electron counting and Al-nonstoichiometry

Now that we have confirmed the presence of the channels of disordered Al atoms in Fe_2Al_5, let's now turn to exploring the role that they play in the stability of the compound. One factor that could potentially play a role is the ability of the Al non-stoichiometry to tune the electron concentration in the compound. In fact, the composition of this compound places it within the domain of an electron counting rule for transition metal-main group (T-E) intermetallic phases, the 18-*n* rule: In these compounds, the T atoms attempt to obtain filled 18-electron configurations, in which an electron pair is associated with each of their valence s, p, and d atomic orbitals. To achieve these closed shells, each T atom requires 18-*n* electrons, where *n* is the number of electron pairs the T atom shares covalently with T atom neighbors through multicenter E-bridged functions known as isolobal T-T bonds. [51,52] Adherence to this rule is correlated to the presence of a bandgap or pseudogap in the Density of States (DOS) distributions at the Fermi energy of the phase, common indicators of electronic stability.

According to the Fe-Al phase diagram, the Fe_2Al_5 phase is stable for an Al content of 70-73 at%, leading to a range of valence electron counts (total valence electron count/number of Fe atoms): from 15 to 16.11 electrons/Fe atom. The composition determined for our crystal, $FeAl_{2.62}$, lies at the Al-rich end of this range, yielding an electron concentration of 15.86 electrons/Fe atom. This count is approximately two electrons/Fe atom short of 18, leading to the prediction that the Fe atoms should each take part in two Fe-Fe isolobal bonds. This is consistent with the observed condensation

of the Fe atoms into zigzag chains in the Fe_2Al_5 structure, providing each Fe atom with two Fe neighbors.

As the above reasoning highlights, one advantage of the 18-*n* rule is that it can be simply applied to compounds where disorder occurs in the main group sublattice. Testing the applicability of this scheme with DFT calculations in such cases, however, is not as straight forward, as these calculations require a periodic, ordered model. We thus generated models with different ordering patterns in the Al2 region; we'll focus here on two of them, with compositions $FeAl_{2.625}$ (15.875 electrons/Fe) and $FeAl_{2.5}$ (15.5 electrons/Fe). Both models are based on a 1×1×2 supercell. In $FeAl_{2.625}$ model every fifth Al2 atom was kept (yielding stoichiometry of $FeAl_{2.75}$) and then one additional Al2 atom was at random removed from one of the columns. For the $FeAl_{2.5}$ model, only half of the Al2a atoms were kept and all of the other Al atom position in the columns were removed. Once these patterns were constructed, they were optimized with GGA-DFT, yielding the coordinates listed in Appendix C.

The density of states (DOS) curves for the two models are shown in Figure 4.3. Despite the differences in the placement and loading of Al2 atoms within the channels, the two distributions bear strong similarities. In both models the Fermi energy falls into a narrow pseudogap centered near -8 eV. The narrowness of the pseudogap forebodes a strong preference for a particular electron count. Below the pseudogap, a large peak, composed predominantly of Fe d states grows in. Similarly, above the pseudogap, the peak is also predominantly of Fe d character. The lowest energy levels, between -15eV and -19eV, are dominated by the Al s and p orbitals.

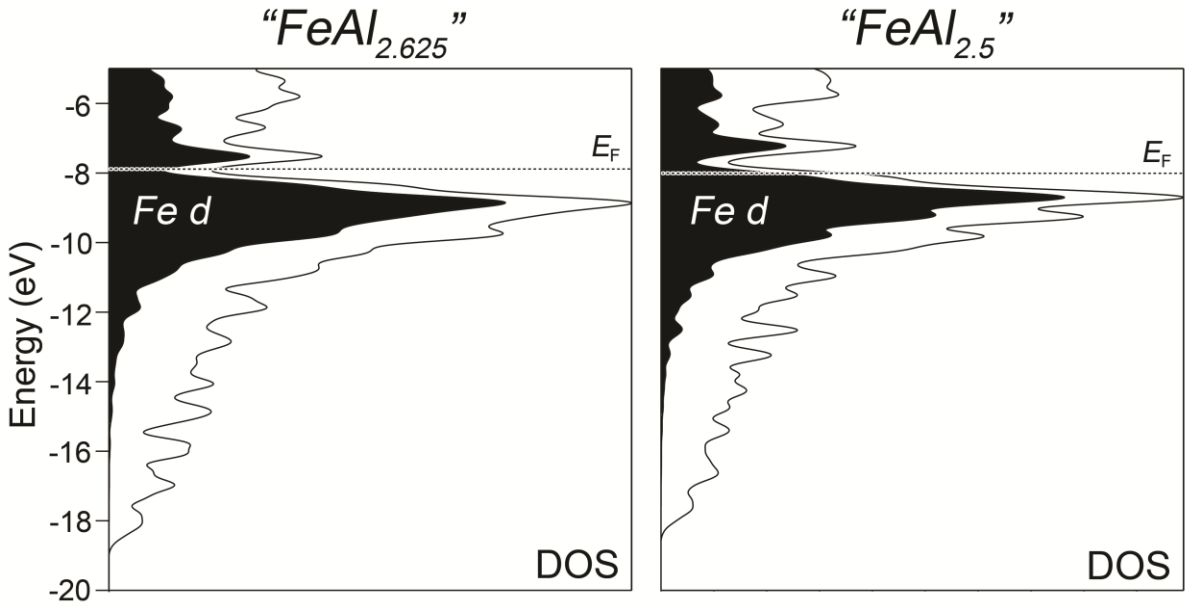

Figure 4.3. DFT electronic density of states (DOS) distributions calculated for two ordered models of Fe_2Al_5.

Once the electronic structures of these models were calculated, and best-fit Hückel models were constructed for them, we used the reversed approximation Molecular Orbital (raMO) analysis to explore their relationship to the 18-*n* bonding scheme. In the raMO approach, the occupied crystal orbitals act as a basis set for the reconstruction of localized atomic-like target functions which are hypothesized to play a key role in the local bonding of the compound[41] For extracting filled 18-electron configurations from the occupied crystal orbitals, the optimal target functions are the 9 s, p, and d valence orbitals of any one T center. The degree to which the raMO analysis can reproduce the target functions reflects the extent to which they are occupied in the compound, while the deviations tell us about how those functions are embedding through bonding interactions into the electronic structure.

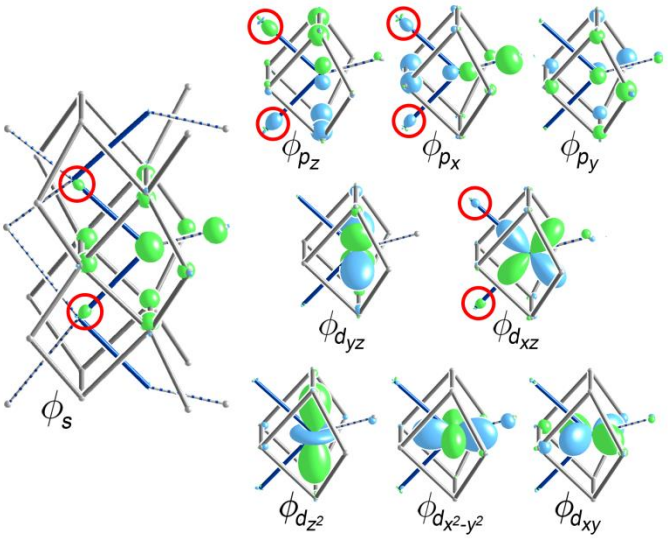

Figure 4.4. raMO reconstructions of the 4s, 4p, and 3d valence orbitals for an Fe atom in the $FeAl_{2.625}$ model. Substantial contributions from neighboring Fe sites are circled in red.

In Figure 4.4, we show the raMO reconstructions of the valence s, p and d orbitals for an Fe atom in our $FeAl_{2.625}$ model. Each of the nine s, p, and d orbitals are seen here to serve as the core of a function that spreads to varying degrees around the first coordination environment through bonding interactions. This observation is consistent with the notion that an electron pair is associated with each of the Fe atom's valence orbitals, and thus the presence of a filled 18 electron configuration.

This configuration cannot be completely assigned to the central Fe atom independently, however: four of the raMOs (those based on the 4s, $4p_y$, $4p_z$ and $3d_{yz}$ orbitals) exhibit bonding contributions from the neighboring Fe atoms in the zigzag chain, indicative of electron sharing between the Fe atoms. The four atomic orbitals at the centers of these raMOs in fact form a set appropriate for the creation of sp^2d hydrid orbitals pointing to the corners of a square, which would closely match the ~90° Fe-Fe-Fe

angles in chains. Taking such linear combinations (with slight variations) of these four raMOs reveals two bonding functions localized along individual Fe-Fe contacts (Figure 4.5, top). These represent Fe-Fe isolobal σ bonds. The remaining two states generated by the linear combinations have the lobes pointing outwards from the Fe chain, toward the neighboring Al2 column (Figure 4.5, bottom). In terms of Fe-Fe interactions, these would be considered as non-bonding. In this way, they resemble Fe lone-pairs that coordinate to the surrounding Al atoms. The remaining five raMOs not involved in this hybridization also identified as Fe-Fe nonbonding states.

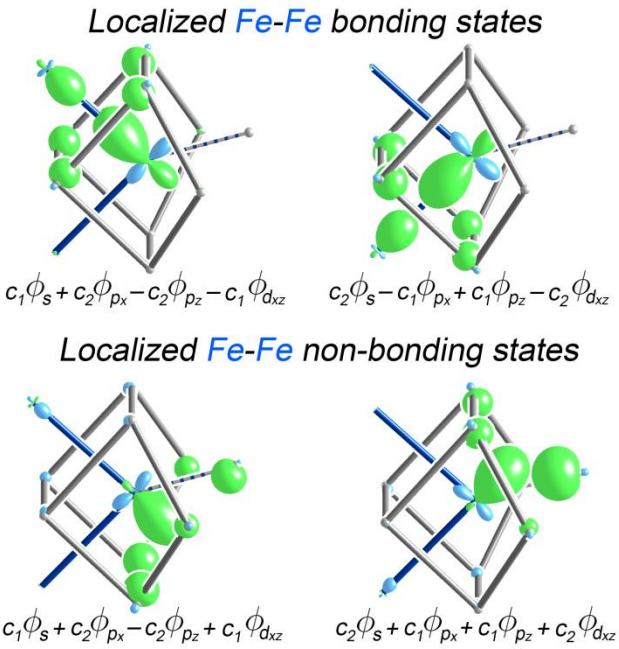

Figure 4.5. sp^2d-hydrids constructed from the raMOs in Figure 4.4, revealing two isolobal Fe-Fe bonds along the Fe-Fe zigzag chains. c_1= 0.5773 and c_2= 0.4083.

The two Fe-Fe isolobal bonds that emerge from this raMO analysis concurs with the hypothesis that the Fe_2Al_5 follows the 18-*n* bonding scheme with *n* = 2. The electronic structure is then optimized at 16 electrons per Fe atom. From this viewpoint, the reasons

for the nonstoichiometry in the Al sublattice become apparent. A perfect 16 electron count would require a stoichiometry of $FeAl_{2.67}$. As the unit cell contains 4 Fe atoms, the desired Al content would be 10.667 atoms, a non-integer number. The Al-rich side of the experimentally observed homogeneity range (electron concentration of 16.11) concides closely with the filling of the band structure up to the pseudogap. Adding more Al atoms into the system beyond this point would be expected to begin filling the Fe σ* antibonding states, leading to destabilization of the structure. The phase appears to show more flexibility in terms of lower electron counts, with Al-poor compositions with electron counts as low as 15 apparently being accessible. This greater flexibility toward electron-poor configurations over electron-rich ones is commonly observed in structures governed by the 18-*n* bonding scheme.

4.6.Chemical pressure quadrupoles along the disordered channel

Thus far, we have traced the Al nonstoichiometry in Fe_2Al_5 to the phase's adherence to the 18-*n* bonding scheme. This bonding scheme, however, focuses almost entirely on the Fe atoms and their placement relative to each other, while the Al atoms are viewed essentially as a stabilizing field for functions whose symmetry properties are templated by the Fe atomic orbitals. As such, little information is given about how these Al partial occupancies are distributed through the unit cell. The question thus remains open as to why the Al disorder becomes concentrated in the Al2 columns. In this section, we will see how a DFT-Chemical Pressure (CP) analysis can account for these

observations in a way that suggests a general approach to identifying potential channel-forming frameworks in other intermetallic structures.

In the CP analysis, the macroscopic pressure of a compound is resolved spatially into a competition between interatomic contacts calling for the expansion and contraction of the structure. In Figure 4.6, we show the CP schemes that result for carrying out this process on two simple models for Fe_2Al_5: one where Al atoms are placed on every other Al2a site along *c*, and one where they are placed on every other Al2b site instead. Here, the sums of the interatomic pressures are represented by radial plots. Black lobes correspond to directions along which the atom feels a desire for the contraction of the structure (negative pressure), while white lobes point along directions where the expansion of the structure is favorable. We focus in this Figure on the CP experiences by the Al2 and nearby Fe atoms, with the full CP schemes including the Al1 sites being available in Appendix C.

The most striking part of the CP scheme which results in two models of Fe_2Al_5 are large white lobes pointing between the Al2 atoms and their Fe neighbors, suggesting that these contacts are too short. In the first of these models, the Al2a sites are half occupied. In this case, each Al2 atom is placed directly between two Fe neighbors and appears pinned to the center of channel by opposing CPs. Negative CP features appear on these Al2 atoms along the directions perpendicular to the Fe-Al-Fe lines corresponding to overly long Al-Al contacts.

In the second model (Figure 4.6b), Al atoms are placed on every other Al2b site. One large positive CP is present on each of these atoms, oriented towards the nearest Fe

neighbor, which is substantially closer than another of the other proximal Fe sites (2.33 Å vs. 2.77 Å for the next closest Fe atom). In response to the lack of another Fe site on the side opposite from this close neighbor, the Al2b site has shifted away from the center of the channel. Full relief of the Fe-Al positive CP on this site is prevented by the growth of negative pressures directed toward Al1 sites on the Fe side of the channel. Also, as with in the Al2a model, negative CPs are directed perpendicular to the Fe-Al contact, with a substantial component along the direction of diffuse electron density in the experimental structure.

For both models, the Al2 atoms show negative and positive pressures oriented perpendicular to each other, giving rise to CP quadrupole moments, a feature strongly correlated with soft phonon modes. In this case, motions of the Al atoms along these negative CP directions would be expected to be quite facile, as they would lengthen the Fe-Al contacts, while leading to shorter Al-Al interactions along the direction of movement. Intriguingly, the component of these motions along c would tend to guide the Al2a site into the Al2b site, and vice versa, creating a channel of diffusion in the space between neighboring Fe zigzag chains that would account for the experimentally observed disorder, as is illustrated schematically in Figure 4.6c.

To explore this possibility of soft motions, we carried out calculations of the phonon band structure of Fe_2Al_5. The phonon band structure and density of states (DOS) distributions that result for the Al2a model are shown in Figure 4.7a. As Al atoms are significantly lighter than Fe ones, we would normally expect them to dominate the high-frequency modes, with the Fe atoms participating in the low-

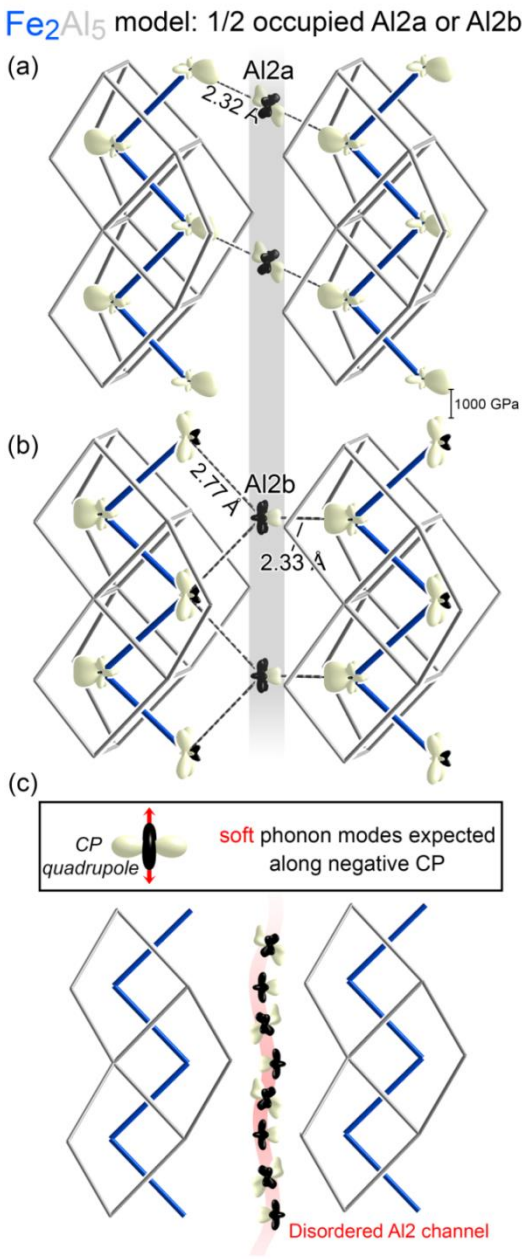

Figure 4.6. DFT-Chemical Pressures (CPs) underlying channel formation in Fe_2Al_5. The CPs experienced by the Fe and Al2 atom sites are shown (a) and (b) in two ordered models. A persistent feature is the negative CP along the Al2 channel. In (c), the Al2 CP features for Al atoms at the Al2a and Al2b sites are collected from the models in (a), and (b), as well as their symmetry-equivalent configurations, resulting in an undulating path of negative CP.

frequency vibrations. It it striking to note, then, that the lowest peak in the DOS arises chiefly from the motions of the Al2 sites (shaded region). In fact, this low frequencies-peak appears to rise almost entirely from a single band, which is relatively flat over a range from Y (0 ½ 0) to T (½ ½ ½) of the Brillouin zone.

To examine the character of this band, we visualize its phonon mode at the q-point T (½ ½ ½) in Figure 4.7b, in which the atomic motions are represented with red arrows. The largest amplitudes appear on the Al2 atoms along the direction of their negative CP lobes, corresponding to a motion along the undulating Al2 disordered column in the experimental structure. In stark contrast, a second peak with substantial Al2 contributions can be found in the phonon DOS at ca. 12.5 THz, near the top of the band structure. These modes correspond to motions of the Al2 atom along the positive Fe-Al CP lobes. The anisotropy of the CP distribution around the Al2 atoms, with negative CPs along the channel and positive CPs towards the channel walls is therefore mirrored in the site's freedom of motion. Motions along the direction of positive CP are stiff and high frequency, while those along the direction of negative CP are much more fluid.

Similar results are obtained from the phonon band structure for the Fe_2Al_5 model with half of the Al2b sites occupied, though in this case the motions of the Al2 atom along the channel create a band with imaginary frequencies (see Appendix C), highlighting the softness of the motions of the Al2 atoms between the Fe atoms of the channel walls.

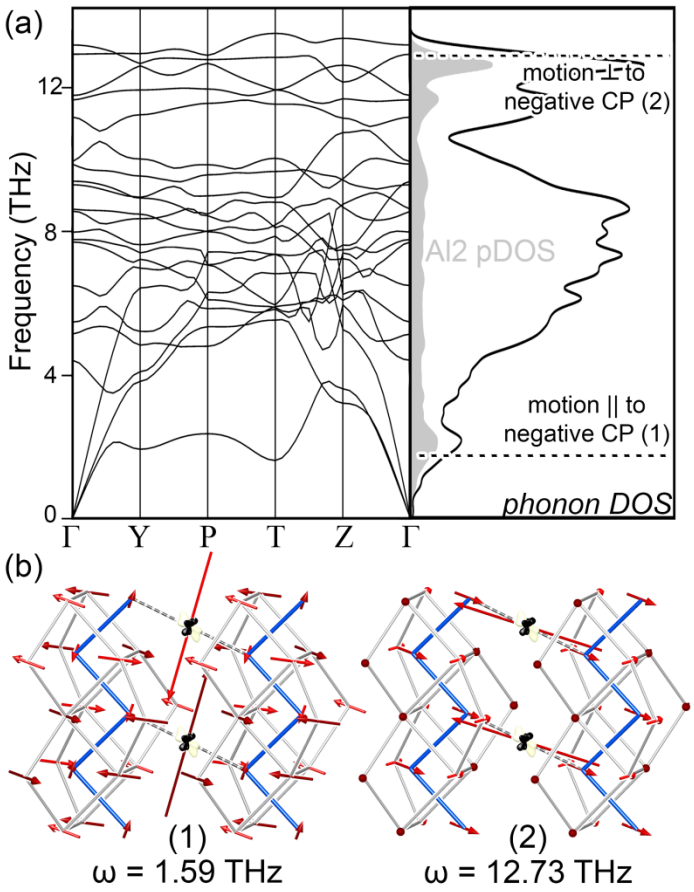

Figure 4.7. Phonon band structure and density of states (a) for the model Fe_2Al_5 compound with Al2a sites half-occupied. The projected phonon DOS for the Al2a site is highlighted in grey. Selected phonon modes (b) from the peaks in the Al2a projected DOS show low frequency modes tied to atomic motions of Al2a along the channel and high frequency modes occurring with atomic motions of Al2a into the channel walls.

In summary, the CP distributions of these ordered models of Fe_2Al_5 reveal CP quadrupoles on the Al2 sites that underlie soft atomic motions along the spaces between the Fe zigzag chains along the *c*-direction of the structure. When we recall that optimizing the bonding scheme of this compound requires non-stoichiometry on the Al sublattice, this region of the structure appears to be ideally suited to accommodating it.

The ease with which atoms move along this path means that they would have little trouble in shifting in response to the addition or removal of another Al atom in the channel.

4.7. Conclusions

This work was inspired by the striking disordered channels of Al atom that appear in the structure of Fe_2Al_5 and contribute to the phase's promise as a thermoelectric material. After confirming experimentally that no signs of order appear in these channels over a wide range of temperatures, we applied a series of theoretical methods to determine the roles they play in stabilizing the structure. Using DFT-calibrated Hückel method and the reversed approximation Molecular Orbital analysis, we traced the nonstoichiometry of the Al content to the desire by the Fe bonding network to achieve an 18 electron configurations following the 18-*n* rule. The DFT-Chemical Pressure (CP) schemes of ordered models then showed why this disordered is localized to the columns of Al2: the placement of these sites between chains of Fe atoms leads to CP quadrupoles that allow for soft motions that thread Al atoms along the path defined by the Fe atoms.

An open question remains why the disorder persists in this case over a range of temperatures, while such non-stoichiometric channels,[7,12,13,19] or sublattices of CP quadrupoles[53] lead to incommensurability in other systems. It would interesting to explore through comparisons with other intermetallic phases with similar channels how much this arises from lack of preference for placing the Al atom in the channel in the

Al2a site versus the Al2b site, as seen in the similarity of their CP schemes, or due to poor communication of structural information along or between the Al2 columns.

One experimental strategy to testing these hypotheses can be derived from the negative CP lobes pointing between Al atoms of the channels in the ordered models, suggesting that shorter Al-Al distances within the columns would be preferred. Introducing a larger atom such as In could alleviate the negative CPs, while disfavoring occupation at the Al2a sites that are squeezed on opposite sides by Fe atoms. Such an effect could drive a preferred ordering within a column. Furthermore, including some larger atoms in the channel would have shorter contacts with the walls of the channels and could induce positional shifts within the Fe zigzag, potentially propagating a specific ordering pattern from one channel to the next.

More generally, the way that electron counts and chemical pressures conspire to produce the disordered Al2 columns suggests an approach by which similar channel structures could be induced in a wider range of intermetallic phases. Compounds that follow the 18-*n* bonding scheme while exhibiting columns or sheets of CP quadrupoles on some of the main group sites would be expected to be structurally responsive to elemental substitutions that would affect the electron concentration. Motions within the soft sublattices defined by the CP quadrupoles would provide a path by which main group atoms could be inserted or removed to maintain the 18-*n* electron counts. We are looking forward to exploring how this idea might apply to such structural series as the Nowotny Chimney Ladder phases, and to the discovery of new intermetallic compounds.

Acknowledgements

We thank Dr. John Fournelle for assistance with the WDS measurements. We also thank Vince Yannello for insightful discussions of the application of the raMO method, and Erdong Lu for conversations regarding the interaction between the 18-n bonding scheme and CP quadrupoles in shaping intermetallic structures. We gratefully acknowledge the financial support of the National Science Foundation (NSF) through grant DMR-1508496. This research involved calculations using computer resources supported by National Science Foundation Grant CHE-0840494.

4.8. References

(1) Rosseinsky, M. J. Recent developments in metal–organic framework chemistry: design, discovery, permanent porosity and flexibility. *Microporous and Mesoporous Materials* **2004**, *73*, 15-30.

(2) Davis, M. E.; Lobo, R. F. Zeolite and Molecular Sieve Synthesis. *Chem. Mater.* **1992**, *4*, 756-768.

(3) Warrier, P.; Khan, M. N.; Srivastava, V.; Maupin, C. M.; Koh, C. A. Overview: Nucleation of clathrate hydrates. *The Journal of Chemical Physics* **2016**, *145*, 211705.

(4) Mählpfordt, W. On the System Magnesium-Europium. V. $(Eu_3Mg_{14})Mg_x$ with $1.7 \geq x \geq 1$: An Intermetallic Phase with Channel Structure. *Zeitschrift für anorganische und allgemeine Chemie* **1997**, *623*, 985-989.

(5) Burkhardt, U.; Ellner, M.; Grin, Y. Powder diffraction data for the intermetallic compounds Co2Al5, monoclinic m-Co_4Al_{13} and orthorhombic o-Co_4Al_{13}. *Powder Diffraction* **2013**, *11*, 123-128.

(6) Zakharova, E. Y.; Churakov, A. V.; Doert, T.; Kuznetsov, A. N. $Pd_{17}In_4Se_4$, a Metal-Rich Palladium-Indium Selenide with an Open-Framework Structure. *European Journal of Inorganic Chemistry* **2013**, *2013*, 6164-6169.

(7) Piao, S. Y.; Lidin, S. Quasicrystal approximant $Ho_{13}Zn_{58+\delta}$ ($\delta \approx 0.6$): an incommensurate modulated tunnel structure. *Philosophical Magazine* **2007**, *87*, 2693-2699.

(8) Beekman, M.; Stefanoski, S.; Wong-Ng, W.; Kaduk, J. A.; Huang, Q.; Reeg, C.; Bowers, C. R.; Nolas, G. S. Structure and thermal conductivity of $Na_{1-x}Ge_{3+z}$. *Journal of Solid State Chemistry* **2010**, *183*, 1272-1277.

(9) Zürcher, F.; Nesper, R. Cationic Channels with Partial Anion Occupation in the Zintl Phases $Ba_2Mg_{12}Ge_{7.33}$ and $Ba_6Mg_{17.4}Li_{2.6}Ge_{12}O_{0.64}$. *Zeitschrift für anorganische und allgemeine Chemie* **2002**, *628*, 1581-1589.

(10) Saparov, B.; Broda, M.; Ramanujachary, K. V.; Bobev, S. New quaternary Zintl phases – Synthesis, crystal and electronic structures of $KA_2Cd_2Sb_3$ (A = Ca, Sr, Ba, Eu, Yb). *Polyhedron* **2010**, *29*, 456-462.

(11) Stegmaier, S.; Kim, S.-J.; Henze, A.; Fässler, T. F. Tetrahedral Framework Structures: Polymorphic Phase Transition with Reorientation of Hexagonal Helical Channels in the Zintl Compound Na_2ZnSn_5 and Its Relation to $Na_5Zn_{2+x}Sn_{10-x}$. *Journal of the American Chemical Society* **2013**, *135*, 10654-10663.

(12) Rohrer, F. E.; Lind, H.; Eriksson, L.; Larsson, A. K.; Lidin, S. In *Zeitschrift für Kristallographie - Crystalline Materials* 2001; Vol. 216, p 190.

(13) Grin, J. N. Ein Aufbaumodell für „Chimney-Ladder"-Strukturen. *Monatshefte für Chemie / Chemical Monthly* **1986**, *117*, 921-932.

(14) Elder, I.; Lee, C.-S.; Kleinke, H. $Zr_{11}Sb_{18}$: A New Binary Antimonide Exhibiting an Unusual Sb Atom

Network with Nonclassical Sb-Sb Bonding. *Inorg Chem* **2002**, *41*, 538-545.

(15) Smetana, V.; Miller, G. J.; Corbett, J. D. Three alkali-metal-gold-gallium systems. Ternary tunnel structures and some problems with poorly ordered cations. *Inorg Chem* **2012**, *51*, 7711-21.

(16) Boström, M.; Lind, H.; Lidin, S.; Niewa, R.; Grin, Y. Synthesis, crystal structure, phase relations and chemical bonding analysis of the new Nowotny chimney-ladder compound $ZrBi_{1.62}$. *Solid State Sciences* **2006**, *8*, 1173-1180.

(17) Kanno, M.; Yamada, T.; Ikeda, T.; Nagai, H.; Yamane, H. Thermoelectric Properties of Na_2ZnSn_5 Dimorphs with Na Atoms Disordered in Tunnels. *Chemistry of Materials* **2017**, *29*, 859-866.

(18) Yamada, T.; Yamane, H.; Nagai, H. A Thermoelectric Zintl Phase $Na_{2+x}Ga_{2+x}Sn_{4-x}$ with Disordered Na Atoms in Helical Tunnels. *Advanced Materials* **2015**, *27*, 4708-4713.

(19) Fredrickson, R. T.; Fredrickson, D. C. The Modulated Structure of $Co_3Al_4Si_2$: Incommensurability and Co–Co Interactions in Search of Filled Octadecets. *Inorg. Chem.* **2013**, *52*, 3178-3189.

(20) A., O. *Kinzoku-no-Kenkuy* **1933**, *10*, 432-445.

(21) Schubert, K.; Roesler, U.; Kluge, M.; Anderko, K.; Haerle, L. Kristallographische Ergebnisse an Phasen mit Durchdringungsbindung. *Naturwissenshaft* **1953**, *40*, 437.

(22) Kraan, A. M. V. d.; Buschow, K. H. J. THE ^{57}Fe MOSSBAUER ISOMER SHIFT IN INTERMETALLIC COMPOUNDS OF IRON. *Physica B* **1986**, *138*, 55-62.

(23) Ellner, M.; Mayer, J. X-RAY AND ELECTRON DIFFRACTION INVESTIGATIONS ON THE LIQUID-QUENCHED Fe_2Al_5. *Scripta Metallurgica* **1992**, *26*, 501-504.

(24) Burkhardt, U.; Grin, Y.; Ellner, M.; Peters, K. Structure Refinement of the Iron-Aluminium Phase with the Approximate Composition Fe_2AI_5. *Acta Crystallographica B* **1994**, *50*, 313-316.

(25) Chi, J.; Zheng, X.; Rodriguez, S. Y.; Li, Y.; Gou, W.; Goruganti, V.; Rathnayaka, K. D. D.; Ross, J. H. Dilute magnetism and vibrational entropy in Fe_2Al_5. *Physical Review B* **2010**, *82*.

(26) Jagličić, Z.; Vrtnik, S.; Feuerbacher, M.; Dolinšek, J. Magnetic properties of $FeAl_2$ and Fe_2Al_5. *Physical Review B* **2011**, *83*.

(27) Mihalkovič, M.; Widom, M. Structure and stability of Al_2Fe and Al_5Fe_2: First-principles total energy and phonon calculations. *Physical Review B* **2012**, *85*.

(28) Tobita, K.; Sato, N.; Kitahara, K.; Takagiwa, Y.; Kimura, K. Effect of Anomalous Crystal Structure of Iron Aluminides Fe_2Al_5 and Fe_4Al_{13}: Low Phonon Thermal Conductivity and Potentiality as Thermoelectric Materials. *MATERIALS TRANSACTIONS* **2016**, *57*, 1045-1049.

(29) *CrysAlisPro Software System, Version 171.37.35*; Rigaku Oxford Diffraction: Yarnton, UK, 2015.

(30) Bruker; Bruker AXS Inc.: Madison, Wisconsin, USA, 2016.

(31) Sheldrick, G. M.; University of Göttingen: Germany, 1996.

(32) Sheldrick, G. SHELXT - Integrated space-group and crystal-structure determination. *Acta Crystallographica Section A* **2015**, *71*, 3-8.

(33) Sheldrick, G. M. Crystal structure refinement with SHELXL. *Acta Crystallographica. Section C, Structural Chemistry* **2015**, *71*, 3-8.

(34) Petříček, V.; Dušek, M.; Palatinus, L. Crystallographic Computing System JANA2006: General features. *Z. Kristallogr.* **2014**, *229*, 345-352.

(35) Kresse, G.; Furthmüller, J. Efficient iterative schemes for ab initio total-energy calculations using a plane-wave basis set. *Physical Review B* **1996**, *54*, 11169-11186.

(36) Kresse, G.; Furthmüller, J. Efficiency of ab-initio total energy calculations for metals and semiconductors using a plane-wave basis set. *Computational Materials Science* **1996**, *6*, 15-50.

(37) Blöchl, P. E. Projector augmented-wave method. *Physical Review B* **1994**, *50*, 17953-17979.

(38) Kresse, G.; Joubert, D. From ultrasoft pseudopotentials to the projector augmented-wave method. *Physical Review B* **1999**, *59*, 1758-1775.

(39) Stacey, T. E.; Fredrickson, D. C. Perceiving Molecular Themes in the Structures and Bonding of Intermetallic Phases: The Role of Hückel Theory in an *ab initio* Era. *Dalton Trans.* **2012**, *41*, 7801-7813.

(40) Landrum, G. A.; Glassey, W. V.

(41) Yannello, V. J.; Kilduff, B. J.; Fredrickson, D. C. Isolobal Analogies in Intermetallics: The Reversed Approximation MO Approach and Applications to CrGa4- and Ir3Ge7-Type Phases. *Inorg Chem* **2014**, *53*, 2730-2741.

(42) Vanderbilt, D. Soft Self-consistent Pseudopotentials in a Generalized Eigenvalue Formalism. *Phys. Rev. B* **1990**, *41*, 7892-7895.

(43) Gonze, X.; Amadon, B.; Anglade, P. M.; Beuken, J. M.; Bottin, F.; Boulanger, P.; Bruneval, F.; Caliste, D.; Caracas, R.; Côté, M.; Deutsch, T.; Genovese, L.; Ghosez, P.; Giantomassi, M.; Goedecker, S.; Hamann, D. R.; Hermet, P.; Jollet, F.; Jomard, G.; Leroux, S.; Mancini, M.; Mazevet, S.; Oliveira, M. J. T.; Onida, G.; Pouillon, Y.; Rangel, T.; Rignanese, G. M.; Sangalli, D.; Shaltaf, R.; Torrent, M.; Verstraete, M. J.; Zerah, G.; Zwanziger, J. W. ABINIT: First-principles approach to material and nanosystem properties. *Computer Physics Communications* **2009**, *180*, 2582-2615.

(44) Gonze, X.; Beuken, J. M.; Caracas, R.; Detraux, F.; Fuchs, M.; Rignanese, G. M.; Sindic, L.; Verstraete, M.; Zerah, G.; Jollet, F.; Torrent, M.; Roy, A.; Mikami, M.; Ghosez, P.; Raty, J. Y.; Allan, D. C. First-principles computation of material properties: the ABINIT software project. *Computational Materials Science* **2002**, *25*, 478-492.

(45) Hartwigsen, C.; Goedecker, S.; Hutter, J. Relativistic separable dual-space Gaussian pseudopotentials from H to Rn. *Physical Review B* **1998**, *58*, 3641-3662.

(46) Berns, V. M.; Engelkemier, J.; Guo, Y.; Kilduff, B. J.; Fredrickson, D. C. Progress in Visualizing Atomic Size Effects with DFT-Chemical Pressure Analysis: From Isolated Atoms to Trends in AB5 Intermetallics. *Journal of Chemical Theory and Computation* **2014**, *10*, 3380-3392.

(47) Oliveira, M. J. T.; Nogueira, F. Generating relativistic pseudo-potentials with explicit incorporation of semi-core states using APE, the Atomic Pseudo-potentials Engine. *Comput. Phys. Commun.* **2008**, *178*, 524-534.

(48) Giannozzi, P.; de Gironcoli, S.; Pavone, P.; Baroni, S. *Ab initio* calculation of phonon dispersions in semiconductors. *Physical Review B* **1991**, *43*, 7231-7242.

(49) Grin, J.; Burkhardt, U.; Ellner, M.; Peters, K. Refinement of the Fe_4Al_{13} structure and its relationship to the quasihomological homeotypical structures. *Zeitschrift für Kristallographie - Crystalline Materials* **1994**, *209*, 479-487.

(50) Kubaschewski, O. *Iron-Binary Phase Diagrams*; Springer-Verlag: Aachen, 1982.

(51) Yannello, V. J.; Fredrickson, D. C. Orbital Origins of Helices and Magic Electron Counts in the Nowotny Chimney Ladders: the 18 – *n* Rule and a Path to Incommensurability. *Inorg. Chem.* **2014**, *53*, 10627-10631.

(52) Yannello, V. J.; Fredrickson, D. C. Generality of the 18-*n* Rule: Intermetallic Structural Chemistry Explained through Isolobal Analogies to Transition Metal Complexes. *Inorg. Chem.* **2015**, *54*, 11385-11398.

(53) Kilduff, B. J.; Fredrickson, D. C. Chemical Pressure-Driven Incommensurability in $CaPd_5$: Clues to High-Pressure Chemistry Offered by Complex Intermetallics. *Inorg. Chem.* **2016**, *55*, 6781-6793.

Chapter 5.

Substitution Patterns Understood through Chemical Pressure Analysis: Atom/dumbbell and Ru/Co Ordering in Derivatives of YCo_5

This chapter has been published: Hilleke, K. P..; Fredrickson, R.T.;Vinokur, A. I.; Fredrickson, D.C., ., *Cryst. Growth Des*, **2017**, 17(4), 1610-1619. Synthesis was done by Fredrickson, R. T.. Material's characterization was done by Fredrickson, R. T. and Vinokur A. I. The theoretical analysis was done by Hilleke, K. P. and Fredrickson D.C.

5.1. Abstract

Interstitials, mixed occupancy, and partial substitution of one geometrical motif for another are frequently encountered in the structure refinements of intermetallic compounds as disorder or the formation of superstructures. In this Article, we illustrate how such phenomena can serve as mechanisms for chemical pressure (CP) release in variants of the $CaCu_5$ type. We begin by comparing the DFT-CP schemes of YCo_5, an f-element free analogue of the permanent magnet $SmCo_5$, and its superstructure variant Y_2Co_{17} = $[Y_2(Co_2)_1]Co_{15}$ (Th_2Zn_{17}-type) in which one-third of the Y atoms are replaced by Co_2 dumbbells. The CP scheme of the original YCo_5 structure reveals intensely anisotropic pressures acting on the Y atoms (similar to CP schemes of other $CaCu_5$-type phases). The Y atoms experience large negative pressures along the length of the hexagonal channels they occupy, while being simultaneously squeezed by the channel walls. Moving to the Y_2Co_{17} structure provides significant relief to this CP scheme: the inserted Co_2 pairs densify the atomic packing along the hexagonal channels while providing space for the bulging of the walls to

better accommodate the remaining Y atoms. This Y/Co_2 substitution pattern thus yields a much smoother CP scheme, but residual pressures remain. The experimental relevance of these remaining stresses is investigated through a structural refinement of a Ru-substituted variant of Y_2Co_{17} using single crystal X-ray diffraction. A comparison of the Y_2Co_{17} CP scheme with the observed Ru/Co ordering reveals that Ru preferentially substitutes for Co atoms whose net CPs are most negative, in accord with the larger size of the Ru atoms. These results hint that a wider variety of elemental site preferences may be understandable from the viewpoint of CP relief.

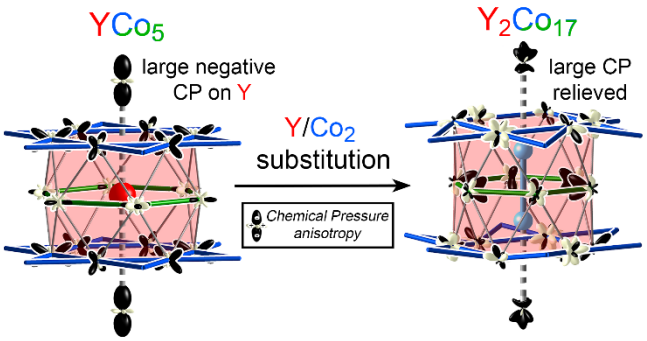

Figure 5.0. On going from the parent structure of YCo_5, substitution of one third of Y atoms for Co dumbbells relieves large negative chemical pressures between the Y atoms, thus stabilizing the superstructure.

5.2. Introduction

The perfect crystal is a philosophical ideal, one that above T = 0 K is made thermodynamically unfavorable due to entropic effects. Deviations from a perfect crystal can be manifested in disorder,[1-3] the simplest cases of which are encountered in molecular crystals[4] and simple alloys.[5] In molecular crystals, intermolecular interactions are often weak

enough that the substitution of one conformation or orientation of a molecule for another is not expected to provide a high energetic cost compared to the entropic and kinetic benefits of positional disorder.[6] Crystallographers have thus become accustomed to different conformations of the same molecular units randomly occupying the same coordinates within the average unit cell at different points within a crystal. In an alloy, meanwhile, very little distinguishes the various atomic sites from each other, making random occupancy by two elements an understandable solution.[7] Many solid state materials, particularly intermetallic phases, however, do not fit into either of these simple cases, with substitution patterns being one part of a larger challenge of explaining a vast structural chemistry. In this Article, we will explore how the recently developed chemical pressure approach can clarify the potential impact of such substitutions in these more complex materials, using as a model system the atom/dumbbell substitutions and mixed occupancies in variants of the $CaCu_5$ type.

Molecular and solid state chemistry both have rich traditions of using theory to predict and explain one type of substitution pattern: elemental site preferences on a framework of atoms. This history perhaps begins with Longuet-Higgins et al.'s observation in 1950 that the relative atomic charges in a hydrocarbon can anticipate the preferred placement of heteroatoms in substituted derivatives,[8] an observation that was later generalized to the concept of Topological Charge Stabilization in molecules.[9] For solid state compounds, both the relative bonding strengths[10-13] and atomic charges[14-20] at atomic sites in non-substituted structures have been (via the framework of perturbation theory) used for explaining the observed distributions of elements over arrays of atomic sites.[21] As first-

principles methods have become wide spread,[22] these semi-empirical approaches have been largely replaced by rigorous calculations of the energy differences between ordering patterns.[23-25]

Despite the significant progress made along this direction, two questions remain: (1) How do the details of a site's geometrical environment determine its affinities for different elements, and (2) how can these principles be generalized from the replacement of one atom with another to the substitution between larger cluster units? In our studies of the origins of structural complexity in intermetallic phases, we have developed a quantum mechanical formulation of the notion of *chemical pressure* (local pressure arising from packing constraints rather than from an externally applied force) that can provide visual and intuitive schemes for a variety of other structural phenomena, such as superstructures,[26-28] local icosahedral order,[29,30] soft phonon modes,[31] and even incommensurate modulations.[32] As we considered the question of atomic and cluster substitutions in solid state structures, we began to wonder whether the DFT-Chemical Pressure (DFT-CP) approach could offer insights into these problems as well.

Here, we present our first investigations along this direction, considering structural derivatives of YCo_5, a $CaCu_5$-type phase that can serve as an f-electron free analogue to the permanent ferromagnet $SmCo_5$.[33-35] The $CaCu_5$ structure type (Figure 5.1a) is built from alternating layers of kagome and honeycomb nets which are formed from the T atoms (T= transition metal or main group element), with the R atoms (R = alkaline earth, lanthanide, or similar electropositive element) occurring in the hexagonal channels of this arrangement. This pattern is parent to a wide range of structures based on the replacement of R

atoms with T dumbbells oriented along the *c* axis. In the $Yb_{0.8}Cu_{5.4}$ type,[36-38] this substitution occurs in a disordered fashion, while in the Al_3Zr_4 type,[39] the R atoms are completely replaced by T_2 pairs. In other derivatives, such as the $ThMn_{12}$,[40] Th_2Zn_{17},[41] Th_2Ni_{17},[42] and $ScFe_6Ge_6$[43] structure types, as well as a diverse family of $ScFe_6Ge_6$ type/$ScFe_6Ga_6$ type intergrowths,[44,45] ordered substitution patterns occur.

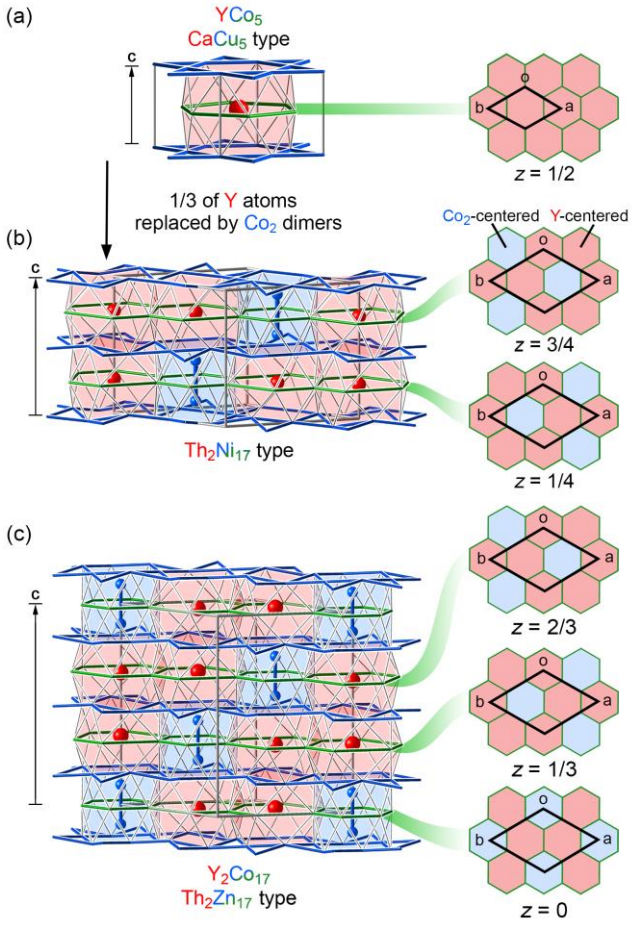

Figure 5.1. Atom/dumbbell substitution in derivatives of the $CaCu_5$ type. (a) The $CaCu_5$-type structure of YCo_5. (b)-(c) Th_2Ni_{17}- and Th_2Zn_{17}-type versions of Y_2Co_{17}, respectively, obtained by the ordered substitution of one third of the Y atoms in YCo_5 by Co_2 dumbbells.

While the principles we will develop in this Article should apply to all of these structures, we will focus on the relatively simple Th_2Zn_{17} type. This structure is derived from the replacement of 1/3 of the R atoms in each *ab* layer by T_2 dumbbells, such that the dumbbells occur in the hexagonal holes of a honeycomb net of R-centered polyhedra. It differs from the closely related Th_2Ni_{17} type in the relative placement of these dumbbells between neighboring layers. In the Th_2Ni_{17} type (Figure 5.1b), the repeat period along *c* contains two layers, with the dumbbell positions alternating in an ABAB fashion. For the Th_2Zn_{17} type (Figure 5.1c), this repeat period contains three layers, to create an ABCABC pattern. The Th_2Zn_{17}-type phases include Y_2Co_{17}, which like YCo_5 undergoes ferromagnetic ordering at low temperatures (T_c = 987 and 1186 K for YCo_5 and Y_2Co_{17}, respectively).[46-49]

Through comparisons of the CP schemes of YCo_5 and Y_2Co_{17}, we will see that such R atom-T_2 dumbbell substitutions, as well as the site preferences of dopants on the T sublattices in ternary variants, can be traced to CP issues in the parent structures. In this way, substitutions become another mechanism for CP release in intermetallic structures, a principle that may be helpful in guiding efforts to tune the composition of a phase in the optimization of its properties.

5.3. Experimental Section

Electronic Structure Calculations. DFT-Chemical Pressure (DFT-CP) analyses were performed on YCo_5, Y_2Co_{17}, and $Y_2Ru_2Co_{15}$ (an ordered model of the $Y_2Ru_xCo_{17-x}$ phase described below). The first step for each analysis was the geometrical optimization of the

crystal structure using the *Vienna Ab initio Simulation Package* (VASP).[50,51] The structures were optimized in the high precision mode with ultrasoft LDA pseudopotentials[52] provided with the package, beginning with the relaxation of the ion positions within fixed unit cells, followed by the release of all structural parameters. After obtaining these geometries, the LDA-DFT electronic structures were calculated with ABINIT program[53-56] and norm-conserving pseudopotentials[57] to generate kinetic energy and electron densities, as well as local components of the Kohn-Sham potential, expressed in terms of a 3D voxel grid. These calculations were performed at the equilibrium geometry as well as slightly contracted and expanded volumes to generate the information necessary to produce chemical pressure maps. Further details regarding the first principles calculations, such as the energy cut-offs and k-point grids used, are provided in Appendix D.

To obtain atomic charges for use in the DFT-CP analysis, additional geometry optimizations and charge density determinations were carried out in VASP using PAW-GGA potentials[58,59] in the high precision mode. Atomic charges were next extracted from the electron density maps of each compound with the Bader program.[60-63] These charges were in turn used to generate radial electron density profiles using the Atomic Pseudopotentials Engine (APE)[64] for free ions with charges from 0% to 50% of those from the Bader charge analysis. The CP results presented in the paper are for 50% ionicity, while the dependence of the results on this parameter is explored in Appendix D.

Chemical pressure maps were generated from the ABINIT output using the *CPmap* module of the CP package (with core unwarping and tricubic interpolation).[65] The *CPintegrate* module was subsequently used to portion out the CP map to contact volumes be-

tween the atoms with the Hirshfeld-inspired scheme. The voxel pressures within each contact volume were averaged to obtain interatomic pressures, which were projected onto real spherical harmonics ($l \leq 6$) centered on the atomic positions. The resulting integrated CP schemes were visualized using Figuretool2, an in-house MATLAB application.

Synthesis. A Ru-substituted variant of Y_2Co_{17} was synthesized in the course of an exploration of the $YCo_{5-x}Ru_x$ line of the Y-Co-Ru system by combining the elements (Y chips, Strem, 99.9%; Ru powder, Strem, 99.95%; Co powder; Aldrich, 99.9%) in the stoichiometric ratio Y:Ru:Co = 17:33:50, pressing the mixtures into pellets, and arc-melting the samples. The resulting ingots were wrapped in Mo foil, sealed in evacuated fused silica tubes, and annealed at 1000 °C for 168 hours, before being slowly cooled to room temperature. These synthetic procedures resulted in silver-colored materials, which when crushed yielded crystals of suitable quality for structural investigations with single crystal X-ray diffraction.

Single Crystal X-ray Diffraction Analysis. Fragments of the reaction products were mounted on pulled glass fibers with epoxy and investigated with a Rigaku Oxford Diffraction XCalibur E diffractometer, fitted with a Mo Kα sealed tube source (λ = 0.71069 Å). The run list consisted of ω scans (in steps of 1° with 80 sec exposures) that covered a full sphere in reciprocal space up to a resolution of 0.8 Å. The CrysAlis Pro software was used for data collection and processing.

Analysis of the collected data set yielded a metrically hexagonal unit cell with a=8.5011(12) Å and c=12.371(2) Å. The systematic absences were consistent with the space group $R\bar{3}m$, which was confirmed by the successful structure solution and refinement in

the subsequent steps. The five symmetry-distinct positions of the structure were obtained with the charge-flipping algorithm[66,67] as implemented in the Superflip program.[68] The resulting model was refined in Jana2006[69] against F^2. All atoms were refined anisotropically. Sites Co2, Co5, Co6, and Ru4 exhibited substitutional disorder, and were modeled as mixed Co/Ru positions each with a total occupancy of 1.0, yielding a composition $Y_2Ru_{4.85(7)}Co_{12.15(7)}$. The final refinement converged with an R value of $R(I>3\sigma)= 0.0221$, with the largest features in the Fourier difference map corresponding to maximum and minimum values of 1.51 and -0.92 electrons/Å^3, respectively. Tables of crystal data, the refined atomic coordinates, atomic displacement parameters, and selected interatomic distances may be found in Appendix D. Further crystallographic details may be obtained from FIZ Karlsruhe, 76344 Eggenstein-Leopoldshafen, Germany (e-mail: crysdata@fiz-karlsruhe.de) on quoting the deposition number CSD-432151.

Powder X-ray Diffraction Analysis. Fragments of the sample were crushed and manually ground for analysis with powder X-ray diffraction. A zero background sample holder was used for data collection on a Bruker D8 Advance diffractometer with Cu Kα (λ =1.5418 Å) radiation. A pattern was collected over the 2θ range of 20° to 70° with step size 0.015° and exposure time of 0.7 sec. Major peaks in the collected diffraction pattern were attributed to the Th_2Zn_{17}-type $Y_2Ru_{4.85}Co_{12.15}$ phase, while some additional minor peaks were attributed to a second phase with a $CaCu_5$-type basic cell.

Elemental Analysis with Energy Dispersive X-ray Spectroscopy. Several small fragments of the product were suspended in epoxy, and after the epoxy hardened, the sample was hand-polished against diamond lapping film to achieve a flat surface. The sample was

carbon coated, and elemental analysis was carried out with an Hitachi S-3100N Scanning Electron Microscope equipped with an EDS probe (Voltage = 15 keV). Back Scattered Electron (BSE) imaging revealed two distinct phases: the composition of the major phase was measured to be $Y_{1.83(5)}Ru_{4.42(9)}Co_{12.7(3)}$, qualitatively similar to the refined composition of the Th_2Zn_{17}-type $Y_2(Ru/Co)_{17}$ phase. The elemental composition of the minority phase was $Y_{1.3(2)}Ru_{2.0(2)}Co_{2.6(5)}$, which is consistent with a $CaCu_5$-type $Y(Co/Ru)_5$ phase. No substantial quantities of elements other than C (due to the carbon coating of the sample), O, Y, Co, and Ru were detected.

5.4. Driving forces for substitution in the CP scheme of YCo_5.

Over the course of this work, we will explore how the chemical pressure (CP) schemes calculated for simple structures can serve as a guide to their tendencies for undergoing substitution on their atomic sites. The ability of a CP scheme to highlight a need for such structural transformations is illustrated in Figure 5.2, where we show the results from calculations on YCo_5. In these plots, each atom is drawn with a radial plot representing the pressure distribution it experiences: the distance of the surface from the nucleus along any given direction is proportional to the sum of the pressures felt by the atom along that direction. The color of the surface, meanwhile, gives the sign of the overall pressure, with black indicating negative pressure (contraction of structure favorable locally) and white denoting positive pressure (expansion favorable).

Here, the CP scheme shows close similarities to those we have obtained previously for other $CaCu_5$-type phases.[31,32] The features on the Y atoms are most striking (Figure 5.2). Large negative pressure lobes (black) on the central Y atom point up and down along the hexagonal channel, calling for the contraction of the structure. These black lobes indicate that the Y atom's contacts to the Co atoms in the kagome nets above and below (blue) are overly long. The situation for the Y atom is different, however, in the *ab* plane: smaller positive CPs (white) point to the Co atoms in the honeycomb layer (green) expressing a desire for the expansion of the structure.

Overall, the CP distribution around the Y atoms appears highly anisotropic, with the atoms being squeezed by the walls of their hexagonal channels but with the packing along the length of the channel being under-optimized. The CP surfaces on the Co atoms largely carry the same information: the Co atoms in the kagome nets bear negative CP lobes toward the Y atoms, while those in the honeycomb layers show positive pressures toward the Y. In addition, positive CPs occur along the Co-Co contacts within the kagome layers and between the honeycomb and kagome layers, with negative CPs appearing between Co atoms of the honeycomb net.

The predominant tension in this structure arises from how the Y atoms fit within the Co sublattice. We would expect that reducing this tension, through improving the size and shape of the Y coordination environment, would be a primary driving force for any structural variations on this structure type.

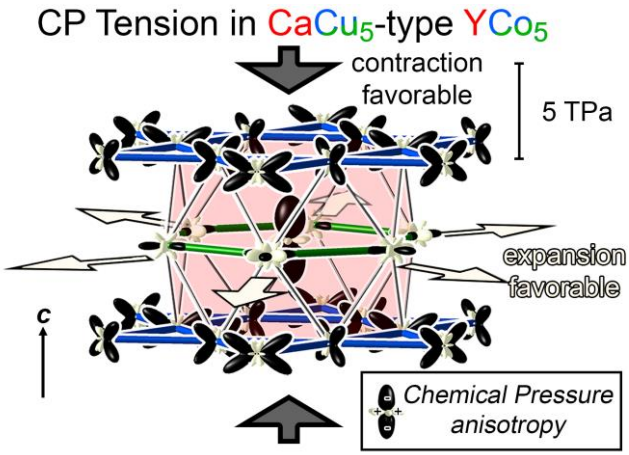

Figure 5.2. Anisotropic chemical pressures (CPs) in the YCo_5 structure. The CP scheme reveals the Y atoms experience strong negative CPs along *c*, but positive CPs in the *ab* plane.

As this compound is known to exhibit ferromagnetic ordering,[34,70,71] one may wonder how its CP scheme may be affected by magnetism. We thus carried out spin-polarized electronic calculations on YCo_5, obtaining a ferromagnetic ground state, with a net magnetization of 9.69 electrons/cell and a spin-density distribution that agrees qualitatively with the magnetic structure determined experimentally from neutron diffraction data.[35] The magnitudes and shapes of the CP features are very similar between the two schemes (see Appendix D for spin-polarized CP schemes), so that the same conclusions could be drawn from the use of either calculation. As we pursue the consequences of these CPs for substitutions, we will focus on the non-spin polarized electronic structures, with selected spin-polarized results being given for comparison in Appendix D.

5.5. CP relief from Y/Co_2 substitution.

In the CP scheme of the simple YCo_5 structure, the Y atoms display large negative pressures lobes up and down along the *c* axis, calling for a tighter coordination at these points. The structure of Y_2Co_{17} (Figure 5.1b) would appear to answer this call, with the added Co atoms filling some of the openings above or below the Y atoms with Co_2 dumbbells. Let's now see whether a CP analysis of Y_2Co_{17} supports this view.

In Figure 5.3, we follow the process of Co_2 dumbbell incorporation in a step-wise fashion, focusing on a single column of Y-centered polyhedra along *c* in YCo_5. In the original YCo_5 structure, the large negative pressure lobes on the central Y atoms pointing up and down along *c* are again visible (Figure 5.3a). These negative CP features create the impression that the space between the Y atoms is under-utilized, and that the structure could benefit from a denser filling of the channel. Next, in Figure 5.3b, we carry out the replacement of every third Y atom with a Co dumbbell, as in the Th_2Zn_{17}-type structure of Y_2Co_{17}, without allowing the surrounding structure to relax. Each Y atom now has one of its Y neighbors either directly above or directly below replaced by a Co_2 dumbbell. The increased packing density of atoms along the hexagonal channel is evident in the removal of half of the Y atoms' large negative CP lobes directed along the *c* axis.

This soothing of CP scheme is enhanced by the structural relaxation that follows (Figure 5.3c). The placement of a dumbbell on one side of each Y atom provides it the freedom to shift slightly closer to its remaining Y neighbor, helping appease the overly long contacts within the hexagonal channels of the structure, as is evident in the nearly complete relief of the black CP lobes on the Y atoms. In addition, the lower symmetry of the

superstructure allows the Co kagome layers to buckle, such that each Co site moves vertically toward the honeycomb layer where it has more Y neighbors. The largest CP features now appear on the Co_2 dumbbells, with positive CPs pointing directly along the dumbbell axis, which are balanced against negative CPs between each dumbbell atom and the Co atoms in the honeycomb layer bisecting that dumbbell.

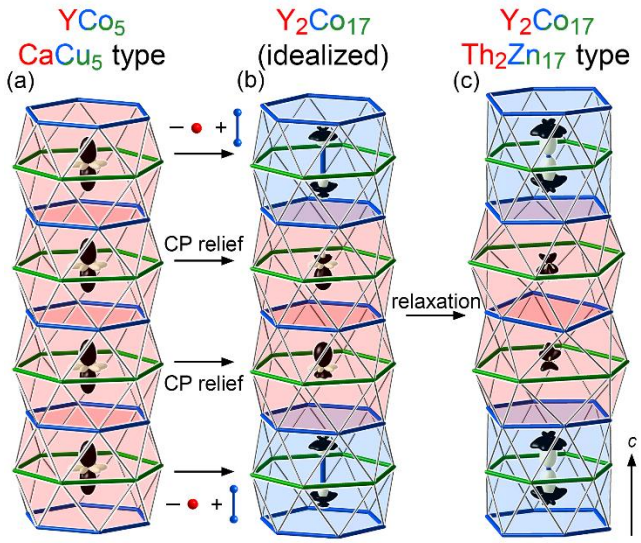

Figure 5.3. CP relief for Y_2Co_{17} in the Th_2Zn_{17} structure type. (a) The Y atoms in the original YCo_5 phase bear large negative pressure features along *c*. (b) Replacement with of one third of the Y atoms with Co_2 dumbbells to create closer contacts along *c* relieves strong negative CPs on the Y atoms. (c) Relaxation of the structure further alleviates the CPs experienced by the Y atoms.

While the Y/Co_2 substitution seems directed at relieving the Y atoms' CP features along the channel, the CPs in the *ab* plane have also been affected. Note that the positive Y-Co pressures in the *ab* plane of YCo_5 have essentially vanished in Y_2Co_{17}. As is shown in Figure 5.4, this effect is part of a larger story of cooperation between the hexagonal chan-

nels. In Figure 5.4a, we start with the CP scheme of a Co honeycomb layer of YCo_5 whose hexagonal holes are centered by Y atoms (Figure 5.4a). The Y-Co contacts within this layer trace out an extended network of positive CP that works against contraction along negative CPs elsewhere in the structure. This scheme changes drastically when the Y/Co_2 substitution to form Y_2Co_{17} is carried out (without allowing any relaxation of the lattice; Figure 5.4b). It is now dominated by large negative pressure lobes in the hexagons surrounding the center of the Co_2 dumbbells; the removal of the Y atom from these spaces has left large voids that the Co_2 dumbbells cannot adequately fill without some adjustments to the structure.

The intense CPs here in fact provide a clear indication of what types of relaxation should be favorable. Contraction of the Co_2-filled hexagons would provide relief to the negative CPs within them, while elongating the remaining Y-Co contacts suffering from positive CP. Such a path is indeed followed during the optimization of the structure (Figure 5.4c): the honeycomb net opens around the Y atoms, drastically reducing the positive CP features observed in YCo_5 while contracting around the Co dimers. The result is near-perfect CP relief around the Y atoms.

In summary, the structure of Y_2Co_{17} appears beautifully adapted to addressing the CP issues of YCo_5. The Y atoms of YCo_5 exhibit strongly anisotropic CPs, with the negative CPs directed along the hexagonal channels and positive CPs pointing toward the channel walls. This provides a rationale for how the YCo_5 phase can accommodate added Co atoms through the formation of the Y_2Co_{17} structure: the staggering of the substitution of Y with

Co_2 dumbbells between neighboring channels provides both denser packing along the channels and the freedom for the walls to bulge around the remaining Y atoms.[72]

5.6. Experimentally observed site preferences in $Y_2(Ru/Co)_{17}$.

This structural solution to the CP issues of YCo_5 shown by Y_2Co_{17} is elegant. However, it is not complete. As we saw in Figure 5.3c, noticeable CP features remain, particularly surrounding the dumbbell atoms. We might wonder if they have any chemical significance. One possible test of the importance of these pressures is in their ability to direct site preferences during elemental substitution. For example, a site experiencing negative pressure in a structure would be expected to have a relative propensity for substitution by larger atoms, while sites with overall positive CPs would tend to prefer smaller atoms. In this section, we will explore this idea of CP-driven site preferences with the experimental determination of a substituted variant of Y_2Co_{17}. As the Y-Ru-Co phase diagram[73] reports that Ru has a relatively high degree of solubility in the Y_2Co_{17} compound, we will focus on this system.

We synthesized Y-Ru-Co samples by arc-melting the elemental metals together, and then annealing the resulting ingots (see the Experimental Section for details). In screening crystals from the reaction products, we identified a unit cell compatible with a Th_2Zn_{17}-type structure. Upon collecting and analyzing a full dataset, this structure type was confirmed, with the refined composition coming out to $Y_2Ru_{4.85}Co_{12.15}$.

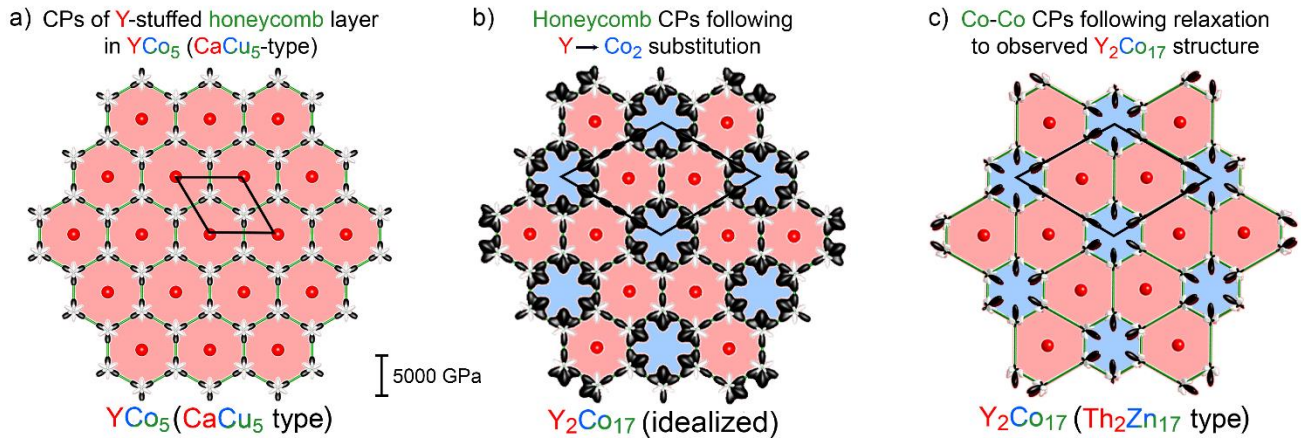

Figure 5.4. CP relief in the honeycomb layer of Y_2Co_{17} in the Th_2Zn_{17} structure type. (a) Large Y-Co positive CPs are present in this layer of the original $CaCu_5$-type YCo_5 phase. (b) Simply substituting Co_2 dumbbells for Y atoms without geometric relaxation creates large pockets of negative CP opposite the remaining positive Y-Co CPs. (c) Geometric relaxation reduces the CPs in the system through motions that simultaneously contract and expand the spaces around the Co_2 dumbbells and Y atoms, respectively.

The relative composition of the reaction product was confirmed with EDS. The experimentally derived formula $Y_{1.83(5)}Ru_{4.42(9)}Co_{12.7(3)}$ matches semiqualitatively with the formula refined from single crystal modeling. The relatively high Ru-content of this phase places it outside the $Y_2Ru_xCo_{17-x}$ homogeneity range reported at 600 °C, but has been obtained previously in $Y_2Ru_xCo_{17-x}$ crystals grown via the Czochralski method.[73,74] These results hint that the homogeneity range becomes extended at our annealing temperature of 1000 °C.

The refined crystal structure for this phase is shown in Figure 5.5, where features familiar from the Y_2Co_{17} structure can be seen. Now, however, the opportunity for mixed occupancy on the sites arises. Such mixed sites are indicated by the placement of color-

coded rings tracing the outlines of the spheres corresponding to the atoms in Figure 5.5b: the color of the sphere gives the majority element on that site (Y: red, Co: blue or green, Ru: yellow), while the color of the ring identifies the minority element. Here, the Y atoms are found to occupy their original sites exclusively, while all of the remaining sites (formerly Co in Y_2Co_{17}, but which we will now denote as T) show varying degrees of mixing between Co and Ru.

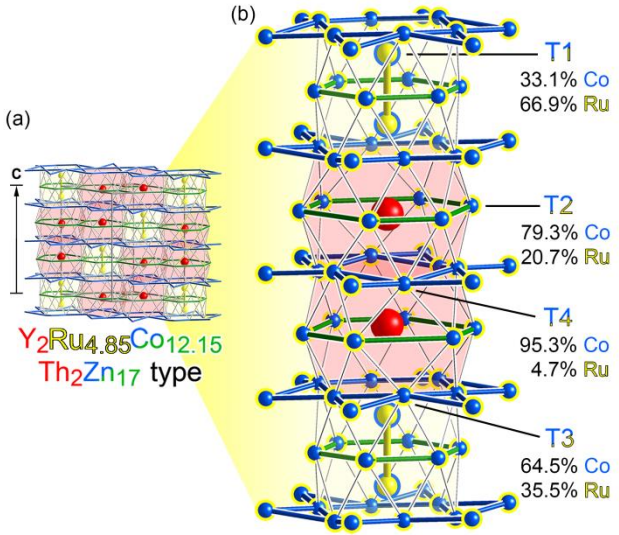

Figure 5.5. The crystal structure of $Y_2Ru_{4.85}Co_{12.15}$ in the Th_2Zn_{17} type. (a) Large section of the structure with the colors of the atoms corresponding to the majority element at each position, with red signifying Y, yellow Ru, and blue or green Co. Only the dumbbells centering every third 18-coordinate polyhedron are primarily occupied by Ru, with Co predominating in the honeycomb and kagome layers. (b) A close-up view of one hexagonal column in the structure with the Ru/Co occupancies on the mixed sites indicated.

The range in the Co:Ru ratios on these latter sites is substantial. The T1 site, located on the T dumbbells, is 66.9% Ru. The remaining T sites show much smaller degrees of Ru

incorporation. The honeycomb T site (T2) exhibits a Ru fraction of 20.7%, while the two kagome T sites (T3 and T4) show at first glance surprisingly different Ru contents given their similar coordination environments: 35.5% and 4.7%, respectively. Overall, these fractions add up to nearly 30% of all sites in the Co/Ru sublattice being occupied by Ru.

The specific degree of order in this system is likely to depend on the thermal history of the sample. However, the general trends in the site preferences mirror those observed in other ternary Th_2Zn_{17}-type phases. In $La_2Co_{17-x}M_x$ (M=Ti, V, Nb, Mo, Mn)[75] and $Ce_2Co_{17-x}T_x$ (T=Mn, Fe),[76] the larger T atoms substituting on the Co sublattice were assigned to the dumbbell sites (on the basis of Rietveld refinements of powder X-ray diffraction data and trends in the magnetic anisotropy fields, respectively). The favorability of substituting a larger atom onto the dumbbell sites is also seen in the $Er_2Fe_{17-x}Al_x$[77] and $Nd_2Co_{17-x}Al_x$[78] systems. In these, however, as well as in the Ce-Co-T system, the T3 site on the kagome layer is nearly as favorable for substitution. This site is 35.5% Ru in the $Y_2(Ru/Co)_{17}$ structure presented here, the second highest in the structure. Another common trend is that the other kagome layer site, T4, is universally the least likely to undergo substitution by a larger atom, with no uptake observed in the Nd-Co-Al and Er-Fe-Al systems, in comparison to the 4.7% Ru observed here in $Y_2Ru_{4.85}Co_{12.15}$.

5.7. CP-based understanding of the experimentally observed site preferences in $Y_2(Ru/Co)_{17}$.

Altogether, the experimental site preferences for the Th_2Zn_{17} type, both those we obtained for $Y_2Ru_{4.85}Co_{12.15}$ and from previous reports, suggest that certain sites on the T sublattice have a strong affinity for relatively large atoms (particularly the T1 dumbbell sites), others prefer smaller atoms (the T4 site), and the remainder appear content to accept whatever atoms are left over. Previously, these trends were interpreted in terms of empirical factors, such as volumes of the Voronoi polyhedra around the atomic sites or the bond enthalpies of various types of interatomic interactions.[75,77] In this section, we will take a different viewpoint, exploring how these occupancy patterns serve as a mechanism for relieving the CPs in the original binary structure. To do this, we will consider the CP scheme we calculated earlier for Y_2Co_{17} and judge whether substitution by Ru (metallic radius = 1.34 Å versus 1.25 Å for Co and 1.80 Å for Y) on each site would exacerbate or soothe the local CP issues.

The Y sites of Y_2Co_{17} provide a simple starting point. These atoms show net negative CPs (albeit smaller than those found in YCo_5), even while being occupied by the largest atom in the system. As such, substitution on this site by a smaller atom (Ru or Co) would seem unfavorable. Indeed, no evidence of such mixed occupancy on the Y sites was detected in the structure refinement of $Y_2Ru_{4.85}Co_{12.15}$. This observation is consistent with the very narrow width of the $Y_2Ru_xCo_{17-x}$ phase along the Y:(Ru/Co) line in the phase diagram,[73] but may also to some degree be reinforced by the relatively Y-poor composition used in the synthesis.

Our focus then moves to the four symmetry-distinct Co sites in Y_2Co_{17}. These sites display a wide range of net CPs, from as low as -543 to as high as 503 GPa (Figure 5.6), consistent with our observation of differences in Ru/Co occupation on these sites in the refined crystal structure. As Ru atoms are larger than Co atoms, we anticipate that they will preferentially segregate to the Co sites with the most negative CPs.

Only one site, T1 (situated on the Co_2 dumbbell), exhibits a net negative CP, with its value being -543 GPa. As is shown in the top panel of Figure 5.6, this site experiences an intense pressure conflict between an overly-short distance along the dumbbell and a desire for the dumbbell atoms to achieve stronger interactions with the atoms of the honeycomb layer between them. While the positive pressure lobe here appears larger, it corresponds to only a single contact vs. the six contacts with strong negative CP to each dumbbell site. When we integrate over all contacts, the result is a large net negative pressure on the T1 site. The placement of a larger atom here should therefore provide overall CP relief. The experimental structure of $Y_2Ru_{4.85}Co_{12.15}$ concurs, with the refined Ru content of the T1 site being 66.9%, the highest of all the sites in the phase.

The remaining Co sites all show positive CPs, but with very different magnitudes. The variability here is perhaps most pronounced for the Co atoms of the kagome nets, T3 and T4, with net CPs of 67 and 503 GPa, respectively. This large difference for nominally similar sites can be traced to their distinct placement relative to the Y/Co_2 substitution pattern. Both take part in the coordination environments of four Y/Co_2 sites, but differ in how many of these positions are occupied by Co_2 dumbbells rather than Y atoms: one for T3 and two for T4.

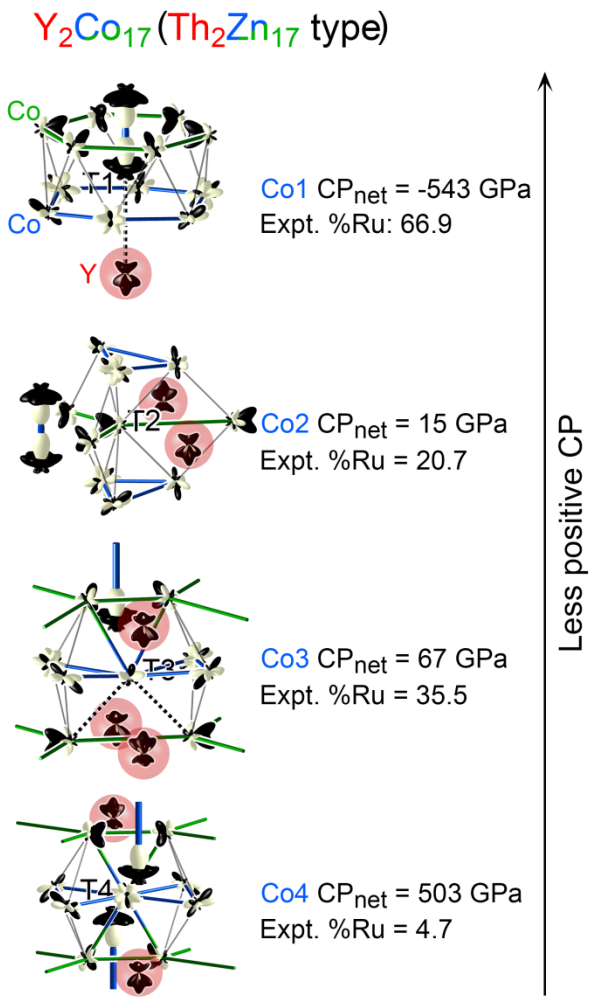

Figure 5.6. CP schemes for each Co site in the Th_2Zn_{17}-type phase Y_2Co_{17} correlated with the experimental percentage of Ru substitution in the ternary variant $Y_2Ru_{4.85}Co_{12.15}$. Smaller net CPs generally correspond to increased substitution by Ru.

This difference in coordination has a striking effect on the CP distributions (Figure 5.6): as the CPs of the dumbbells are predominantly negative, they lead to the squeezing of the interatomic interactions in their local environments. While T3 experiences this squeeze on only one side, the T4 site feels it in two opposite directions, resulting in short distances (and positive CP) to the honeycomb nets above and below. As a Co atom at the

T4 site already experiences a strongly positive CP, it is unlikely that it would be chosen by a larger atom such as Ru. The site preferences for the T3 site, with its moderately positive net CP, remain more ambiguous. These results are consistent with Ru occupancies of the sites being respectively small (4.7%) and moderate (35.5%) in $Y_2Ru_{4.85}Co_{12.15}$.

We now have only one more symmetry-distinct Co site in Y_2Co_{17} to consider: T2, which defines the honeycomb layers of the structure. Its CP features can be easily understood in terms of interactions we have already discussed: overly-long contacts to the Co_2 dumbbells give rise to some strong negative CPs (two lobes, one to each of the Co atoms in the dumbbell). These negative CPs are balanced by smaller positive lobes oriented towards kagome Co atoms above and below (with other minor negative CP lobes pointing to other kagome atoms and Y neighbors). Averaging over these features results in a weakly positive net CP of 15 GPa. Just as for the T3 site, this relatively low magnitude indicates the site should accept a larger atom with little difficulty but maintain a slight preference for a smaller one. This prediction is in line with the observed Ru fraction on this site of 20.7%.

In a broad sense, the net CP of each site matches well with its experimental occupancy by Ru: the site with negative net CP is mostly Ru in the ternary phase, the site with a large positive net CP strongly disfavors Ru substitution, and the two sites with moderately positive net CPs both undergo correspondingly moderate amounts of Ru substitution. A closer comparison, however, reveals that the resolution between the various sites is not as good for small differences in net CP. While the T3 site is calculated to have a larger net CP than the T2 site (67 vs. 15 GPa) its occupancy by the larger Ru atoms is refined to be higher rather than lower (35.5 % vs. 20.7 %). This inability to correctly order the site preferences

for small CP differences may reflect the way the balance between the positive and negative CP features on the atoms of this structure can be weakly affected by the ionicity parameter and the ambiguity that this variable introduces for the net CP on an atom.

There is another potential reason this CP difference is not reflected in the experimental substitution pattern. So far, we have discussed the driving force for Ru to substitute onto a Y-Co binary sublattice. By the time we start occupying the low-priority T2 and T3 sites, however, there will already be substantial quantities of Ru on the highly desirable T1 sites. Given similar CP magnitudes on the T2 and T3 sites, the placement of Ru on the T1 sites could significantly affect their relative abilities to attract Ru atoms. Indeed, the negative pressures on the T2 site are directed towards the atoms of the Ru-rich T1 dumbbell. Placing a larger Ru atom on the dumbbell site should help relieve this negative CP. The biggest negative pressures on the Co3 site, meanwhile, are directed towards Y atoms and are unlikely to be affected by Ru substitution. The placement of Ru on the T1 site is then expected to make the net CP of the T2 more positive (and less attractive to Ru), while leaving that of the T3 site largely unchanged.

To test this prediction, we calculated the CP scheme for a model phase in which the T1 dumbbell site is the completely occupied by Ru (see Appendix D). The net CP for a Co atom in the T2 site is found to increase from 15 GPa to 63 GPa in this process, making it more similar to that for the T3 site (which increases from 63 to 80 GPa). These CPs now better reflect the similar amount of Ru substitution in $Y_2Ru_{4.85}Co_{12.15}$, where T3 has 35.5% Ru and T2 has 20.7% Ru, although the relative order remains reversed.

In summary, the CP scheme of Y_2Co_{17} provides a clear explanation for the relative preferences of the sites for larger or smaller atoms in the $Y_2Ru_xCo_{17-x}$ (x=4.85) compound. The CP scheme of T1, the dumbbell site, is dominated by negative pressures which demonstrate its attractiveness to relatively large atoms. The T4 site, meanwhile, should be filled with high priority by relatively small atoms. The T2 and T3 sites then take up the remaining atoms, a behavior explained by their moderate net CP values, which can be modulated by the substitution patterns of the higher priority sites.

5.8 Conclusions.

In the crystal structures of solid state inorganic phases, mixed occupancy is a frequent occurrence. Most often, this involves atoms of two different elements randomly distributed over the same crystallographic sites. Substitutions of larger atom groups can arise as well, such as disorder in the coordination environment of an atom, leading to the possibility of several different polyhedra fitting into the same space.[7,79-84] In this Article, we began examining how such substitution can be anticipated from the CP scheme of an idealized, unsubstituted parent structure, drawing specific examples from the Y-Co system. We considered two cases: the partial replacement of Y atoms with Co_2 dumbbells in YCo_5 to create the Th_2Zn_{17}-type compound Y_2Co_{17}, and the elemental site preferences in Ru-substituted variants of Y_2Co_{17}.

For the transition from YCo_5 to Y_2Co_{17}, we saw cooperativity in the Y/Co_2 substitution along and between hexagonal channels of the Co sublattice, which provides signifi-

cant relief to the anisotropic CP distributions of the Y atoms in the original YCo_5 phase. The placement of Co_2 dumbbells on the Y atoms leads to deformation of the walls of the hexagonal channels, which stabilize the Y atoms in the neighboring channels. This effect results in the staggering of the Co_2 placements between channels, analogous to the forces stabilizing the $ScFe_6Ga_6$-type end member of the stuffed CoSn-type series.[44,45]

This picture of the origin of the Th_2Zn_{17}-type structure of Y_2Co_{17} adds a new avenue to the many paths to CP relief observed for $CaCu_5$-type lattices of the form RT_5 (R = lanthanide or other electropositive metal, T = late transition metal), alongside interface formation,[85] the incorporation of incommensurately spaced layers of atoms,[32] and the formation of multi-shelled icosahedral clusters.[29] Earlier, we divided these structural mechanisms into two classes: the T-rich and T-poor branches, in which CP relief is accomplished through polyhedral contraction and interface insertion, respectively. The case of Th_2Zn_{17} can be viewed along similar lines if we consider the R coordination environments in the $CaCu_5$-type as including the rather distant R neighbors along *c*, such that their total coordination is $T_{18} + R_2$. The R/T_2 substitution then replaces one of these R neighbors with a much closer T neighbor. This tightening of the coordination environment through added T atoms would belong to the T-rich path.

While the partial R/T_2 replacement leads to substantial CP relief to the original YCo_5 structure, residual pressures remain in Y_2Co_{17}. The experimental relevance of these pressures was demonstrated with their correlations to the site preferences in Th_2Zn_{17} structures and a newly refined structure of $Y_2Ru_{4.85}Co_{12.15}$. The ability of the CP method to sort the T sites according to their affinities for Ru vs. Co hints that this approach could serve as

a tool to elucidating elemental ordering patterns in other solid state structures, complementing first principles total energy calculations[22] and semi-empirical approaches such as relative Mulliken population analysis.[18,86,87] We are looking forward to pursuing this idea through a more systematic study of site-preferences in intermetallic phases.

Acknowldegements

We thank Dr. Joshua Engelkemier for expanding the DFT-Chemical Pressure Package's capabilities to include spin-polarized electronic structures. We also gratefully acknowledge the financial support of the National Science Foundation (NSF) through grant DMR-1508496. The research involved computational resources supported by NSF grant CHE-0840494.

5.9 References.

(1) Clegg, W.; Blake, A. J.; Gould, R. O.; Main, P. *Crystal Structure Analysis: Principles and Practice*; Oxford University Press: Oxford, 2001.

(2) Wooster, W. A. *Diffuse X-ray reflections from crystals*; Clarendon Press: Oxford, 1962.

(3) Wilson, C. C. A basic introduction to thermal motions of atoms in crystal structures, the underlying potentials and the physical information available from their analysis. *Crystallogr. Rev.* **2009**, *15*, 3-56.

(4) Nield, V. M.; Keen, D. A. *Diffuse Neutron Scattering from Crystalline Materials*; Oxford University Press: Oxford, 2001.

(5) Schweika, W. *Disordered Alloys*; Springer-Verlag Berlin Heidelberg: Berlin, 1998; Vol. 141.

(6) Welberry, T. R.; Weber, T. One hundred years of diffuse scattering. *Crystallogr. Rev.* **2016**, *22*, 2-78.

(7) Urban, K.; Feuerbacher, M. Structurally complex alloy phases. *J. Non-Cryst. Solids* **2004**, *334–335*, 143-150.

(8) Longuet-Higgins, H. C.; Rector, C. W.; Platt, J. R. Molecular Orbital Calculations on Porphine and Tetrahydroporphine. *The Journal of Chemical Physics* **1950**, *18*, 1174-1181.

(9) Gimarc, B. M. Topological charge stabilization. *J. Am. Chem. Soc.* **1983**, *105*, 1979-1984.

(10) Franzen, H. F.; Köckerling, M. The stabilization of ternary early transition-metal sulfides and phosphides at high temperatures by differential site occupancy. *Prog. Solid State Chem.* **1995**, *23*, 265-289.

(11) Kleinke, H.; Franzen, H. F. Bonding and Site Preferences in the New Quasi-Binary Zr2.7Hf11.3P9. *J. Solid State Chem.* **1998**, *136*, 221-226.

(12) Deringer, V. L.; Goerens, C.; Esters, M.; Dronskowski, R.; Fokwa, B. P. T. Chemical Modeling of Mixed Occupations and Site Preferences in Anisotropic Crystal Structures: Case of Complex Intermetallic Borides. *Inorg. Chem.* **2012**, *51*, 5677-5685.

(13) Han, M.-K.; Morosan, E.; Canfield, P. C.; Miller, G. J. The coloring problem in intermetallics: bonding and properties of $Tb_3Zn_{3.6}Al_{7.4}$ with the La_3Al_{11} structure type. *Z. Kristallogr.* **2005**, *220*, 95-101.

(14) Schmidt, J. T.; Lee, S.; Fredrickson, D. C.; Conrad, M.; Sun, J.; Harbrecht, B. $Pd_{(0.213)}Cd_{(0.787)}$ and $Pd_{(0.235)}Cd_{(0.765)}$ structures: their long c axis and composite crystals, chemical twinning, and atomic site preferences. *Chem. Eur. J.* **2007**, *13*, 1394-410.

(15) Berns, V. M.; Stacey, T. E.; Sapiro, M.; Fredrickson, D. C. Mg11Cu6Al12, A New Link in the Structural Chemistry of MgCu2-Type Clusters. *Eur. J. Inorg. Chem.* **2011**, 3936-3949.

(16) Fredrickson, D. C.; Lee, S.; Hoffmann, R. Interpenetrating Polar and Nonpolar Sublattices in Intermetallics: The $NaCd_2$ Structure. *Angew. Chem. Int. Ed.* **2007**, *46*, 1958-1976.

(17) Ponou, S.; Lidin, S.; Zhang, Y.; Miller, G. J. Valence State Driven Site Preference in the Quaternary Compound $Ca_5MgAgGe_5$: An Electron-Deficient Phase with Optimized Bonding. *Inorg. Chem.* **2014**, 53, 4724-4732.

(18) Lee, C.-S.; Miller, G. J. Experimental and Theoretical Studies of Elemental Site Preferences in Quasicrystalline Approximants (R-Phases) within the Li–Mg–Zn–Al System. *Inorg. Chem.* **2001**, *40*, 338-345.

(19) Jeon, B.-Y.; Nam, G.; Lee, D. W.; Min Ok, K.; You, T.-S. $Ce_{11}Ge_{3.73(2)}In_{6.27}$: Solid-state synthesis, crystal structure and site-preference. *J. Solid State Chem.* **2016**, *236*, 195-202.

(20) Makino, Y. Structural design of intermetallics: structural mapping, site preference of third alloying element and planar defects. *Intermetallics* **1996**, *4*, S11-S16.

(21) Miller, G. J. The "Coloring Problem" in Solids: How It Affects Structure, Composition and Properties. *Eur. J. Inorg. Chem.* **1998**, *1998*, 523-536.

(22) Martin, R. M. *Electronic structure : basic theory and practical methods*; 1st pbk. ed.; Cambridge University Press: Cambridge, UK ; New York, 2008.

(23) Jinlong, Y.; Chuanyun, X.; Shangda, X.; Kelin, W. Site preference of alloying additions in intermetallic compounds. *J. Phys. Condens. Matter* **1993**, *5*, 6653.

(24) Jiang, S.; Ping, Q.; Nan-Xian, C. Theoretical Investigation on the Phase Stability and Site Preference of $R(Co,T)_{12}$ and $R(Co,T)_{12}N_x$ (R=Y, Ce, Pr, Nd, Sm, Gd, Tb, Ho, Er, Dy, T=Mo, Mn, Ni). *Mod. Phys. Lett. B* **2003**, *17*, 897.

(25) Brgoch, J.; Mahmoud, Y. A.; Miller, G. J. Atomic site preferences and its effect on magnetic structure in the intermetallic borides $M_2Fe(Ru_{0.8}T_{0.2})_5B_2$ (M=Sc, Ti, Zr; T=Ru, Rh, Ir). *J. Solid State Chem.* **2012**, *196*, 168-174.

(26) Fredrickson, D. C. Electronic Packing Frustration in Complex Intermetallic Structures: The Role of Chemical Pressure in Ca_2Ag_7. *J. Am. Chem. Soc.* **2011**, *133*, 10070-10073.

(27) Fredrickson, D. C. DFT-Chemical Pressure Analysis: Visualizing the Role of Atomic Size in Shaping the Structures of Inorganic Materials. *J. Am. Chem. Soc.* **2012**, *134*, 5991-5999.

(28) Engelkemier, J.; Berns, V. M.; Fredrickson, D. C. First-Principles Elucidation of Atomic Size Effects Using DFT-Chemical Pressure Analysis: Origins of $Ca_{36}Sn_{23}$'s Long-Period Superstructure. *J. Chem. Theory Comput.* **2013**, *9*, 3170-3180.

(29) Berns, V. M.; Fredrickson, D. C. Problem Solving with Pentagons: Tsai-Type Quasicrystal as a Structural Response to Chemical Pressure. *Inorg. Chem.* **2013**, *52*, 12875-12877.

(30) Hadler, A. B.; Harris, N. A.; Fredrickson, D. C. New Roles for Icosahedral Clusters in Intermetallic Phases: Micelle-like Segregation of Ca-Cd and Cu-Cd Interactions in $Ca_{10}Cd_{27}Cu_2$. *J. Am. Chem. Soc.* **2013**, *135*, 17369-17378.

(31) Engelkemier, J.; Fredrickson, D. C. Chemical Pressure Schemes for the Prediction of Soft Phonon Modes: A Chemist's Guide to the Vibrations of Solid State Materials. *Chem. Mater.* **2016**, *28*, 3171-3183.

(32) Kilduff, B. J.; Fredrickson, D. C. Chemical Pressure-Driven Incommensurability in $CaPd_5$: Clues to High-Pressure Chemistry Offered by Complex Intermetallics. *Inorg. Chem.* **2016**, *55*, 6781-6793.

(33) Hoffer, G.; Strnat, K. Magnetocrystalline anisotropy of YCo_5 and Y_2Co_{17}. *IEEE Trans. Magn.* **1966**, *2*, 487-489.

(34) Larson, P.; Mazin, I. I. Magnetic properties of $SmCo_5$ and YCo_5. *J. Appl. Phys.* **2003**, *93*, 6888-6890.

(35) Schweizer, J.; Tasset, F. Polarised neutron study of the RCo_5 intermetallic compounds. I. The cobalt magnetisation in YCo_5. *J. Phys. F* **1980**, *10*, 2799.

(36) Buschow, K. H. J.; van der Goot, A. S. Composition and crystal structure of hexagonal Cu-rich rare earth-copper compounds. *Acta Crystallogr., Sect. B: Struct. Sci.* **1971**, *27*, 1085-1088.

(37) Černý, R.; Filinchuk, Y.; Brühne, S. Local atomic order in the vicinity of Cu_2 dumbbells in $TbCu_7$-type $YCu_{6.576}$ studied by Bragg and total scattering techniques. *Intermetallics* **2009**, *17*, 818-825.

(38) Psycharis, V.; Gjoka, M.; Kalogirou, O.; Devlin, E.; Niarchos, D. Structural and magnetic properties of a novel compound with $Y_3(Fe,V)_{29}$ stoichiometry and disordered $CaCu_5$-type structure. *J. Alloys Compd.* **1998**, *270*, 21-27.

(39) Wilson, C. G.; Thomas, D. K.; Spooner, F. J. The crystal structure of Zr_4Al_3. *Acta Crystallogr.* **1960**, *13*, 56-57.

(40) Florio, J. V.; Rundle, R. E.; Snow, A. I. Compounds of thorium with transition metals. I. The thorium-manganese system. *Acta Crystallogr.* **1952**, *5*, 449-457.

(41) Makarov, E. S.; Vinogradov, S. I. The crystal structures of Th_2Zn_{17} and U_2Zn_{17}. *Kristallografiya* **1956**, *1*, 634-43.

(42) Florio, J. V.; Baenziger, N. C.; Rundle, R. E. Compounds of thorium with transition metals. II. Systems with iron, cobalt and nickel. *Acta Crystallogr.* **1956**, *9*, 367-372.

(43) Andrusyan, R. I.; Kotur, B. Y. Phase equilibria in Sc-Mn-Ge and Sc-Fe-Ge systems at 870 K. *Isv. Akad. Nauk SSSR, Met.* **1991**, 198-202.

(44) Venturini, G. Filling the CoSn host-cell. The $HfFe_6Ge_6$-type and the related structures. *Z. Kristallogr.* **2006**, *221*, 511-520.

(45) Fredrickson, D. C.; Lidin, S.; Venturini, G.; Malaman, B.; Christensen, J. Origins of superstructure ordering and incommensurability in stuffed CoSn-Type phases. *J. Am. Chem. Soc.* **2008**, *130*, 8195-8214.

(46) Ostertag, W.; Strnat, K. L. Rare earth cobalt compounds with the A_2B_{17} structure. *Acta Crystallogr.* **1966**, *21*, 560-565.

(47) Ostertag, W. Crystallographic data for YCo_3 and Y_2Co_{17}. *Acta Crystallogr.* **1965**, *19*, 150-151.

(48) Khan, Y. On the crystal structures of the R_2Co_{17} intermetallic compounds. *Acta Crystallogr., Sect. B: Struct. Sci.* **1973**, *29*, 2502-2507.

(49) Buschow, K. H. J. Intermetallic compounds of rare-earth and 3d transition metals. *Rep. Prog. Phys.* **1977**, *40*, 1179.

(50) Kresse, G.; Furthmüller, J. Efficient Iterative Schemes for Ab Initio Total-Energy Calculations using a Plane-Wave Basis Set. *Phys. Rev. B* **1996**, *54*, 11169-11186.

(51) Kresse, G.; Furthmüller, J. Efficiency of Ab-Initio Total Energy Calculations for Metals and Semiconductors using a Plane-Wave Basis Set. *Comput. Mater. Sci.* **1996**, *6*, 15-50.

(52) Vanderbilt, D. Soft Self-consistent Pseudopotentials in a Generalized Eigenvalue Formalism. *Phys. Rev. B* **1990**, *41*, 7892-7895.

(53) Gonze, X.; Amadon, B.; Anglade, P.-M.; Beuken, J.-M.; Bottin, F.; Boulanger, P.; Bruneval, F.; Caliste, D.; Caracas, R.; Côté, M.; Deutsch, T.; Genovese, L.; Ghosez, P.; Giantomassi, M.; Goedecker, S.; Hamann, D. R.; Hermet, P.; Jollet, F.; Jomard, G.; Leroux, S.; Mancini, M.; Mazevet, S.; Oliveira, M. J. T.; Onida, G.; Pouillon, Y.; Rangel, T.; Rignanese, G.-M.; Sangalli, D.; Shaltaf, R.; Torrent, M.; Verstraete, M. J.; Zerah, G.; Zwanziger, J. W. ABINIT: First-principles approach to material and nanosystem properties. *Comput. Phys. Commun.* **2009**, *180*, 2582-2615.

(54) Gonze, X.; Rignanese, G.-m.; Verstraete, M.; Beuken, J.-m.; Pouillon, Y.; Caracas, R.; Raty, J.-y.; Olevano, V.; Bruneval, F.; Reining, L.; Godby, R.; Onida, G.; Hamann, D. R.; Allan, D. C. A Brief Introduction to the ABINIT Software Package. *Z. Kristallogr.* **2005**, *220*, 558-562.

(55) Gonze, X.; Beuken, J. M.; Caracas, R.; Detraux, F.; Fuchs, M.; Rignanese, G. M.; Sindic, L.; Verstraete, M.; Zerah, G.; Jollet, F.; Torrent, M.; Roy, A.; Mikami, M.; Ghosez, P.; Raty, J. Y.; Allan, D. C. First-principles computation of material properties: the ABINIT software project. *Comput. Mater. Sci,* **2002**, *25*, 478-492.

(56) Goedecker, S.; Teter, M.; Hutter, J. Separable dual-space Gaussian pseudopotentials. *Phys. Rev. B* **1996**, *54*, 1703-1710.

(57) Hartwigsen, C.; Goedecker, S.; Hutter, J. Relativistic separable dual-space Gaussian pseudopotentials from H to Rn. *Phys. Rev. B* **1998**, *58*, 3641-3662.

(58) Blöchl, P. E. Projector Augmented-wave Method. *Phys. Rev. B* **1994**, *50*, 17953-79.

(59) Kresse, G.; Joubert, D. From Ultrasoft Pseudopotentials to the Projector Augmented-wave Method. *Phys. Rev. B* **1999**, *59*, 1758-1775.

(60) Bader, R. F. W. *Atoms in molecules: a quantum theory*; Oxford University Press: Oxford, England, 1990.

(61) Henkelman, G.; Arnaldsson, A.; Jónsson, H. A fast and robust algorithm for Bader decomposition of charge density. *Comput. Mater. Sci.* **2006**, *36*, 254-360.

(62) Sanville, E.; Kenny, S. D.; Smith, R.; Henkelman, G. Improved grid-based algorithm for Bader charge allocation. *J. Comput. Chem.* **2007**, *28*, 899-908.

(63) Tang, W.; Sanville, E.; Henkelman, G. A grid-based Bader analysis algorithm without lattice bias. *J. Phys. Condens. Matter* **2009**, *21*, 084204.

(64) Oliveira, M. J. T.; Nogueira, F. Generating relativistic pseudo-potentials with explicit incorporation of semi-core states using APE, the Atomic Pseudo-potentials Engine. *Comput. Phys. Commun.* **2008**, *178*, 524-534.

(65) Berns, V. M.; Engelkemier, J.; Guo, Y.; Kilduff, B. J.; Fredrickson, D. C. Progress in Visualizing Atomic Size Effects with DFT-Chemical Pressure Analysis: From Isolated Atoms to Trends in AB_5 Intermetallics. *J. Chem. Theory Comput.* **2014**, *10*, 3380-3392.

(66) Oszlányi, G.; Sütő, A. Ab initio structure solution by charge flipping. *Acta Crystallogr. Sect. A: Found. Crystallogr.* **2004**, *60*, 134-141.

(67) Oszlányi, G.; Sütő, A. Ab initio structure solution by charge flipping. II. Use of weak reflections. *Acta Crystallogr. Sect. A: Found. Crystallogr.* **2005**, *61*, 147-152.

(68) Palatinus, L.; Chapuis, G. SUPERFLIP - a computer program for the solution of crystal structures by charge flipping in arbitrary dimensions. *J. Appl. Crystallogr.* **2007**, *40*, 786-790.

(69) Petříček, V.; Dušek, M.; Palatinus, L. *Jana2006. The Crystallographic Computing System*; Institute of Physics: Praha, Czech Republic, 2006.

(70) Szpunar, B. Density of states and magnetic properties of YCo_5 and Y_2Co_{17} compounds. *Physica B* **1985**, *130*, 29-33.

(71) Pareti, L.; Solzi, M.; Marusi, G. Phenomenological analysis of the magnetocrystalline anisotropy of the Co sublattice in some rhombohedral and hexagonal intermetallic structures derived from the $CaCu_5$ unit cell. *J. Appl. Phys.* **1992**, *72*, 3009-3012.

(72) Note, however, that this analysis on its own does not draw conclusions about the thermodynamic relationships among the phases of the Y-Co system. Determining such relations requires consideration of balanced reactions, such as $2YCo_5+7Co \rightarrow Y_2Co_{17}$ (as can be accomplished with total energy calculations), whereas the CP analysis focuses on packing issues within individual compounds.

(73) Sokolovskaya, E. M.; Raevskaya, M. V.; Kazakova, E. F. The influence of ruthenium on the stability of intermetallic compounds of the rare-earth metals. *Moscow Univ. Chem. Bull.* **1985**, *40*, 71-76.

(74) Andreev, A. V.; Tereshina, E. A.; Gorbunov, D. I.; Šantavá, E.; Šebek, J.; Žáček, M.; Daniš, S.; Pospíšil, J.; Havela, L. Influence of Ru on magnetic properties of Y_2T_{17} (T = Fe, Co) and $Y_2Fe_{16}Si$ single crystals. *J. Alloys Compd.* **2015**, *621*, 415-422.

(75) Liu, Q. L.; Liang, J. K.; Huang, F.; Chen, Y.; Rao, G. H.; Chen, X. L.; Shen, B. G. Crystal structure and magnetic properties of the intermetallic compounds $La_2Co_{17-x}M_x$ (M = Nb, Mo, Mn). *J. Phys. Condens. Matter* **1999**, *11*, 9797.

(76) Fujii, H.; Satyanarayana, M. V.; Wallace, W. E. Magnetic and crystallographic properties of substituted $Ce_2Co_{17-x}T_x$ compounds (T = Ti, V, Cr, Mn, Fe, Cu, Zr, and Hf). *J. Appl. Phys.* **1982**, *53*, 2371-2373.

(77) Cheng, Z.-h.; Shen, B.-g.; Yan, Q.-w.; Guo, H.-q.; Chen, D.-f.; Gou, C.; Sun, K.; de Boer, F. R.; Buschow, K. H. J. Structure, exchange interactions, and magnetic phase transition of $Er_2Fe_{17-x}Al_x$ intermetallic compounds. *Phys. Rev. B* **1998**, *57*, 14299-14309.

(78) de Groot, C. H.; de Boer, F. R.; Buschow, K. H. J.; Hu, Z.; Yelon, W. B. Magnetic properties of $Nd_2Co_{17-x}Al_x$ compounds studied by magnetic measurements and neutron diffraction. *J. Alloys Compd.* **1996**, *233*, 188-191.

(79) Hornfeck, W.; Thimmaiah, S.; Lee, S.; Harbrecht, B. Structure–Composition Relations for the Partly Disordered Hume-Rothery Phase $Ir_{7+7\delta}Zn_{97-11\delta}$ ($0.31 \leq \delta \leq 0.58$). *Chemistry – A European Journal* **2004**, *10*, 4616-4626.

(80) Feuerbacher, M.; Thomas, C.; Makongo, J. P. A.; Hoffmann, S.; Carrillo-Cabrera, W.; Cardoso, R.; Grin, Y.; Kreiner, G.; Joubert, J.-M.; Schenk, T.; Gastaldi, J.; Nguyen-Thi, H.; Mangelinck-Noël, N.; Billia, B.; Donnadieu, P.; Czyrska-Filemonowicz, A.; Zielinska-Lipiec, A.; Dubiel, B.; Weber, T.; Schaub, P.; Krauss, G.; Gramlich, V.; Christensen, J.; Lidin, S.; Fredrickson, D.; Mihalkovic, M.; Sikora, W.; Malinowski, J.; Brühne, S.; Proffen, T.; Assmus, W.; de Boissieu, M.; Bley, F.; Chemin, J. L.; Schreuer, J.; Steurer, W. The Samson Phase, β-Mg_2Al_3, Revisited. *Z. Kristallogr.* **2007**, *222*, 259-288.

(81) Thimmaiah, S.; Crumpton, N. A.; Miller, G. J. Crystal Structures and Stabilities of γ- and γ′ -Brass Phases in $Pd_{2-x}Au_xZn_{11}$ (x = 0.2–0.8): Vacancies vs. Valence Electron Concentration. *Z. Anorg. Allg. Chem.* **2011**, *637*, 1992-1999.

(82) Jana, P. P.; Lidin, S. Structures of $NiCd_{6+\delta}$ (-0.32 ≤ δ ≤ 0.35) - a γ-brass related phase, and $NiCd_{1+\delta}$ (0 ≤ δ ≤ 0.05) - a Ti_2Ni type phase in the nickel-cadmium system. *CrystEngComm* **2013**, *15*, 745-753.

(83) Jana, P. P. $CrZn_{17+\delta}$ (–0.75 ≤ δ ≤ 2.00): A partly disordered complex intermetallic compound. *J. Alloys Compd.* **2014**, *610*, 55-61.

(84) Thimmaiah, S.; Miller, G. J. On the Structural Chemistry of γ-Brasses: Two Different Interpenetrating Networks in Ternary F-Cell Pd–Zn–Al Phases. *Chem. Eur. J.* **2010**, *16*, 5461-5471.

(85) Berns, V. M.; Fredrickson, D. C. Structural Plasticity: How Intermetallics Deform Themselves in Response to Chemical Pressure, and the Complex Structures That Result. *Inorg. Chem.* **2014**, *53*, 10762-10771.

(86) Li, B.; Corbett, J. D. Synthesis, Structure, and Characterization of a Cubic Thallium Cluster Phase of the Bergman Type, $Na_{13}(Cd_{0.70}Tl_{0.30})_{27}$. *Inorg. Chem.* **2004**, *43*, 3582-3587.

(87) Jana, P. P.; Henderson, R.; Harbrecht, B.; Lidin, S. Site Preference and Ordering Induced by Au Substitution in the γ-Brass Related Complex Au–Cr–Zn Phases. *Inorg. Chem.* **2013**, *52*, 4812-4818.

Appendix A.

Supplemental Information for Chapter 2:

Toward Design Principles for Diffusionless Transformations: The Frustrated Formation of Co-Co Bonds in a Low-Temperature Polymorph of $GdCoSi_2$

A.1. CRYSTALLOGRAPHIC TABLES

Table A.1. Atomic coordinates and displacement parameters for $GdCoSi_2$ at 293K.

Site	Wyckoff Position	*x*	*y*	*z*	U_{equiv}	Occupancy
Gd1	4d	0.22346(7)	0.147518(19)	0.25000	0.00647(12)	1.0
Co1	4d	0.3260(2)	0.94072(6)	0.25000	0.0112(3)	1.0
Si1	4d	0.2840(4)	0.79538(13)	0.25000	0.0084(5)[a]	1.0
Si2	4d	0.8153(4)	0.99625(12)	0.25000	0.0101(5)	1.0

[a]To check that the relatively low U_{equiv} value of Si1 (compared to that of Si2) is not due to mixed occupancy, we tested the refinement of a model in which Si1 is handled as a mixed Co/Si site. The fraction of Co on the Si1 site obtained during this refinement was negative and within a factor of two of the standard uncertainty for the value. Similar results were obtained for models in which Co1 and Si2 were treated as mixed Co/Si sites.

Table A.2. Anisotropic atomic displacement parameters for $GdCoSi_2$ at 293K.

Site	U_{11}	U_{22}	U_{33}	U_{12}	U_{13}	U_{23}
Gd1	0.0074(2)	0.0065(2)	0.0055(2)	-0.00078(9)	0.00000	0.00000
Co1	0.0096(4)	0.0131(5)	0.0108(5)	0.0031(3)	0.00000	0.00000
Si1	0.0093(8)	0.0107(9)	0.0052(8)	0.0008(6)	0.00000	0.00000
Si2	0.0120(8)	0.0096(9)	0.0087(9)	-0.0032(6)	0.00000	0.00000

Table A.3. Selected interatomic distances for $GdCoSi_2$ at 293K.

Site	Neighbor	Distance (Å)

Gd1	Co1(×2)	3.0995(8)
	Si1(×2)	3.0773(14)
	Si1(×2)	3.0317(14)
	Si2	2.956(2)
	Si2(×2)	3.0280(17)
Co1	Si1	2.303(3)
	Si2	2.345(2)
	Si2	2.262(2)
	Si2(×2)	2.3105(12)
Si1	Si1(×2)	2.457(2)

Table A.4. Atomic coordinates and displacement parameters for $GdCoSi_2$ at 400K.

Site	Wyckoff Position	*x*	*y*	*z*	U_{equiv}	Occupancy
Gd1	4c	0.50000	0.107106(17)	0.25000	0.00858(11)	1.0
Co1	4c	0.50000	0.31955(6)	0.25000	0.0144(3)	1.0
Si1	4c	0.50000	0.45743(11)	0.25000	0.0102(5)	1.0
Si2	4c	0.50000	0.24985(11)	-0.25000	0.0144(6)	1.0

Table A.5. Anisotropic atomic displacement parameters for $GdCoSi_2$ at 400K.

Site	U_{11}	U_{22}	U_{33}	U_{12}	U_{13}	U_{23}
Gd1	0.00874(19)	0.0090(2)	0.0080(2)	0.00000	0.00000	0.00000
Co1	0.0159(5)	0.0137(5)	0.0136(5)	0.00000	0.00000	0.00000
Si1	0.0126(9)	0.0098(9)	0.0082(9)	0.00000	0.00000	0.00000
Si2	0.0175(10)	0.0105(9)	0.0152(10)	0.00000	0.00000	0.00000

Table A.6. Selected interatomic distances for $GdCoSi_2$ at 400K.

Site	Neighbor	Distance (Å)
Gd1	Co1(×4)	3.0942(4)
	Si1(×4)	3.0419(6)
	Si2(×2)	3.0327(13)
	Si2(×2)	3.0631(14)
	Si2(×2)	3.0919(14)
Co1	Si1	2.2412(19)
	Si2(×2)	2.2984(10)
	Si2(×2)	2.3293(10)
Si1	Si1(×2)	2.4319(14)

A.2. POWDER X-RAY DIFFRACTION PATTERNS FOR SAMPLE USED IN VARIABLE TEMPERATURE SINGLE CRYSTAL DIFFRACTION AND DIFFERENTIAL SCANNING CALORIMETRY EXPERIMENTS

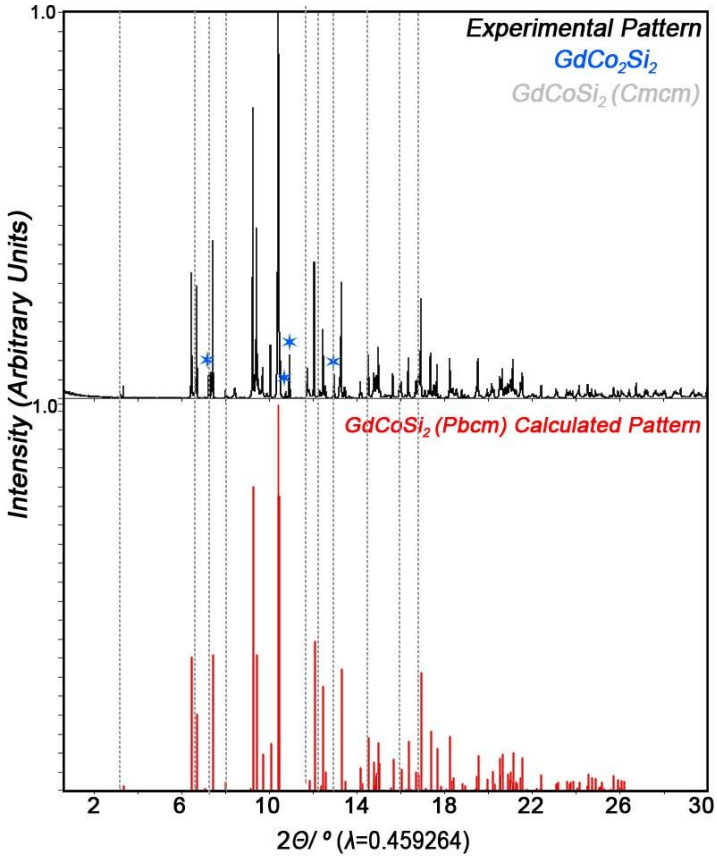

Figure A.1. Powder X-ray diffraction pattern collected at 295K with synchrotron radiation at 11BM beamline, APS, Argonne National Laboratory.

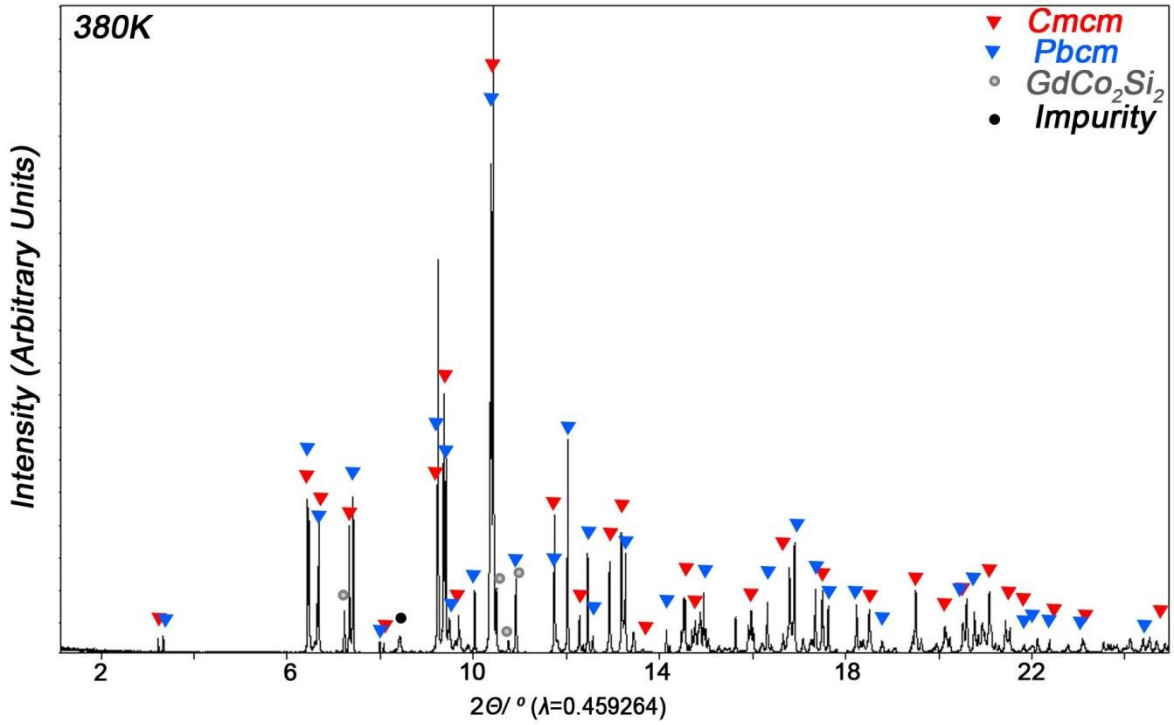

Figure A.2. Powder X-ray diffraction pattern collected at 380K with synchrotron radiation at 11BM beamline, APS, Argonne National Laboratory.

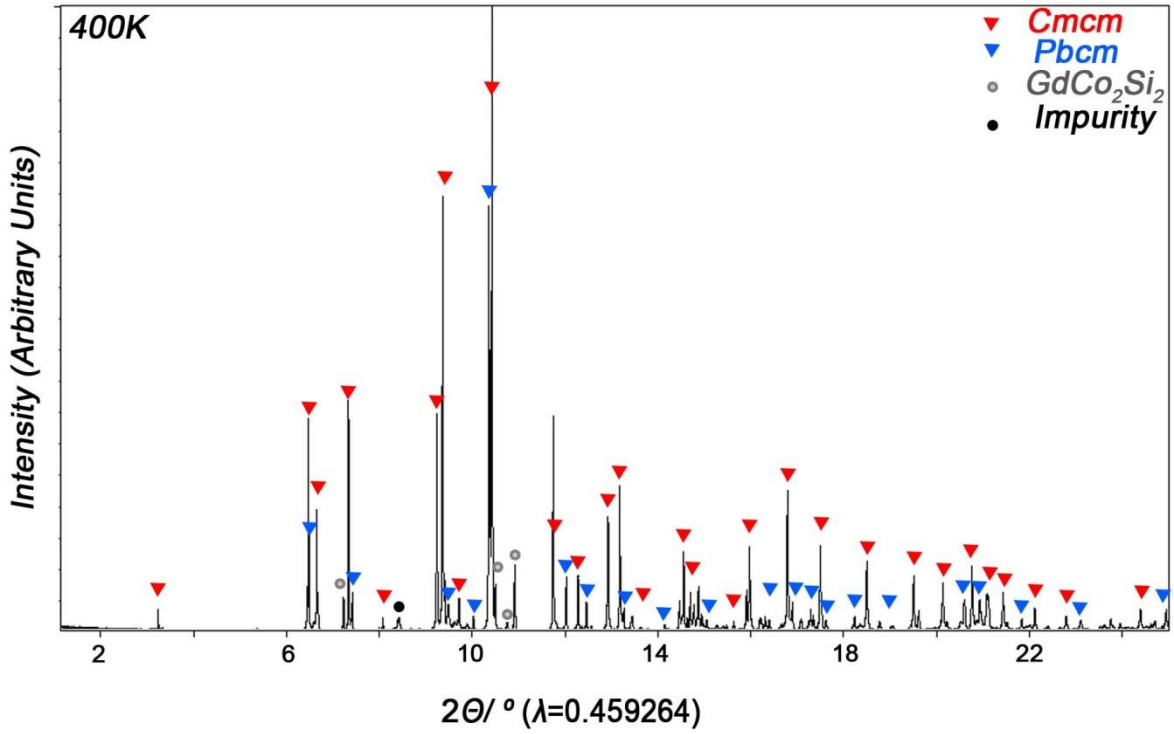

Figure A.3. Powder X-ray diffraction pattern collected at 400K with synchrotron radiation at 11BM beamline, APS, Argonne National Laboratory.

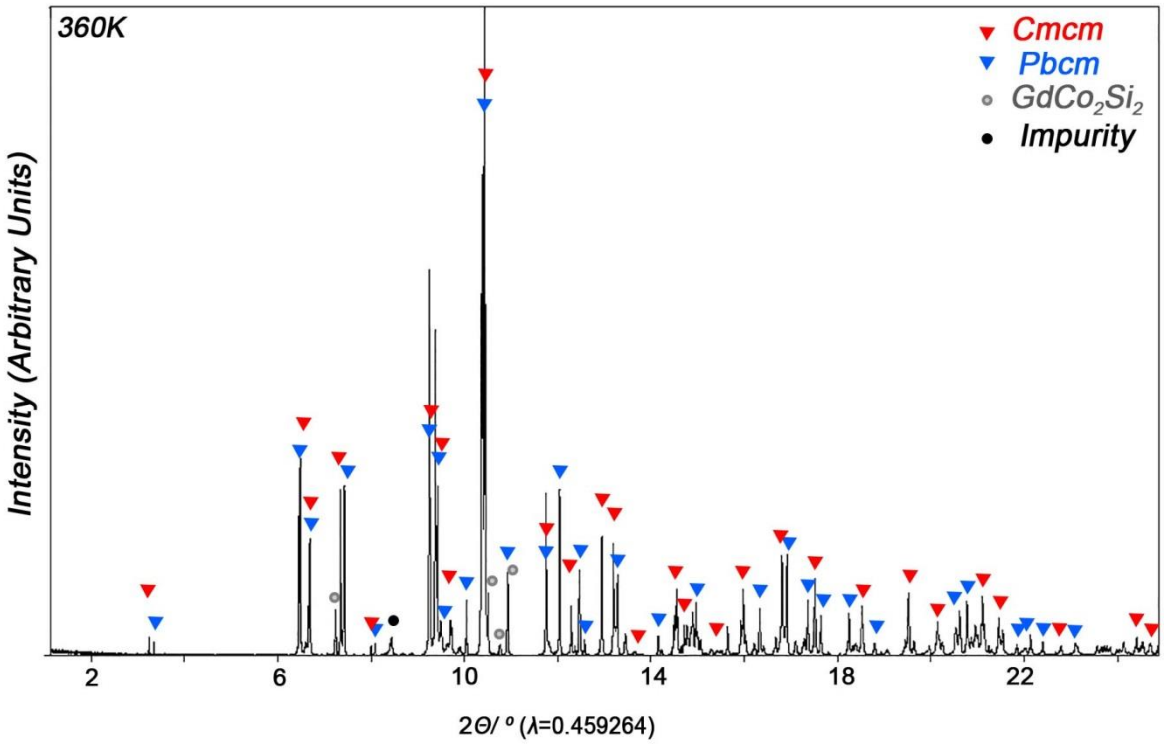

Figure A.4. Powder X-ray diffraction pattern collected at 360K with synchrotron radiation at 11BM beamline, APS, Argonne National Laboratory.

A.3. COMPUTATIONAL DETAILS AND OPTIMIZED GEOMETRIES

Table A.7. DFT-optimized geometry for *Pbcm* $GdCoSi_2$.

Cell Vectors	*x* (Å)	*y* (Å)	*z* (Å)
a (Å)	3.9808473394258517	0.0	0.0
b (Å)	0.0	4.2335902095547393	0.0
c (Å)	0.0	0.0	15.6872283216067228
	x	*y*	*z*
Co	0.7500000000000000	0.2234412650041637	0.1479671804220253
Co	0.2500000000000000	0.7765587199958317	0.8520328495779773
Co	0.2500000000000000	0.2234412650041637	0.3520328195779747
Co	0.7500000000000000	0.7765587199958317	0.6479671504220227
Gd	0.2500000000000000	0.6763707171024380	0.0593041521236530
Gd	0.7500000000000000	0.3236292828975620	0.9406958218763448
Gd	0.2500000000000000	0.3236292528975667	0.5593041781236552
Gd	0.7500000000000000	0.6763707171024380	0.4406958218763448
Si	0.2500000000000000	0.7164751913328522	0.2040601551284559
Si	0.7500000000000000	0.2835248086671476	0.7959398298715465
Si	0.2500000000000000	0.2835248376671465	0.7040601701284535

Si	0.7500000000000000	0.7164751323328509	0.2959398298715464
Si	0.2500000000000000	0.1850747574124028	0.0038936279122787
Si	0.7500000000000000	0.8149252275875996	0.9961063710877177
Si	0.7500000000000000	0.1850747574124028	0.4961063710877177
Si	0.2500000000000000	0.8149252275875996	0.5038936289122823
Total Energy: -6.391269 eV/atom			

Table A.8. DFT-optimized geometry for *Cmcm* $GdCoSi_2$.

Cell Vectors	*x* (Å)	*y* (Å)	*z* (Å)
a (Å)	8.3752466568340900	0.0043621560364165	0.0
b (Å)	7.3919669347768151	3.9374611649109017	0.0
c (Å)	0.0	0.0	4.0114793306786876
	x	*y*	*z*
Co	0.8926812510300759	0.1073187719699225	0.2500000000000000
Co	0.1073187489699241	0.8926812510300759	0.7500000000000000
Gd	0.6799717328548502	0.3200282671451495	0.2500000000000000
Gd	0.3200282671451496	0.4570788278113649	0.7500000000000000
Si	0.5429211721886351	0.4570788278113649	0.2500000000000000
Si	0.4570788278113649	0.5429211721886351	0.7500000000000000
Si	0.2497254636839854	0.7502745363160147	0.2500000000000000
Si	0.7502745363160147	0.2497254636839854	0.7500000000000000
Total Energy: -6.39890 eV/atom			

Table A.9. DFT-calibrated Hückel Parameters.

Compound, RMS deviation[a]	Orbital	H_{ii}(eV)	c_1	ζ_1(a_o^{-1})	c_2	ζ_2(a_o^{-1})
Pbcm $GdCoSi_2$, 0.12 eV	Gd 6s	-4.427	2.2690	0.0000	1.0000	0.0000
	Gd 6p	-2.363	2.2690 [b]	0.0000	1.0000	0.0000
	Gd 5d	-6.150	5.2096	2.1317	0.5000	1.2484
	Co 4s	-6.061	2.7588	0.0000	1.0000	0.0000
	Co 4p	-3.613	2.6695	0.0000	1.0000	0.0000
	Co 3d	-9.203	4.9035	2.2514	0.6372	0.8224
	Si 3s	-11.525	2.3396	0.0000	1.0000	0.0000
	Si 3p	-5.950	1.9882	0.0000	1.0000	0.0000
Cmcm $GdCoSi_2$, 0.19 eV	Gd 6s	-6.276	2.5999	0.0000	1.0000	0.0000
	Gd 6p	-4.616	2.5999 [b]	0.0000	1.0000	0.0000
	Gd 5d	-7.498	3.7613	2.3171	0.5000	2.2721
	Co 4s	-5.826	2.8322	0.0000	1.0000	0.0000
	Co 4p	-1.440	2.4304	0.0000	1.0000	0.0000
	Co 3d	-8.723	5.1187	2.3275	0.6372	1.2323

Si 3s	-11.856	2.2196	0.0000	1.0000	0.0000
Si 3p	-6.075	1.9857	0.0000	1.0000	0.0000

[a] Root-mean-squared deviation between the DFT and Hückel band energies up to ca. 1eV above E_F.

[b] For Gd the ζ_{6p} parameter was constrained to be equal to ζ_{6s}.

A.4. COMPARISON OF GGA-DFT AND DFT-CALIBRATED HÜCKEL DOS DISTRIBUTIONS

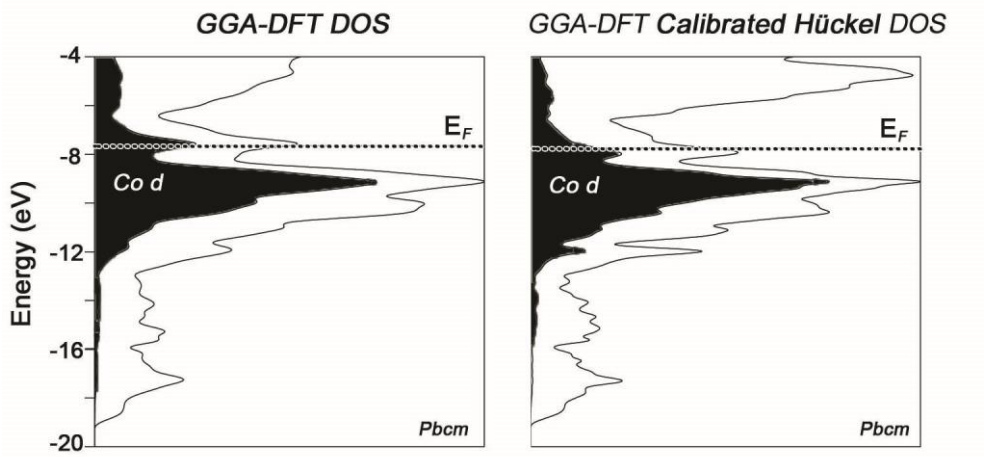

Figure A.5. Electronic DOS curves calculated for *Pbcm* $GdCoSi_2$ with GGA-DFT (left) and best-fit Hückel model (right).

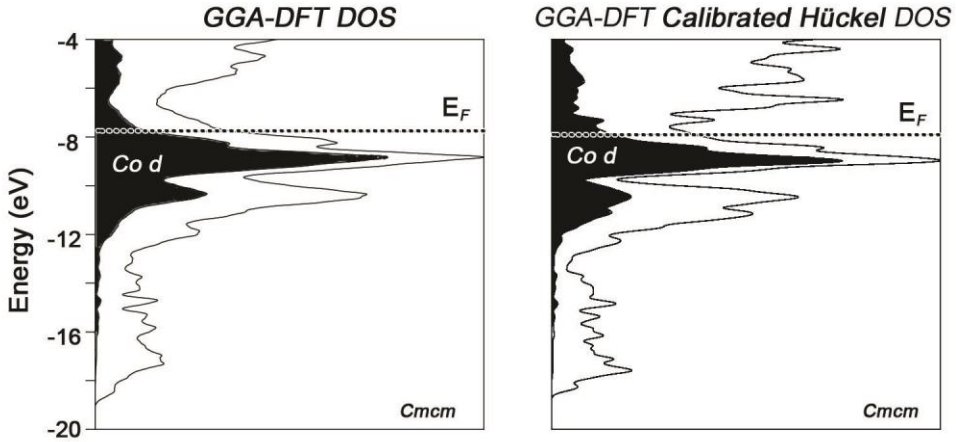

Figure A.6. Electronic DOS curves calculated for *Cmcm* GdCoSi2 with GGA-DFT (left) and best-fit Hückel model (right).

A.5. DIFFERENTIAL SCANNING CALORIMETRY RESULTS

Differential scanning calorimetry experiments were carried out on two samples: one sample from the initial syntheses and one from the subsequent syntheses. For the initial synthesis sample, a $GdCo_2Si_2$ impurity was identified by powder X-ray diffraction. Sample from subsequent syntheses appeared to be phase pure according to powder X-ray diffraction.

Table A.10. Differential Scanning Calorimetry Results for sample from initial synthesis.

Cycle		Onset Temperature (K)	Heat of reaction (J/g)
1	Heating	389.94	1.220
2	Cooling	360.9	1.179
	Heating	375.85	1.224
3	Cooling	363.33	1.068
	Heating	379.62	0.9969

Table A.11. Differential Scanning Calorimetry Results for sample from subsequent synthesis.

Cycle	Type	Onset Temperature (K)	Heat of reaction (J/g)
1	Heating	386.85	1.622
2	Cooling	367.94	1.818
	Heating	383.65	1.668
3	Cooling	368.74	1.795
	Heating	380.91	1.716

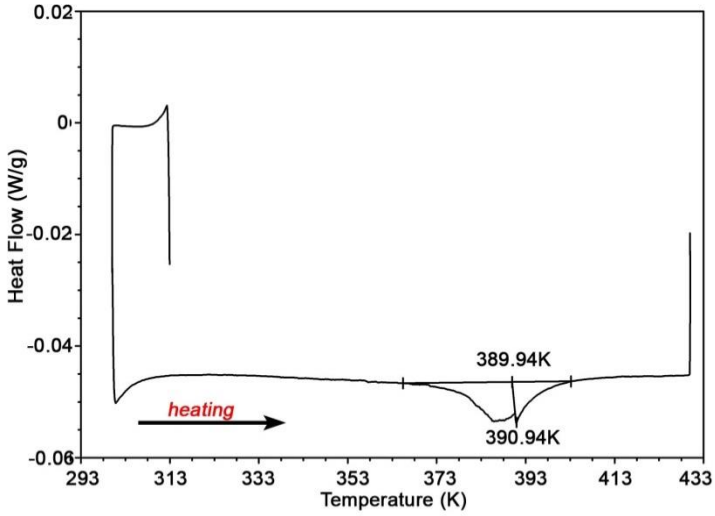

Figure A.7. Differential scanning calorimetry curve for cycle 1 of the sample from initial synthesis. The unusual peak shape and the consequent difficulty of fitting the peaks here and in Figures S8-S9 are most likely due to the $GdCo_2Si_2$ impurity.

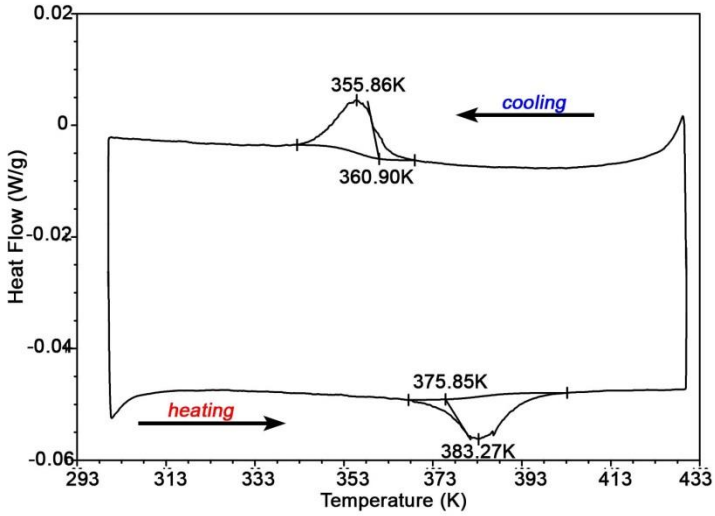

Figure A.8. Differential scanning calorimetry curve for cycle 2 of the sample from initial synthesis.

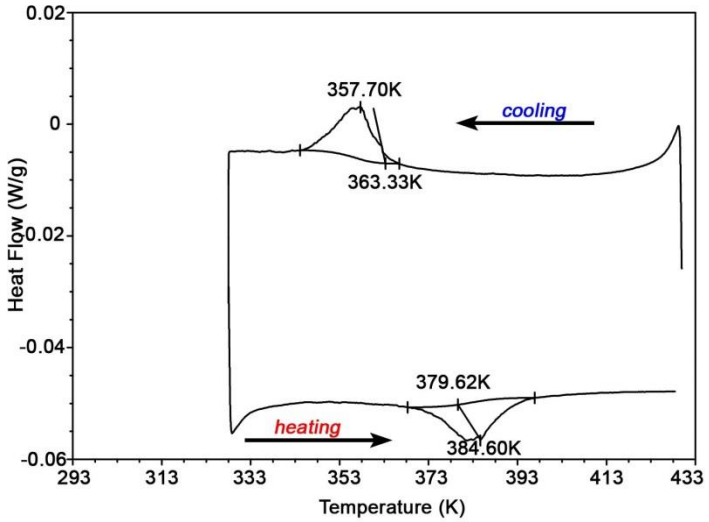

Figure A.9. Differential scanning calorimetry curve for cycle 3 of the sample from initial synthesis.

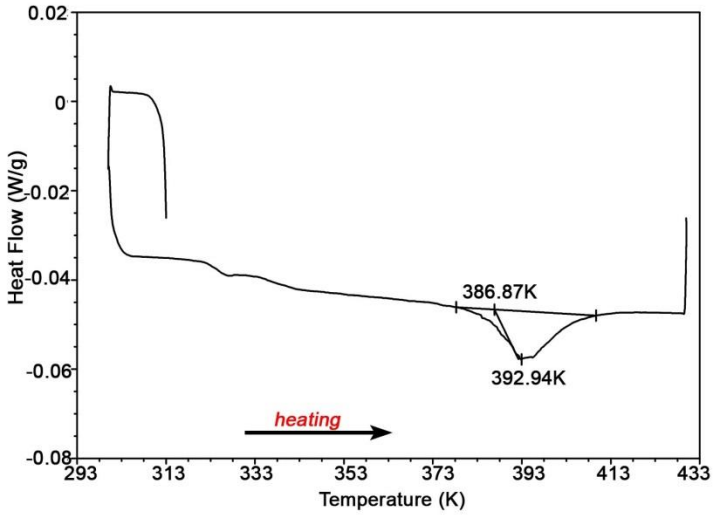

Figure A.10. Differential scanning calorimetry curve for cycle 1 of the sample from subsequent synthesis.

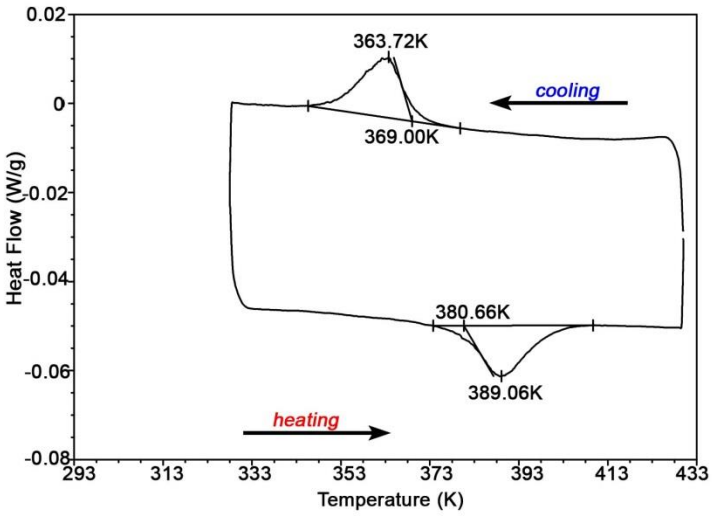

Figure A.11. Differential scanning calorimetry curve for cycle 3 of the sample from subsequent synthesis.

A.6. SINGLE CRYSTAL VARIABLE TEMPERATURE RESULTS

For the variable temperature single crystal x-ray diffraction experiments, single crystals of $GdCoSi_2$ were screened until a sufficiently high quality crystal was identified. A full data set at room temperature was collected. Then the crystal was heated to 400K and a full data set was collected again. The unit cell parameters reported below were measured upon cooling from 400K to 300K and then heating to 400K.

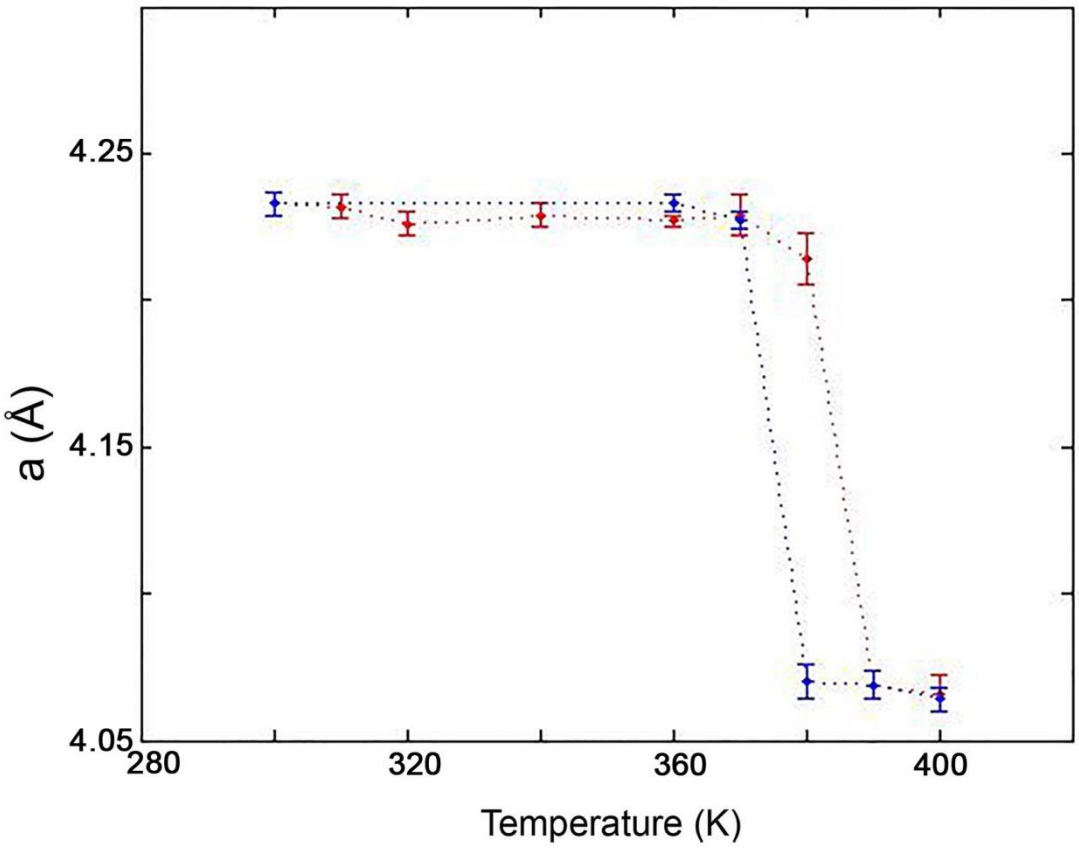

Figure A.12. Variation in the unit cell *a* parameter measured over the temperature range 300K to 400K, determined from 15 frame unit cell runs using single crystal X-ray diffractometer. Red bars: determined upon heating. Blue bars: determine upon cooling.

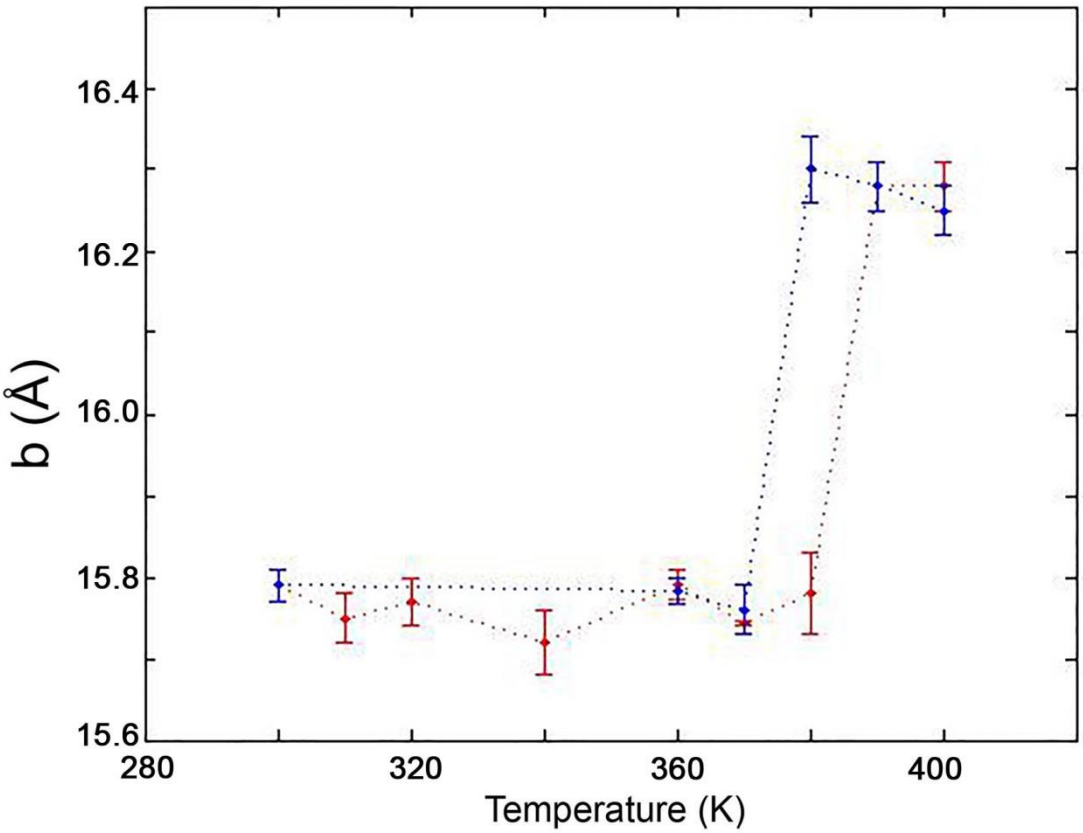

Figure A.13. Variation in the unit cell *b* parameter measured over the temperature range 300K to 400K, determined from 15 frame unit cell runs using single crystal X-ray diffractometer. Red bars: determined upon heating. Blue bars: determine upon cooling.

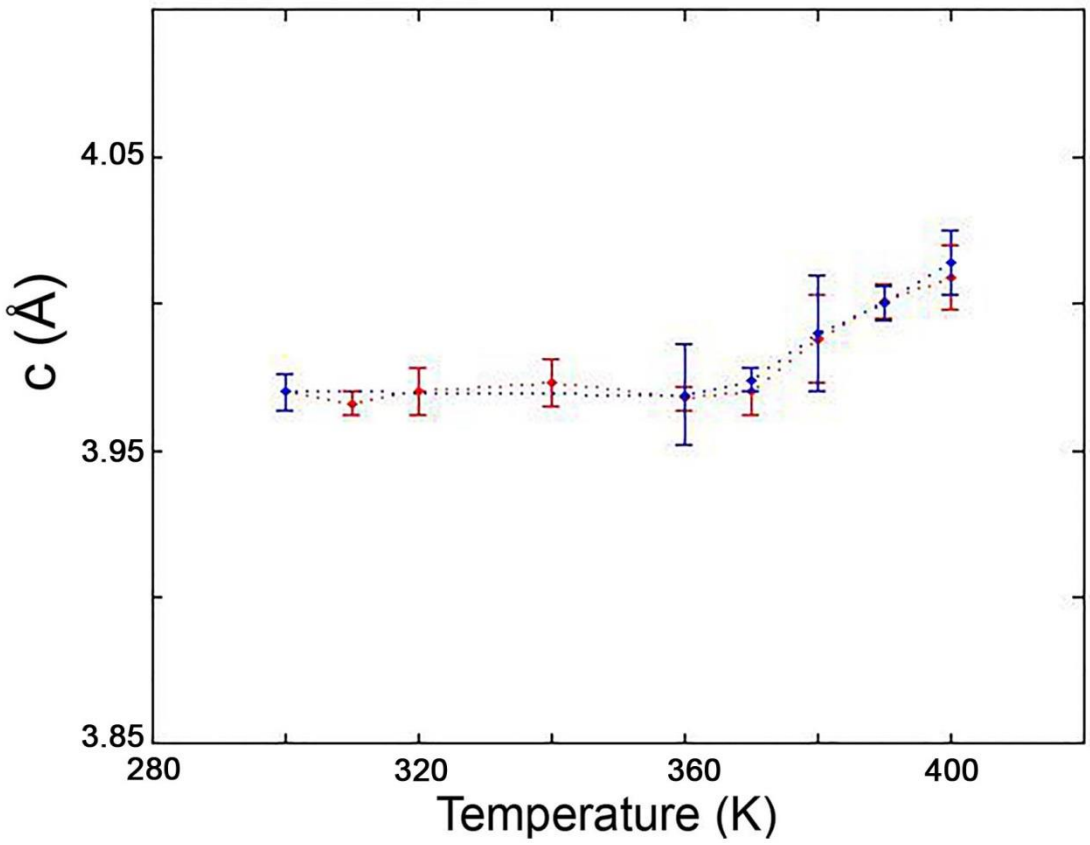

Figure A.14. Variation in the unit cell *c* parameter measured over the temperature range 300K to 400K, determined from 15 frame unit cell runs using single crystal X-ray diffractometer. Red bars: determined upon heating. Blue bars: determine upon cooling. Note that relative to the changes in the *a* and *b* parameters, the *c* parameter variation is very small (< 0.1Å).

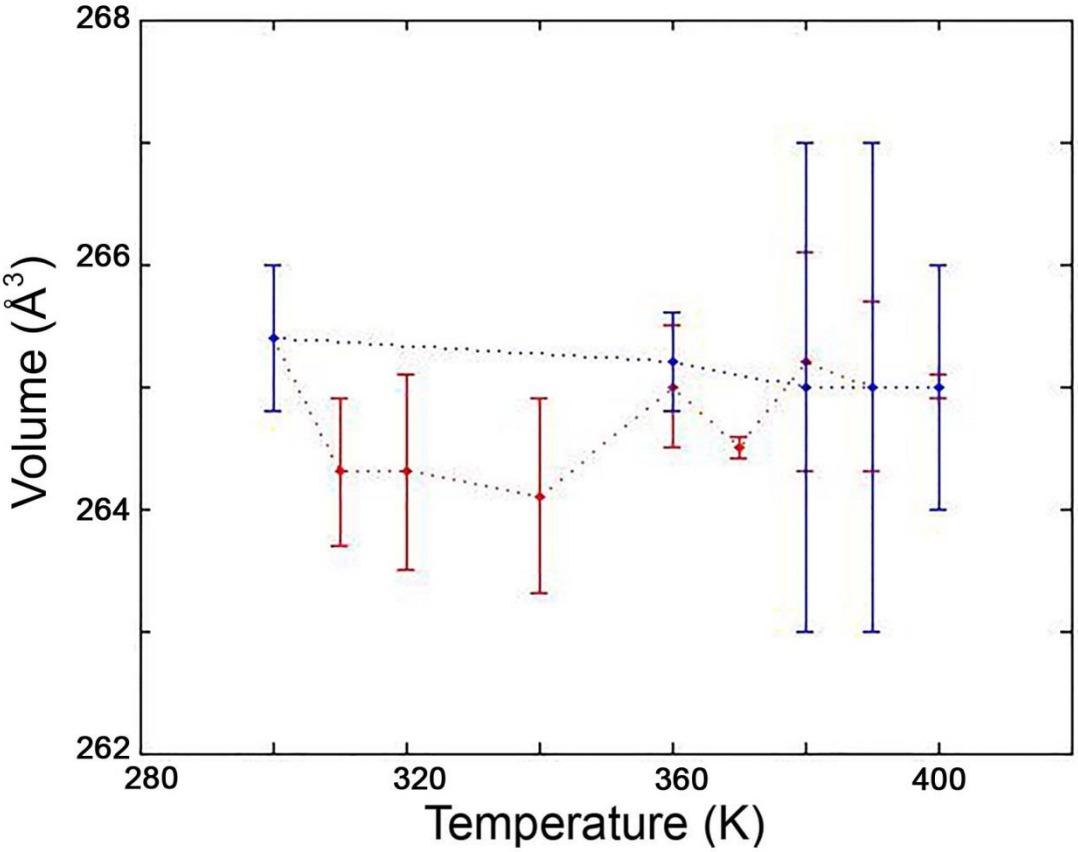

Figure A.15. Variation in the unit cell volume measured over the temperature range 300K to 400K, determined from 15 frame unit cell runs using single crystal X-ray diffractometer. Red bars: determined upon heating. Blue bars: determine upon cooling. The absence of a clear change in volume across this series may in part be understood by opposing effects of the expansion along **b** and contraction along **a** on going from the low-temperature to the high-temperature polymorph of $GdCoSi_2$. Because of the small volume change for this transition, more complete data sets than unit cell runs would be needed to definitively detect the transition in this plot.

Appendix B.

Supplemental Information for Chapter 3:

18-electron resonance structure in the BCC transition metals and their CsCl-type derivatives

B.1. COMPUTATIONAL DETAILS AND OPTIMIZED GEOMETRIES

Table B.1. DFT-optimized geometry for bcc-Mo

Cell Vectors	*x* (Å)	*y* (Å)	*z* (Å)
a (Å)	2.7290	-0.0000	-0.0000
b (Å)	-0.9097	2.5729	-0.0000
c (Å)	-0.9097	-1.2865	2.2282
	x	*y*	*z*
Mo	0.0000000000000000	0.0000000000000000	0.0000000000000000
Total Energy: -10.910311 eV/atom			

Table B.2. DFT-optimized geometry for ZrRu

Cell Vectors	*x* (Å)	*y* (Å)	*z* (Å)
a (Å)	3.2723	0.0	0.0
b (Å)	0.0	3.2723	0.0
c (Å)	0.0	0.0	3.2723
	x	*y*	*z*
Ru	0.0000000000000000	0.0000000000000000	0.0000000000000000
Zr	0.5000000000000000	0.5000000000000000	0.5000000000000000
Total Energy: -9.483446 eV/atom			

Table B.3. DFT-optimized geometry for RuSn

Cell Vectors	*x* (Å)	*y* (Å)	*z* (Å)
a (Å)	3.2366	0.0	0.0
b (Å)	0.0	3.2366	0.0
c (Å)	0.0	0.0	3.2366
	x	*y*	*z*
Ru	0.0000000000000000	0.0000000000000000	0.0000000000000000
Sn	0.5000000000000000	0.5000000000000000	0.5000000000000000
Total Energy: -6.597993 eV/atom			

Table B.4. DFT-calibrated Hückel Parameters.

Compound, RMS deviation[a]	Orbital	H_{ii}(eV)	c_1[b]	$\zeta_1(a_0^{-1})$	c_2[b]	$\zeta_2(a_0^{-1})$
Mo	Mo 5s	-3.926	1.0000	2.4151	0.0000	0.0000
0.189266 eV	Mo 5p	-1.236	1.0000	2.1474	0.0000	0.0000
	Mo 4d	-7.474	1.0000	6.4006	4.8943	2.4064
ZrRu	Ru 5s	-4.087	1.0000	2.0774	0.0000	0.0000
0.104132 eV	Ru 5p	-1.014	1.0000	1.7988	0.0000	0.0000
	Ru 4d	-8.634	1.0000	6.7014	7.4307	2.4642
	Zr 5s	-4.803	1.0000	3.2002	0.0000	0.0000
	Zr 5p	-4.432	1.0000	3.4526	0.0000	0.0000
	Zr 4d	-6.327	0.4228	7.1884	0.3498	1.9691
RuSn	Ru 5s	-5.729	1.0000	2.4581	0.0000	0.0000
0.095771 eV	Ru 5p	-3.909	1.0000	2.4159	0.0000	0.0000
	Ru 4d	-8.046	1.0000	5.2694	8.7470	2.3987
	Sn 5s	-10.302	1.0000	2.9773	0.0000	0.0000
	Sn 5p	-3.446	1.0000	2.4130	0.0000	0.0000

[a] Root-mean-squared deviation between the DFT and Hückel band energies up to ca. 1 eV above E_F

[b] For the double-ζ d orbitals, the c_1 and c_2 coefficients are scaled for normalization inside the YAeHMOP program.

Table B.5. Model Hückel parameters for transition between ZrRu and RuSn[a].

Compound	Orbital	H_{ii}(eV)	c_1[b]	$\zeta_1(a_0^{-1})$	c_2[b]	$\zeta_2(a_0^{-1})$
1	Ru 5s	-4.087	1.0000	2.0774	0.0000	0.0000
	Ru 5p	-1.014	1.0000	1.7988	0.0000	0.0000
	Ru 4d	-8.634	1.0000	6.7014	7.4307	2.4642
	Zr 5s	**-6.803**	1.0000	**3.3002**	0.0000	0.0000
	Zr 5p	-4.432	1.0000	3.4526	0.0000	0.0000
	Zr 4d	**-4.327**	0.4228	**6.1884**	0.3498	1.9691
2	Ru 5s	-4.087	1.0000	2.0774	0.0000	0.0000
	Ru 5p	-1.014	1.0000	1.7988	0.0000	0.0000
	Ru 4d	-8.634	1.0000	6.7014	7.4307	2.4642
	Zr 5s	**-7.803**	1.0000	**3.4002**	0.0000	0.0000
	Zr 5p	-4.432	1.0000	3.4526	0.0000	0.0000
	Zr 4d	**-3.327**	0.4228	**5.1884**	0.3498	1.9691
3	Ru 5s	-4.087	1.0000	2.0774	0.0000	0.0000
	Ru 5p	-1.014	1.0000	1.7988	0.0000	0.0000
	Ru 4d	-8.634	1.0000	6.7014	7.4307	2.4642
	Zr 5s	**-10.803**	1.0000	**3.6002**	0.0000	0.0000
	Zr 5p	-4.432	1.0000	3.4526	0.0000	0.0000
	Zr 4d	**-0.010**	0.4228	**4.1884**	0.3498	1.9691

[a] Parameters changing across the series are shown in bold.

[b] For the double-ζ d orbitals, the c_1 and c_2 coefficients are scaled for normalization inside the YAeHMOP program.

B.2. COMPARISON OF GGA-DFT AND DFT-CALIBRATED HÜCKEL DOS DISTRIBUTIONS

In all of the following DOS curves and those appearing in the main text, Gaussian broadening has been applied to emphasize general features of the distributions.

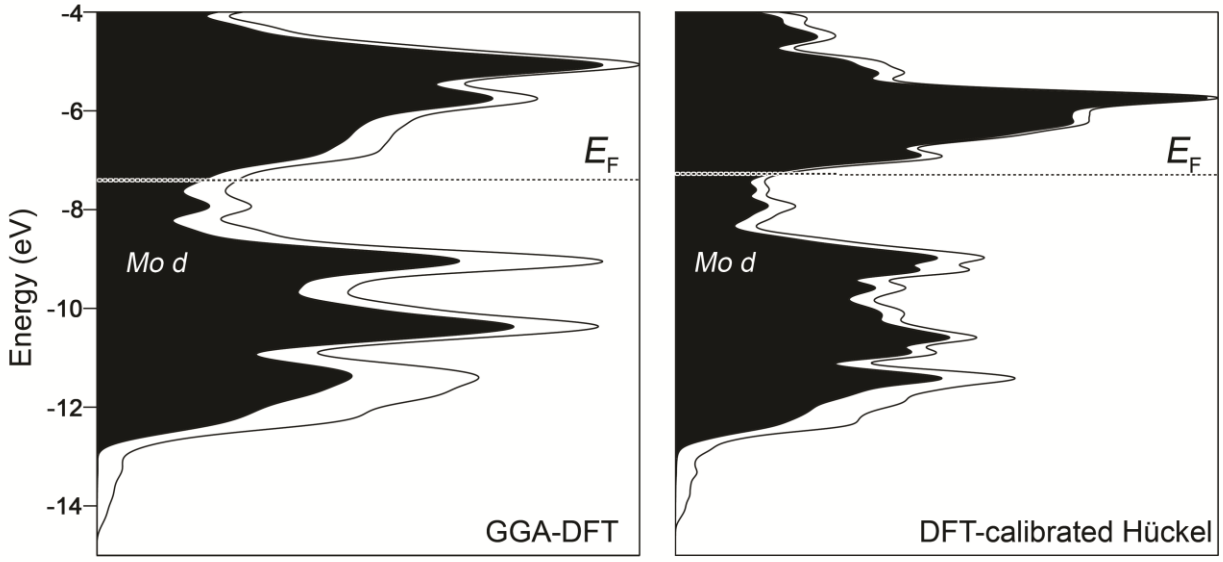

Figure B.1. Electronic DOS curves calculated for bcc-Mo with GGA-DFT (left) and best-fit Hückel model (right).

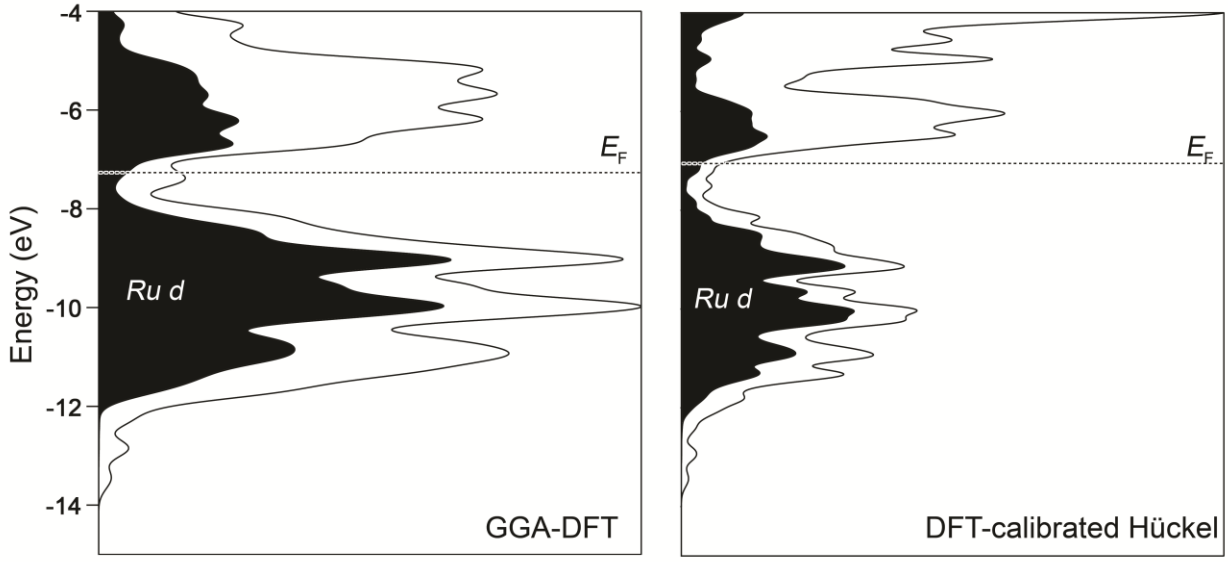

Figure B.2. Electronic DOS curves calculated for ZrRu with GGA-DFT (left) and best-fit Hückel model (right).

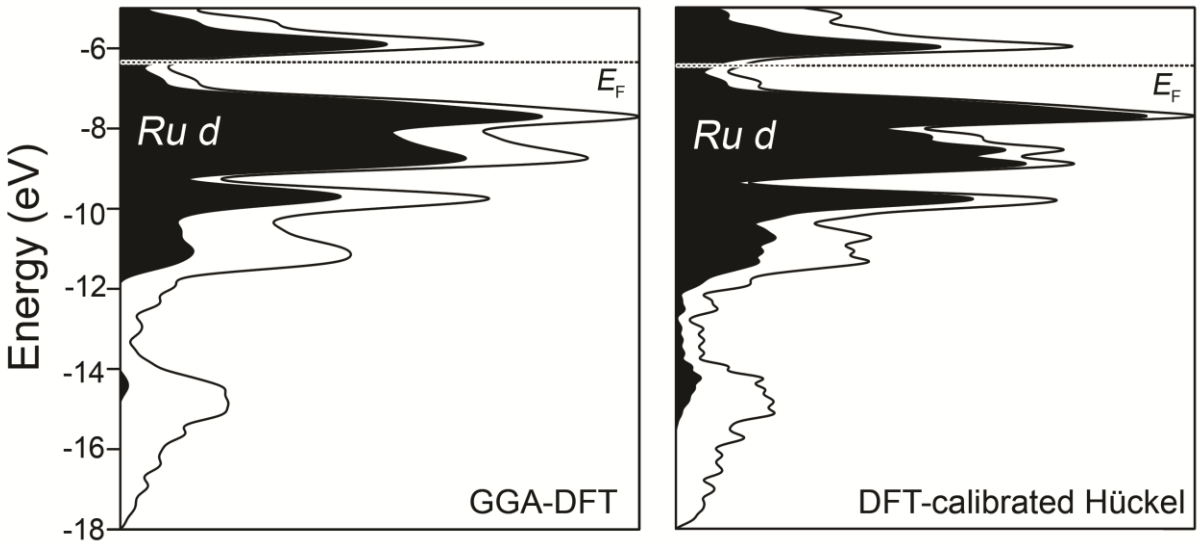

Figure B.3. Electronic DOS curves calculated for the hypothetical CsCl-type RuSn with GGA-DFT (left) and best-fit Hückel model (right).

B.3. raMO RESULTS FOR MODEL INTERMEDIATES BETWEEN ZrRu AND RuSn

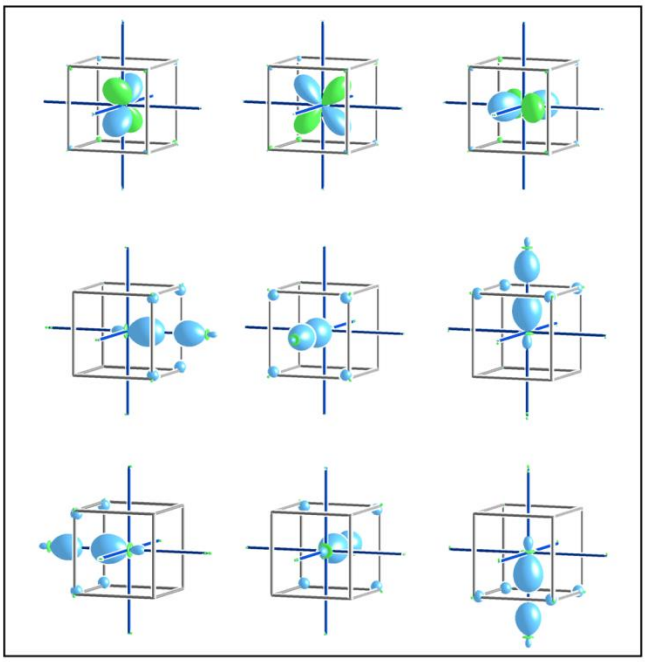

Figure B.4. raMO reconstructions of the Ru spd set for RuSn(hypothetical) in the CsCl type. For s, p_x, p_y, p_z, d_{z2} and d_{x2-y2} linear combinations of the sp^3d^2 type are taken to highlight isolobal bonds along the Ru-Ru contacts of the structure.

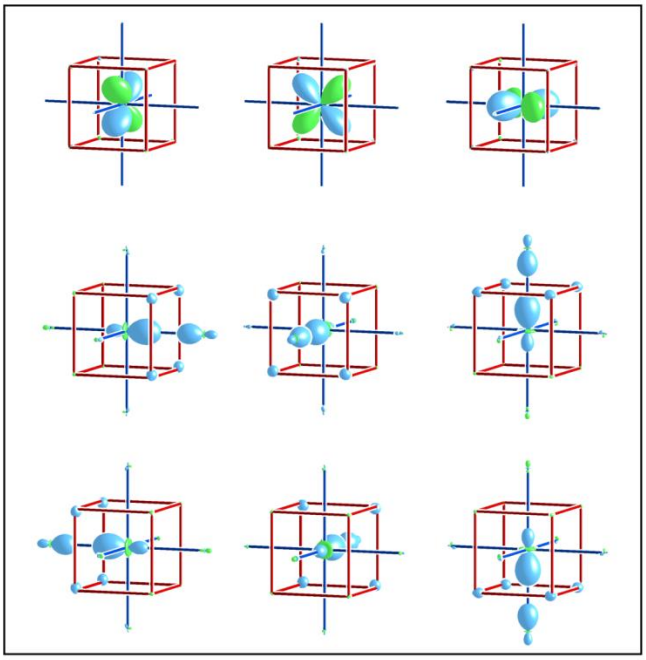

Figure B.5. raMO reconstructions for ZrRu intermediate 1 corresponding to those of RuSn in Figure S4.

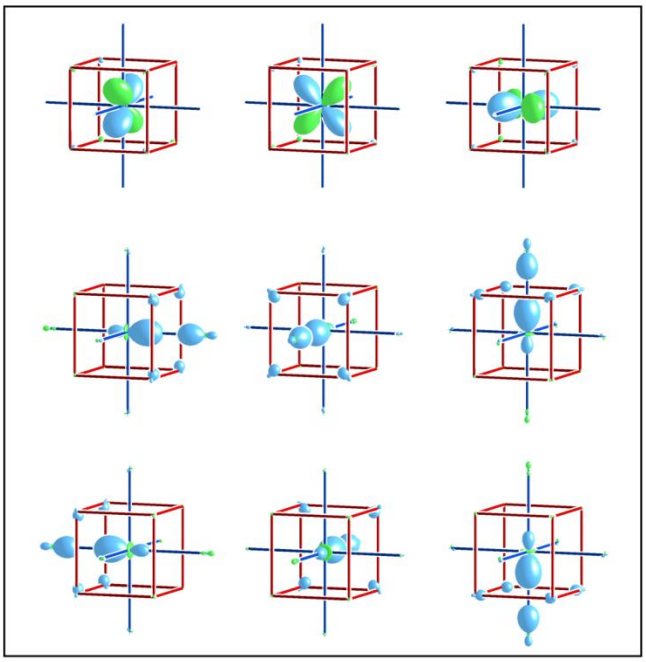

Figure B.6. raMO reconstructions for ZrRu intermediate 2.

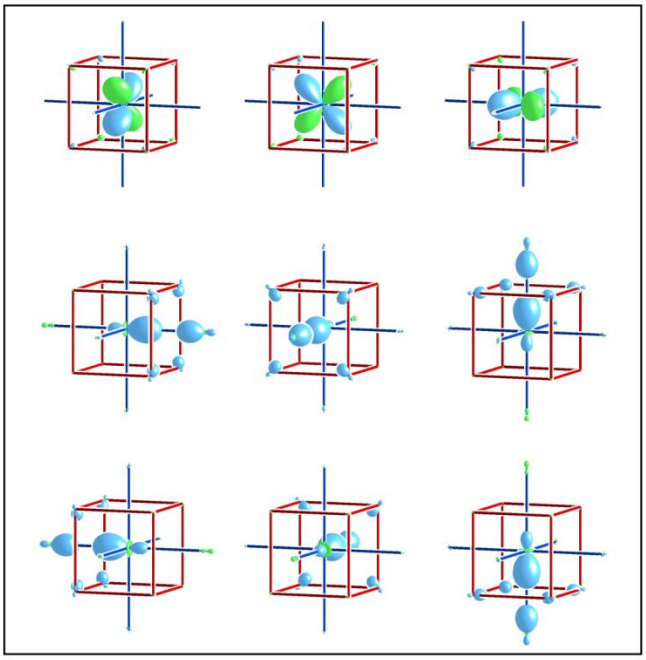

Figure B.7. raMO reconstructions for ZrRu intermediate 3.

B.4. DISCUSSION OF THE COMPLETENESS OF THE 18-*n* SCHEME FOR bcc-Mo

To explore how well the 18-*n* scheme describes the full electronic structure of bcc-Mo, we calculated the projected DOS for the isolobal bonds and t_{2g} d-orbital raMOs of all Mo atoms in one primitive cubic sublattice. Due to the non-orthogonality of raMOs generated for neighboring atoms in a non-sequential manner, the following procedure was used. First, a raMO function was obtained for each isolobal bond using the full basis set of occupied crystal orbitals. Then, these raMO functions were interacted with each other to create raMO band energies and crystal orbitals, which form an orthogonal set representing all linear combinations of the raMOs. These functions were next projected onto the full crystal orbitals of the supercell to obtain the projected DOS distribution of the isolobal bonds (Figure S8a for a 3×3×3 supercell). This procedure was also applied to

the t_{2g} d-orbital-based raMOs, yielding the projected DOS distribution in Figure S8b. The comparison of the sum of the two projected DOS curves (Figure S8c) with the total DOS gives a sense of the completeness of the 18-*n* bonding scheme. However, as no precaution was taken to orthogonalize the LC-raMO set to the t_{2g} d-orbital raMO set, there may be some double-counting of electrons.

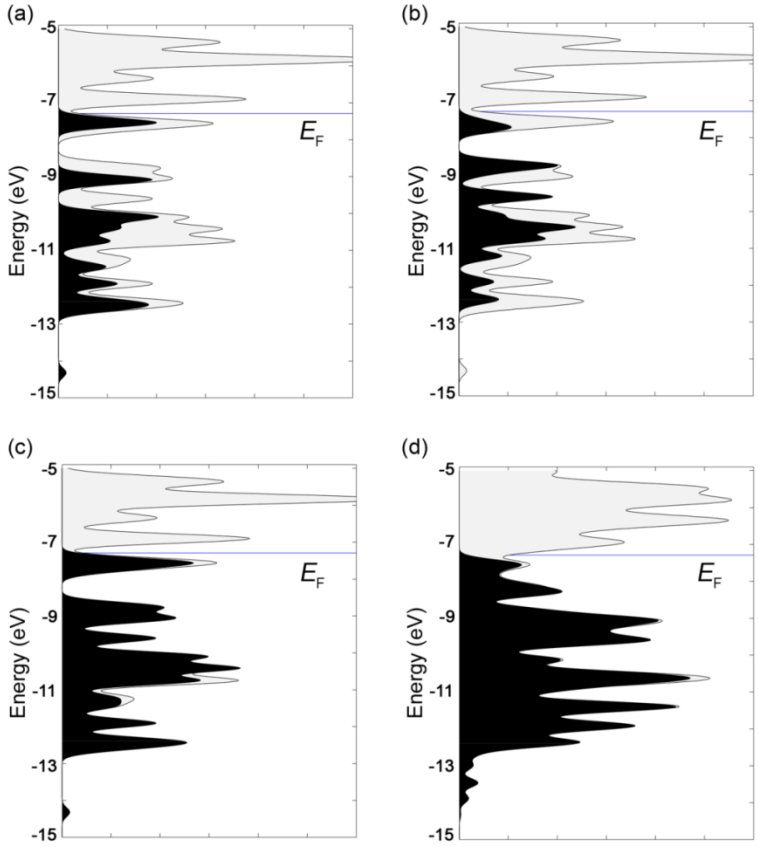

Figure B.8. Projected DOS curves for supercells of bcc-Mo with the shaded areas representing the electrons accounted for by the Mo-Mo isolobal bonds (LC-raMOs) and Mo t_{2g} d-centered raMOs for one primitive cubic sublattice. (a) DOS curve of 3×3×3 supercell with shaded region corresponding to electrons in the LC-raMOs. (b) DOS of 3×3×3supercell with shaded region corresponding to electrons in the t_{2g} d-orbital raMOs. (c) DOS curve of 3×3×3 supercell with the shaded region being the sum of the projected DOS curves from (a) and (b). (d) The result corresponding to (c) obtained for a 6×6×6 supercell.

Overall, the sum of the DOS for the 18-*n* raMO functions corresponds very closely with the total DOS below the Fermi energy (E_F). Similar results are also obtained for a 6×6×6 supercell (Figure S8d). The small areas of the DOS distribution left unaccounted for may partly result from the raMOs on neighboring atoms being constructed independently of each other (rather than in sequence, in which the character of the raMOs can evolve as different portions of the electron structure are accounted for in each step).

B.5. COMPARISON OF THE DOS DISTRIBUTIONS CALCULATED FOR Mo IN THE BCC, FCC, AND HCP STRUCTURES.

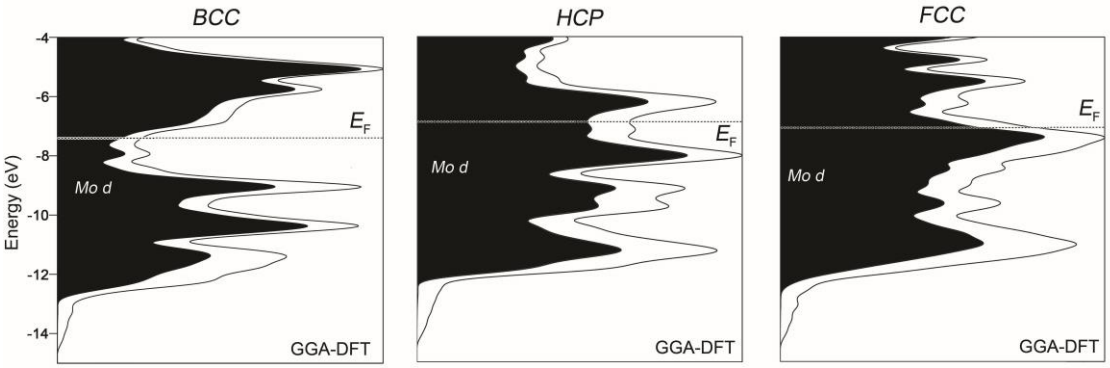

Figure B.9. Electronic DOS distributions calculated for metallic Mo in the bcc, hcp, and fcc structures.

Appendix C.

Supplemental Information for Chapter 4:

Principles of Channel Formation in Intermetallics: Structure-Property Relationships for Fe_2Al_5 Rooted in the 18-n Bonding Scheme and Chemical Pressure Quadrupoles

C.1. CRYSTALLOGRAPHIC DETAILS

Table C.1. Atomic coordinates and displacement parameters for $FeAl_{2.75}$ at 100K.

Site	Wyckoff Position	*x*	*y*	*z*	U_{equiv}/U_{iso}	Occupancy
Fe1	8g	0.5000	0.82803(4)	0.2500	0.00633(11)	1.0
Al1	8f	0.31298(7)	0.14790(8)	0.2500	0.01036(13)	1.0
Al2a	4c	0.5000	0.5000	0.5000	0.0064(5)	0.251(4)
Al2b	4c	0.5000	0.4617(6)	0.2500	0.0064(5)	0.184(4)
Al2c	4a	0.5000	0.5230(5)	0.6214(18)	0.0064(5)	0.1594(15)

Table C.2. Anisotropic atomic displacement parameters for $FeAl_{2.75}$ at 100K.

Site	U_{11}	U_{22}	U_{33}	U_{12}	U_{13}	U_{23}
Fe1	0.00414(17)	0.00602(17)	0.00883(17)	0.00000	0.00000	0.00000
Al1	0.0083(2)	0.0165(3)	0.0063(2)	0.00000	0.00000	0.00726(18)

Table C.3. Selected interatomic distances for $FeAl_{2.75}$ at 100K.

Site	Neighbor	Distance (Å)
Fe1	Al1(×3)	2.5485(7)
	Al1(×2)	2.4950(7)
	Al2a(×2)	2.3469(6)
	Al2b	2.343(4)
	Al2c(×2)	2.309(3)
	Al2c(×2)	2.500(5)
Al1	Al1(×2)	2.6573(8)
	Al2b	2.463(3)
	Al2b	2.6709(19)
	Al2c(×2)	2.601(3)
	Al2c(×2)	2.6837(19)
Al2a	Al2a(×2)	2.1049(7)
	Al2c(×2)	1.0806(10)
Al2b	Al2b(×2)	2.1613(19)

	Al2c(×2)	1.612(8)
	Al2c(×2)	0.550(8)
	Al2c	2.675(7)
Al2c	Al2c(×2)	2.1253(11)
	Al2c(×2)	1.064(15)

Table C.4. Atomic coordinates and displacement parameters for $FeAl_{2.75}$ at 150K.

Site	Wyckoff Position	*x*	*y*	*z*	U_{equiv}/U_{iso}	Occupancy
Fe1	8g	0.5000	0.82803(5)	0.2500	0.00708(12)	1.0
Al1	8f	0.31293(7)	0.14788(8)	0.2500	0.01129(15)	1.0
Al2a	4c	0.5000	0.5000	0.5000	0.0073(5)	0.254(5)
Al2b	4c	0.5000	0.4613(7)	0.2500	0.0073(5)	0.179(4)
Al2c	4a	0.5000	0.5232(5)	0.623(2)	0.0073(5)	0.1599(16)

Table C.5. Anisotropic atomic displacement parameters for $FeAl_{2.75}$ at 150K.

Site	U_{11}	U_{22}	U_{33}	U_{12}	U_{13}	U_{23}
Fe1	0.00473(18)	0.00702(18)	0.00949(18)	0.00000	0.00000	0.00000
Al1	0.0092(3)	0.0178(3)	0.0069(2)	0.00000	0.00000	0.00718(19)

Table C.6. Selected interatomic distances for $FeAl_{2.75}$ at 150K.

Site	Neighbor	Distance (Å)
Fe1	Al1(×3)	2.5496(7)
	Al1(×2)	2.4962(8)
	Al2a(×2)	2.3479(6)
	Al2b	2.346(4)
	Al2c(×2)	2.310(3)
	Al2c(×2)	2.505(5)
Al1	Al1(×2)	2.6582(9)
	Al2b	2.463(4)
	Al2b	2.673(2)
	Al2c(×2)	2.599(4)
	Al2c(×2)	2.683(2)
Al2a	Al2a(×2)	2.1056(7)
	Al2b(×2)	1.0815(11)
Al2b	Al2b(×2)	2.163(2)
	Al2c(×2)	1.621(9)
	Al2c(×2)	0.542(8)
	Al4	2.668(8)
Al2c	Al2c(×2)	
	Al2c(×2)	

Table C.7. Atomic coordinates and displacement parameters for $FeAl_{2.75}$ at 300K.

Site	Wyckoff Position	*x*	*y*	*z*	U_{equiv}/U_{iso}	Occupancy
Fe1	8g	0.5000	0.82792(5)	0.2500	0.00860(12)	1.0
Al1	8f	0.31295(8)	0.14786(8)	0.2500	0.01332(15)	1.0
Al2a	4c	0.5000	0.5000	0.5000	0.0093(5)	0.252(5)
Al2b	4c	0.5000	0.4614(7)	0.2500	0.0093(5)	0.176(5)
Al2c	4a	0.5000	0.5232(5)	0.623(2)	0.0093(5)	0.1621(17)

Table C.8. Anisotropic atomic displacement parameters for $FeAl_{2.75}$ at 300K.

Site	U_{11}	U_{22}	U_{33}	U_{12}	U_{13}	U_{23}
Fe1	0.00634(18)	0.00811(18)	0.01135(19)	0.00000	0.00000	0.00000
Al1	0.0112(3)	0.0197(3)	0.0090(3)	0.00000	0.00000	0.0076(2)

Table C.9. Selected interatomic distances for $FeAl_{2.75}$ at 300K.

Site	Neighbor	Distance (Å)
Fe1	Al1(×3)	2.5531(7)
	Al1(×2)	2.5004(8)
	Al2a(×2)	2.3512(6)
	Al2b	2.349(5)
	Al2c(×2)	2.313(3)
	Al2c(×2)	2.508(5)
Al1	Al1(×2)	2.6624(9)
	Al2b	2.467(4)
	Al2b	2.676(2)
	Al2c(×2)	2.603(4)
	Al2c(×2)	2.687(2)
Al2a	Al2a(×2)	2.1087(7)
	Al2b(×2)	1.0830(11)
Al2b	Al2b(×2)	2.166(2)
	Al2c(×2)	1.623(9)
	Al2c(×2)	0.544(8)
	Al2c	2.673(8)
Al2c	Al2c(×2)	2.1295(12)
	Al2c(×2)	1.081(17)

Table C.10. Atomic coordinates and displacement parameters for $FeAl_{2.75}$ at 400K.

Site	Wyckoff Position	*x*	*y*	*z*	U_{equiv}/U_{iso}	Occupancy
Fe1	8g	0.5000	0.82782(5)	0.2500	0.00996(12)	1.0
Al1	8f	0.31294(8)	0.14776(9)	0.2500	0.01514(15)	1.0
Al2a	4c	0.5000	0.5000	0.5000	0.0111(5)	0.249(5)
Al2b	4c	0.5000	0.4609(8)	0.2500	0.0111(5)	0.175(5)
Al2c	4a	0.5000	0.5225(6)	0.622(2)	0.0111(5)	0.1637(19)

Table C.11. Anisotropic atomic displacement parameters for $FeAl_{2.75}$ at 400K.

Site	U_{11}	U_{22}	U_{33}	U_{12}	U_{13}	U_{23}
Fe1	0.00781(18)	0.00916(18)	0.01290(19)	0.00000	0.00000	0.00000
Al1	0.0130(3)	0.0218(3)	0.0106(3)	0.00000	0.00000	0.0079(2)

Table C.12. Selected interatomic distances for $FeAl_{2.75}$ at 400K.

Site	Neighbor	Distance (Å)
Fe1	Al1(×3)	2.5563(7)
	Al1(×2)	2.5039(8)
	Al2a(×2)	2.3540(6)
	Al2b	2.355(5) .
	Al2c(×2)	2.312(4)
	Al2c(×2)	2.512(6)
Al1	Al1(×2)	2.6663(9)
	Al2b	2.468(4)
	Al2b	2.680(2)
	Al2c(×2)	2.612(4)
	Al2c(×2)	2.689(2)
Al2a	Al2a(×2)	2.1112(7)
	Al2b(×2)	1.0850(12)
Al2b	Al2b(×2)	2.170(2)
	Al2c(×2)	1.623(9)
	Al2c(×2)	0.549(9)
	Al2c	2.679(9)
Al2c	Al2c(×2)	2.1309(12)
	Al2c(×2)	1.073(19)

C.2. EXPERIMENTAL POWDER X-RAY DIFFRACTION PATTERN

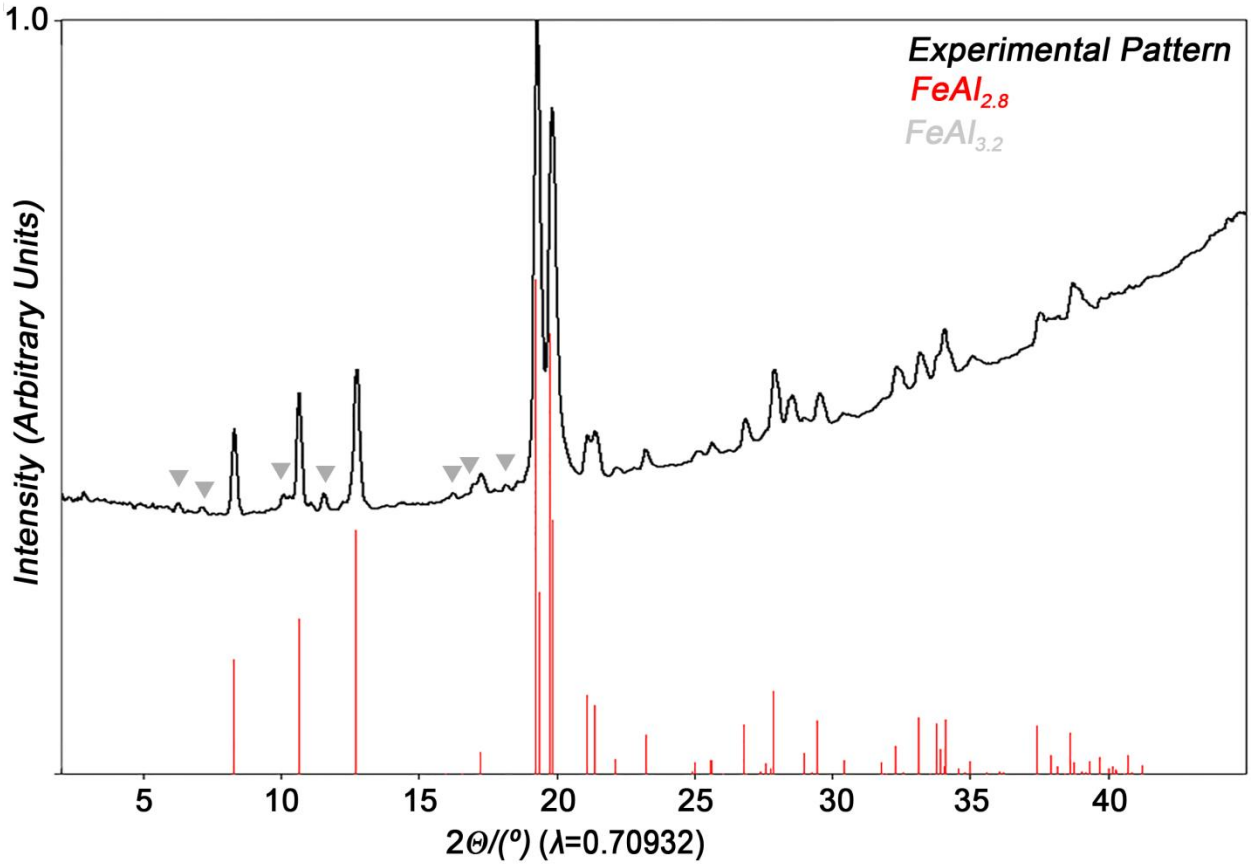

Figure C.1. Experimental powder X-ray diffraction pattern.

C.3. PRECESSION IMAGES FOR THE VARIBLE TEMPERATURE EXPERIMENTS

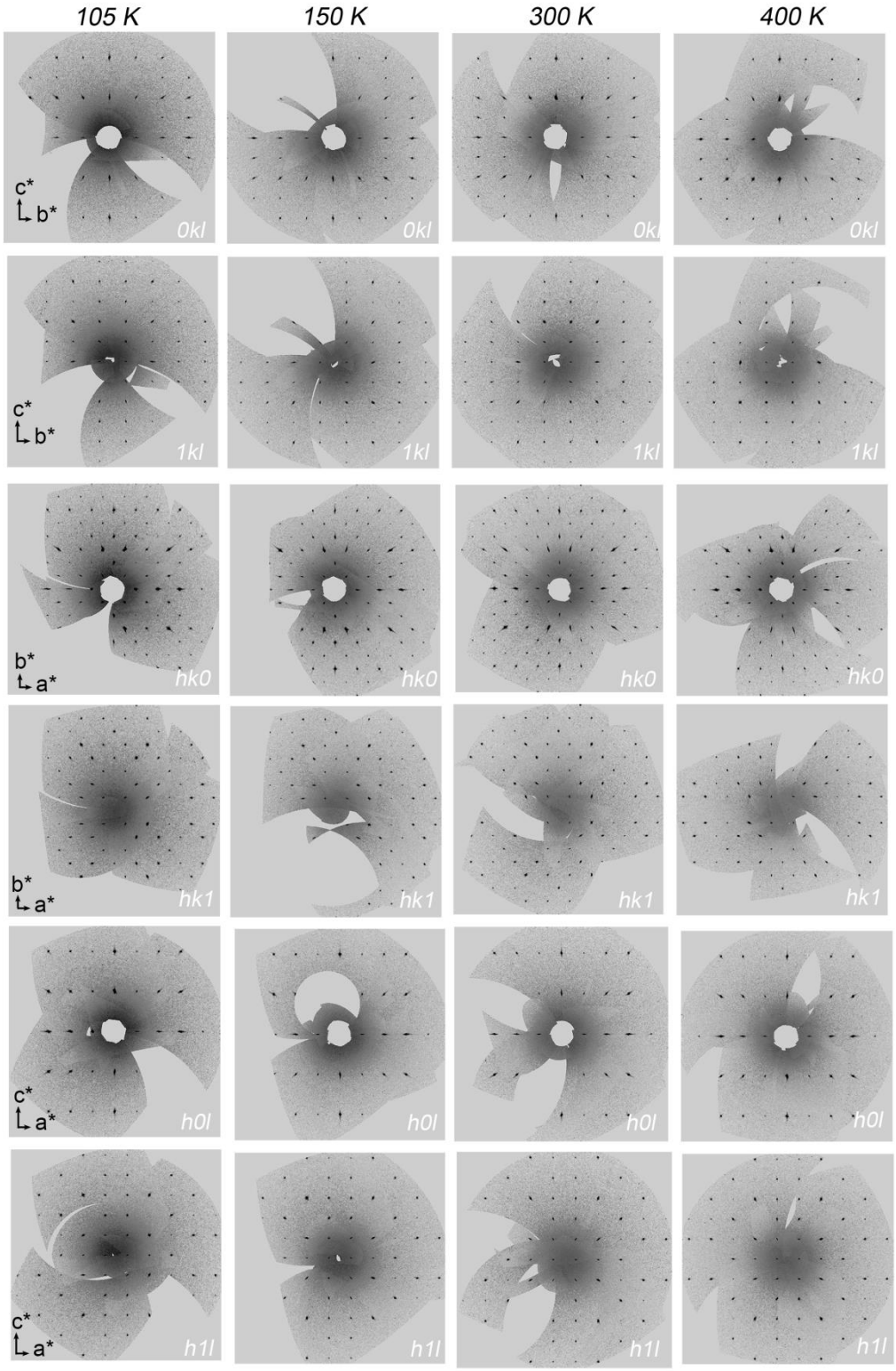

Figure C.2. Rreciprocal space reconstructions of okl, ıkl, hko, hkı, hol, and hıl layers. No formation of superstructure upon cooling or heating. was observed.

C.4. ENERGY DISPERSIVE X-RAY SPECTROSCOPY RESULTS

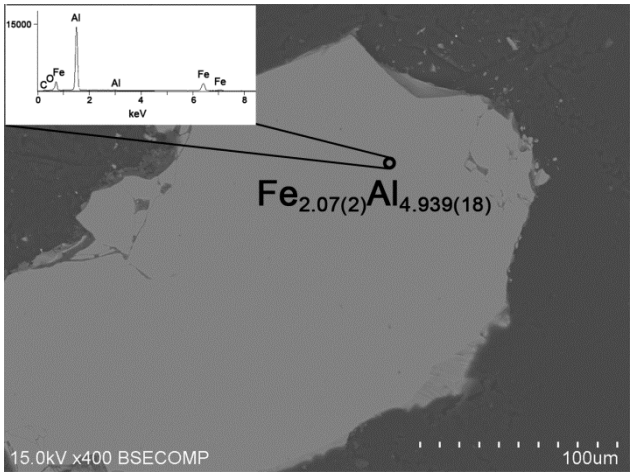

Figure C.3. Back scattered electron image of the sample shows only one phase, as evidenced by the observed single shade of gray in the image.

C.5. COMPUPATION DETAILS AND OPTIMIZED GEOMETRIES for raMO

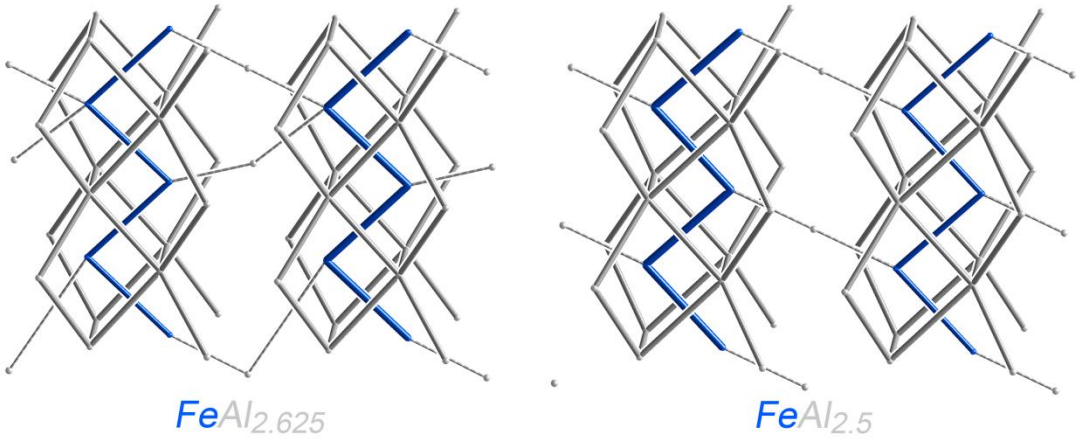

Figure C.4. Ordered models for stoichiometry of $FeAl_{2.625}$ and $FeAl_{2.5}$ used for electronic structure calculations.

Table C.13. DFT-optimized geometry for $FeAl_{2.625}$ model.

Cell Vectors	*x* (Å)	*y* (Å)	*z* (Å)
a (Å)	7.5073088716811 3457	0.0	0.0
b (Å)	0.0	6.4022835217282674	-0.00205950180676 75
c (Å)	0.0	-0.0027044037439530	8.4055356542294550
	x	*y*	*z*
Fe	0.5000000000000000	0.8177268479162928	0.1299730207628850
Fe	0.5000000000000000	0.8453147342087978	0.6278795982030294
Fe	0.5000000000000000	0.1659512708310177	0.3759622929357095
Fe	0.5000000000000000	0.1648509315349287	0.8830646198195269
Fe	0.0000000000000000	0.3215668421017429	0.1288041209064729
Fe	0.0000000000000000	0.3303958197854167	0.6297541770565580
Fe	0.0000000000000000	0.6720704840689798	0.3882795908173120
Fe	0.0000000000000000	0.6723645077767849	0.8686851444096846
Al	0.3217721784985529	0.1549254310623098	0.1291250041066531
Al	0.3257762495050863	0.1720022405122511	0.6296520792025114
Al	0.6866739814137159	0.8569290853681012	0.3882740189329492
Al	0.6848483101742543	0.8528706627294723	0.8695753071989597
Al	0.6782278215014473	0.1549254310623098	0.1291250041066531
Al	0.6742237504949137	0.1720022405122511	0.6296520792025114
Al	0.3133260185862840	0.8569290853681012	0.3882740189329492
Al	0.3151516898257457	0.8528706627294723	0.8695753071989597
Al	0.8161781699979922	0.6544147432047405	0.1292693027360805
Al	0.7802090109429147	0.6201224307717133	0.6282850791019219
Al	0.1827222370771223	0.3462480239432285	0.3810522830798195
Al	0.1839589651213630	0.3493240164236130	0.8772991123036962
Al	0.1838218300020078	0.6544147432047405	0.1292693027360805
Al	0.2197909890570855	0.6201224307717133	0.6282850791019219
Al	0.8172777629228779	0.3462480239432285	0.3810522830798195
Al	0.8160410348786371	0.3493240164236130	0.8772991123036962
Al	0.5000000000000000	0.5141750561316951	0.9569155720736267
Al	0.0000000000000000	0.0113152210115852	0.9646825271376616
Al	0.0000000000000000	0.9508699964234433	0.6266370507552911
Al	0.5000000000000000	0.5190741652433334	0.3144181277788695
Al	0.0000000000000000	0.0083508969351109	0.2862791360181945
Total Energy: -5.277276 eV/atom			

Table C.14. DFT-optimized geometry for $FeAl_{2.5}$ model.

Cell Vectors	*x* (Å)	*y* (Å)	*z* (Å)
a (Å)	7.3881076145399893	0.0	0.0
b (Å)	0.0	6.4853063865299507	-0.16828830685469 66
c (Å)	0.0	-0.2196602326501776	8.4220588198942217
	x	*y*	*z*
Fe	0.4999999990000035	0.8372788234583258	0.1204219977872812
Fe	0.4999999990000035	0.8372788234583258	0.6204220257872837

Fe	0.4999999990000035	0.1627212015416798	0.3795780302127140
Fe	0.4999999990000035	0.1627212015416798	0.8795779392127170
Fe	0.0000000000000000	0.3372788114583247	0.1204219977872812
Fe	0.0000000000000000	0.3372788114583247	0.6204220257872837
Fe	0.0000000000000000	0.6627212135416737	0.3795780302127140
Fe	0.0000000000000000	0.6627212135416737	0.8795779392127170
Al	0.3173457944911697	0.1565647715592769	0.1276052600207477
Al	0.3173457944911697	0.1565647715592769	0.6276052880207499
Al	0.6826542035088301	0.8434352524407250	0.3723947679792476
Al	0.6826542035088301	0.8434352524407250	0.8723946769792508
Al	0.6826542035088301	0.1565647715592769	0.1276052600207477
Al	0.6826542035088301	0.1565647715592769	0.6276052880207499
Al	0.3173457944911697	0.8434352524407250	0.3723947679792476
Al	0.3173457944911697	0.8434352524407250	0.8723946769792508
Al	0.8173457934911661	0.6565647835592779	0.1276052600207477
Al	0.8173457934911661	0.6565647835592779	0.6276052880207499
Al	0.1826542045088337	0.3434352404407240	0.3723947679792476
Al	0.1826542045088337	0.3434352404407240	0.8723946769792508
Al	0.1826542045088337	0.6565647835592779	0.1276052600207477
Al	0.1826542045088337	0.6565647835592779	0.6276052880207499
Al	0.8173457934911661	0.3434352404407240	0.3723947679792476
Al	0.8173457934911661	0.3434352404407240	0.8723946769792508
Al	0.4999999990000035	0.5000000120000010	0.0000000000000000
Al	0.4999999990000035	0.5000000120000010	0.5000000280000023
Al	0.0000000000000000	0.0000000000000000	0.0000000000000000
Al	0.0000000000000000	0.0000000000000000	0.5000000280000023
Total Energy: -5.307218 eV/atom			

Table C.15. DFT-calibrated Hückel Parameters.

Compound, RMS deviation[a]	Orbital	H_{ii}(eV)	c_1	ζ_1(a$_0^{-1}$)	c_2	ζ_2(a$_0^{-1}$)
$FeAl_{2.625}$	Fe 4s	-4.446	1.0000	2.3371	0.0000	0.0000
0.107 eV	Fe 4p	-3.598	1.0000	2.4117	0.0000	0.0000
	Fe 3d	-8.804	0.5680	5.9016	0.9633	2.2427
	Al 3s	-10.496	1.0000	2.1896	0.0000	0.0000
	Al 3p	-5.747	1.0000	1.9484	0.0000	0.0000
$FeAl_{2.5}$	Fe 4s	-5.608	1.0000	2.7893	0.0000	0.0000
0.119 eV	Fe 4p	-3.110	1.0000	2.5862	0.0000	0.0000
	Fe 3d	-8.701	0.5680	5.9016	0.9633	2.2805
	Al 3s	-10.292	1.0000	2.0994	0.0000	0.0000
	Al 3p	-5.873	1.0000	1.9322	0.0000	0.0000

[a] Root-mean-squared deviation between the DFT and Hückel band energies up to ca. 1 eV above E_F

[b] For the double-ζ d orbitals, the c_1 and c_2 coefficients are scaled for normalization inside the YAeHMOP program.

C.6. COMPARISON OF GGA-DFT AND DFT-CALIBRATED HÜCKEL DOS DISTRIBUTIONS

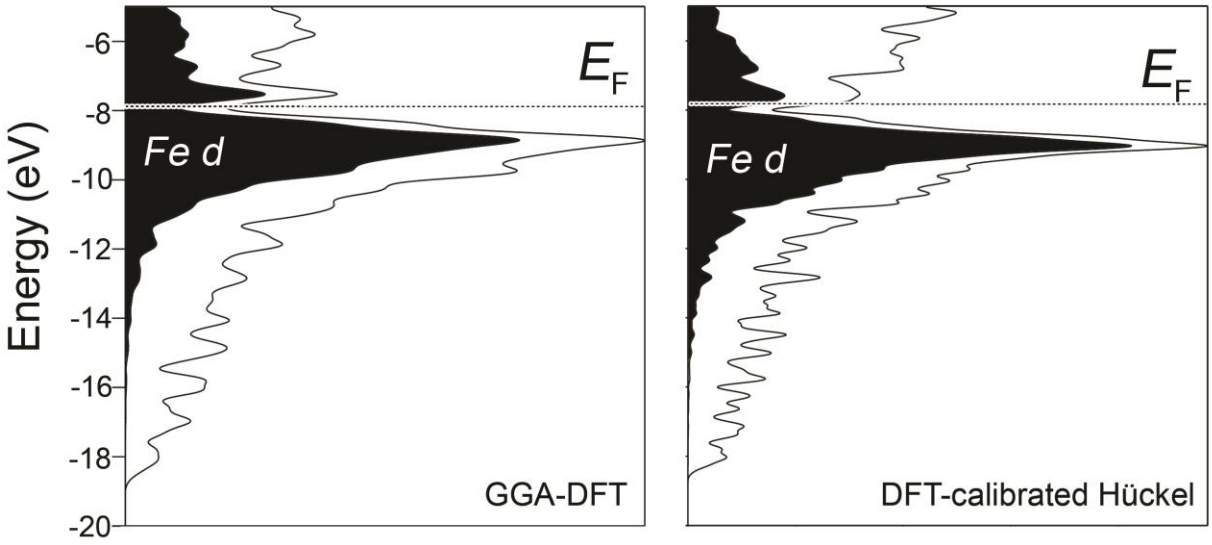

Figure C.5. Electronic DOS distributions calculated for the $FeAl_{2.625}$ model with GGA-DFT (left) and the best fit Hückel model (right).

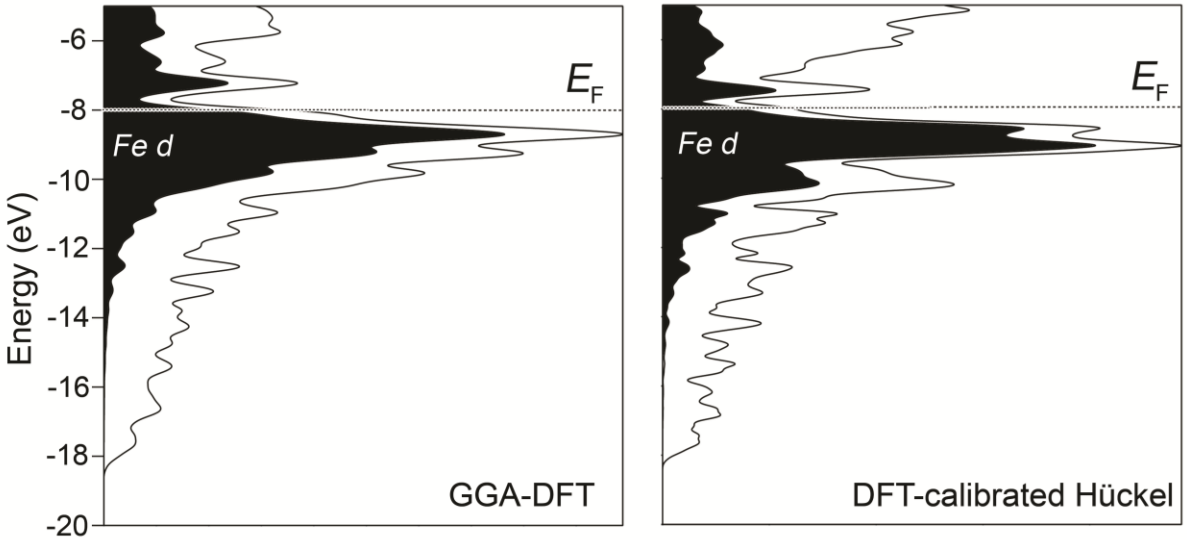

Figure C.6. Electronic DOS distributions calculated for the $FeAl_{2.5}$ model with GGA- DFT (left) and the best fit Hückel model (right).

C.7. raMO RESULTS FOR SYMMETRY INDEPENDENT Fe ATOMS IN "$FeAl_{2.625}$"

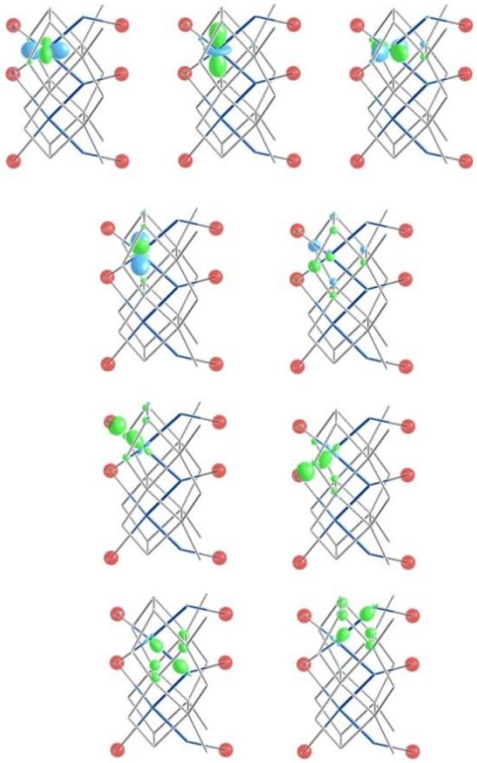

Figure C.6. LC-raMO results for Fe1.

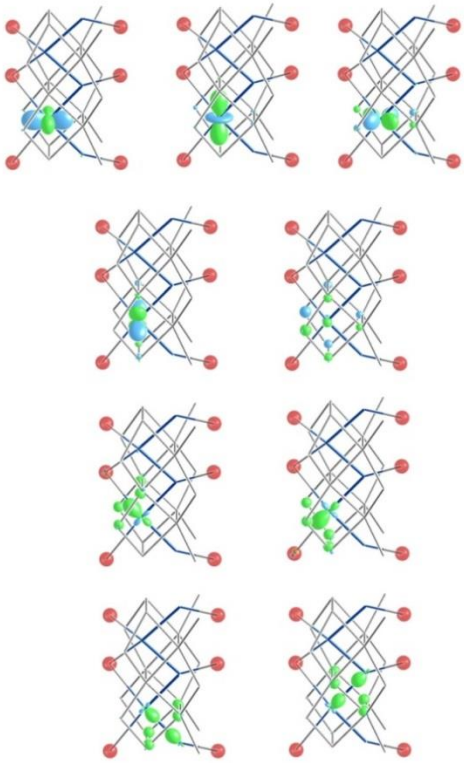

Figure C.8. LC-raMO results for Fe2.

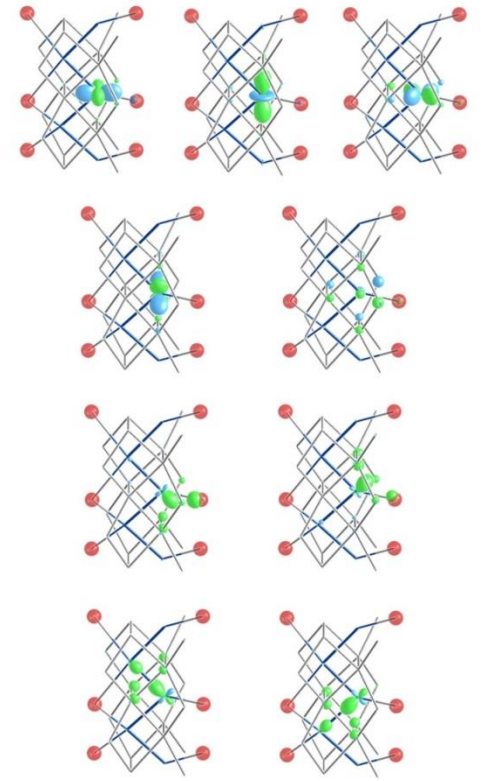

Figure C.9. LC-raMO results for Fe3.

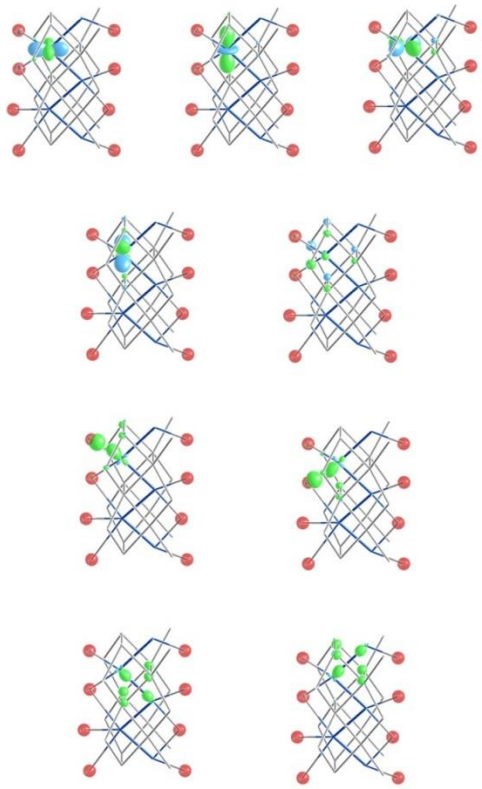

Figure C.10. LC-raMO results for Fe5.

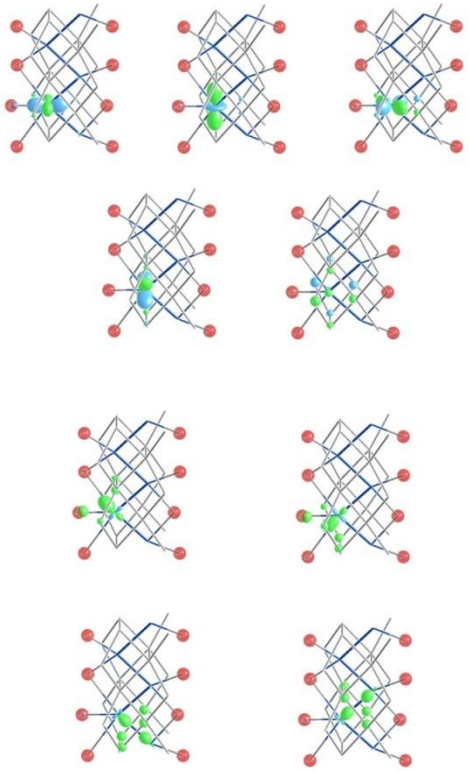

Figure C.11. LC-raMO results for Fe6.

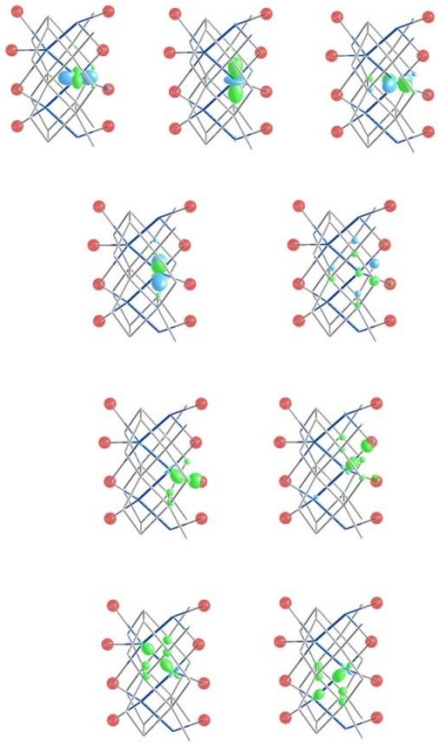

Figure C.12. LC-raMO results for Fe7

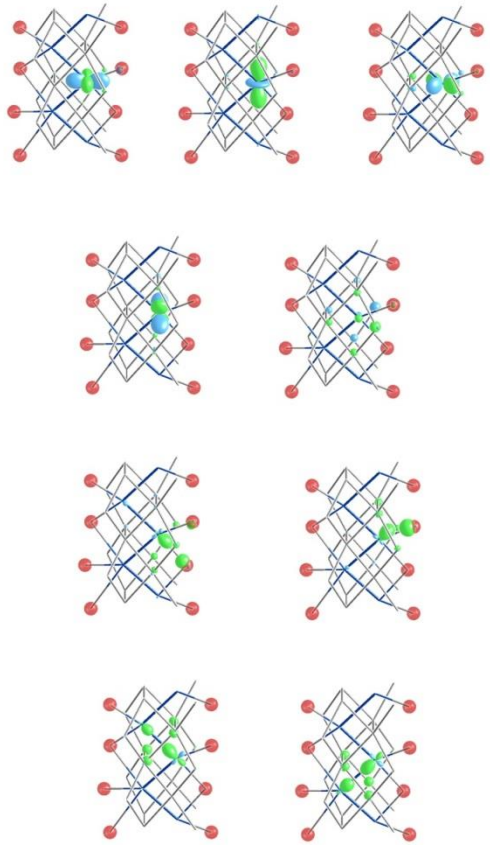

Figure C.13. LC-raMO results for Fe8

C.8. COMPUPATION DETAILS AND OPTIMIZED GEOMETRIES for CP

Table C.16. DFT-optimized geometry for $FeAl_{2.5}$ model with half-occupied Al2a.

Cell Vectors	*x* (Å)	*y* (Å)	*z* (Å)
a (Å)	7.2773241997	0.0000048452	0.0
b (Å)	0.0	6.3238773346	0.0
c (Å)	-0.0000001196	0.1796519512	4.1321176198
	x	*y*	*z*
Fe	0.0	0.338585198	0.257914394
Fe	0.5	0.838585198	0.257914394
Fe	0.0	0.661414862	0.742085576
Fe	0.5	0.161414862	0.742085576
Al	0.816180110	0.655719399	0.245548323
Al	0.316180110	0.155719399	0.245548323
Al	0.0	0.0	0.5
Al	0.5	0.5	0.5
Al	0.183819860	0.344280571	0.754451692
Al	0.683819890	0.844280601	0.754451692
Al	0.183819860	0.655718399	0.245548323
Al	0.683819890	0.155719399	0.245548323

Al	0.816180110	0.344280571	0.754451692
Al	0.316180110	0.844280601	0.754451692

Table C.17. DFT-optimized geometry for $FeAl_{2.5}$ model with half-occupied Al2b.

Cell Vectors	*x* (Å)	*y* (Å)	*z* (Å)
a (Å)	7.3948931694	0.0	0.0
b (Å)	0.0	6.4204559326	0.0
c (Å)	0.0	0.0	3.9902400970
	x	*y*	*z*
Fe	0.0	0.335728049	0.75
Fe	0.5	0.835728049	0.75
Fe	0.0	0.673431873	0.25
Fe	0.5	0.173431873	0.25
Al	0.814151883	0.347530425	0.25
Al	0.314151883	0.847530425	0.25
Al	0.185850784	0.642567039	0.75
Al	0.685850799	0.142567039	0.75
Al	0.185848132	0.347530425	0.25
Al	0.685848117	0.847530425	0.25
Al	0.814149201	0.642567039	0.75
Al	0.314149201	0.142567039	0.75
Al	0.0	0.972345114	0.75
Al	0.5	0.472345114	0.75

Table C.18. Computational parameters of CP calculations with Abinit.

Structure	*Energy cutoff*	*k-point vectors**	*k-point shift*	*FFT grid*	*Total Energy*
$FeAl_{2.5}$ with Al2a	85.00 Ha	7 0 0 0 7 0 0 0 7	0.0 0.0 0.0	80 × 80 × 72	-52.005794 Ha
$FeAl_{2.5}$ with Al2b	85.00 Ha	7 0 0 0 7 0 0 0 7	0.0 0.0 0.0	80 × 80 × 64	-51.992687 Ha

*Three vectors that define a real-space super-lattice whose reciprocal lattice defines the k-point grid

Table C.19. Computational parameters of response function calculations with Abinit.

Structure	*Energy cutoff*	*k-point grid*	*k-point shift*	*FFT grid*	*q-points*
$FeAl_{2.5}$ with Al2a	85.00 Ha	3 × 3 × 3	0.0 0.0 0.0	80 × 80 × 72	8
$FeAl_{2.5}$ with Al2b	85.00 Ha	3 × 3 × 3	0.0 0.0 0.0	80 × 80 × 64	8

Table C.20. Hirshfeld charges on atoms for CP calculations.

Structure	*Site*	*charge*
$FeAl_{2.5}$ with Al2a half-occupied	Fe	-0.458432
	Al1	0.171414
	Al2a	0.231209
$FeAl_{2.5}$ with Al2b half-occupied*	Fe1	-0.461702
	Fe2	-0.427117
	Al1a	0.226028
	Al1b	0.099993
	Al2b	0.236776

* Symmetry breaking in this model resulted in two Fe sites (Fe1 and Fe2) and splitting the Al1 site into two; labeled here Al1a and Al1b.

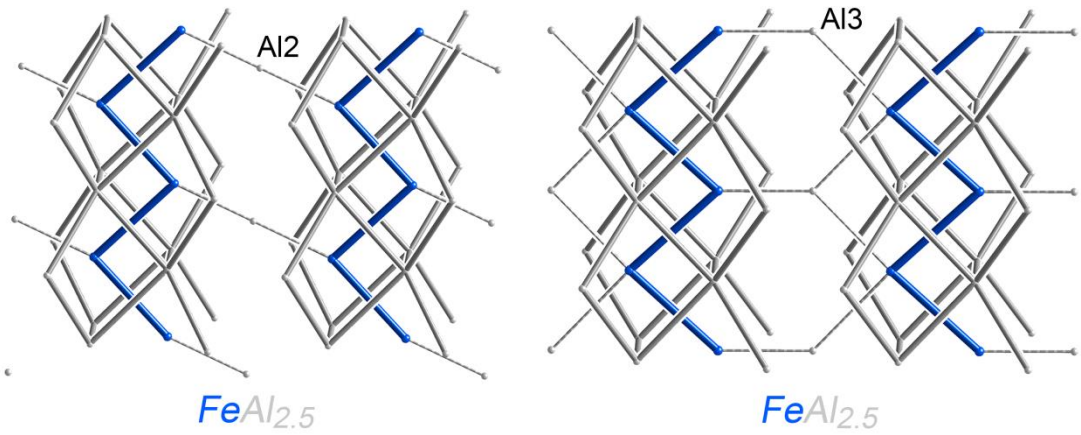

Figure C.14. Ordered models with stoichiometry of $FeAl_{2.5}$ used in DFT-Chemical Pressure calculations

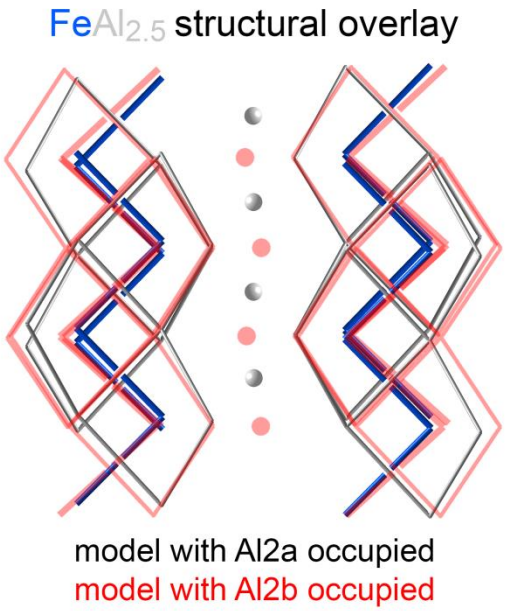

Figure C.15. Structural superposition of structural models with half-occupied Al2a and Al2b sites. The model with Al2a sites occupied is in blue (Fe) and grey (Al), while the model with Al2b sites occupied is in translucent red.

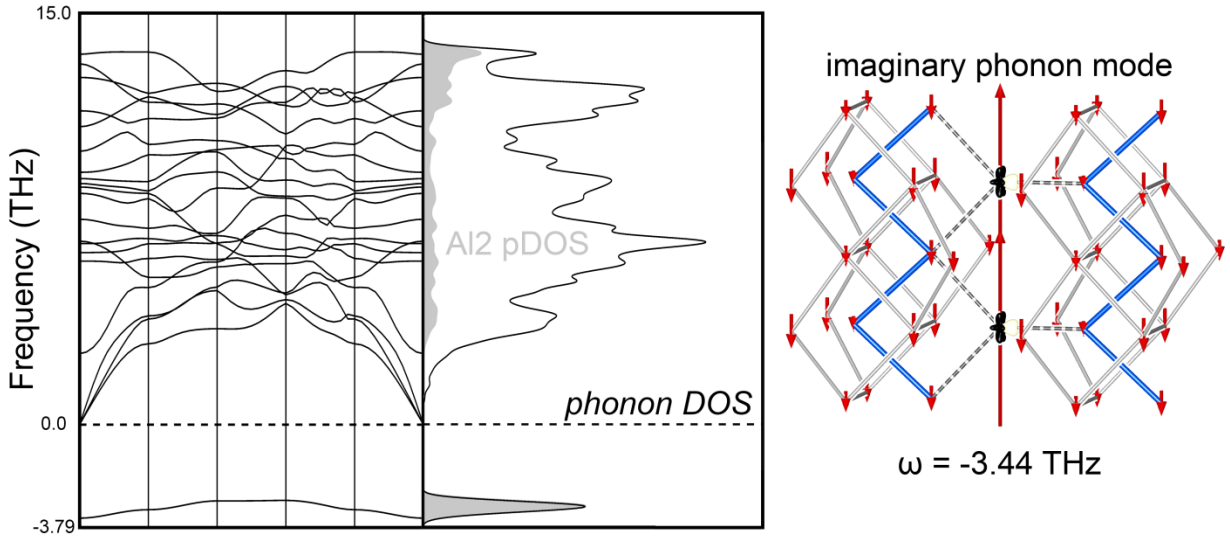

Figure C.16. Phonon DOS and imaginary phonon mode in $FeAl_{2.5}$ model with half-occupied Al2b site

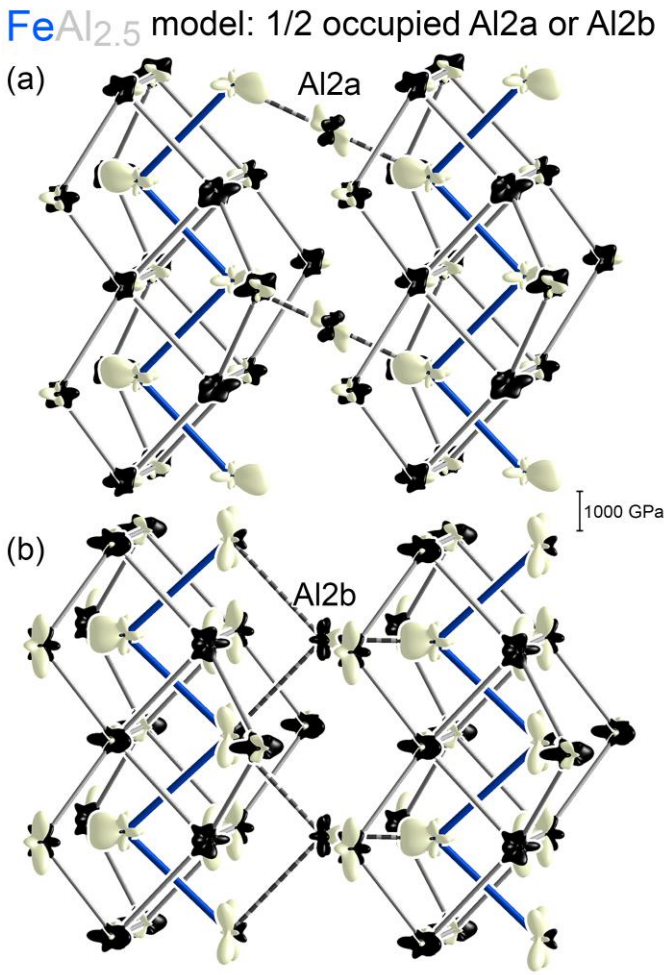

Figure C.17. CP scheme for $FeAl_{2.5}$ models with Al2a and Al2b half-occupied, respectively. CP lobes are drawn on all atoms; the schemes on Al1 and Fe sites remain relatively unchanged in both cases.

Appendix D.

Supplemental Information for Chapter 2:

Substitution Patterns in Intermetallics Understood through Chemical Pressure Analysis: Atom/dumbbell and Ru/Co ordering in derivatives of YCo_5

D.1. Crystallographic Tables for $Y_2Ru_{4.85}Co_{12.15}$

Table D.1. Crystal Data for $Y_2Ru_{4.85}Co_{12.15}$

Chemical Formula	$Y_2Ru_{4.85}Co_{12.15}$
EDS composition	$Y_{1.83(5)}Ru_{4.42(9)}Co_{12.7(3)}$
Space group	*R-3m* (No. 166)
Unit cell *a*=*b* [Å]	8.5011(12)
c [Å]	12.3705(18)
α=β [°]	90
γ [°]	120
Cell volume	774.23(19)
Z	3
Pearson Symbol	*hR*57
Cryst. Dimensions [mm^3]	0.09×0.06×0.03
Crystal color	Silver
Crystal habit	block
Data collection temp.	RT
Radiation source, λ [Å]	Mo K*α*, 0.71073
Absorption coefficient [mm^{-1}]	36.801
Absorption correction	analytical
Min/max transmission	0.140/0.339
θ_{min}, θ_{max}	3.22, 28.92
Number of reflections	3980
Unique refl. [I>3σ(I), all]	383, 435
Refinement method	F^2

Rint . [I>3σ(I), all]	6.34, 0.0651
Number of parameters	28
R[I>3σ(I)], Rw[I>3σ(I)]	0.0221, 0.0456
R(all), Rw(all)	0.0271, 0.0482
S[I>3σ(I)], S(all)	0.95, 0.94
Δρmax, Δρmin(e^-/Å-3)	1.51, -0.92

[a]Three vectors that define a real-space super-lattice whose reciprocal lattice defines the k-point grid
[b]Hypothetical structure

Table D.2. Refined atomic coordinates of $Y_2Ru_{4.85}Co_{12.15}$.

Site	Wyckoff position	*x*	*y*	*z*	U_{equiv}	Occupancy
Y1	6c	0.333333	0.66667	0.01100(7)	0.0061(3)	1
Co1	6c	0.00000	0.00000	0.09856(7)	0.0058(3)	0.331(13)
Ru1	6c	0.00000	0.00000	0.09856(7)	0.0058(3)	0.669(13)
Co2	18h	0.66893(9)	0.83447(5)	0.18150(5)	0.0073(3)	0.645(9)
Ru2	18h	0.66893(9)	0.83447(5)	0.18150(5)	0.0073(3)	0.355(9)
Co3	9d	0.666667	0.833333	0.833333	0.0071(4)	0.953(9)
Ru3	9d	0.666667	0.833333	0.833333	0.0071(4)	0.047(9)
Co4	18f	0.70802(9)	0.000000	0.000000	0.0069(3)	0.793(9)
Ru4	18f	0.70802(9)	0.000000	0.000000	0.0069(3)	0.207(9)

Table D.3. $Y_2Ru_{4.85}Co_{12.15}$ anisotropic atomic displacement parameters.

Site	U_{11}	U_{22}	U_{33}	U_{12}	U_{13}	U_{23}
Y1	0.0057(4)	0.0057(4)	0.0070(5)	0.00283(18)	0	0
Co/Ru1	0.0063(4)	0.0063(4)	0.0049(5)	0.00315(18)	0	0
Co/Ru2	0.0074(4)	0.0058(3)	0.0092(4)	0.00368(18)	0.0009(4)	0.00045(19)
Co/Ru3	0.0096(6)	0.0064(5)	0.0065(6)	0.0048(3)	-0.0023(6)	-0.0012(3)
Co/Ru4	0.0086(3)	0.0056(4)	0.0054(4)	0.00279(19)	-0.00020(13)	-0.0004(3)

Table D.4. Selected interatomic distances for $Y_2Ru_{4.85}Co_{12.15}$.

Site	*Neighbor*	*Distance (Å)*
Ru1/Co1	Ru1/Co1	2.4385(13)
	3×Co4/Ru4	2.5947(4)
	3×Co3/Ru3	2.6445(6)
	6×Co2/Ru2	2.7654(6)
Co3/Ru3	2×Co4/Ru4	2.4526(5)
	Co3/Ru3	2.4978(11)
	Co3/Ru3	2.4979(6)
	2×Co2/Ru2	2.5798(7)

	2×Co2/Ru2	2.5815(7)
Co2/Ru2	2×Co4/Ru4	2.4256(3)
	2×Co2/Ru2	2.4822(6)
Y1	3×Co3/Ru3	3.0232(9)
	6×Co2/Ru2	3.0279(9)
	Ru1/Co1	3.0403(13)
	3×Co3/Ru3	3.1620(9)
	3×Co3/Ru3	3.2485(9)
	3×Co4/Ru4	3.2944(6)

D.2. Powder X-ray diffraction pattern for sample used in single crystal diffraction

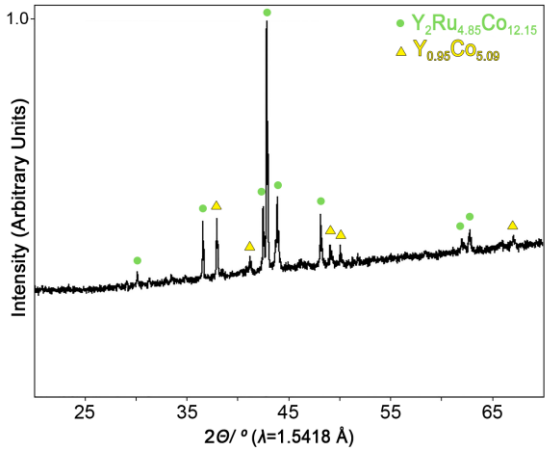

Figure D.1. The powder X-ray diffraction pattern of $Y_2Ru_{4.85}Co_{12.15}$ is shown with highlighted peaks corresponding to this phase (green) and to the $CaCu_5$-type YCo_5 species (yellow).

D.3. Energy Dispersive X-Ray Spectroscopy

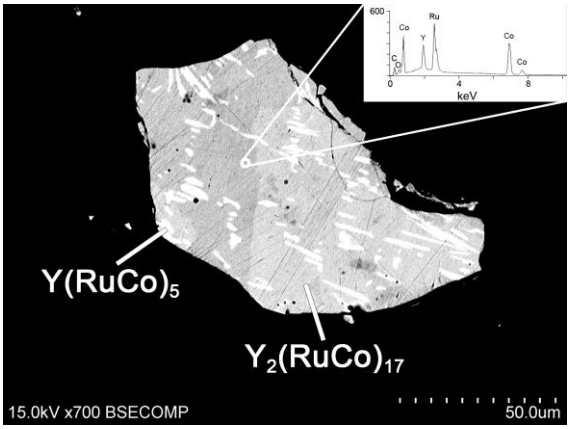

Figure D.2. Back-scattered electron images of a sample of $Y_2(Ru/Co)_{17}$ used for single-crystal X-ray diffraction. A Ru-substituted $CaCu_5$-type $Y(Ru/Co)_5$ phase was detected as the minor species.

D.4. Computational Details

Parameters used in the GGA-DFT calculations for all compounds are shown in Table S1, while the optimized cell parameters obtained are given in Table S2. Tables S3-S42 give the optimized atomic positions and total energies for each phase.

Table D.5. Computational parameters and total energies of CP calculations with Abinit.

Structure	Energy cutoff	k-point vectors[a]	k-point shift	FFT grid	Total energy
YCo_5 (LDA)	100.00 Ha	8 0 0 0 8 0 0 0 10	0.0 0.0 0.5	125×125×100	-179.506468 Ha
YCo_5 (LDA) Spin-polarized	100.00 Ha	8 0 0 0 8 0 0 0 10	0.0 0.0 0.5	128×128×100	-179.661254 Ha
Y_2Co_{17} (LDA)	100.00 Ha	-3 3 3 3 -3 3 3 3 -3	0.5 0.5 0.5	160×160×160	-556.513847 Ha
Y_2Co_{17} (LDA) Spin-polarized	100.00 Ha	-3 3 3 3 -3 3 3 3 -3	0.5 0.5 0.5	160×160×160	-557.072519 Ha
Y_2Co_{17} (LDA) $CaCu_5$ model[b]	100.00 Ha	-3 3 3 3 -3 3 3 3 -3	0.5 0.5 0.5	160×160×160	-556.442723 Ha
$Y_2Ru_2Co_{15}$ (LDA)[b]	100.00 Ha	-4 4 4 4 -4 4 4 4 -4	0.5 0.5 0.5	160×160×160	-532.864740 Ha

[a]Three vectors that define a real-space super-lattice whose reciprocal lattice defines the k-point grid
[b]Hypothetical structure

Table D.6. Computational parameters and total energies of Bader calculations with VASP.

Structure	Energy cutoff	k-point grid	FFT grid	Fine FFT grid	Total energy
YCo_5 (PAW-GGA) Non spin-polarized	12.31 Ha	7×7×9	30×30×24	48×48×36	-41.561728 eV
YCo_5 (PAW-GGA) Spin-polarized	12.31 Ha	7×7×9	30×30×24	48×48×40	-42.068336 eV
Y_2Co_{17}	12.31 Ha	5×5×5	40×40×40	60×60×60	-130.914900

(PAW-GGA)					eV
Y_2Co_{17} (PAW-GGA) Spin-polarized	12.31 Ha	5×5×5	40×40×40	60×60×60	-133.694382 eV
Y_2Co_{17} (PAW-GGA) $CaCu_5$ model[a]	12.31 Ha	6×6×4	48×48×70	80×80×112	-129.181691 eV
$Y_2Ru_2Co_{15}$ (PAW-GGA)[b]	12.31 Ha	9×9×9	40×40×40	60×60×60	-135.666281 eV

[a]Hypothetical structure in which all symmetry in the $CaCu_5$-type YCo_5 compound is maintained except for the replacement of every third Y atom with a Co_2 dumbbell according to the substitution pattern in the Th_2Zn_{17}-type. Atomic positions were not allowed to relax, but the unit cell was.
[b]Modification of Th_2Zn_{17}-type Y_2Co_{17} where Ru has replaced Co on the dumbbell sites.

Table D.7. Cell parameters for all DFT-optimized compounds (converted to conventional cell for convenience)

Structure	*a (Å)*	*b (Å)*	*c (Å)*	*α (°)*	*β (°)*	*γ (°)*
YCo_5 (LDA) Non spin-polarized	4.75278	4.75278	3.79758	90	90	120
YCo_5 (PAW-GGA) Non spin-polarized	4.86388	4.86388	3.86236	90	90	120
YCo_5 (LDA) Spin-polarized	4.93600	4.93600	3.88118	90	90	120
YCo_5 (PAW-GGA) Spin-polarized	4.91667	4.91667	3.94409	90	90	120
Y_2Co_{17} (LDA)	8.03297	8.03297	11.61623	90	90	120
Y_2Co_{17} (PAW-GGA)	8.20431	8.20431	11.87243	90	90	120
Y_2Co_{17} (LDA) Spin-polarized	8.11072	8.11072	11.80517	90	90	120
Y_2Co_{17} (PAW-GGA) Spin-polarized	8.30197	8.30197	12.07732	90	90	120
Y_2Co_{17} (LDA) $CaCu_5$ model[a]	8.02486	8.02486	11.67236	90	90	120

Y_2Co_{17} (PAW-GGA) $CaCu_5$ model [a]	8.19899	8.19899	11.92585	90	90	120
$Y_2Ru_2Co_{15}$ (LDA) [b]	8.08973	8.08973	11.82911	90	90	120
$Y_2Ru_2Co_{15}$ (PAW-GGA)[b]	8.25211	8.25211	12.08492	90	90	120

[a]Hypothetical structure in which all symmetry in the $CaCu_5$-type YCo_5 compound is maintained except for the replacement of every third Y atom with a Co_2 dumbbell according to the substitution pattern in the Th_2Zn_{17}-type. Atomic positions were not allowed to relax, but the unit cell was.
[b]Modification of Th_2Zn_{17}-type Y_2Co_{17} where Ru has replaced Co on the dumbbell sites.

Table D.8. Fractional atomic coordinates for the LDA-DFT optimized $CaCu_5$-type compound YCo_5 with no spin polarization

Element	*x*	*y*	*z*
Y	0.00000	0.00000	0.00000
Co	0.33333	0.16667	0.00000
Co	0.66667	0.83333	0.00000
Co	0.50000	0.00000	0.50000
Co	0.00000	0.50000	0.50000
Co	0.50000	0.50000	0.50000

Table D.9. Fractional atomic coordinates for the GGA-DFT optimized $CaCu_5$-type compound YCo_5 with no spin polarization

Element	*x*	*y*	*z*
Y	0.00000	0.00000	0.00000
Co	0.33333	0.16667	0.00000
Co	0.66667	0.83333	0.00000
Co	0.50000	0.00000	0.50000
Co	0.00000	0.50000	0.50000
Co	0.50000	0.50000	0.50000

Table D.10. Fractional atomic coordinates for the LDA-DFT optimized $CaCu_5$-type compound YCo_5 with spin polarization

Element	*x*	*y*	*z*
Y	0.00000	0.00000	0.00000
Co	0.33333	0.16667	0.00000
Co	0.66667	0.83333	0.00000
Co	0.50000	0.00000	0.50000
Co	0.00000	0.50000	0.50000
Co	0.50000	0.50000	0.50000

Table S11. Fractional atomic coordinates for the GGA-DFT optimized $CaCu_5$-type compound YCo_5 with spin polarization

Element	*x*	*y*	*z*
Y	0.00000	0.00000	0.00000
Co	0.33333	0.16667	0.00000
Co	0.66667	0.83333	0.00000
Co	0.50000	0.00000	0.50000
Co	0.00000	0.50000	0.50000
Co	0.50000	0.50000	0.50000

Table D.12. Fractional atomic coordinates for the LDA-DFT optimized Th_2Zn_{17}-type compound Y_2Co_{17}

Element	*x*	*y*	*z*
Y	0.00000	0.00000	0.34318
Y	0.00000	0.00000	0.65682
Y	0.66667	0.33333	0.67651
Y	0.66667	0.33333	0.99016
Y	0.33333	0.66667	0.00984
Y	0.33333	0.66667	0.32349
Co	0.50000	0.00000	0.50000
Co	0.00000	0.50000	0.50000
Co	0.50000	0.50000	0.50000
Co	0.16667	0.33333	0.83333
Co	0.66667	0.83333	0.83333
Co	0.16667	0.83333	0.83333
Co	0.83333	0.66667	0.16667
Co	0.33333	0.16667	0.16667
Co	0.83333	0.16667	0.16667
Co	0.28820	0.00000	0.00000
Co	0.71179	0.00000	0.00000
Co	0.00000	0.28820	0.00000
Co	0.00000	0.71179	0.00000
Co	0.71179	0.71179	0.00000
Co	0.28820	0.28820	0.00000
Co	0.95487	0.33333	0.33333
Co	0.37846	0.33333	0.33333
Co	0.66667	0.62154	0.33333
Co	0.66667	0.04513	0.33333
Co	0.37846	0.04513	0.33333
Co	0.95487	0.62154	0.33333
Co	0.62154	0.66667	0.66667
Co	0.04513	0.66667	0.66667

Co	0.33333	0.95487	0.66667
Co	0.33333	0.37846	0.66667
Co	0.04513	0.37846	0.66667
Co	0.62154	0.95487	0.66667
Co	0.50237	0.49763	0.15225
Co	0.49763	0.50237	0.84775
Co	0.50237	0.00474	0.15225
Co	0.49763	0.99525	0.84775
Co	0.99525	0.49763	0.15225
Co	0.00474	0.50237	0.84775
Co	0.16904	0.83096	0.48558
Co	0.16430	0.83570	0.18109
Co	0.16904	0.33808	0.48558
Co	0.16430	0.32859	0.18109
Co	0.66192	0.83096	0.48558
Co	0.67141	0.835700	0.18109
Co	0.83570	0.16430	0.81891
Co	0.83096	0.16904	0.51442
Co	0.83570	0.67141	0.81891
Co	0.83096	0.66192	0.51442
Co	0.32859	0.16430	0.81891
Co	0.33808	0.16904	0.51442
Co	0.00000	0.00000	0.09853
Co	0.00000	0.00000	0.90147
Co	0.66667	0.33333	0.43186
Co	0.66667	0.33333	0.23480
Co	0.33333	0.66667	0.76520
Co	0.33333	0.66667	0.56814

Table D.13. Fractional atomic coordinates for the GGA-DFT optimized Th_2Zn_{17}-type compound Y_2Co_{17}

Element	*x*	*y*	*z*
Y	0.00000	0.00000	0.34245
Y	0.00000	0.00000	0.65755
Y	0.66667	0.33333	0.67578
Y	0.66667	0.33333	0.99089
Y	0.33333	0.66667	0.00911
Y	0.33333	0.66667	0.32422
Co	0.83333	0.66667	0.16667
Co	0.16667	0.33333	0.83333
Co	0.33333	0.16667	0.16667
Co	0.66667	0.83333	0.83333

Co	0.83333	0.16667	0.16667
Co	0.16667	0.83333	0.83333
Co	0.50000	0.0000	0.50000
Co	0.00000	0.50000	0.50000
Co	0.50000	0.50000	0.50000
Co	0.95514	0.3333	0.33333
Co	0.04486	0.66667	0.66667
Co	0.66667	0.62180	0.33333
Co	0.33333	0.37820	0.66667
Co	0.37820	0.04486	0.33333
Co	0.62180	0.95514	0.66667
Co	0.33333	0.95514	0.66667
Co	0.66667	0.04486	0.33333
Co	0.62180	0.66667	0.66667
Co	0.37820	0.33333	0.33333
Co	0.04486	0.37820	0.66667
Co	0.95514	0.62180	0.33333
Co	0.71153	0.00000	0.00000
Co	0.00000	0.71153	0.0000
Co	0.28847	0.28847	0.00000
Co	0.00000	0.28847	0.00000
Co	0.28847	0.00000	0.00000
Co	0.71153	0.71153	0.00000
Co	0.16872	0.83128	0.48623
Co	0.83130	0.16872	0.51377
Co	0.16872	0.33744	0.48523
Co	0.83128	0.66256	0.51377
Co	0.66256	0.83128	0.48623
Co	0.33744	0.16872	0.51377
Co	0.83539	0.16461	0.81956
Co	0.49795	0.50205	0.84710
Co	0.83539	0.67077	0.81956
Co	0.49795	0.99589	0.84740
Co	0.32923	0.16461	0.81956
Co	0.00411	0.50205	0.84710
Co	0.50205	0.49795	0.15290
Co	0.16461	0.83539	0.18044
Co	0.50205	0.00511	0.15290
Co	0.16461	0.32923	0.18043
Co	0.99589	0.49795	0.15290
Co	0.67077	0.83539	0.18044
Co	0.00000	0.00000	0.09875
Co	0.00000	0.00000	0.90125

Co	0.66667	0.33333	0.43209
Co	0.66667	0.33333	0.23458
Co	0.33333	0.66667	0.76542
Co	0.33333	0.66667	0.56791

Table D.14. Fractional atomic coordinates for the LDA-DFT optimized Th_2Zn_{17}-type compound Y_2Co_{17} with spin polarization

Element	*x*	*y*	*z*
Y	0.00000	0.00000	0.34456
Y	0.00000	0.00000	0.65544
Y	0.66667	0.33333	0.67789
Y	0.66667	0.33333	0.98878
Y	0.33333	0.66667	0.01122
Y	0.33333	0.66667	0.32211
Co	0.16667	0.33333	0.83333
Co	0.66667	0.83333	0.83333
Co	0.16667	0.83333	0.83333
Co	0.83333	0.66667	0.16667
Co	0.33333	0.16667	0.16667
Co	0.83333	0.16667	0.16667
Co	0.28819	0.00000	0.00000
Co	0.71181	0.00000	0.00000
Co	0.00000	0.28819	0.00000
Co	0.00000	0.71181	0.00000
Co	0.71181	0.71181	0.00000
Co	0.28819	0.28819	0.00000
Co	0.95486	0.33333	0.33333
Co	0.37847	0.33333	0.33333
Co	0.66667	0.62153	0.33333
Co	0.66667	0.04514	0.33333
Co	0.37847	0.04514	0.33333
Co	0.95486	0.62153	0.33333
Co	0.62153	0.66667	0.66667
Co	0.04514	0.66667	0.66667
Co	0.33333	0.95486	0.66667
Co	0.33333	0.37847	0.66667
Co	0.04514	0.37847	0.66667
Co	0.62123	0.95486	0.66667
Co	0.50172	0.49878	0.15210
Co	0.49828	0.50172	0.84790
Co	0.50172	0.00345	0.15210
Co	0.49828	0.99656	0.84790

Co	0.99656	0.49828	0.15210
Co	0.00345	0.50172	0.84790
Co	0.16390	0.83161	0.48543
Co	0.16494	0.83506	0.18124
Co	0.16839	0.33678	0.48543
Co	0.16494	0.32989	0.18124
Co	0.66322	0.83161	0.48543
Co	0.67011	0.83506	0.18124
Co	0.83506	0.16494	0.81876
Co	0.83161	0.16839	0.51457
Co	0.83506	0.67011	0.81876
Co	0.83161	0.66322	0.51457
Co	0.32989	0.16494	0.81876
Co	0.33678	0.16839	0.51457
Co	0.00000	0.00000	0.09681
Co	0.00000	0.00000	0.90319
Co	0.66667	0.33333	0.43014
Co	0.66667	0.33333	0.23653
Co	0.33333	0.66667	0.76348
Co	0.33333	0.66667	0.56986

Table D.15. Fractional atomic coordinates for the GGA-DFT optimized Th_2Zn_{17}-type compound Y_2Co_{17} with spin polarization

Element	*x*	*y*	*z*
Y	0.00000	0.00000	0.34436
Y	0.00000	0.00000	0.65564
Y	0.66667	0.33333	0.67769
Y	0.66667	0.33333	0.98897
Y	0.33333	0.66667	0.01103
Y	0.33333	0.66667	0.32231
Co	0.83333	0.66667	0.16667
Co	0.16667	0.33333	0.83333
Co	0.33333	0.16667	0.16667
Co	0.66667	0.83333	0.83333
Co	0.83333	0.16667	0.16667
Co	0.16667	0.83333	0.83333
Co	0.50000	0.00000	0.50000
Co	0.00000	0.50000	0.50000
Co	0.50000	0.50000	0.50000
Co	0.95487	0.33333	0.33333
Co	0.04513	0.66667	0.66667
Co	0.66667	0.62153	0.33333

Co	0.33333	0.37847	0.66667
Co	0.37847	0.04513	0.33333
Co	0.62153	0.95487	0.66667
Co	0.33333	0.95487	0.66667
Co	0.66667	0.04513	0.33333
Co	0.62153	0.66667	0.66667
Co	0.37847	0.33333	0.33333
Co	0.04513	0.37847	0.66667
Co	0.95487	0.62153	0.33333
Co	0.71180	0.00000	0.00000
Co	0.00000	0.71180	0.00000
Co	0.28820	0.28820	0.00000
Co	0.00000	0.28820	0.00000
Co	0.28820	0.00000	0.00000
Co	0.71180	0.71180	0.00000
Co	0.16820	0.83180	0.48611
Co	0.83180	0.16820	0.51389
Co	0.16820	0.33640	0.48611
Co	0.83180	0.66361	0.51389
Co	0.66361	0.83180	0.48611
Co	0.33640	0.16820	0.51389
Co	0.83486	0.16514	0.81944
Co	0.49847	0.50153	0.84722
Co	0.83486	0.66973	0.81944
Co	0.49847	0.50153	0.84722
Co	0.83486	0.66973	0.81944
Co	0.49847	0.99694	0.84722
Co	0.33027	0.16514	0.81944
Co	0.00306	0.50153	0.84722
Co	0.50153	0.49847	0.15278
Co	0.16514	0.83486	0.18056
Co	0.50153	0.00306	0.15278
Co	0.16514	0.33027	0.18056
Co	0.99694	0.49847	0.15278
Co	0.66973	0.83486	0.18056
Co	0.00000	0.00000	0.09668
Co	0.00000	0.00000	0.90333
Co	0.66667	0.33333	0.43001
Co	0.66667	0.33333	0.23666
Co	0.33333	0.66667	0.76334
Co	0.33333	0.66667	0.56999

Table D.16. Fractional atomic coordinates for the GGA-DFT optimized compound Y_2Co_{17} in a modified $CaCu_5$-type

Element	*x*	*y*	*z*
Y	0.00000	0.00000	0.34264
Y	0.00000	0.00000	0.65736
Y	0.66667	0.33333	0.67597
Y	0.66667	0.33333	0.99069
Y	0.33333	0.66667	0.00931
Y	0.33333	0.66667	0.32403
Co	0.50000	0.00000	0.50000
Co	0.00000	0.50000	0.50000
Co	0.50000	0.50000	0.50000
Co	0.16667	0.33333	0.83333
Co	0.66667	0.83333	0.83333
Co	0.16667	0.83333	0.83333
Co	0.83333	0.66667	0.16667
Co	0.33333	0.16667	0.16667
Co	0.83333	0.16667	0.16667
Co	0.33333	0.00000	0.00000
Co	0.66667	0.00000	0.00000
Co	0.00000	0.33333	0.00000
Co	0.00000	0.66667	0.00000
Co	0.66667	0.66667	0.00000
Co	0.33333	0.33333	0.00000
Co	0.00000	0.33333	0.33333
Co	0.33333	0.33333	0.33333
Co	0.66667	0.66667	0.33333
Co	0.66667	0.00000	0.33333
Co	0.33333	0.00000	0.33333
Co	0.00000	0.66667	0.33333
Co	0.66667	0.66667	0.66667
Co	0.00000	0.66667	0.66667
Co	0.33333	0.00000	0.66667
Co	0.33333	0.33333	0.66667
Co	0.00000	0.33333	0.66667
Co	0.66667	0.00000	0.66667
Co	0.50000	0.50000	0.16667
Co	0.50000	0.50000	0.83333
Co	0.50000	0.00000	0.16667
Co	0.50000	0.00000	0.83333
Co	0.00000	0.50000	0.16667
Co	0.00000	0.50000	0.83333
Co	0.16667	0.83333	0.50000

Co	0.16667	0.83333	0.16667
Co	0.16667	0.33333	0.50000
Co	0.16667	0.33333	0.16667
Co	0.66667	0.83333	0.50000
Co	0.66667	0.83333	0.16667
Co	0.83333	0.16667	0.83333
Co	0.83333	0.16667	0.50000
Co	0.83333	0.66667	0.83333
Co	0.83333	0.66667	0.50000
Co	0.33333	0.16667	0.833333
Co	0.33333	0.16667	0.50000
Co	0.00000	0.00000	0.09876
Co	0.00000	0.00000	0.90124
Co	0.66667	0.33333	0.43209
Co	0.66667	0.33333	0.23457
Co	0.33333	0.66667	0.76543
Co	0.33333	0.66667	0.56791

Table D.17. Fractional atomic coordinates for the GGA-DFT optimized compound Y_2Co_{17} in a modified $CaCu_5$-type

Element	*x*	*y*	*z*
Y	0.00000	0.00000	0.34264
Y	0.00000	0.00000	0.65736
Y	0.66667	0.33333	0.67597
Y	0.66667	0.33333	0.99069
Y	0.33333	0.66667	0.00931
Y	0.33333	0.66667	0.32403
Co	0.50000	0.00000	0.50000
Co	0.00000	0.50000	0.50000
Co	0.50000	0.50000	0.50000
Co	0.16667	0.33333	0.83333
Co	0.66667	0.83333	0.83333
Co	0.16667	0.83333	0.83333
Co	0.83333	0.66667	0.16667
Co	0.33333	0.16667	0.16667
Co	0.83333	0.16667	0.16667
Co	0.33333	0.00000	0.00000
Co	0.66667	0.00000	0.00000
Co	0.00000	0.33333	0.00000
Co	0.00000	0.66667	0.00000
Co	0.66667	0.66667	0.00000
Co	0.33333	0.33333	0.00000

Co	0.00000	0.33333	0.33333
Co	0.33333	0.33333	0.33333
Co	0.66667	0.66667	0.33333
Co	0.66667	0.00000	0.33333
Co	0.33333	0.00000	0.33333
Co	0.00000	0.66667	0.33333
Co	0.66667	0.66667	0.66667
Co	0.00000	0.66667	0.66667
Co	0.33333	0.00000	0.66667
Co	0.33333	0.33333	0.66667
Co	0.00000	0.33333	0.66667
Co	0.66667	0.00000	0.66667
Co	0.50000	0.50000	0.16667
Co	0.50000	0.50000	0.83333
Co	0.50000	0.00000	0.16667
Co	0.50000	0.00000	0.83333
Co	0.00000	0.50000	0.16667
Co	0.00000	0.50000	0.83333
Co	0.16667	0.83333	0.50000
Co	0.16667	0.83333	0.16667
Co	0.16667	0.33333	0.50000
Co	0.16667	0.33333	0.16667
Co	0.66667	0.83333	0.50000
Co	0.66667	0.83333	0.16667
Co	0.83333	0.16667	0.83333
Co	0.83333	0.16667	0.50000
Co	0.83333	0.66667	0.83333
Co	0.83333	0.66667	0.50000
Co	0.33333	0.16667	0.833333
Co	0.33333	0.16667	0.50000
Co	0.00000	0.00000	0.09876
Co	0.00000	0.00000	0.90124
Co	0.66667	0.33333	0.43209
Co	0.66667	0.33333	0.23457
Co	0.33333	0.66667	0.76543
Co	0.33333	0.66667	0.56791

Table D.18. Fractional atomic coordinates for the LDA-DFT optimized compound $Y_2Ru_2Co_{15}$ in the Th_2Zn_{17}-type

Element	*x*	*y*	*z*
Y	0.00000	0.00000	0.34662
Y	0.00000	0.00000	0.65338

Y	0.66667	0.33333	0.67995
Y	0.66667	0.33333	0.98672
Y	0.33333	0.66667	0.01328
Y	0.33333	0.66667	0.32005
Ru	0.00000	0.00000	0.09808
Ru	0.00000	0.00000	0.90192
Ru	0.66667	0.33333	0.43141
Ru	0.66667	0.33333	0.23525
Ru	0.33333	0.66667	0.76475
Ru	0.33333	0.66667	0.56859
Co	0.50000	0.00000	0.50000
Co	0.00000	0.50000	0.50000
Co	0.50000	0.50000	0.50000
Co	0.16667	0.33333	0.83333
Co	0.66667	0.83333	0.83333
Co	0.16667	0.83333	0.83333
Co	0.83333	0.66667	0.16667
Co	0.33333	0.16667	0.16667
Co	0.83333	0.16667	0.16667
Co	0.29681	0.00000	0.00000
Co	0.70318	0.00000	0.00000
Co	0.00000	0.29681	0.00000
Co	0.00000	0.70318	0.00000
Co	0.70318	0.70318	0.00000
Co	0.29681	0.29681	0.00000
Co	0.96348	0.33333	0.33333
Co	0.36985	0.33333	0.33333
Co	0.66667	0.63015	0.33333
Co	0.66667	0.03652	0.33333
Co	0.36985	0.03652	0.33333
Co	0.96348	0.63015	0.33333
Co	0.63015	0.66667	0.66667
Co	0.03652	0.66667	0.66667
Co	0.33333	0.96345	0.66667
Co	0.33333	0.36985	0.66667
Co	0.03652	0.36985	0.66667
Co	0.63015	0.96348	0.66667
Co	0.50162	0.49838	0.15458
Co	0.49838	0.50162	0.84542
Co	0.50162	0.00325	0.15458
Co	0.49838	0.99675	0.84542
Co	0.99675	0.49838	0.15458
Co	0.00325	0.50162	0.84542

Co	0.16829	0.83171	0.48791
Co	0.16504	0.83496	0.17876
Co	0.16829	0.33658	0.48791
Co	0.16504	0.33009	0.17876
Co	0.66342	0.83171	0.48791
Co	0.66991	0.83496	0.17876
Co	0.83496	0.16504	0.82124
Co	0.83171	0.16829	0.51209
Co	0.83496	0.66991	0.82124
Co	0.83171	0.66342	0.51209
Co	0.33009	0.16504	0.82124
Co	0.33658	0.16829	0.51209

Table S19. Fractional atomic coordinates for the GGA-DFT optimized compound $Y_2Ru_2Co_{15}$ in the Th_2Zn_{17}-type

Element	*x*	*y*	*z*
Y	0.00000	0.00000	0.34647
Y	0.00000	0.00000	0.65353
Y	0.66667	0.33333	0.67980
Y	0.66667	0.33333	0.98687
Y	0.33333	0.66667	0.01314
Y	0.33333	0.66667	0.32020
Ru	0.00000	0.00000	0.09817
Ru	0.00000	0.00000	0.90183
Ru	0.66667	0.33333	0.43151
Ru	0.66667	0.33333	0.23516
Ru	0.33333	0.66667	0.76484
Ru	0.33333	0.66667	0.56849
Co	0.83333	0.66667	0.16667
Co	0.16667	0.33333	0.83333
Co	0.33333	0.16667	0.16667
Co	0.66667	0.83333	0.83333
Co	0.83333	0.16667	0.16667
Co	0.16667	0.83333	0.83333
Co	0.50000	0.00000	0.50000
Co	0.00000	0.50000	0.50000
Co	0.50000	0.50000	0.50000
Co	0.96302	0.33333	0.33333
Co	0.03698	0.66667	0.66667
Co	0.66667	0.62969	0.33333
Co	0.33333	0.37032	0.66667
Co	0.37032	0.03698	0.33333

Co	0.62969	0.96302	0.66667
Co	0.33333	0.96302	0.66667
Co	0.66667	0.03698	0.33333
Co	0.62969	0.66667	0.66667
Co	0.37032	0.33333	0.33333
Co	0.03698	0.37032	0.66667
Co	0.96302	0.62969	0.33333
Co	0.70365	0.00000	0.00000
Co	0.00000	0.70365	0.00000
Co	0.29635	0.00000	0.00000
Co	0.70365	0.70365	0.00000
Co	0.16841	0.83160	0.48820
Co	0.83160	0.16841	0.51180
Co	0.16841	0.33681	0.48820
Co	0.83160	0.66319	0.51180
Co	0.66319	0.83160	0.48820
Co	0.33681	0.16841	0.51180
Co	0.83507	0.16493	0.82153
Co	0.49826	0.50174	0.84514
Co	0.83507	0.67014	0.82153
Co	0.49826	0.99652	0.84514
Co	0.32986	0.16493	0.82153
Co	0.00348	0.50174	0.84514
Co	0.50174	0.49826	0.15487
Co	0.16493	0.83507	0.17847
Co	0.50174	0.00348	0.15487
Co	0.16493	0.32986	0.17487
Co	0.99652	0.49826	0.15487
Co	0.67014	0.83507	0.17847

D.4. Magnetization on atoms in spin-polarized calculations

Table D.20. Magnetization of atoms[a] in LDA-DFT optimized $CaCu_5$-type compound YCo_5 with spin polarization, calculated in ABINIT.

Site	Wyckoff Position	magnetization
Y	1a	-0.67171153
Co1	2c	2.07990169
Co2	3g	2.09615244

[a]Wigner-Seitz radii of 1.889 Å and 1.355 Å for Y and Co, respectively, were used to determine atomic volumes for integration of spin density

Table D.21. Magnetization of atoms[a] in GGA-DFT optimized $CaCu_5$-type compound YCo_5 with spin polarization, calculated in VASP.

Site	Wyckoff Position	magnetization
Y	1a	-0.233
Co1	2c	1.477
Co2	3g	1.490

[a]Wigner-Seitz radii of 1.906 Å and 1.367 Å for Y and Co, respectively, were used to determine atomic volumes for integration of spin density

Table D.22. Magnetization of atoms[a] in LDA-DFT optimized Th_2Zn_{17}-type compound Y_2Co_{17} with spin polarization, calculated in ABINIT.

Site	Wyckoff Position	magnetization
Y	6c	-0.690004085
Co1	6c	2.06452439
Co2	18h	2.00759545
Co3	9d	1.99636877
Co4	18f	1.96757142

[a]Wigner-Seitz radii of 1.779 Å and 1.276 Å for Y and Co, respectively, were used to determine atomic volumes for integration of spin density

Table D.23. Magnetization of atoms[a] in GGA-DFT optimized Th_2Zn_{17}-type compound Y_2Co_{17} with spin polarization, calculated in VASP.

Site	Wyckoff Position	magnetization
Y	6c	-0.240
Co1	6c	1.629
Co2	18h	1.489
Co3	9d	1.531
Co4	18f	1.534

[a]Wigner-Seitz radii of 1.907 Å and 1.368 Å for Y and Co, respectively, were used to determine atomic volumes for integration of spin density

D.5. CP schemes with varying ionicity (50% of Bader charge used for main text)

Radial electron density profiles were generated for all symmetry-distinct sites in each structure for charges equal to 100%, 75%, 50%, and 0% of the Bader charge on each site. Below are CP schemes with this weak dependence demonstrated.

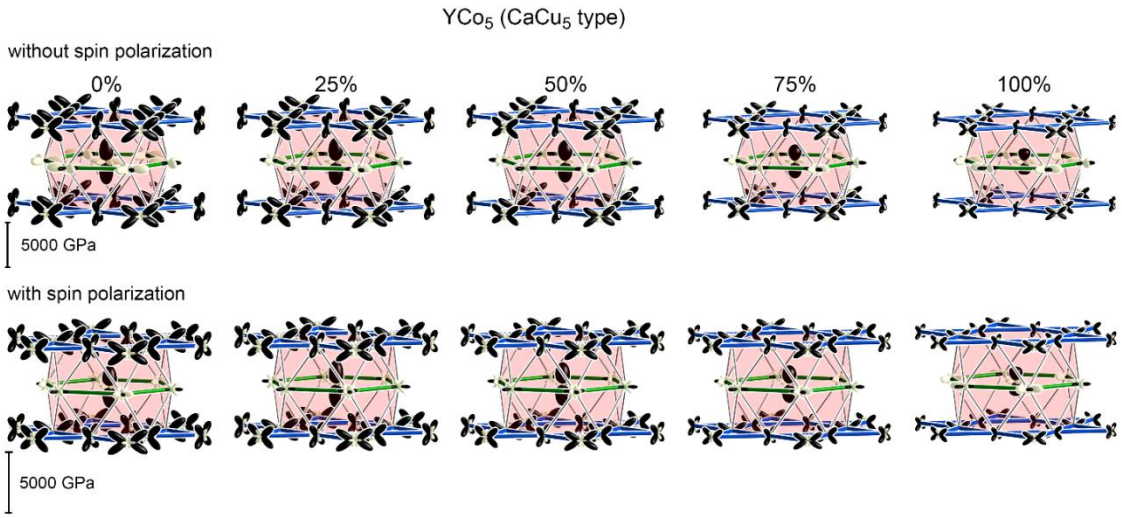

Figure D.3. Chemical pressure schemes for YCo_5 in the $CaCu_5$ type, without (above) and with (below) spin-polarization included. Radial electron density files for atoms at 0, 25,50, 75, and 100% of the calculated Bader charges were used to generate these schemes; the results for 50% ionicity are shown in the main text.

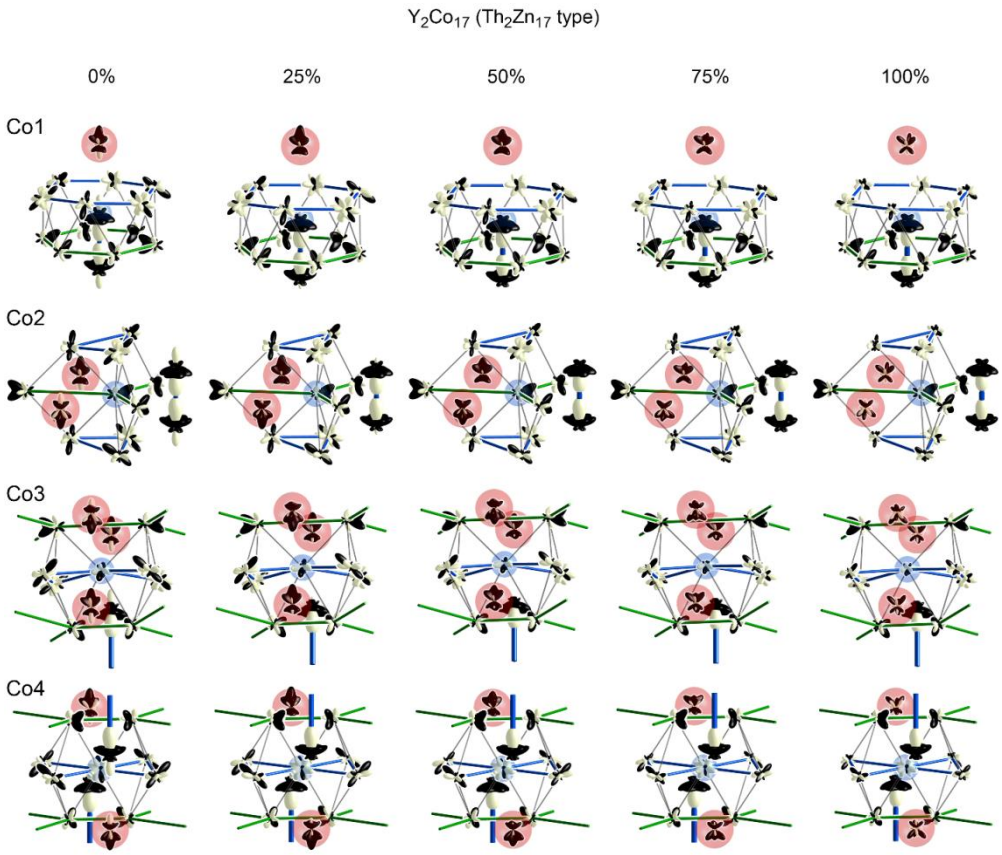

Figure D.4. Chemical pressure schemes for all Co sites in Y_2Co_{17} in the Th_2Zn_{17} type without spin-polarization. The results for 50% ionicity are presented in the main text.

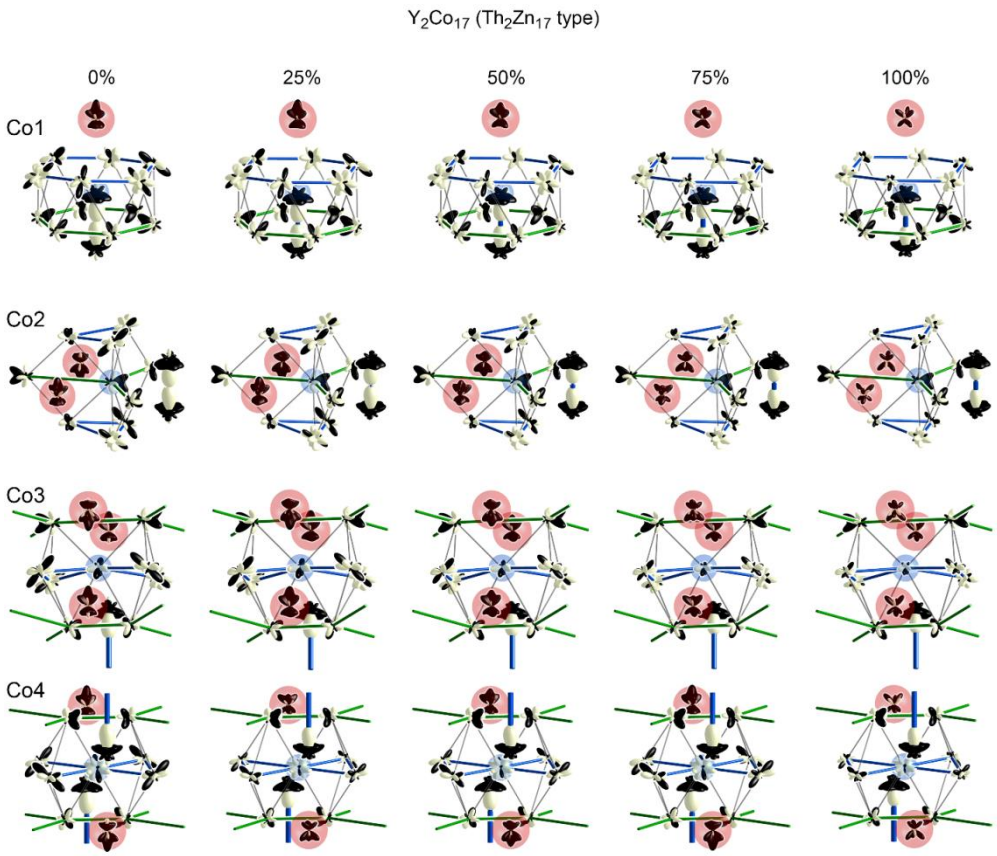

Figure D.5. Chemical pressure schemes for all Co sites in Y_2Co_{17} in the Th_2Zn_{17} type with spin-polarization. The results for 50% ionicity are shown in the main text.

Appendix E.

An enantiotropic disorder–partial order solid-state transformation in a molecular solid involving a phase with Z′=12

This chapter has been submitted: Vinokur, A. I.; Guzei, I. A.; Yakovenko, A.; Liu, L.; Schomaker, J. M., *Cryst. Growth Des*, *submitted*. Synthesis was done by Liu.L. Single crystal X-ray diffraction experiments were done by Vinokur A. I. The variable temperature Powder X-ray diffraction was done by Yakovenko, A.

E.1. Abstract

A structural study of the complex aminated stereotriads, [(*tert*-butyldimethylsilyl)oxy]-4-ethynyl-4-(1-fluorohexyl)-1,2,3-oxathiazocane-2,2-dione (**1**) and its reduced analogue, [(*tert*-butyldimethylsilyl)oxy]-4-ethenyl-4-(1-fluorohexyl)-1,2,3-oxathiazocane-2,2-dione (**2**), revealed a *k*12-type second-order phase transition in **1** and phase stability of **2** over the same temperature range. The observed phase change in **1** has been linked to the partial ordering of the extensive positional disorder of the high temperature phase upon cooling as revealed by single-crystal X-ray diffraction. The ordering breaks the translational symmetry, introduces differences in the molecular volumes of the packed species, and results in a low-temperature crystal structure with Z′=12. The *in situ* powder X-ray diffraction studies suggest that the transition occurs between 237 K and 180 K upon cooling, but complete amorphization in the range of 244–274 K complicated the assignment of the transition temperature upon heating. The observed loss of crystallinity has been linked to the phase transition and implies that the loss of long range order is due to the crystallites undergoing the transformation independent of one another. Furthermore, the observed ongoing changes in the cell

parameters at 100 K indicate the existence of a second low-temperature phase with potentially even higher Z′ value.

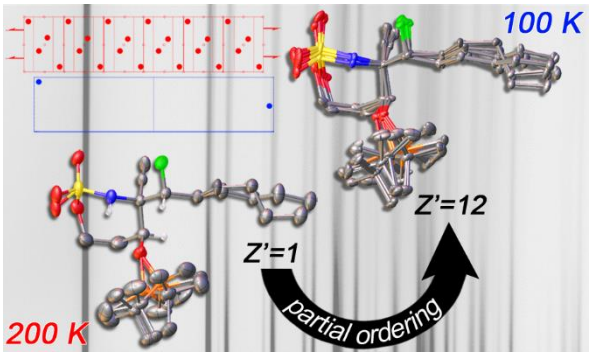

Figure E.0. An aminated stereotriad, [(*tert*-butyldimethylsilyl)oxy]-4-ethynyl-4-(1-fluorohexyl)-1,2,3-oxathiazocane-2,2-dione (**1**) undergoes a second-order phase transition over the temperature range of room temperature and 100 K. The transformation was linked to the partial ordering of the positional disorder of the high temperature phase, which yields a low temperature phase with Z′=12. *In situ* powder X-ray diffraction studies reveal amorphization during transition and a potential for a new phase below 100 K.

E.2. Introduction

Small molecule crystal structures with more than one molecule in the asymmetric unit constitute 9.3% of all entries reported to the Cambridge Structural Database (CSD, Version 5.37, May 2016).[1] The vast majority, 86%, of the encountered structures with Z′>1 consists of phases with Z′=2. The breakdown of the percentage of Z′>2 structures by the Z′ value is shown in Figure E.1. The frequency of occurrence for phases Z′>4 falls sharply and comprises less than 1% of the entries in the CSD. Only 46 structures of 39 unique

compounds with Z′≥12 have been reported to the CSD; there are only single instances of Z′=32 described by Kasai, et al.[2] for trimethyltin hydroxide and of the record holder of Z′=56 observed for 1,3,5-tris(4-carboxyphenyl)benzene by Zentner, et al.[3]

For many of the Z′>1 crystal structures, the chemically identical symmetry-independent molecules in the asymmetric unit are related by pseudosymmetry and exhibit minor conformational differences.[4] [5] Polymorphism occurs frequently in this group: 4.7% of the reported structures have known structurally characterized polymorphs.[6] These high rates of pseudosymmetry and polymorphism in crystal structures with multiple molecules in the asymmetric unit are believed to result from crystallization kinetics.[4, 7] J.W. Steed even described high Z′ structures as "fossil relics", kinetic metastable intermediates of a thermodynamically preferred lower Z′ polymorphs.[8]

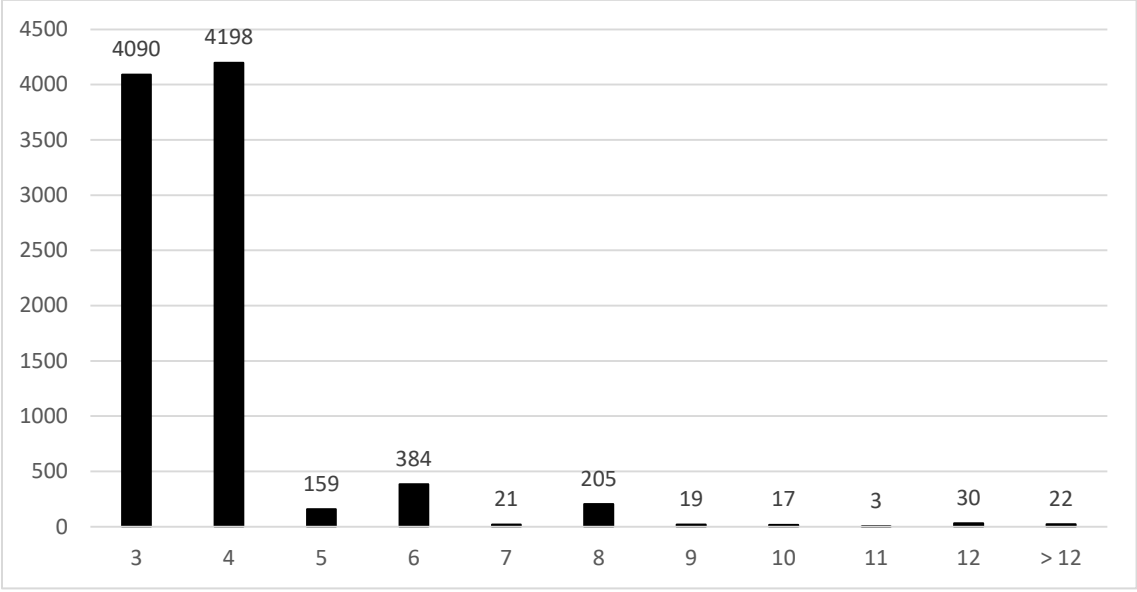

Figure E.1. Crystal structures for selected integer Z′ values. The number of high-Z structures falls dramatically above Z′= 4.

Kinetics also appear to play a role in several of the reported phase transitions in the high Z′ structures as exemplified by the phases in the Z′=12 group. Ordering of static or dynamic disorder caused by rotation of a functional group or a long chain was described in transformations of pyrrole-2,5-dithioamide[9] and ciclopirox.[10] In the case of ciclopirox, the various conformations arising from the rotation of the cyclohexyl group force changes in packing once there is insufficient thermal energy to sustain the dynamic disorder of the high temperature phase. Similarly, the positional disorder in the long carbon chain of the high temperature pyrrole-2,5-dithioamide phase resolves upon cooling into twelve molecules with various ordered chain conformations.

In addition to kinetics, statistical studies of the reported crystal structures in CSD revealed that several structural factors, such as extensive intermolecular bonding, low molecular symmetry, and molecular chirality leading to crystallization in a chiral space group, are correlated with high Z′. As a result, nucleosides,[8] nucleotides,[8, 11] steroids [12,13] and monoalcohols[14] have disproportionally high rates of crystal structures with more than one molecule in the asymmetric unit. It is proposed that molecules with a terminal alkynyl group exhibit a high number of high Z′ crystal structures due to the extensive hydrogen bonding[15].

Herein we report structural investigations of compounds that fit several criteria for adopting a high Z′ crystal structure: they possess several stereogenic carbons, low molecular symmetry, and one of them also contains a terminal alkynyl group. The molecules of interest, [(tert-butyldimethylsilyl)oxy]-4-ethynyl-4-(1-fluorohexyl)-1,2,3-oxathiazocane-2,2-dione (**1**) and its reduced congener, [(tert-butyldimethylsilyl)oxy]-4-

ethenyl-4-(1-fluorohexyl)-1,2,3-oxathiazocane-2,2-dione (**2**), Scheme 1, are precursors to analogues of bioactive molecules. Compounds **1** and **2** were synthesized as part of an effort to develop new methodology to transform allenes into complex aminated stereotriads with both heteroatoms and stereochemical diversity.[16]

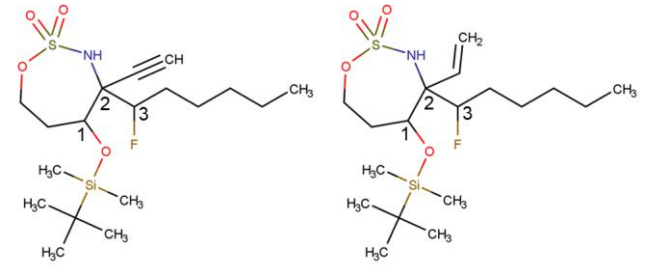

Figure E.2. The two observed stereoisomers for **1** and **2** are *SRR* and *RSS*.

Despite similarities between the two species, **1** exhibits extensive positional disorder in both of its polymorphs, whereas **2** is ordered in its one known phase. At room temperature, **1** exists in a $P2_1/c$, Z′=1 structure (phase I), but upon cooling it undergoes a non-destructive, enantiotropic, and reproducible second-order phase transition into a *Pc*, Z′=12 structure (phase II) with a six-fold increase in unit cell volume. Compound **2** exhibits no changes in crystal symmetry over the same temperature range. We link the phase transition and the high Z′ value in **1** to the partial ordering of the positional disorder upon cooling and subtle concomitant changes in the volume of individual molecules in the crystal leading to small positional modulation. The variable temperature powder X-ray diffraction results further suggest that the ordering continues below 100 K. Whereas the alkynyl group is not involved in hydrogen-bonding interactions, the

importance of its presence cannot be dismissed (even if it is incidental), as corroborated by the stability of the alkene analogue over the same temperature range.

E.3. Experimental Section

Synthesis and crystallization of $C_{18}H_{34}FNO_4SSi$ (1) The starting enesulfamate was prepared according to the published procedure.[17] The starting enesulfamate (0.400 g, 1.10 mmol, 1 equiv) was added to a flame-dried, 25 mL round-bottom flask. Selectfluor (0.589 g, 1.66 mmol, 1.5 equiv) was added, followed by 4 Å MS (0.589 g). Distilled CH_3NO_2 (11.0 mL) was then added to the same round-bottom flask to make a 0.1 M solution of the substrate. The reaction was stirred under nitrogen at 353 K. After 1 hour, the flask was removed from the oil bath and dry CH_2Cl_2 (40.0 mL) was added to the reaction. The resulting precipitate was removed by filtration through a pad of celite and concentrated by rotary evaporation to yield the imine. Dry THF (2.2 mL) was then added to the crude imine to furnish a 0.5 M solution. A solution of ethynyl magnesium bromide solution (0.5 M in THF) (6.6 mL, 3.30 mmol, 3 equiv) was cooled at 273 K for 15 min before use. The imine solution was then transferred to the cooled ethynyl magnesium bromide solution via cannulation. An additional 1 mL of dry THF was used to ensure quantitative transfer. The reaction was stirred at 273 K for 60 min until complete consumption of the starting material was observed by TLC (50% CH_2Cl_2/hexanes, $KMnO_4$ stain) then quenched through the addition of 20 mL of a saturated NH_4Cl solution. The mixture was transferred

to a separatory funnel, and the organic layer was extracted three times with portions of EtOAc, washed once with saturated NH_4Cl solution and once with brine. The organics were then dried over Na_2SO_4 and concentrated by rotary evaporation to yield a diastereomeric mixture of products. The product was purified by column chromatography (0%-100% CH_2Cl_2 in hexane, 1% Et_2O) to give the major diastereomer (0.314 g, 0.77 mmol, 70%) with an Rf = 0.3 (70% CH_2Cl_2 in hexane). ^{1}H NMR (500 MHz, $CDCl_3$) δ 5.36 (s, 1H), 4.65 (t, *J* = 12.2 Hz, 1H), 4.44 (ddd, *J* = 48.3, 10.4, 2.1 Hz, 1H), 4.23 (dd, *J* = 4.8, 1.8 Hz, 1H), 4.17 (ddd, *J* = 12.8, 4.2, 2.8 Hz, 1H), 2.78 (s, 1 H), 2.74 (ddt, *J* = 16.0, 11.6, 2.5 Hz, 1H), 1.72-2.00 (m, 3H), 1.55-1.65 (m, 1H), 1.27-1.41 (m, 5H), 0.87-0.96 (m, 12H), 0.10-0.12 (m, 6H). ^{13}C NMR (126 MHz, $CDCl_3$) δ 95.86 (d, J = 189.1 Hz), 80.60 (d, *J* = 1.2 Hz), 76.23 (d, *J* = 6.1 Hz), 73.71, 64.17, 60.70 (d, *J* = 19.0 Hz), 34.42, 31.46, 30.47 (d, *J* = 21.4 Hz), 25.77, 24.86 (d, *J* = 3.2 Hz), 22.47, 17.95, 13.95, 1.01, -4.18, -5.03, -5.05. ^{19}F NMR (471 MHz, $CDCl_3$) δ -191.34 (ddd, *J* = 48.8, 41.5, 13.5 Hz). HRMS (ESI) m/z calculated for $C_{18}H_{34}FNO_4SSi$ [M + NH_4^+] 425.2300, found 425.2299. Melting range: 381-383 K. IR: ν = 3354 (w), 3276 (w), 2928 (m), 2857 (w), 2127 (w), 1464 (w), 1417 (w), 1346 (m), 1260 (w), 1181 (s), 1090 (s), 999 (s), 934 (s), 873 (s), 834 (s), 802 (s), 772 (s), 720 (m), 674 (m),584 (m), 553 (m), 514 (m), 485 (m), 441 (m).

Synthesis and crystallization of $C_{18}H_{36}FNO_4SSi$ (2) The starting enesulfamate was prepared according to the published procedure.[17] The starting enesulfamate (0.351 g, 0.96 mmol, 1.0 equiv) was added to a 25 mL round-bottom flask, and Selectfluor (0.513 g, 1.44 mmol, 1.5 equiv), 4 Å MS (0.513 g, 1.5 equiv) were added to the same round-bottom flask. CH_3NO_2 (9.6 mL) was added to make a 0.1 M solution. The reaction was stirred at 353 K

under nitrogen for 1 h. Dry CH_2Cl_2 (40 mL) was added to the reaction until a precipitate was observed. The reaction mixture was then filtered through a pad of celite and concentrated by rotary evaporation to yield the crude imine product. Vinyl magnesium bromide (2.9 mL, 2.89 mmol, 3 equiv) was cooled at 195 K for at least 15 min prior to use. Dry THF (1.9 mL) was added to the imine to make a 0.5 M solution. The imine solution was then transferred to the cooled vinyl magnesium bromide via cannulation. The reaction was stirred at 195 K for 30 min until complete consumption of the starting material was observed by TLC (50% DCM/hex, $KMnO_4$ stain). The reaction was quenched by adding 20 mL of saturated NH_4Cl solution. The mixture was transferred to a separatory funnel, and the organic layer was extracted three times with EtOAc, washed once with saturated NH_4Cl solution and once with brine. The combined organics were dried over Na_2SO_4 and concentrated by rotary evaporation to yield a diastereomeric mixture of products. Purification by column chromatography (0%-100% DCM/hex, 1% Et_2O) gave the major diastereomer in 61% yield (0.2437 g, 0.59 mmol). ^{1}H NMR (500 MHz, $CDCl_3$) δ 6.17 (dd, *J* = 18.0, 11.5 Hz, 1H), 5.41 (d, *J* = 11.5 Hz, 1H), 5.29 (d, *J* = 17.7 Hz, 1H), 5.21 (s, 1H), 4.68 – 4.54 (m, 1H), 4.54 – 4.48 (m, 1H), 4.31 (d, *J* = 6.6 Hz, 1H), 4.12 (ddd, *J* = 12.7, 6.6, 2.4 Hz, 1H), 2.31 (dd, *J* = 15.9, 9.3 Hz, 1H), 2.08 (dt, *J* = 14.7, 6.5 Hz, 1H), 1.70 – 1.43 (m, 2H), 1.27 (tdd, *J* = 16.3, 10.4, 4.4 Hz, 6H), 0.91 (s, 9H), 0.87 (t, *J* = 6.9 Hz, 3H), 0.09-0.11 (m, 6H). ^{13}C NMR (126 MHz, $CDCl_3$) δ 133.84 (d, J = 4.3 pHz), 118.10, 96.01 (d, J = 185.3 Hz), 74.18, 66.22 (d, J = 16.3 Hz), 65.68, 53.44, 34.30 (d, J = 3.3 Hz), 31.41, 29.69 (d, J = 21.7 Hz), 25.79, 25.02 (d, J = 3.3 Hz), 22.44, 17.93, 13.93, 0.99, -4.07, -4.97. ^{19}F NMR (471 MHz, $CDCl_3$) δ -191.22 (td, J = 46.2, 13.2 Hz). HRMS (ESI) m/z calculated for $C_{18}H_{36}FNO_4SSi$ [M + H^+] 410.2191,

found 410.2187. Melting range: 344-347 K. IR: ν = 3339 (w), 2952 (w), 2926 (m), 2858 (w), 1466 (w), 1410 (m), 1344 (m), 1314 (m), 1256 (m), 1174 (s), 1088 (s), 1002 (s), 929 (s), 837 (s), 779 (s), 730 (m), 677 (w), 645 (w), 616 (w), 567 (m), 501 (s).

Single Crystal X-ray Diffraction. The data were collected by using the full sphere data collection routine to survey the reciprocal space to a resolution of 0.80 Å. Table E.1 summarizes the crystal data, data collection and structural refinement details for both phases of **1** and for **2**. For all structures, a successful solution by the direct methods provided most non-hydrogen atoms from the E-map. Alternating series of least-squares cycles and difference Fourier maps yielded the remaining non-hydrogen atoms. Unless stated otherwise, the non-hydrogen atoms were refined with anisotropic displacement parameters. All hydrogen atoms were included in the structure factor calculations at idealized positions and were allowed to ride on the neighboring atoms with relative isotropic displacement coefficients.

The high temperature structure of compound **1** (phase I) exhibited positional disorder. The fluorohexyl chain was disordered over two positions with the major component contributing 77.1(6) %. The disorder of the (*tert*-butyldimethylsilyl)oxy group was modelled as follows: atom O4 was split over two positions with the major component contributing 78.9(2) %; Si1 exhibited disorder over three positions with a ratio of 39.8(2):39.1(2):21.114(19); two positions of O2 were modelled with the major component present 72(6) % of the time.

The low temperature structure of compound **1**, the achiral phase II, was refined as an inversion twin with Flack x parameter of 0.387(16), consistent with both Hooft y =

0.384(8) and Parson's z = 0.376(12) parameters. The twin component ratio remained essentially invariant after cycling the test crystal through several phase transitions. There are 12 symmetry-independent molecules of **1** in the asymmetric unit. For all twelve molecules, the N–H distance was restrained to 0.860(3) Å. Six of the 12 symmetry independent molecules exhibit positional disorder either in the fluorohexyl chain or in the (*tert*-butyldimethylsilyl)oxy group. A detailed description of the treatment of the disorder in both phases can be found in the Supporting Information.

Table E.1. Crystallographic data for **1** and **2**.

Crystal data	**1** (phase I)	**1** (phase II)	**2**
Chemical formula	$C_{18}H_{34}FNO_4SSi$		$C_{18}H_{36}FNO_4SSi$
Mr	407.61		409.63
Crystal system, space group	Monoclinic, $P2_1/c$	Monoclinic, Pc	Monoclinic, $P2_1/c$
Temperature (K)	200	100	100
a, b, c (Å)	16.0697 (14), 10.0140 (7), 14.2762 (9)	15.7977 (14), 59.820 (5), 14.1775 (8)	7.712(3), 29.739(12), 10.654(5)
β (°)	97.805 (8)	97.574 (9)	110.599(19)
V (Å^3)	2276.1 (3)	13281.2(17)	2287.3(16)
Z, Z′	4, 1	24, 12	4, 1
Radiation type	Cu Kα		Mo Kα
μ (mm^{-1})	2.02	2.07	0.223
Crystal size (mm)	0.4 × 0.3 × 0.2		0.4 × 0.3 × 0.2
Diffractometer	Bruker SMART APEX2		Bruker Quazar APEX2
Absorption correction	Multi scan, SADABS2014/5 [23] (Bruker,2014/5) [18]		
T_{min}, T_{max}	0.583, 0.754	0.612, 0.750	0.6087, 0.7452
No. of measured,	33598, 4528, 4164	206894, 47817, 4290	30764, 4210,3010

independent and observed [$I > 2\sigma(I)$] reflections		8	
R_{int}	0.025	0.045	0.0880
$(\sin \theta/\lambda)_{max}$ ($Å^{-1}$)	0.621	0.622	0.602
$R[F^2 > 2\sigma(F^2)]$, $wR(F^2)$, S	0.052, 0.152, 1.03	0.055, 0.143, 1.01	0.0471,0.1189,1.023
No. of reflections	4528	47817	4210
No. of parameters	438	3045	245
No. of restraints	414	922	1
H-atom treatment	H atoms treated by a mixture of independent and constrained refinement		
$\Delta\rho_{max}$, $\Delta\rho_{min}$ (e/ $Å^{-3}$)	0.36, –0.32	1.07, –0.38	0.38, -0.31
Absolute structure	-	Inversion twin	-
Absolute structure parameter	-	0.387 (16)	-

***In Situ* Variable Temperature Powder X-ray Diffraction.** *In situ* variable temperature diffraction data for **1** were collected using the monochromatic X-rays available at the 17-BM (0.72768 Å) beamline (300 μm diameter beam size) at the Advanced Photon Source, Argonne National Laboratory, in combination with a Perkin-Elmer amorphous-Si flat panel detector. The sample was loaded into a 1.0 mm Kapton capillary, with glass wool on either side. The capillary was sealed on both sides and attached to the powder diffractometer, which was equipped with an Oxford Cryosystems Cryostream 700 plus, to perform an *in situ* PXRD experiment.

The temperature of the sample was decreased from ambient temperature (~300 K) to 100 K at the rate of 3 K/min. The sample was stabilized at that temperature for 20 min,

then warmed up to 400 K at the same rate. During the entire time, the powder diffraction data on the material were collected at a rate of one data point per minute.

The raw images were processed within GSAS-II,[24] refining the sample-to-detector distance and tilt of the detector relative to the beam based on the data obtained for a LaB_6 standard. [25] Collected and integrated *in situ* powder diffraction data sets were truncated, normalized, and plotted using 2DFLT software.[26]

The changes in the unit cell dimensions during the experiment were evaluated by sequential LeBail fits to the diffraction data with JANA2006.[27] The LeBail refinements were performed for patterns #0–20 (temperature region 300–240 K) using the starting unit cell parameters from the 200 K single-crystal experiment on **1** (phase I). The region between patterns #40 and #110 (180 K –~~1~~00 K–~~2~~26 K) was found to be best fitted by using phase II parameters only. For the first pattern of the run acquired at 100 K (pattern #67) the refinement was performed using the unit cell parameters from the 100 K single-crystal experiment. Once a satisfactory LeBail fit was achieved, other patterns were refined sequentially in the forward (#67–#110) and reverse orders (#67–#40). The region between patterns #21–39 was found to be best fitted by various combinations of both phase I and phase II unit cell parameters in the sequential LeBail refinements. Additional LeBail refinements were performed for patterns #135–155 (301–361 K) to find suitable unit cell parameters for phase I after material recrystallization. The region between patterns #111–134 (229–298 K) was difficult to refine due to a drastic loss in sample crystallinity.

Differential Scanning Calorimetry. Differential Scanning Calorimetry data for 1 were collected on a TA Differential Scanning Calorimeter Q2000. The heating rate was 10

K/min under a nitrogen gas flow rate of 50 mL/min over the range of 283–373 K, followed by heating at the rate of 2 K/min to 398 K. A melting event was observed at ~383 K. Subsequently, the sample was cooled at the rate of 10 K/min in the range of 283–263 K and then heated at a rate of 2 K/min up to 398 K. Again, only a melting event at ~383 K was observed. All data analyses were carried out with the TA Universal Analysis software.

E.4. Crystal structure description of 1 and 2

Compound **1** exists in the monoclinic space group $P2_1/c$ with Z′=1 (phase I) at RT. The molecule consists of a heterocycle, a *tert*-butyldimethylsilanolate protecting group (TBDMSO), a fluorohexyl chain ($C_6H_{12}F$), and an alkynyl group (Scheme 1). The molecule exhibits extensive positional disorder of both the TBDMSO and the $C_6H_{12}F$ chain, as well as of one of the sulphonyl oxygen atoms (Figure E.2a). The $C_6H_{12}F$ chain and the sulphonyl oxygen atom are disordered over two positions each, whereas the disorder of the TBDMSO was modelled with three conformations.

Upon cooling to 100 K, compound **1** undergoes a solid-state phase transition with a concomitant six-fold increase in the unit cell volume, *vide infra*. At 100 K, compound **1** has a monoclinic *Pc* structure (phase II) with 12 symmetry-independent molecules. The twelve molecules possess a variety of conformations of the TBDMSO and $C_6H_{12}F$ chain (Figure E.2b). Six of the twelve molecules also exhibit positional disorder in these functional groups. The increase in the Z′ value is consistent with a typical phase behavior

observed upon crystal cooling, when local order increases at the expense of the loss of symmetry.

Distinct groupings in the ranges of conformations can be identified for the TBDMSO and $C_6H_{12}F$ chain. In the case of the silyl protecting group, these conformations are grouped according to the location of the *t*-Bu group with respect to the fluorohexyl chain: "under" refers to the position of the *t*-Bu group under the chain, "middle" – nearly perpendicular to the chain and "out" refers to rotation of greater than 90°. The observed conformation for the fluorohexyl chain can be divided into two groups, depending on the positions of atom C17.

Table E2. Summary of spatial distribution of TBDMSO group in phases I and II.

	Phase II			Phase I		
Position of *tert*-butyl	under	middle	out	under	middle	out
∠ (C13-C10-Si1-C3) (°)	2.4-9.1	56.1-82.6	123.7-129.9	10.4	87.3	125.6
Occupancy	32.7%	44.2%	23.1%	21.6%	38.3%	40.1%
Molecular Volume (Å^3)	1361	1319	1268[a]	1427		

[a] Minor disorder components of fluorohexyl chain were excluded for this measurement.

Since the angles of rotation for the *t*-Bu group and the location of C17 show minimal changes between the two polymorphs, the spatial groupings of the conformations are visually similar in the two phases; however, the contributions of the major configurations vary. For phase I, the "middle" and "out" *tert*-butyl configurations have similar contributions, 38.3% and 40.1% respectively. In phase II, the contribution

from the "out" configuration in the twelve molecules drops by nearly half, yielding 23.1%, while the previously minor "in" contribution increases to 32.7% from 21.6%. The various configurational contributions for the TBDMSO are summarized in Table E.2.

Similarly, albeit not as dramatically, the major contribution in the fluorohexyl chain decreases from 77.1(6)% in the single phase I molecule to 68.0(15)% contribution in the twelve molecules of phase II (seven molecules fully occupied, one molecules with 61.1(7)% occupancy, one molecule with 33.0(9)%, and one molecule with 22.3(11)%).

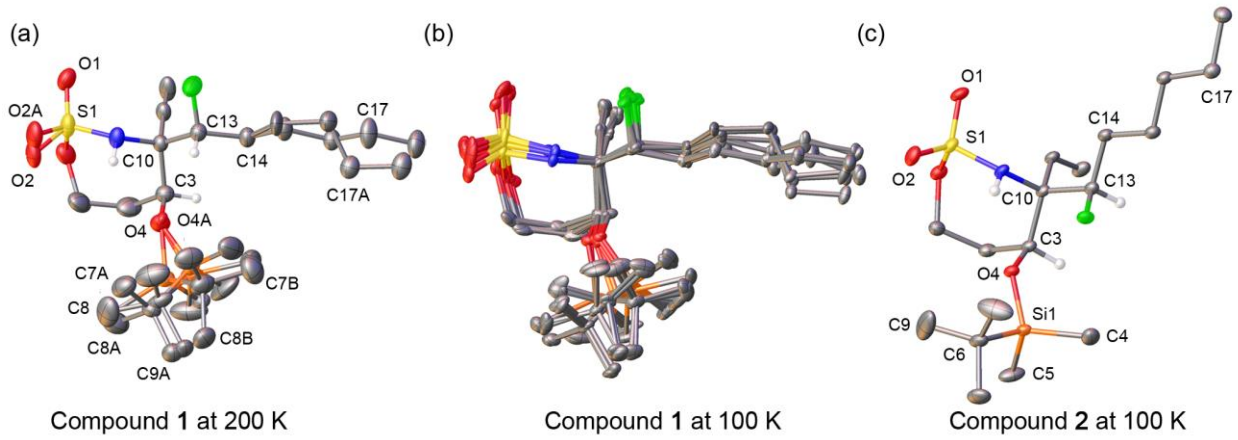

Figure E.3. Molecular drawings of compounds **1** and **2** shown with 50% probability ellipsoids. (a) The crystal structure of **1** at 200 K, phase I. All disorder components are shown. All hydrogen atoms, except on the stereogenic centers and the amine were omitted; (b) the crystal structure of **1** at 100 K, phase II. The twelve symmetry independent molecules are superimposed with the minor disorder components and all hydrogens omitted for clarity; (c) the crystal structure of **2** at 100 K. All hydrogen atoms, except on the stereogenic centers and amine are omitted.

Compound **2** bears many molecular and crystal structure similarities to compound **1** at 200 K. It has the same stereochemistry at the three anomeric carbon atoms C3, C10,

and C13. However, as can be seen in Figure E.2c, in addition to the geometrical changes associated with alkene group vs. an alkynyl group, the position of fluorine atom F1 in relation to the heterocycle drastically changes. The dihedral angle N1–C10–C13–F1 in **2** (58.7(3)°) is smaller than in corresponding angle in **1** (-179.77(15)°). The difference in the dihedral angles affects the molecular shape; even though both compound **2** and phase I of **1** (200 K) crystallize in monoclinic space group $P2_1/c$ with similar unit cell volumes, their axial lengths and beta angles differ. Finally, in contrast to compound **1**, the crystal structure of **2** shows no disorder (Figure E.2c) and retains the same crystal symmetry over the 100-298 K temperature range.

E.5. Crystal structure comparison of the two polymorphs of 1

Compound **1** exhibits different crystal symmetry at 200 K (phase I, $P2_1/c$, Z′=1) and at 100 K (phase II, *Pc*, Z′=12). The space group diagrams of both phases are compared in Figure E.3. In the high temperature phase I, there are four molecules in the unit cell. In the low temperature phase II, whose unit cell volume is six times larger due to a six-fold elongation of the *b* axis, there are 24 molecules, 12 of which are symmetry-independent and arranged in two columns of opposite handedness along *b*. During the phase transition, *vide infra*, the crystal lattice of phase II retains every sixth *c* glide plane of phase I, but loses its centrosymmetric nature, thereby eliminating the two-fold screw axis.

The breaking of the symmetry along the *b* axis is illustrated by the intermolecular distances (Figure E.3c). The S…S separation distances between the sulphur atoms in

adjacent molecules of phase II vary between 9.549(2)–10.448(2) Å with the average of 10.0(3) Å and the expected value of $b/6$ = 9.97 Å. This range is a substantial departure from the single S…S distance of 10.0140(7) Å observed in phase I.

It is instructive to examine the crystal packings of phases I and II, Figure E.4. The view along *b* (Figure E.4a) demonstrates the very similar arrangements of the molecules in the *ac* plane. This observation suggests that the phase transition leaves the symmetry of the *ac* plane essentially intact. On the other hand, the view along *c* (Figure E.4b) reveals the need to stack six phase I unit cells along *b* in order to match the unit cell size and molecular arrangement of phase II.

Whereas the average molecular positions of the packed species are comparable, as shown in Figure E.4a, the molecular conformations at each site differ in the two phases (Figures 4b,c). In fact, the presence of only six ordered molecules in phase II means that molecules previously related by inversion centers, glide planes, and screw axes in phase I no longer possess the same conformations or the same fragment disorder distributions, rendering them symmetry inequivalent.

The overlay of the calculated powder X-ray diffraction patterns of the two phases shown in Figure S1 further confirms the intimate relationship between phases I and II. The strongest reflections in the two patterns have similar positions, but there are additional super-structure peaks in phase II and the diffracted intensities vary. These observations are consistent with the packing overlay inspection (Figure E.4c). The supercell reflections appear as the centrosymmetric nature of phase I is lost, while the differences in the molecular conformations give rise to disparities in intensities. Phase II

can then be described as a six-fold supercell of phase I: the twenty-four molecules generated by the $P2_1/c$ symmetry for six phase I unit cells stacked along *b* correspond to the twenty-four molecules that reside in a single unit cell of *Pc* symmetry of phase II.

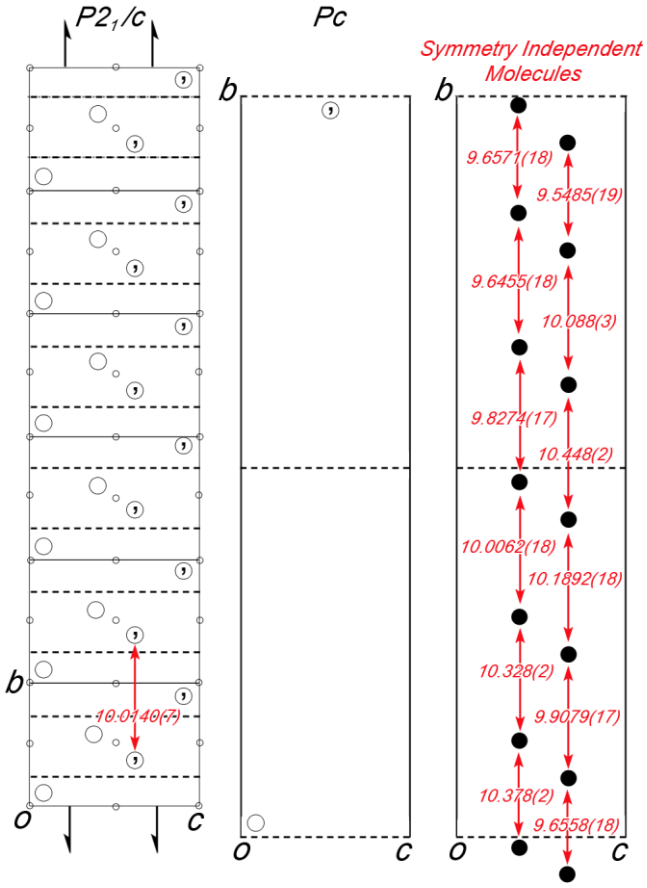

Figure E.4. Comparison of unit cells and S...S distances (shown in red) in phase I ($P2_1/c$ symmetry) and phase II (*Pc* symmetry) of **1**. (a) The space group diagram of the six unit cells of phase I. (b) The space group diagram of a unit cell of phase II. (c) Positions of the twelve symmetry independent molecules in phase II.

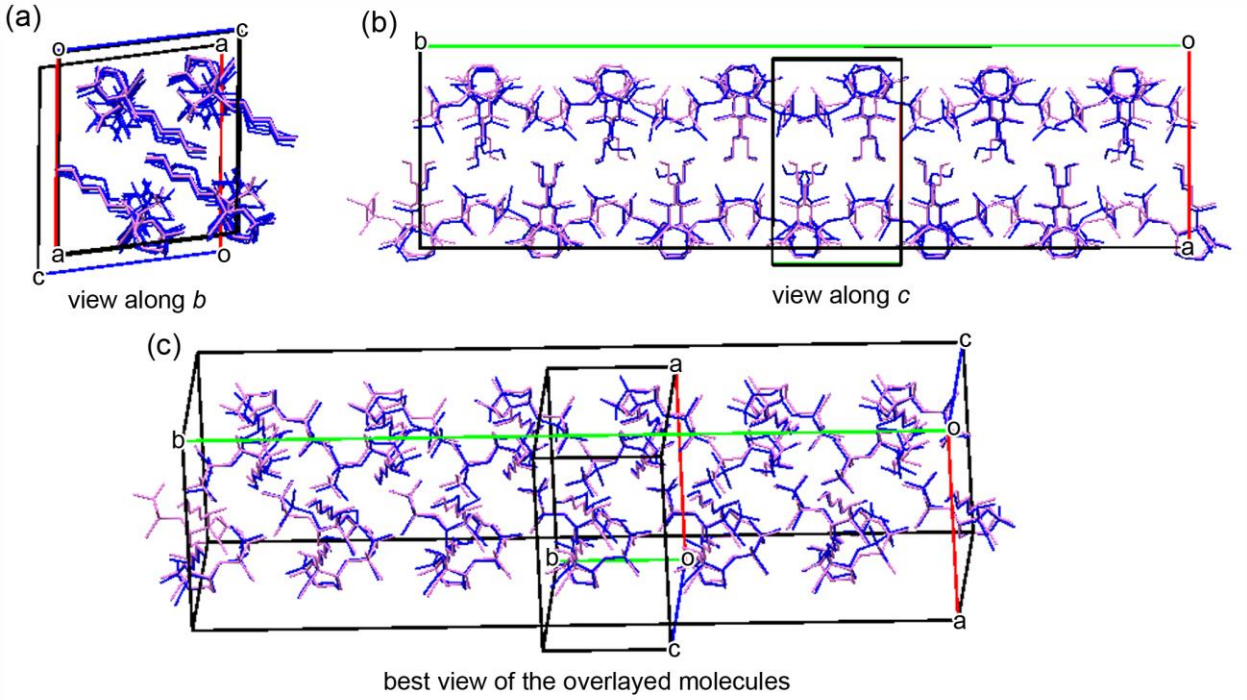

Figure E.5. Overlay of the packing of molecules in six unit cells of phase I (lilac) and one unit cell of phase II (blue). All minor disorder components have been omitted for clarity. Six molecules were found to be in common with a root mean square of 0.556. [28] (a) Projection of the overlaid unit cells along *b*. (b) Projection of the overlaid unit cells along *c*. (c) Projection of the overlaid unit cells along the least crowded direction.

The observed decrease in the symmetry from $P2_1/c$ to *Pc* can be attributed to the following related phenomena: disappearance (ordering) of positional disorder in the fluorohexyl chain and (*tert*-butyldimethylsilyl)oxy group at selected sites; changes in the conformational distribution of the disorder components at other sites; concomitant changes in the individual molecular volumes at all sites; subsequent unequal positional shifts of the individual molecules along the *b* axis.

E.6. Investigation of the phase transition by single-crystal and powder X-ray diffraction

The I→II phase transition was first identified by means of single-crystal X-ray diffraction. Initially, phase II was discovered during a routine structural examination of **1** at 100 K. The large magnitude of the *b* axial length and the arrangement of the twelve molecules into two columns of opposite handedness motivated us to conduct structural investigations of **1** at other temperatures. Collecting a data set at 200 K revealed a drastic reduction in the *b* cell constant dimension from 59.820(5) Å to 10.0140(7) Å and disappearance of supercell reflections.

The transition was further studied by unit cell determinations in 10–20 K intervals between 100 and 270 K. The temperature dependence of the *b* axial length is shown in Figure E.5. Upon heating from 100 K to 130 K there is a positive thermal expansion in the *b* direction, but at 140 K a discontinuity occurs. Following the sudden drop, the magnitude of *b* continuously increases to 270 K, suggesting a positive thermal expansion coefficient.

Surprisingly, the data collected at 120 K and 130 K could be indexed with the phase I unit cell parameters, despite the discontinuity observed slightly above 130 K. Whereas visual inspection of the diffracted intensities for these data sets indicated the presence of supercell reflections, they were not intense enough for harvesting and indexation. At 140 K, the supercell reflections could not be visually distinguished from the background. Thus, the onset of the transition I→II based on the single crystal data could begin at ~120 K and complete somewhere between 130 K and 140 K. No additional phase transformations

of **1** were identified with differential scanning calorimetry or single-crystal X-ray diffraction in the 100–383 K range.

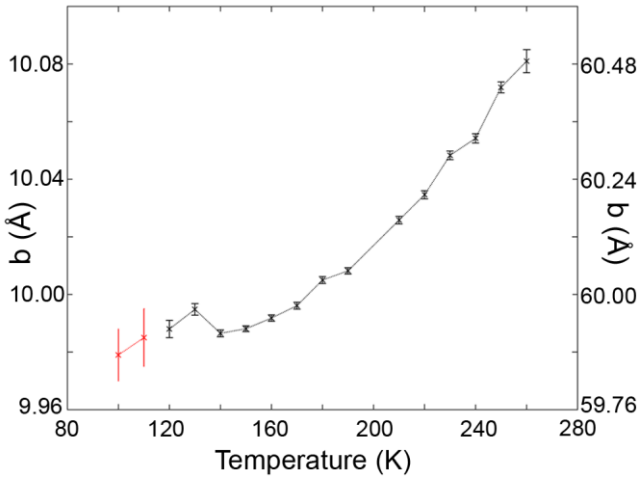

Figure E.6. Length of the *b* axis as a function of temperature shown as a graph with error bars. The red data points at 100 and 110 K were indexed with the larger cell (rightmost ordinate).

In order to corroborate the single crystal variable temperature results, additional *in situ* powder X-ray diffraction experiments were carried out at a synchrotron source. The powder sample was cooled from 300 K to 100 K at a rate of 3 K/min. After 20 minutes at 100 K, the sample was heated to 400 K at the same rate. The full range of the collected data is shown in the Supporting Information. As seen in Figure E.6a, upon the cool down, the intensity of the peaks begins to decrease, as illustrated by their diffuseness in the region between scan #20 and #40, which corresponds to the temperature range of 240 K and 180 K. The loss of peak intensity suggests loss of crystallinity within this region, which partially reverses upon continued cooling, but never recovers. This is illustrated by the comparison of the individual scans at 300 K and 100 K, where the intensity drops from

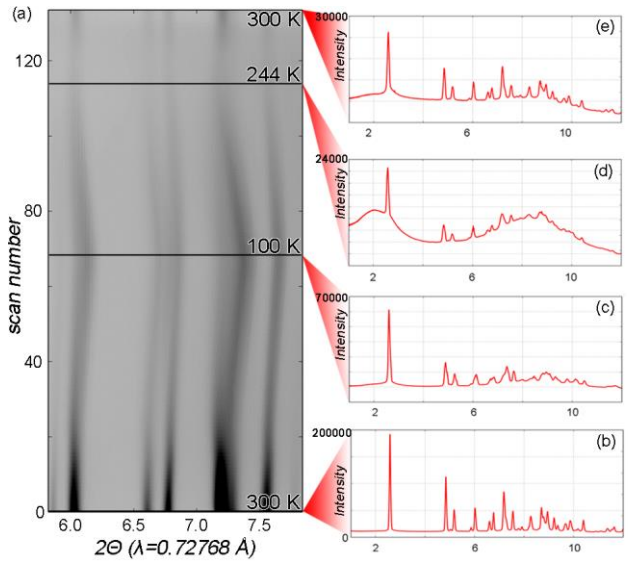

Figure E.7. Variable temperature powder X-ray diffraction results. (a) Full range of the measurement is shown as an overlay of 134 collected patterns acquired as the sample was cooled from 300 K to 100 K and then heated back to 300 K. The large, but gradual shifts, in the peak positions from 300 K to 100 K indicate a second order phase transition. (b) Initial powder X-ray diffraction pattern collected at 300 K. The high intensity of the peaks and the low background suggest crystalline material. (c) Powder X-ray diffraction pattern collected at 100 K upon cooling. The disappearance of some peaks and shifting of the remaining peaks are consistent with a phase transition. (d) Powder X-ray diffraction pattern collected at 244 K upon heating. The high background and the low intensity of the remaining peaks suggest loss of crystallinity. (e) Powder X-ray diffraction pattern collected at 300 K upon heating. The location of the peaks is comparable to the initial pattern, suggesting that the transition is reversible. The reduction in the background compared to (d) signals partial recovery of the sample's crystallinity.

200000 to 70000 counts (Figure E.6b and c). Simultaneously with the loss of crystallinity, the positions of the peaks begin to drastically change around scan #20. This observed

change in the rate of the thermal response of the sample unit cell parameters is indicative of a phase transition.

The patterns collected at 100 K before and after the 20 minute wait period appear to be identical. Upon heating, the trend in peak intensities reverses. The crystallinity gained upon cooling below 180 K is nearly completely lost in the region between scan #116 and #126 (244K and 274 K) as evidenced by the faintness of the observed peaks. Looking at the individual pattern at 244 K, the background dominates and the maximum intensity is recorded at 24000 counts (Figure E.6d). Above this region of the intense amorphization, crystallinity again partially returns (Figure E.6e). Relative shifts of the peak positions upon heating mirror the responses observed during cooling. Between 100 K and the region of amorphization (scans #67–116), the peak positions change noticeably. Above the region of amorphization, the positions remain nearly the same. The patterns collected initially at 300 K and after the temperature cycling appear similar (although the background increases after cycling), confirming the reversible nature of the observed phase transition.

The collected patterns were analyzed using sequential LeBail fits. Initially, patterns in the full range of the cool down (scans #0 through #67) were fit with parameters from phase I. The range, in reverse order, was then fit with parameters from phase II. The individual fits, as well as indicators of fit quality (R_p, R_{wp}, and GOF as functions of temperature), were evaluated to determine the regions of phase stability and the onset phase transition temperature. Based on the fits, the region from scan #0 and #15 can be best described with parameters from phase I. Within the region of scan #15-#20, early

signs of the transition emerge as unexplained peak broadening and shoulders. Scans #21–67 are poorly described by phase I. The region between scans #21–40 was poorly described by either of the phases and subsequent sequential LeBail fits with parameters from both phases yielded better results. The fit with two phases was also run in the scan range #15–20, but the presence of the shoulders was too weak to be refined as phase II. The best LeBail fits for region #41–67 are obtained for phase II. Thus, for the cooling part of the cycle, the onset transition temperature nominally is at 237 K, where we can confidently assign the presence of both phases, but the onset might be as early as 255 K if the visually observed shoulders are attributed to phase II. The transition is completed by 180 K. Below this temperature, there are no visual signs of phase I retention and the patterns are fit best by phase II alone. The regions of lost crystallinity match well with the regions described by the two phases indicating the possibility of the loss of the long-range order during the phase change.

The sequential LeBail analysis of the heating portion of the cycle is complicated by the amorphization in the region between 244–274 K. The presence of phase I was confirmed by fitting the region 301–361 K. Similarly, the presence of phase II was confirmed at 100 K after a 20 minute waiting period. If the trend observed upon cooling applies to the heating part of the cycle, the region of amorphization (244–274 K) is likely to be the region of phase transition. In this case the observed differences in the two transition regions (one with partial loss of crystallinity and the other with near-complete amorphization) are not a function of greater or lesser degree of amorphization. Rather, it is more likely that these are the function of the crystallinity of the sample at the

beginning of the transition for the sample showed greater crystallinity at 300 K than at 100 K.

Above 364 K, a complete loss of crystallinity is detected. This temperature is lower than the melt temp recorded by DSC, but different heating/cooling rates used for the two experiments may contribute to the disparity. Figure E.7 summarizes the results from the LeBail fit analysis and maps them onto the full cooling and heating range.

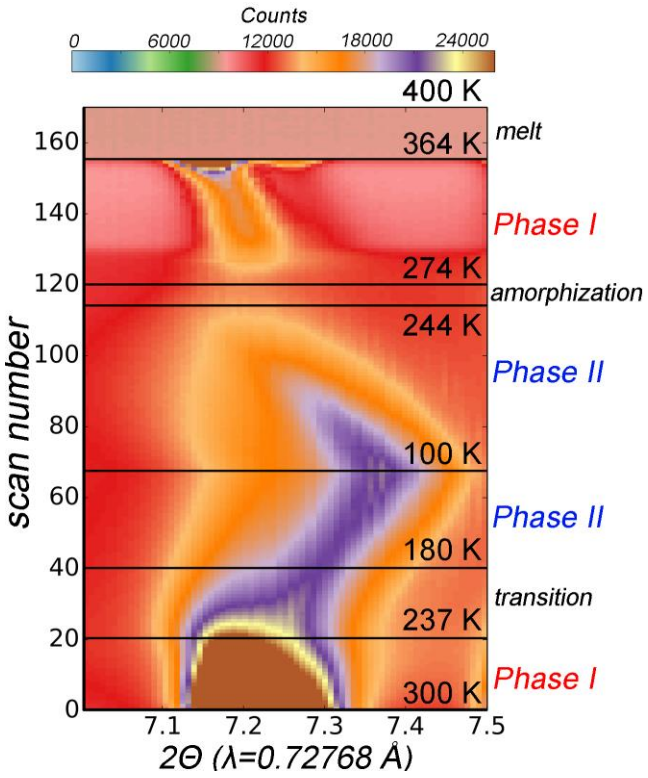

Figure E.8. *In situ* variable temperature powder X-ray diffraction results for the range 7-7.5°, which shows clearly the observed phase transition. The boundaries are marked according to results from sequential LeBail fitting of unit cell parameters from phase I, phase II or both.

E.7. Description and causes of the I–II transition

The gradual nature of the I–II phase transformation is characteristic of a second order transition. The transformation from space group $P2_1/c$ to Pc retains the crystal class and Pc is classified as a type I k minimal non-isomorphic subgroup of $P2_1/c$. The index of the transition is 12 as computed from eq (1), where i_k is the number of antiphase domains, i_l is the number of twin domains, Z is the number of molecules in the unit cell, and P is the order of the point group.[29] [30] Therefore, the observed I–II transition is assigned type $k12$.

$$\boldsymbol{i = i_k \times i_t = \frac{Z(H)}{Z(G)} \times \frac{|P(G)|}{|P(H)|} = \frac{Z(Pc)}{Z(P2_1/c)} \times \frac{P(P2_1/c)}{P(Pc)} = \frac{24}{4} \times \frac{4}{2} = 12} \qquad (1)$$

The changes in the relative orientation of the two polymorphs were evaluated with the TOPO program.[31] [32] The angles between the a^*, b^*, and c^* axial directions of the two phases differ by 0.56°, 0.35°, and 0.74°, respectively. These directional differences may or may not be structural. The structural interpretation of the change is favored by the fact that the two structures cannot be precisely overlaid. The 3DSEARCH algorithm[28] implemented in the Crystal Packing Similarity application of Mercury 3.7[28] could match only six molecules out of 20 with a RMSD = 0.556. The similarity overlay was computed for the major disorder components in each phase only, thus extensive disorder in both phases is a convincing reason for the inferior match. An alternative, non-structural explanation for random minor phase alignment discrepancies is that small variations in the crystal orientation on the diffractometer resulting from the temperature change.

What is the driving force for the observed changes in the crystal structure? As discussed previously, the three broad groupings of the conformation of the TBDMSO group in phase II match well in terms of location and orientation with the observed disorder components in phase I. The relative contributions of each conformation do change during the transformation, but the largest differences between phase I and phase II occurs in the values of the individual molecular volumes defined by the smallest box inscribing each molecule.

For phase I, the "molecular box" has a volume of 1427 $Å^3$, as all three possible conformations must be accommodated for every packed molecule. In phase II, the twelve symmetry independent molecules have different molecular volumes, ranging from 1268 $Å^3$ to 1361 $Å^3$, due to the multiple conformations of the six disordered molecules and distinct conformations of the fully ordered ones. We propose that without the thermal energy necessary to interconvert the different rotational conformers at all sites, the crystal assumes a different packing arrangement in order to accommodate the wider variety of shapes and sizes of the species in phase II. The difference in packing is best illustrated by the wide range of the S…S distances in phase II, which ultimately results in breaking of the twofold translational symmetry (Fig. 3). Therefore, the partial localization of conformational disorder at selected sites drives the phase transition and results in the high Z′ value. A similar mechanism has been observed in pyrrole-2,5-dithioamide[9] and ciclopirox.[10]

In the bulk sample, the results from the *in situ* powder X-ray diffraction experiments suggest that the process of ordering by which the transition occurs manifests

itself as a loss of long range order. Thus during the transition, the molecules within each crystallite order in a wide variety of positions and at different rates, independent of their neighbor crystallites. This would explain why it was possible to acquire a complete single-crystal dataset for phase I at 200 K, a temperature that falls within the phase transition region. The partial recrystallization above and below the transition region imply convergence in the spatial distribution of the molecular orderings, most likely due to the thermodynamic stability they offer. Under these circumstances, we can expect to observe a disagreement between the bounds of the phase transition in the variable temperature single crystal and the powder experiments as a single crystal provides a single instance of the transition, unique to the picked crystal, while the powder shows the average response.

We noted earlier that one of the literature explanations for a high Z′ value and polymorphism is the possibility of hydrogen-bonding interactions of the alkynyl group. Although there is an alkynyl group in **1**, it does not participate in hydrogen bonding in either phase, and thus could not be implicated in the phase transition or as the driving force of the high Z′ value. On the other hand, compound **2**, which lacks an alkynyl group, is ordered and exists as a single polymorph. This observation is either inconsequential or implies that the presence of alkynyl group is somehow relevant to the observed conformational change in molecules of **1** that cause the formation of different phases.

E.8. Conclusions

In summary, compound **1** undergoes a second-order, *k*12-type disorder–partial order phase transition upon cooling. The transition is in contrast to the stable, disorder-free crystal structure of its reduced analogue **2** over the same temperature range. The transition in **1** has been linked to the partial ordering of the positional disorder in the TBDMSO group and fluorohexyl chain upon cooling, which results in a low temperature phase II with Z′=12. The conformational changes vary among the different sites and this inhomogeneity of site localization renders previously symmetry-related molecules inequivalent. The differences in the molecular volumes associated with each rotational conformer cause positional shifts of the molecules, ultimately leading to a reduction of crystal symmetry from $P2_1/c$ to *Pc* and a six-fold supercell structure formation.

Initial investigation of the phase transition by variable temperature single-crystal X-ray diffraction suggested that the transition occurred in the window of 120–140 K due to the observed discontinuity in the *b* axial length. A subsequent *in situ* variable temperature powder X-ray diffraction studies revealed a gradual phase transition and suggested a presence of a third phase below 100 K with an even higher Z′ value as the ordering continues. Upon cooling, the nominal onset of the transition was determined to be at 237 K with completion at 180 K but some observations suggest that the transition occurs as early as 255 K. Upon heating, the near complete amorphization in the temperature region of 244 K to 274 K complicates the identification of the transition temperature range. We correlate the phase transition with the observed loss of the long range order, which could explain

the disagreement between the single crystal and the powder results as each crystallite transitions at a different temperature than its neighbors.

Finally, despite the previous investigations of the alkynyl-containing compounds associating alkynyl hydrogen bonding with high Z′ values, hydrogen bonding was not observed in **1.** However, it evidently still plays an important role in assisting in the positional disorder of the compound, as evidenced by the contrasting conformational stability of the alkene analogue **2**.

Acknowledgement

We thank Mr. Men Zhu (UW–Madison) for his assistance in acquiring DSC measurements. All single-crystal X-ray diffraction measurements were carried out in Molecular Structure Laboratory supported by Department of Chemistry and Graduate School of University of Wisconsin-Madison and the Bender fund. All variable temperature powder X-ray diffraction measurements were collected on 17 BM B at the Advanced Photon Source in Argonne National Laboratory.

E.9. References

1. Groom, C. R.; Bruno, I. J.; Lightfoot, M. P.; Ward, S. C., The Cambridge Structural Database. *Acta Crystallographica Section B* **2016,** *72* (2), 171-179.

2. Kasai, N.; Yasuda, K.; Okawara, R., The Crystal Structure of Trimethyltin Hydroxide. *J. Organomet. Chem.* **1965,** *3*, 172-173.

3. Zentner, C. A.; Lai, H. W.; Greenfield, J. T.; Wiscons, R. A.; Zeller, M.; Campana, C. F.; Talu, O.; FitzGerald, S. A.; Rowsell, J. L., High surface area and Z' in a thermally stable 8-fold polycatenated hydrogen-bonded framework. *Chem. Commun. (Camb.)* **2015,** *51* (58), 11642-5.

4. Das, D.; Banerjee, R.; Mondal, R.; Howard, J. A.; Boese, R.; Desiraju, G. R., Synthon evolution and unit cell evolution during crystallisation. A study of symmetry-independent molecules (Z' > 1) in crystals of some hydroxy compounds. *Chem. Commun. (Camb.)* **2006,** (5), 555-7.

5. Brock, C., High-Z' structures of organic molecules: their diversity and organizing principles. *Acta Crystallographica Section B* **2016,** *72* (6), 807-821.

6. Steed, K. M.; Steed, J. W., Packing problems: high Z' crystal structures and their relationship to cocrystals, inclusion compounds, and polymorphism. *Chem. Rev.* **2015,** *115* (8), 2895-933.

7. Davey, R. J.; Blagden, N.; Righini, S.; Alison, H.; Ferrari, E. S., Nucleation Control in Solution Mediated Polymorphic Phase Transformations: The Case of 2,6-Dihydroxybenzoic Acid. *J. Phys. Chem. B* **2002,** *106*, 1954-1959.

8. Steed, J. W., Should solid-state molecular packing have to obey the rules of crystallographic symmetry? *CrystEngComm* **2003,** *5* (32), 169-179.

9. Dobrzycki, L.; Zielinski, T.; Jurczak, J.; Wozniak, K., Structural aspects of phase transition in pyrrole-2,5-dithioamide single crystals. *Journal of Physical Organic Chemistry* **2005,** *18* (8), 864-869.

10. Brandel, C.; Cartigny, Y.; Couvrat, N.; Eusébio, M. E. S.; Canotilho, J.; Petit, S.; Coquerel, G., Mechanisms of Reversible Phase Transitions in Molecular Crystals: Case of Ciclopirox. *Chemistry of Materials* **2015,** *27* (18), 6360-6373.

11. Steiner, T., Frequency of Z' Values in Organic and Organometallic Crystal Structures. *Acta Crystallogr B* **2000,** *56*, 673-676.

12. Brock, C. P.; Stoilov, I.; Watt, D. S., A Steroid Derivative that Crystallizes with Three Molecules in the Asymmetric Unit. *Acta Cryst. C* **1994,** *50*, 434--438.

13. Hsu, L.; Nordman, C., Phase transition and crystal structure of the 37 degrees C form of cholesterol. *Science* **1983,** *220* (4597), 604-606.

14. Brock, C. P.; Duncan, L. L., Anomalous Space-Group Frequencies for Monoalcohols CnH,OH1. *Chem. Mater.* **1994,** *6*, 1307-1312.

15. Batsanov, A. S.; Collings, J. C.; Ward, R. M.; Goeta, A. E.; Porrès, L.; Beeby, A.; Howard, J. A. K.; Steed, J. W.; Marder, T. B., Crystal engineering with ethynylbenzenes : Part 2. Structures of 4-trimethylsilylethynyl-N,N-dimethylaniline, and 4-ethynyl-N,N-dimethylaniline with Z′ = 12 and a single-crystal to single-crystal phase transition at 122.5 ± 2 K. *CrystEngComm* **2006,** *8* (8), 622-628.

16. Adams, C. S.; Boralsky, L. A.; Guzei, I. A.; Schomaker, J. M., Modular functionalization of allenes to aminated stereotriads. *J. Am. Chem. Soc.* **2012,** *134* (26), 10807-10.

17. Adams, C. S.; Grigga, R. D.; Schomaker, J. M., *Chem. Sci.* **2014,** *5*, 3046-3056.

18. Bruker-AXS *APEX2*, Version 2014.11-0; Madison, Wisconsin, USA, 2014.

19. Sheldrick, G. M. *SADABS*, University of Göttingen: Germany, 1996.

20. Sheldrick, G. M., Crystal structure refinement with SHELXL. *Acta Crystallogr C* **2015,** *71*, 3-8.

21. Dolomanov, O. V.; Bourhis, L. J.; Gildea, R. J.; Howard, J. A. K.; Puschmann, H., *J. Appl. Crystallogr.* **2009,** *42*, 339-341.

22. Spek, A. L., *Acta Cryst. D* **2009,** *65*, 148-155.

23. *SADABS 2014/5*, Bruker AXS Inc.: Madison, WI, USA, 2014.

24. Toby, B. H.; Von Dreele, R. B., GSAS-II: the genesis of a modern open-source all purpose crystallography software package. *J. Appl. Crystallogr.* **2013,** *46* (2), 544-549.

25. Hammersley, A. P.; Svensson, S. O.; Hanfland, M.; Fitch, A. N.; Hausermann, D., Two-dimensional detector software: From real detector to idealised image or two-theta scan. *High Pressure Research* **1996,** *14* (4-6), 235-248.

26. Yakovenko, A. A. *2DFLT*, 3.4.3; Brookhaven National Laboratory: Upton, NY, USA, 2014.

27. Petříček, V.; Dušek, M.; Palatinus, L., Crystallographic Computing System JANA2006: General features. In *Zeitschrift für Kristallographie - Crystalline Materials*, 2014; Vol. 229, p 345.

28. Macrae, C. F.; Bruno, I. J.; Chisholm, J. A.; Edgington, P. R.; McCabe, P.; Pidcock, E.; Rodriguez-Monge, L.; Taylor, R.; van de Streek, J.; Wood, P. A., Mercury CSD 2.0-new features for the visualization and investigation of crystal structures. *J. Appl. Cryst.* **2008,** *41*, 466-470.

29. Ivantchev, S.; Kroumova, E.; Madariaga, G.; Perez-Mato, J. M.; Aroyo, M. I., SUBGROUPGRAPH : a computer program for analysis of group-subgroup relations between space groups. *Appl. Crystallogr.* **2000,** *33*, 1190-1191.

30. Guzei, I. A.; Mitra, A.; Spencer, L. C., Concomitant Twinning and POlymirphism of Ti (C5H4tBu)2Cl2. *Cryst. Growth Des.* **2009,** *9* (5), 2287-2292.

31. Posner, S. R.; Lorson, L. C.; Gell, A. R.; Foxman, B. M., Experimental Establishment of Mother–Daughter Orientation Relationships and Twinning Effects in Phase Transitions: A Great Legacy from Jack Gougoutas and Peggy Etter. *Crystal Growth & Design* **2015,** *15* (7), 3407-3416.

32. Foxman, B. Solid-State Reactions and Polymorphism of Molecular Crystals. http://people.brandeis.edu/~foxman1/.

Supporting Information

E.10. CRYSTALLOGRAPHIC REFINEMENT DETAILS

Phase I

The disorder in the (*tert*-butyldimethylsilyl)oxy moiety was initially modelled with an idealized geometry [19]. For final rounds of refinement, the idealized geometry was lifted and instead 1,2 and 1,3 bond distance restraints were used to ensure refinement convergence. The distances C3–O4 and C3–O4a were restrained to 1.417 Å. The disorder of the fluorohexyl chain was modelled with 1,2 and 1,3 bond distance restraints.

Phase II

Molecule A exhibited disorder of the (*tert*-butyldimethylsilyl)oxy group over three positions (denoted as A, L, and M) in the ratio of 56.4(3):30.5(3):13.1(2). Rigid bond restraints for 1,2 and 1,3 distances were applied to the (*tert*-butyldimethylsilyl)oxy group of components A and L. The anisotropic displacement parameters of Si1a, Si1l and Si1m were constrained to be the same. The anisotropic displacement parameters of the following pairs were constrained to be the same: C6l and C8l; C6l and C9l.

For molecule B, rigid bond restraints for 1,2 and 1,3 distances were applied to the (*tert*-butyldimethylsilyl)oxy group.

Molecule C exhibited disorder of the (*tert*-butyldimethylsilyl)oxy group over two positions (denoted as C and N) with the major component contributing 63.6(2)%. The anisotropic displacement parameters for Si1c and Si1n, C9c and C5n, as well as C4c and C4n were constrained to be pairwise the same. Rigid bond restraints for 1,2 and 1,3 distances were applied to O4, Si1, C3, C4, C5, C6, C7, C8 and C9 atoms of both components.

Molecule E exhibited a disorder of the fluorohexyl chain over two positions (denoted as E and P) with the major component contributing 77.6(11) %. The distances C14e–C15e and C14e–C15p were restrained to be the same. The anisotropic displacement parameters of C18e were restrained to approximate isotropic behaviour. Rigid bond restraints for 1,2 and 1,3 distances as well as 1,2 and 1,3 bond distance restraints were applied to the fluorohexyl chain. Finally, anisotropic displacement parameters were constrained to be the same for C15p, C16p, and C17p.

For molecule F, anisotropic displacement parameters were constrained to be the same for C6f and C7f, as well as for C1f and C2f.

Molecule G exhibited disorder of the (*tert*-butyldimethylsilyl)oxy group over two positions (denoted as G and R) with the major component contributing 92.6(9)%. The Si–C bond distances in both components were restrained to be the same. The C–C distances in the (*tert*-butyldimethylsilyl)oxy group in both components were restrained to be the same. Anisotropic displacement parameters for the following pairs were constrained to be the same: C17g and C18g; Si1g and Si1r; C9g and C9r; and C8g and C8r. Anisotropic displacement parameters for Si1g, C4g, and C4r were restrained to be equal in the direction of the bond. Rigid bond restraints for 1,2 and 1,3 distances were applied to both the (*tert*-butyldimethylsilyl)oxy group and the fluorohexyl chain.

For molecule H, anisotropic displacement parameters for Si1h and O4h were restrained to be equal in the direction of the bond.

Molecule J exhibited a disorder of the fluorohexyl chain over two positions (denoted as J and S) with the major component contributing 61.1(7) %. For both disorder components 1,2 and 1,3 bond distance restraints and rigid bond restraints were applied to the fluorohexyl chain. Anisotropic displacement parameters for C15j, C16j, C17j, and C17s were restrained to be equal. Anisotropic displacement parameters for C18j, C8c, and C4n were also restrained to be equal.

Molecule K exhibited a disorder of the fluorohexyl chain over two positions (denoted as K and T) with the major component contributing 67.0(9) %. For both disorder components 1,2 and 1,3 bond distance restraints and rigid bond restraints were

applied to the fluorohexyl chain. The bond distances Si1k–C5k and Si1k–C4k were restrained to be the same. The bond distances C17k–C18k and C16k–C17k were restrained to be the same. The anisotropic displacement parameters of the fluorohexyl chain in the K component were restrained to be the same. The anisotropic displacement parameters of C4k and C5k were restrained to approximate isotropic behaviour. The anisotropic displacement parameters of C14k and C15k were constrained to be the same. The anisotropic displacement parameters of C15t–C18t were constrained to be the same.

E.11. CRYSTALLOGRAPHIC TABLES

Table E.3. Refined atomic coordinates ($\times 10^4$) and equivalent isotropic displacement parameters ($Å^2 \times 10^3$) for 1 Phase I.

Atom	*x*	*y*	*z*	U(eq)	Atom	*x*	*y*	*z*	U(eq)
S1	8864.9(3)	939.8(6)	6927.0(3)	62.8(2)	C9A	7035(11)	7976(11)	6610(11)	73(3)
F1	6965.0(8)	625.7(13)	4788.2(10)	75.7(4)	O2A	8631(11)	970(20)	7846(6)	86(3)
O1	9053.4(11)	-357.8(16)	6620.6(11)	74.5(4)	O4A	7863(7)	4202(8)	5774(9)	50(3)
O2	8815(15)	1510(50)	7884(10)	77(5)	C4B	8391(9)	6771(14)	5056(8)	57(3)
O3	9657.2(9)	1752.5(17)	6747.7(11)	73.2(4)	Si1B	7860.7(19)	5891(2)	5981(3)	53.3(8)
N1	8085.0(9)	1588.2(16)	6244.2(10)	50.9(4)	C5B	8238(9)	6494(16)	7224(7)	52(3)
C1	9578.6(19)	3207(3)	6733(2)	95.3(9)	C6B	6720(5)	6267(9)	5720(8)	82(3)
C2	9354.3(16)	3672(3)	5736(2)	84.4(7)	C7B	6469(10)	6170(20)	4621(9)	112(6)
C3	8440.9(11)	3515.0(18)	5281.9(14)	53.3(4)	C8B	6562(9)	7766(11)	6033(12)	88(4)
O4	7910(3)	4287(3)	5791(4)	64.3(14)	C9B	6168(7)	5404(13)	6146(12)	93(4)
C4	6855(8)	5941(10)	4434(7)	131(5)	C10	8121.9(10)	2052.4(16)	5265.5(11)	41.7(3)
Si1	7708(3)	5940(2)	5473(2)	58.3(6)	C11	8668.5(12)	1206.1(19)	4771.1(11)	49.9(4)
C5	8626(8)	6977(13)	5263(11)	123(5)	C12	9118.3(15)	604(3)	4345.7(14)	72.5(7)
C6	7247(6)	6457(10)	6534(6)	79(3)	C13	7209.4(11)	1969.1(18)	4772.5(13)	49.4(4)
C7	6918(12)	7933(11)	6386(11)	74(4)	C14	7063.2(13)	2443(2)	3760.9(13)	58.5(5)
C8	7990(8)	6418(18)	7406(7)	118(5)	C15	6168.8(18)	2429(6)	3291(3)	64.3(11)
C9	6605(8)	5639(10)	6855(10)	120(4)	C16	6056.9(17)	3059(4)	2324.4(19)	58.1(8)
C4A	7906(8)	6548(9)	4662(7)	127(4)	C17	5158.1(19)	3095(5)	1874(2)	86.7(13)
Si1A	7363.5(18)	5695(2)	5565.2(19)	63.4(6)	C18	5028(3)	3725(5)	912(3)	93.8(14)

C5A	6203(5)	5412(9)	5121(9)	117(3)	C15A	6091(7)	2220(20)	3475(11)	91(5)
C6A	7403(5)	6640(10)	6684(5)	55.0(18)	C16A	5692(9)	2502(10)	2477(8)	79(3)
C7A	6983(7)	5782(9)	7388(6)	94(3)	C17A	5720(7)	3941(10)	2215(7)	70(3)
C8A	8375(8)	6799(16)	7107(9)	112(5)	C18A	5289(10)	4249(16)	1239(9)	87(4)

Table E.4. Anisotropic displacement parameters ($Å^2 \times 10^3$) for 1 phase I.

Atom	U_{11}	U_{22}	U_{33}	U_{23}	U_{13}	U_{12}
S1	66.5(3)	83.9(4)	36.7(3)	5.1(2)	2.1(2)	22.4(2)
F1	66.5(7)	64.1(7)	89.2(9)	18.7(6)	-15.5(6)	-16.7(6)
O1	86.4(10)	68.1(9)	66.5(9)	14.2(7)	1.1(8)	22.1(8)
O2	78(6)	116(13)	34(3)	-1(4)	1(3)	24(6)
O3	59.9(8)	80.5(10)	73.1(9)	-16.4(8)	-12.8(7)	11.8(7)
N1	52.1(8)	64.8(9)	36.8(7)	4.7(6)	10.0(6)	13.4(7)
C1	86.9(17)	75.7(16)	109(2)	-24.2(14)	-37.8(15)	0.5(13)
C2	66.8(13)	63.5(13)	118(2)	-5.5(13)	-3.9(13)	-15.4(11)
C3	59(1)	46.5(9)	54.6(10)	-1.8(7)	8.5(8)	0.7(8)
O4	82(2)	50.6(18)	59(3)	-9.9(16)	7(2)	16.3(15)
C4	196(11)	79(5)	101(6)	-9(5)	-45(7)	50(7)
Si1	94.0(18)	37.6(9)	46.7(12)	1.7(8)	21.4(13)	1.1(9)
C5	147(9)	66(5)	176(12)	-26(6)	92(8)	-21(5)
C6	112(7)	39(4)	95(5)	13(4)	50(5)	22(4)
C7	104(10)	47(4)	66(8)	-5(4)	0(6)	27(5)
C8	160(9)	143(11)	56(4)	-6(5)	27(5)	49(8)
C9	156(9)	77(5)	147(10)	8(7)	88(8)	6(6)
C4A	212(11)	73(5)	107(6)	47(5)	66(7)	43(6)
Si1A	93.6(17)	46.4(11)	47.8(10)	5.0(8)	0.3(12)	19.8(11)
C5A	93(5)	88(5)	152(8)	-23(5)	-46(5)	29(4)
C6A	70(3)	41(3)	53(3)	-10(2)	5(2)	-4(2)
C7A	142(7)	68(4)	78(5)	9(4)	32(5)	9(4)
C8A	108(6)	88(8)	131(10)	-21(7)	-22(5)	-6(5)
C9A	92(6)	56(4)	70(7)	-5(3)	5(5)	14(4)
O2A	102(4)	119(7)	37.4(14)	7(2)	9(2)	34(5)
O4A	78(7)	36(5)	33(6)	6(4)	-5(5)	12(4)
C4B	81(7)	40(6)	51(5)	3(5)	16(5)	-3(5)
Si1B	60.2(17)	38.9(12)	58(2)	2.6(12)	-2.3(15)	-0.9(10)
C5B	65(7)	60(7)	29(4)	3(4)	3(4)	-7(6)
C6B	76(5)	58(5)	110(7)	2(5)	6(4)	18(4)
C7B	89(10)	139(16)	98(8)	-15(7)	-18(6)	6(9)
C8B	98(10)	65(6)	98(11)	3(6)	-4(8)	28(6)
C9B	67(6)	72(6)	142(11)	-7(7)	20(6)	21(5)

C10	46.1(8)	44.6(8)	34.6(7)	-0.5(6)	6.2(6)	4.3(6)
C11	57.2(10)	56.6(10)	34.9(8)	-2.2(7)	2.4(7)	11.4(8)
C12	82.5(14)	93.8(16)	40.3(9)	-7.3(10)	4.9(9)	39.2(12)
C13	49.6(9)	50.2(9)	47.3(9)	2.3(7)	1.8(7)	3.4(7)
C14	66.1(11)	61.9(11)	44.9(9)	0.1(8)	-2.4(8)	10.6(9)
C15	55.5(16)	85(3)	50.1(18)	4.6(17)	0.3(13)	16.2(14)
C16	53.1(15)	67.7(19)	51.6(14)	5.7(12)	0.3(11)	4.4(13)
C17	52.4(16)	141(3)	64.0(18)	21.4(19)	-2.8(13)	16.6(18)
C18	83(3)	117(4)	73(2)	24(2)	-19(2)	9(2)
C15A	109(7)	92(10)	56(7)	14(6)	-42(6)	13(6)
C16A	89(8)	67(6)	69(6)	1(4)	-24(5)	10(5)
C17A	64(6)	78(6)	66(5)	9(4)	6(4)	7(5)
C18A	76(8)	109(10)	76(7)	20(6)	7(6)	18(7)

Table E5. Bond Lengths for 1 phase I.

Atom	Atom	Length/Å	Atom	Atom	Length/Å
S1	O1	1.4169(17)	Si1A	C6A	1.850(6)
S1	O2	1.492(18)	C6A	C7A	1.546(10)
S1	O3	1.5613(19)	C6A	C8A	1.603(10)
S1	N1	1.6157(15)	C6A	C9A	1.460(11)
S1	O2A	1.414(5)	O4A	Si1B	1.717(7)
F1	C13	1.402(2)	C4B	Si1B	1.885(8)
O3	C1	1.462(3)	Si1B	C5B	1.894(9)
N1	C10	1.481(2)	Si1B	C6B	1.858(7)
C1	C2	1.494(4)	C6B	C7B	1.569(12)
C2	C3	1.530(3)	C6B	C8B	1.597(11)
C3	O4	1.421(2)	C6B	C9B	1.432(11)
C3	O4A	1.417(4)	C10	C11	1.468(2)
C3	C10	1.551(2)	C10	C13	1.540(2)
O4	Si1	1.736(4)	C11	C12	1.172(3)
O4	Si1A	1.670(4)	C13	C14	1.508(3)
C4	Si1	1.877(8)	C14	C15	1.501(3)
Si1	C5	1.861(8)	C14	C15A	1.576(9)
Si1	C6	1.848(6)	C15	C16	1.506(4)
C6	C7	1.575(11)	C16	C17	1.500(4)
C6	C8	1.604(10)	C17	C18	1.499(5)
C6	C9	1.441(11)	C15A	C16A	1.508(9)
C4A	Si1A	1.859(7)	C16A	C17A	1.491(9)
Si1A	C5A	1.907(7)	C17A	C18A	1.502(10)

Table E6. Bond angle for 1 phase I.

Atom	Atom	Atom	Angle/°	Atom	Atom	Atom	Angle/°
O1	S1	O2	132.2(17)	C7A	C6A	C8A	107.4(8)
O1	S1	O3	102.36(10)	C8A	C6A	Si1A	107.1(6)
O1	S1	N1	111.29(9)	C9A	C6A	Si1A	116.1(7)
O2	S1	O3	95.6(18)	C9A	C6A	C7A	110.3(7)
O2	S1	N1	105.4(8)	C9A	C6A	C8A	107.5(9)
O3	S1	N1	105.94(9)	C3	O4A	Si1B	125.5(6)
O2A	S1	O1	113.8(9)	O4A	Si1B	C4B	109.2(5)
O2A	S1	O3	117.7(11)	O4A	Si1B	C5B	117.9(7)
O2A	S1	N1	105.5(4)	O4A	Si1B	C6B	101.0(5)
C1	O3	S1	116.80(17)	C4B	Si1B	C5B	112.9(6)
C10	N1	S1	124.62(11)	C6B	Si1B	C4B	107.0(5)
O3	C1	C2	109.5(2)	C6B	Si1B	C5B	107.7(5)
C1	C2	C3	117.7(2)	C7B	C6B	Si1B	107.5(8)
C2	C3	C10	113.54(16)	C7B	C6B	C8B	108.0(9)
O4	C3	C2	109.6(3)	C8B	C6B	Si1B	109.0(7)
O4	C3	C10	107.53(19)	C9B	C6B	Si1B	116.4(7)
O4A	C3	C2	113.3(6)	C9B	C6B	C7B	107.3(9)
O4A	C3	C10	103.2(4)	C9B	C6B	C8B	108.5(9)
C3	O4	Si1	119.3(3)	N1	C10	C3	109.73(14)
C3	O4	Si1A	134.2(3)	N1	C10	C13	104.86(13)
O4	Si1	C4	107.3(4)	C11	C10	N1	112.05(13)
O4	Si1	C5	116.7(5)	C11	C10	C3	109.52(14)
O4	Si1	C6	97.7(4)	C11	C10	C13	110.10(14)
C5	Si1	C4	112.5(6)	C13	C10	C3	110.50(14)
C6	Si1	C4	108.5(5)	C12	C11	C10	175.6(2)
C6	Si1	C5	113.0(5)	F1	C13	C10	107.21(13)
C7	C6	Si1	108.5(8)	F1	C13	C14	108.02(15)
C7	C6	C8	109.2(9)	C14	C13	C10	115.82(15)
C8	C6	Si1	106.9(6)	C13	C14	C15A	102.9(5)
C9	C6	Si1	119.0(7)	C15	C14	C13	116.1(2)
C9	C6	C7	109.5(7)	C14	C15	C16	113.2(3)
C9	C6	C8	103.3(9)	C17	C16	C15	113.0(3)
C4A	Si1A	C5A	111.5(5)	C18	C17	C16	114.1(3)
C6A	Si1A	C4A	113.5(5)	C16A	C15A	C14	119.8(10)
C6A	Si1A	C5A	106.3(4)	C17A	C16A	C15A	113.3(11)
C7A	C6A	Si1A	108.0(6)	C16A	C17A	C18A	113.9(9)

Table E.7. Torsion Angles for 1 phase I.

A	B	C	D	Angle/°	A	B	C	D	Angle/°
S1	O3	C1	C2	-94.9(3)	C4	Si1	C6	C8	179.0(8)
S1	N1	C10	C3	-86.37(17)	C4	Si1	C6	C9	62.7(10)
S1	N1	C10	C11	35.5(2)	C5	Si1	C6	C7	62.0(10)
S1	N1	C10	C13	154.94(13)	C5	Si1	C6	C8	-55.6(10)
F1	C13	C14	C15	62.8(3)	C5	Si1	C6	C9	-172.0(10)
F1	C13	C14	C15A	59.4(10)	C4A	Si1A	C6A	C7A	-176.4(6)
O1	S1	O3	C1	163.12(16)	C4A	Si1A	C6A	C8A	-61.0(8)
O1	S1	N1	C10	-71.18(17)	C4A	Si1A	C6A	C9A	59.1(9)
O2	S1	O3	C1	-61.4(13)	C5A	Si1A	C6A	C7A	60.6(7)
O2	S1	N1	C10	140(2)	C5A	Si1A	C6A	C8A	176.0(7)
O3	S1	N1	C10	39.32(17)	C5A	Si1A	C6A	C9A	-63.9(10)
O3	C1	C2	C3	77.9(3)	O2A	S1	O3	C1	-71.3(5)
N1	S1	O3	C1	46.43(18)	O2A	S1	N1	C10	164.9(12)
N1	C10	C13	F1	-61.60(17)	O4A	C3	C10	N1	-56.5(7)
N1	C10	C13	C14	177.76(15)	O4A	C3	C10	C11	-179.9(6)
C1	C2	C3	O4	62.2(3)	O4A	C3	C10	C13	58.7(7)
C1	C2	C3	O4A	59.2(5)	O4A	Si1B	C6B	C7B	-72.4(10)
C1	C2	C3	C10	-58.1(3)	O4A	Si1B	C6B	C8B	170.9(9)
C2	C3	O4	Si1	88.9(4)	O4A	Si1B	C6B	C9B	47.9(10)
C2	C3	O4A	Si1B	59.5(12)	C4B	Si1B	C6B	C7B	41.8(11)
C2	C3	C10	N1	66.6(2)	C4B	Si1B	C6B	C8B	-75.0(10)
C2	C3	C10	C11	-56.8(2)	C4B	Si1B	C6B	C9B	162.1(10)
C2	C3	C10	C13	-178.29(18)	C5B	Si1B	C6B	C7B	163.5(10)
C3	O4	Si1	C4	81.4(6)	C5B	Si1B	C6B	C8B	46.7(10)
C3	O4	Si1	C5	-45.9(7)	C5B	Si1B	C6B	C9B	-76.3(10)
C3	O4	Si1	C6	-166.5(5)	C10	C3	O4	Si1	-147.3(3)
C3	O4A	Si1B	C4B	24.4(14)	C10	C3	O4A	Si1B	-177.2(9)
C3	O4A	Si1B	C5B	-106.2(12)	C10	C13	C14	C15	-177.0(3)
C3	O4A	Si1B	C6B	136.9(11)	C10	C13	C14	C15A	179.6(10)
C3	C10	C13	F1	-179.78(14)	C11	C10	C13	F1	59.11(18)
C3	C10	C13	C14	59.58(19)	C11	C10	C13	C14	-61.5(2)
O4	C3	C10	N1	-54.8(3)	C13	C14	C15	C16	173.4(3)
O4	C3	C10	C11	-178.2(3)	C13	C14	C15A	C16A	-176.5(15)
O4	C3	C10	C13	60.3(3)	C14	C15	C16	C17	-177.6(4)
O4	Si1	C6	C7	-174.6(8)	C14	C15A	C16A	C17A	-65(2)
O4	Si1	C6	C8	67.8(8)	C15	C16	C17	C18	179.7(4)
O4	Si1	C6	C9	-48.6(9)	C15A	C16A	C17A	C18A	-177.3(12)
C4	Si1	C6	C7	-63.4(9)					

Table E.8. Hydrogen Atom Coordinates (Å×10⁴) and Isotropic Displacement Parameters (Å²×10³) for 1 phase I.

Atom	*x*	*y*	*z*	U(eq)	Atom	*x*	*y*	*z*	U(eq)
H1	7857	2218	6556	61	H5BB	8525	7354	7195	78
H1A	10116	3617	7011	114	H5BC	8629	5840	7549	78
H1B	9138	3484	7114	114	H7BA	6862	6697	4305	167
H2A	9713	3184	5339	101	H7BB	5898	6517	4450	167
H2B	9503	4629	5712	101	H7BC	6489	5235	4424	167
H3A	8388	3854	4617	64	H8BA	6739	7862	6714	133
H3B	8385	3858	4618	64	H8BB	5963	7977	5888	133
H4A	7070	5553	3885	197	H8BC	6886	8380	5689	133
H4B	6671	6860	4290	197	H9BA	6453	5082	6755	139
H4C	6379	5410	4586	197	H9BB	6011	4642	5729	139
H5A	9063	6913	5810	185	H9BC	5661	5899	6247	139
H5B	8449	7910	5170	185	H12	9483	116	4001	87
H5C	8847	6655	4698	185	H13	6844	2502	5147	59
H7A	7394	8533	6344	110	H14A	7279	3367	3740	70
H7B	6632	8198	6921	110	H14B	7400	1877	3385	70
H7C	6524	7988	5800	110	H14C	7392	1909	3357	70
H8A	8518	6179	7177	178	H14D	7213	3397	3713	70
H8B	7859	5752	7868	178	H15A	5816	2912	3697	77
H8C	8047	7298	7707	178	H15B	5969	1493	3235	77
H9A	6134	5545	6345	180	H16A	6278	3982	2377	70
H9B	6407	6060	7404	180	H16B	6391	2552	1911	70
H9C	6836	4755	7033	180	H17A	4939	2170	1822	104
H4AA	7809	6049	4067	190	H17B	4825	3595	2293	104
H4AB	8510	6589	4883	190	H18A	5271	3150	464	141
H4AC	7684	7456	4561	190	H18B	5304	4599	940	141
H5AA	5890	6237	5191	175	H18C	4426	3835	705	141
H5AB	5986	4700	5492	175	H15C	5970	1276	3613	109
H5AC	6138	5153	4453	175	H15D	5798	2775	3901	109
H7AA	6385	5672	7151	141	H16C	5985	1974	2034	94
H7AB	7043	6226	8005	141	H16D	5100	2205	2402	94
H7AC	7253	4903	7453	141	H17C	6314	4225	2262	84
H8AA	8587	5948	7384	169	H17D	5453	4472	2678	84
H8AB	8433	7491	7597	169	H18D	5649	3971	772	131
H8AC	8698	7054	6601	169	H18E	5184	5212	1181	131
H9AA	7277	8487	6128	110	H18F	4755	3766	1127	131
H9AB	7155	8431	7221	110	H4BC	8211	6367	4436	85
H9AC	6426	7905	6432	110	H5BA	7756	6602	7570	78
H4BA	9002	6685	5212	85	H4BB	8237	7718	5038	85

Table E.9. Atomic Occupancy for 1 phase I.

Atom	*Occupancy*	Atom	*Occupancy*	Atom	*Occupancy*
O2	0.29(6)	H3A	0.784(2)	H3B	0.216(2)
O4	0.784(2)	C4	0.383(2)	H4A	0.383(2)
H4B	0.383(2)	H4C	0.383(2)	Si1	0.383(2)
C5	0.383(2)	H5A	0.383(2)	H5B	0.383(2)
H5C	0.383(2)	C6	0.383(2)	C7	0.383(2)
H7A	0.383(2)	H7B	0.383(2)	H7C	0.383(2)
C8	0.383(2)	H8A	0.383(2)	H8B	0.383(2)
H8C	0.383(2)	C9	0.383(2)	H9A	0.383(2)
H9B	0.383(2)	H9C	0.383(2)	C4A	0.401(2)
H4AA	0.401(2)	H4AB	0.401(2)	H4AC	0.401(2)
Si1A	0.401(2)	C5A	0.401(2)	H5AA	0.401(2)
H5AB	0.401(2)	H5AC	0.401(2)	C6A	0.401(2)
C7A	0.401(2)	H7AA	0.401(2)	H7AB	0.401(2)
H7AC	0.401(2)	C8A	0.401(2)	H8AA	0.401(2)
H8AB	0.401(2)	H8AC	0.401(2)	C9A	0.401(2)
H9AA	0.401(2)	H9AB	0.401(2)	H9AC	0.401(2)
O2A	0.71(6)	O4A	0.216(2)	C4B	0.216(2)
H4BA	0.216(2)	H4BB	0.216(2)	H4BC	0.216(2)
Si1B	0.216(2)	C5B	0.216(2)	H5BA	0.216(2)
H5BB	0.216(2)	H5BC	0.216(2)	C6B	0.216(2)
C7B	0.216(2)	H7BA	0.216(2)	H7BB	0.216(2)
H7BC	0.216(2)	C8B	0.216(2)	H8BA	0.216(2)
H8BB	0.216(2)	H8BC	0.216(2)	C9B	0.216(2)
H9BA	0.216(2)	H9BB	0.216(2)	H9BC	0.216(2)
H14A	0.770(6)	H14B	0.770(6)	H14C	0.230(6)
H14D	0.230(6)	C15	0.770(6)	H15A	0.770(6)
H15B	0.770(6)	C16	0.770(6)	H16A	0.770(6)
H16B	0.770(6)	C17	0.770(6)	H17A	0.770(6)
H17B	0.770(6)	C18	0.770(6)	H18A	0.770(6)
H18B	0.770(6)	H18C	0.770(6)	C15A	0.230(6)
H15C	0.230(6)	H15D	0.230(6)	C16A	0.230(6)
H16C	0.230(6)	H16D	0.230(6)	C17A	0.230(6)
H17C	0.230(6)	H17D	0.230(6)	C18A	0.230(6)
H18D	0.230(6)	H18E	0.230(6)	H18F	0.230(6)

Table E.10. Refined atomic coordinates ($\times 10^4$) and equivalent isotropic displacement parameters ($Å^2 \times 10^3$) for 1 Phase II.

Atom	*x*	*y*	*z*	U(eq)	Atom	*x*	*y*	*z*	U(eq)
S1	1791.1(8)	5508.0(2)	2083.9(9)	19.8(3)	O4E	3110(2)	2792.4(5)	3157(3)	21.2(8)
C3	2166(3)	5977.0(8)	3562(4)	14.2(10)	N1E	2756(3)	2347.4(7)	2723(3)	18.6(9)

O4	2768(2)	6088.7(5)	3086(3)	17.8(8)	C1E	1359(4)	2650.1(9)	2186(6)	46.6(18)
Si1	2897.0(9)	6368.2(2)	2960.3(10)	16.2(3)	C2E	1599(4)	2732.5(9)	3204(6)	42.1(16)
C4	2686(4)	6432.3(9)	1667(4)	26.3(13)	C3E	2504(4)	2683.9(9)	3678(5)	26.0(13)
C5	2147(4)	6519.6(9)	3642(5)	31.0(14)	C4E	2989(5)	3197.8(10)	4263(5)	51(2)
C6	4032(3)	6438.2(7)	3459(3)	20.0(11)	C5E	4702(4)	2982.9(11)	3968(5)	51.6(19)
C7	4247(4)	6675.5(9)	3130(5)	31.8(14)	C6E	3557(3)	3191.1(8)	2274(4)	19.5(11)
C8	4144(5)	6435.4(11)	4549(4)	41.8(17)	C7E	3928(4)	3428.3(9)	2450(4)	28.1(13)
C9	4657(4)	6271.2(10)	3092(5)	32.7(14)	C8E	4108(4)	3063.8(8)	1624(4)	29.0(12)
F1	3645(2)	5499.8(5)	4295(2)	25.0(7)	C9E	2662(4)	3208.2(10)	1742(5)	30.5(14)
O1	1576(3)	5298.4(6)	2473(3)	30.3(10)	C10E	2746(4)	2431.4(8)	3711(4)	19.7(11)
O2	2028(3)	5515.8(7)	1143(3)	29.7(9)	C11E	2146(4)	2307.1(9)	4221(4)	23.5(12)
O3	972(2)	5654.9(6)	2140(3)	23.3(9)	C12E	1642(5)	2224(1)	4661(4)	40.6(16)
N1	2559(3)	5633.7(7)	2754(3)	14.1(9)	C13E	3671(4)	2399.3(9)	4208(4)	27.0(13)
C1	1075(4)	5897.8(9)	2053(4)	24.3(12)	C14E	3878(4)	2476.2(10)	5212(4)	32.5(14)
C2	1262(3)	6001.2(9)	3036(4)	20.9(11)	C15P	4727(13)	2416(5)	5785(16)	36(5)
C10	2484(3)	5733.1(8)	3704(4)	15.2(10)	C16P	4693(12)	2562(4)	6695(14)	36(5)
C11	1887(3)	5606.9(8)	4221(4)	18.4(11)	C17P	5599(11)	2602(3)	7134(13)	36(5)
C12	1412(4)	5513.7(10)	4660(4)	28.7(13)	C18E	5540(5)	2787.6(13)	7865(5)	54(2)
C13	3381(3)	5724.5(8)	4245(3)	14.6(10)	C15E	4845(5)	2441.9(15)	5550(5)	45(3)
C14	3498(3)	5817.3(9)	5238(3)	18.0(11)	C16E	5142(5)	2498.2(11)	6598(5)	31.3(19)
C15	4432(3)	5827.9(9)	5672(3)	18.1(11)	C17E	5090(4)	2743.4(10)	6830(5)	24.3(16)
C16	4551(3)	5921.4(9)	6688(3)	16.7(10)	S1F	9590.8(10)	8663.1(2)	6113.6(10)	27.4(3)
C17	5483(3)	5952.0(11)	7094(4)	23.7(12)	Si1F	8714.7(10)	7796.6(2)	5140.0(13)	27.5(4)
C18	5585(4)	6033.7(10)	8126(4)	29.2(14)	F1F	7758(2)	8660.2(5)	3869(2)	25.9(7)
S1A	2118.0(9)	7178.3(2)	2016.7(10)	22.3(3)	O1F	9741(3)	8877.8(7)	5761(3)	38.6(12)
C3A	2310(3)	7630.3(7)	3608(4)	18.3(11)	O2F	9352(3)	8639.6(8)	7045(3)	39.4(11)
O4A	2868(2)	7763.3(5)	3154(3)	26.1(9)	O3F	10445(3)	8533.5(6)	6038(3)	27.7(9)
Si1A	2905.5(14)	8041.2(3)	2971.7(18)	16.8(5)	O4F	8771(2)	8074.1(6)	5055(3)	19.6(8)
C4A	2657(6)	8106.0(14)	1684(4)	29(2)	N1F	8859(3)	8530.5(8)	5423(4)	24.7(11)
C5A	2125(5)	8176.4(13)	3676(6)	23.4(19)	C1F	10399(4)	8288.9(9)	6089(5)	27.4(9)
C6A	4025(4)	8128.9(11)	3456(5)	22.3(17)	C2F	10266(4)	8194.9(10)	5086(4)	27.4(9)
C7A	4188(7)	8367.9(14)	3102(9)	48(3)	C3F	9346(3)	8199.2(8)	4558(4)	20.5(11)
C8A	4142(6)	8131.1(18)	4543(5)	41(2)	C4F	9492(5)	7657.0(11)	4447(6)	45.8(19)
C9A	4679(5)	7968.0(16)	3098(8)	34(3)	C5F	8954(5)	7731.1(12)	6440(5)	40.7(16)
Si1L	2983(3)	8043.8(6)	3472(3)	16.8(5)	C6F	7596(4)	7708.3(10)	4677(6)	41.7(12)
C5L	3322(12)	8077(3)	4757(6)	63(6)	C7F	7438(4)	7473.6(10)	5049(6)	41.7(12)
C4L	1954(7)	8186(2)	3060(12)	42(5)	C8F	6945(4)	7869.3(11)	4987(6)	45.9(19)
C6L	3833(6)	8134.7(15)	2733(7)	37(3)	C9F	7474(5)	7711.2(13)	3581(5)	50.5(19)
C8L	4696(7)	8035(3)	3191(13)	37(3)	C10F	8972(4)	8441.6(8)	4466(4)	17.6(11)
C7L	3637(11)	8041(3)	1725(8)	43(4)	C11F	9521(3)	8583.2(9)	3958(4)	18.1(11)
C9L	3898(11)	8391.4(17)	2713(13)	37(3)	C12F	9970(4)	8685.3(10)	3514(4)	29.8(14)
F1A	3937(2)	7177.8(5)	4266(2)	23.8(7)	C13F	8041(3)	8437.1(8)	3921(4)	16.3(10)
O1A	1994(3)	6957.6(6)	2335(3)	31.6(10)	C14F	7955(3)	8344.1(9)	2917(4)	16.9(10)
O2A	2340(3)	7212.3(8)	1083(3)	37.3(10)	C15F	7019(3)	8332.4(10)	2472(4)	20.3(11)

O3A	1247(2)	7298.8(6)	2107(3)	24.3(9)	C16F	6918(4)	8250.9(9)	1441(4)	21.4(11)
N1A	2823(3)	7311.5(7)	2733(3)	18.0(9)	C17F	5990(4)	8209.0(11)	1026(4)	30.8(14)
C1A	1249(4)	7544.6(9)	2098(5)	30.4(13)	C18F	5894(4)	8136.8(11)	-8(4)	30.1(13)
C2A	1404(3)	7635.6(9)	3093(5)	27.7(12)	S1G	1944.7(8)	638.9(2)	2102.1(9)	19.9(3)
C10A	2713(3)	7391.6(8)	3693(4)	15.1(10)	Si1G	3163.7(10)	1425.2(2)	3649.7(11)	22.4(3)
C11A	2177(4)	7242.9(9)	4182(4)	21.8(12)	F1G	4097(2)	558.8(5)	3932(3)	30.7(8)
C12A	1720(4)	7140.6(10)	4622(4)	28.1(13)	O1G	1897(3)	405.2(7)	2226(3)	29.1(9)
C13A	3626(4)	7398.8(8)	4236(4)	19.3(11)	O2G	1969(3)	725.9(7)	1166(3)	30.6(9)
C14A	3721(3)	7487.9(9)	5241(4)	21.0(11)	O3G	1144(2)	732.6(7)	2532(3)	20.8(8)
C15A	4661(4)	7499.6(10)	5677(4)	25.0(12)	O4G	2856(2)	1160.3(6)	3391(3)	19.5(8)
C16A	4767(3)	7589.6(9)	6685(4)	21.5(11)	N1G	2776(3)	741.0(8)	2753(3)	19.0(9)
C17A	5687(4)	7627.8(11)	7105(4)	28.5(13)	C1G	1110(3)	969.4(10)	2716(4)	24.8(12)
C18A	5818(4)	7710.7(11)	8114(5)	36.8(15)	C2G	1484(3)	1023.7(9)	3732(4)	22.1(11)
S1B	2118.4(10)	8904.6(3)	2140.6(11)	36.2(4)	C3G	2449(3)	1010.9(9)	3973(4)	17.5(11)
Si1B	3010.9(11)	9732.5(3)	3587.9(12)	25.7(4)	C4R	2110(20)	1546(10)	3160(50)	22.4(3)
F1B	4025(2)	8850.7(5)	4354(3)	27.9(7)	C5R	3480(60)	1479(11)	4938(14)	27(12)
O1B	2023(3)	8673.2(8)	2346(4)	49.3(13)	C6G	3589(3)	1512.4(7)	2536(4)	32.1(13)
O2B	2290(4)	8969.5(11)	1222(3)	65.5(18)	C7G	3981(4)	1748.2(9)	2648(5)	30.9(14)
O3B	1263(3)	9012.5(8)	2363(3)	34.8(11)	C8G	4239(9)	1339.3(18)	2272(10)	59(3)
O4B	2916(2)	9453.7(6)	3438(3)	17.3(8)	C9G	2838(6)	1533(3)	1727(5)	45(3)
N1B	2872(3)	9017.9(8)	2861(3)	20.0(9)	C10G	2834(3)	775.0(8)	3803(4)	17.4(11)
C1B	1243(4)	9253.2(11)	2473(5)	40.5(16)	C11G	2395(3)	602.1(9)	4273(4)	17.7(11)
C2B	1469(3)	9319.4(10)	3495(5)	30.9(14)	C12G	2028(4)	473.2(10)	4719(4)	30.2(13)
C3B	2398(3)	9310.0(9)	3914(4)	19.7(11)	C13G	3802(3)	769.1(8)	4165(4)	17.9(11)
C4B	2033(4)	9876.0(11)	3025(5)	36.3(15)	C14G	4045(3)	804.2(9)	5223(4)	19.2(11)
C5B	3208(7)	9800.8(13)	4876(5)	60(2)	C15G	5019(4)	795.7(10)	5498(4)	28.9(12)
C6B	3932(4)	9804.5(9)	2936(5)	29.6(14)	C16G	5302(4)	829.8(9)	6556(4)	26.0(9)
C7B	4041(5)	10063(1)	2899(6)	43.6(18)	C17G	5133(4)	1060.5(9)	6930(4)	26.0(9)
C8B	4766(4)	9699.0(11)	3433(6)	49(2)	C18G	5561(4)	1096.9(11)	7945(4)	34.6(15)
C9B	3752(4)	9718.8(12)	1907(5)	39.4(16)	S1H	9815.0(8)	10317.9(2)	5986.5(10)	19.9(3)
C10B	2798(3)	9072.2(9)	3873(4)	16.3(10)	Si1H	8664.1(10)	9460.2(2)	5116.6(12)	22.9(3)
C11B	2302(4)	8909.0(9)	4328(4)	21.2(12)	F1H	7987(2)	10331.9(5)	3764(3)	27.0(8)
C12B	1865(4)	8795.5(11)	4759(4)	31.0(14)	O1H	10047(2)	10521.2(6)	5583(3)	23.9(8)
C13B	3739(3)	9074.0(8)	4365(4)	18.3(11)	O2H	9577(3)	10317.6(7)	6917(3)	28.8(9)
C14B	3877(4)	9156.4(9)	5382(4)	24.3(12)	O3H	10618(3)	10164.5(6)	5943(3)	24.1(9)
C15B	4813(4)	9142.6(11)	5813(4)	31.6(13)	O4H	8789(2)	9735.2(6)	5022(3)	20.4(8)
C16B	4995(4)	9269.7(10)	6746(4)	31.5(13)	N1H	9044(3)	10195.1(8)	5313(4)	19.6(10)
C17B	5903(4)	9240.9(13)	7214(5)	45.7(17)	C1H	10490(4)	9921.7(9)	6039(4)	25.1(12)
C18B	6099(4)	9378.7(12)	8102(5)	46.1(18)	C2H	10316(3)	9817.0(9)	5067(4)	23.2(12)
S1C	1816.1(8)	3865.2(2)	2115.2(10)	18.5(3)	C3H	9409(3)	9841.4(8)	4523(4)	16(1)
C3C	2260(3)	4334.1(8)	3592(4)	17.4(10)	C4H	9348(4)	9305.3(9)	4350(5)	40.7(16)
O4C	2898(2)	4439.3(5)	3146(3)	18.2(8)	C5H	8946(4)	9393.0(11)	6411(4)	34.7(14)
Si1N	2939(2)	4718.2(5)	3012(2)	15.9(4)	C6H	7518(4)	9392.6(9)	4700(4)	29.9(13)
C4N	2265(8)	4863(2)	3803(9)	36.0(12)	C7H	7342(4)	9152.6(9)	5012(5)	36.3(15)

C5N	2617(10)	4792(3)	1739(6)	28(2)	C8H	6915(4)	9554.5(10)	5119(6)	47.5(19)
C6N	4105(4)	4786.2(13)	3381(6)	22(3)	C9H	7339(5)	9409.6(12)	3620(5)	49.4(19)
C7N	4314(8)	4759(2)	4473(7)	35(3)	C10H	9123(3)	10091.2(9)	4394(4)	16.6(11)
C8N	4278(7)	5027.2(14)	3111(9)	26(3)	C11H	9735(3)	10209.7(9)	3874(4)	19.6(11)
C9N	4679(6)	4622.9(19)	2912(10)	33(3)	C12H	10229(4)	10292.5(10)	3426(4)	24.3(12)
Si1C	3370.5(13)	4695.1(3)	3411.9(14)	15.9(4)	C13H	8199(3)	10104.9(9)	3828(4)	19.5(11)
C4C	2744(5)	4851.8(13)	4210(6)	36.0(12)	C14H	8104(3)	10008.2(10)	2832(4)	19.0(11)
C5C	4485(4)	4642.7(15)	3986(7)	52(3)	C15H	7170(3)	10007.8(10)	2374(4)	24.8(12)
C6C	3391(4)	4842.4(8)	2242(4)	15.5(14)	C16H	7063(3)	9905.7(10)	1385(4)	23.2(12)
C7C	3710(5)	5085.2(10)	2431(5)	23.9(17)	C17H	6132(4)	9884.1(11)	936(4)	31.2(14)
C8C	3997(5)	4723.2(13)	1652(6)	36.0(12)	C18H	6025(4)	9794.8(10)	-61(4)	28.8(13)
C9C	2485(5)	4847.8(16)	1678(6)	28(2)	S1I	9709.2(8)	3527.6(2)	6022.0(9)	17.8(3)
F1C	3623.8(19)	3834.9(5)	4364(2)	21.6(7)	Si1I	8455.7(9)	2737.0(2)	4498.4(10)	19.3(3)
O1C	1554(2)	3662.1(7)	2504(3)	25.8(9)	F1I	7556.2(17)	3602.0(5)	4222(2)	24.8(7)
O2C	2062(3)	3865.8(7)	1180(3)	27.7(9)	O1I	9777(3)	3762.5(6)	5853(3)	24.6(9)
O3C	1032(2)	4025.6(7)	2163(3)	24.4(9)	O2I	9692(2)	3446.5(7)	6966(3)	27.6(8)
N1C	2599(3)	3982.0(7)	2790(3)	13.4(8)	O3I	10503(2)	3429.2(6)	5612(3)	21.5(8)
C1C	1199(4)	4265.9(10)	2062(5)	28.9(13)	O4I	8780(2)	2997.0(6)	4764(3)	19.8(7)
C2C	1373(3)	4371.6(9)	3043(4)	21.6(11)	N1I	8877(3)	3422.4(7)	5388(3)	14.4(9)
C10C	2525(3)	4084.7(8)	3735(4)	13.3(10)	C1I	10531(3)	3183.9(8)	5450(4)	23.8(11)
C11C	1901(3)	3967.6(8)	4243(4)	13.8(10)	C2I	10160(3)	3131.0(8)	4428(4)	22.2(11)
C12C	1383(4)	3885.5(9)	4659(4)	21.1(12)	C3I	9179(3)	3145.8(8)	4191(4)	18.1(11)
C13C	3417(3)	4063.4(8)	4305(4)	15(1)	C4I	9371(4)	2561.3(9)	4210(5)	42.6(15)
C14C	3535(3)	4158.7(9)	5294(4)	17(1)	C5I	7629(5)	2737.9(10)	3444(4)	48.8(18)
C15C	4453(3)	4146.1(10)	5773(4)	22.1(11)	C6I	8024(3)	2642.9(8)	5617(4)	23.2(12)
C16C	4571(3)	4256.6(9)	6741(4)	19.6(10)	C7I	8767(5)	2642.9(13)	6434(5)	50(2)
C17C	5504(3)	4264.2(12)	7206(4)	32.9(14)	C8I	7652(4)	2406.2(9)	5513(5)	31.2(14)
C18C	5592(4)	4366.2(11)	8201(4)	36.2(15)	C9I	7333(5)	2804(1)	5847(6)	54(2)
S1D	9466.3(9)	6960.3(2)	5987(1)	24.5(3)	C10I	8816(3)	3381.3(8)	4352(4)	12.2(10)
Si1D	8638.8(10)	6116.0(2)	4567.6(11)	19.2(3)	C11I	9267(3)	3552.6(9)	3845(4)	19.5(11)
F1D	7623(2)	6989.9(5)	3727(2)	23.0(7)	C12I	9630(3)	3676.0(9)	3393(4)	24.4(12)
O1D	9563(3)	7187.1(7)	5722(3)	32.6(10)	C13I	7850(3)	3391.4(8)	3983(4)	15.8(10)
O2D	9255(3)	6912.0(8)	6909(3)	42.2(12)	C14I	7593(3)	3353.8(9)	2930(4)	17.8(10)
O3D	10340(3)	6848.8(7)	5838(3)	27.2(9)	C15I	6630(3)	3366.5(9)	2651(4)	21.9(11)
O4D	8730(2)	6392.1(6)	4725(3)	17.7(7)	C16I	6332(3)	3336.7(9)	1584(4)	22.5(11)
N1D	8741(3)	6836.1(8)	5251(3)	19.0(9)	C17I	6501(4)	3103(1)	1209(4)	27.0(12)
C1D	10351(4)	6601.9(10)	5772(4)	32.2(15)	C18I	6080(4)	3075.9(12)	176(4)	34.5(15)
C2D	10201(3)	6532.2(10)	4736(4)	27.2(13)	S1J	9708.4(8)	1931.5(2)	6099.7(10)	21.2(3)
C3D	9259(3)	6536.8(8)	4250(4)	16.5(10)	Si1J	8083.0(11)	1135.3(2)	4732.9(12)	26.1(3)
C4D	9629(3)	5969.8(10)	5102(5)	36.6(15)	F1J	7893(2)	2007.6(6)	3863(3)	32.0(8)
C5D	8443(5)	6044.8(11)	3281(5)	43.8(16)	O1J	9993(3)	2138.3(7)	5750(3)	25.1(9)
C6D	7712(3)	6044.6(8)	5204(4)	23.0(11)	O2J	9475(3)	1923.7(8)	7038(3)	37.0(11)
C7D	7597(4)	5789.1(9)	5232(5)	35.4(15)	O3J	10459(2)	1767.4(7)	6000(3)	30.6(10)
C8D	6892(4)	6151.7(10)	4704(5)	34.2(14)	O4J	8545(2)	1383.4(6)	5002(3)	22.6(8)

C9D	7881(4)	6132.8(10)	6233(4)	33.3(13)	N1J	8898(3)	1834.0(8)	5399(3)	19.7(10)
C10D	8843(3)	6772.6(8)	4258(4)	15.3(10)	C1J	10282(4)	1526.7(10)	6026(5)	39.2(16)
C11D	9376(3)	6931.4(9)	3806(4)	15.6(10)	C2J	10060(4)	1436.8(10)	5034(5)	33.3(14)
C12D	9813(4)	7043.1(9)	3385(4)	23.0(12)	C3J	9174(3)	1487.4(8)	4514(4)	19.4(11)
C13D	7920(3)	6770.3(8)	3745(4)	14.7(10)	C4J	6957(4)	1193.0(11)	4197(5)	43.9(17)
C14D	7798(3)	6679.7(9)	2749(4)	20.1(11)	C5J	8669(6)	982.6(11)	3886(5)	55(2)
C15D	6863(3)	6675.8(10)	2330(4)	24.3(12)	C6J	8088(4)	979.7(8)	5882(4)	22.3(11)
C16D	6693(4)	6561.4(10)	1359(4)	25.5(12)	C7J	7725(4)	743.1(9)	5685(5)	30.6(14)
C17D	5748(4)	6556.9(13)	952(5)	39.5(16)	C8J	9009(4)	966.7(10)	6403(5)	33.9(15)
C18D	5580(4)	6433.0(11)	9(4)	34.3(14)	C9J	7530(4)	1105.1(9)	6513(5)	35.1(14)
S1E	1932.0(8)	2253.2(2)	2044.2(10)	23.9(3)	C10J	8948(3)	1740.3(9)	4447(4)	18.3(11)
Si1E	3576.8(10)	3040.2(2)	3427.1(10)	24.8(3)	C11J	9587(4)	1854.1(9)	3959(4)	23.1(12)
F1E	3823(2)	2167.5(5)	4195(3)	40.1(9)	C12J	10099(4)	1932.9(10)	3502(4)	30.3(14)
O1E	1685(3)	2042.3(7)	2356(3)	29.0(9)	C13J	8039(3)	1775.8(8)	3908(3)	21.2(11)
O2E	2135(3)	2271.4(8)	1097(3)	44.5(12)	C14J	7896(4)	1686.2(10)	2902(4)	31.9(13)
O3E	1177(3)	2410.6(7)	2223(4)	38.8(12)	C15S	6958(6)	1726(3)	2512(9)	38.0(12)
S1K	9526.8(8)	5213.8(2)	6025.2(9)	17.5(3)	C16S	6679(10)	1661.5(19)	1475(8)	38.0(12)
Si1K	8512.8(10)	4421.0(2)	4482.0(11)	20.2(3)	C17S	6529(10)	1412.7(19)	1337(8)	38.0(12)
F1K	7470(2)	5303.2(5)	4017(3)	40.2(10)	C18S	6103(11)	1360(2)	327(8)	38.0(12)
O1K	9597(3)	5448.9(6)	5898(3)	27.4(9)	C15J	7012(5)	1715(3)	2375(7)	38.0(12)
O2K	9460(3)	5122.4(7)	6941(3)	31.4(9)	C16J	6914(5)	1586.2(19)	1420(6)	38.0(12)
O3K	10347(2)	5120.9(6)	5647(3)	19.0(8)	C17J	5997(5)	1604.7(16)	941(5)	38.0(12)
O4K	8655(2)	4691.9(6)	4645(3)	16.1(7)	C18J	5865(7)	1482.1(16)	-15(6)	36.0(12)
N1K	8724(3)	5113.0(7)	5324(3)	15.4(9)	C4G	2264(4)	1599.0(9)	3934(5)	39.1(17)
C1K	10387(3)	4876.6(8)	5458(4)	21.1(11)	C5G	4003(5)	1424.9(11)	4703(5)	46(2)
C2K	10070(3)	4832.7(9)	4417(4)	21.5(11)	C8R	4435(12)	1387(5)	2476(16)	59(3)
C3K	9098(3)	4846.2(8)	4118(4)	13.2(10)	C9R	2946(13)	1450(6)	1663(6)	45(3)
C4K	9532(4)	4270.0(12)	4907(7)	64(2)	Si1M	3414(6)	8011.7(12)	3469(6)	16.8(5)
C5K	8199(8)	4361.9(14)	3206(5)	75(3)	C5M	4561(7)	7966(3)	4016(11)	22(3)
C6K	7670(4)	4348.5(9)	5241(5)	31.0(13)	C4M	2815(12)	8149(3)	4387(9)	22(3)
C7K	7547(4)	4093.4(10)	5274(6)	41.8(18)	C6M	3333(9)	8179(2)	2313(7)	22(3)
C8K	6820(4)	4458.7(11)	4805(7)	59(2)	C8M	3811(14)	8056(4)	1585(8)	22(3)
C9K	7900(5)	4436.8(11)	6232(5)	52(2)	C7M	2386(10)	8205(4)	1889(11)	22(3)
C10K	8707(3)	5079.4(8)	4289(4)	13(1)	C9M	3730(14)	8413(2)	2503(14)	22(3)
C11K	9181(3)	5254.5(9)	3830(4)	18.1(11)	C18T	5405(9)	4811(2)	8(9)	24(2)
C12K	9553(4)	5380.4(9)	3406(4)	22.8(12)	C15K	6553(4)	5048.6(14)	2585(5)	28.4(12)
C13K	7752(3)	5086.0(9)	3876(4)	20.2(11)	C16K	6235(5)	5007(1)	1532(5)	25.7(17)
C14K	7527(3)	5026.5(10)	2845(4)	28.4(12)	C17K	6373(5)	4766.5(11)	1232(5)	26.6(18)
C15T	6647(6)	5063(3)	2328(8)	24(2)	C18K	5929(5)	4716.5(15)	233(5)	34(2)
C16T	6496(7)	4926(3)	1395(8)	24(2)	C17T	5610(7)	4966(2)	865(8)	24(2)

Table E.11. Anisotropic displacement parameters ($Å^2 \times 10^3$) for 1 phase II.

Atom	U_{11}	U_{22}	U_{33}	U_{23}	U_{13}	U_{12}
S1	25.4(6)	14.6(6)	17.1(6)	0.5(5)	-6.0(5)	-5.8(5)

C3	13(2)	17(2)	12(2)	3.0(18)	-0.4(19)	-3.2(18)
O4	19.0(18)	9.2(16)	27(2)	0.7(14)	9.2(16)	-1.1(13)
Si1	20.9(7)	14.4(7)	13.3(7)	0.0(5)	2.7(5)	-1.0(5)
C4	38(3)	19(3)	21(3)	2(2)	-2(3)	-10(2)
C5	33(3)	17(3)	45(4)	-1(2)	16(3)	4(2)
C6	24(3)	14(2)	22(3)	-0.6(19)	1(2)	-2.2(18)
C7	30(3)	27(3)	38(4)	-1(2)	1(3)	-10(2)
C8	66(5)	33(3)	23(3)	-4(3)	-8(3)	-11(3)
C9	22(3)	30(3)	45(4)	-5(3)	0(3)	1(2)
F1	27.3(16)	14.9(14)	28.9(18)	-4.9(12)	-10.9(13)	8.1(12)
O1	41(2)	16.0(18)	29(2)	4.8(15)	-12.3(18)	-11.3(16)
O2	42(2)	32(2)	15(2)	-6.8(16)	0.3(17)	-6.8(18)
O3	20.1(18)	22.3(19)	25(2)	6.3(15)	-6.5(15)	-3.8(14)
N1	17(2)	12.4(19)	12(2)	-4.0(15)	0.5(16)	-3.3(15)
C1	24(3)	16(2)	29(3)	6(2)	-9(2)	0.9(19)
C2	18(2)	18(2)	27(3)	4(2)	1(2)	1.5(19)
C10	21(3)	14(2)	10(2)	0.9(18)	1(2)	-4.3(19)
C11	21(2)	15(2)	19(3)	5.2(19)	-2(2)	-7.4(19)
C12	31(3)	34(3)	18(3)	6(2)	-8(2)	-18(2)
C13	12(2)	12(2)	19(3)	-1.6(18)	1.4(19)	0.4(17)
C14	16(2)	14(2)	23(3)	0(2)	0(2)	1.4(18)
C15	14(2)	19(2)	21(3)	-5(2)	2(2)	0.2(18)
C16	10(2)	20(2)	18(3)	1(2)	-2.6(19)	-1.2(18)
C17	12(2)	36(3)	22(3)	-4(2)	-2(2)	-4(2)
C18	26(3)	30(3)	28(3)	4(3)	-10(2)	-6(2)
S1A	29.1(7)	20.7(6)	15.7(6)	-0.2(5)	-2.9(5)	-0.1(5)
C3A	21(2)	11(2)	24(3)	1.1(18)	6(2)	0.6(17)
O4A	27.8(19)	13.0(16)	37(2)	3.0(14)	3.5(16)	-4.6(14)
Si1A	25.3(10)	10.2(8)	15.0(12)	-0.3(9)	2.8(11)	-2.2(7)
C4A	42(5)	24(4)	22(4)	1(3)	5(4)	2(4)
C5A	29(4)	15(4)	29(5)	-1(4)	11(4)	3(3)
C6A	25(4)	22(4)	18(4)	1(3)	1(3)	-5(3)
C7A	45(7)	29(5)	70(8)	9(5)	4(6)	-13(4)
C8A	46(6)	47(6)	26(4)	0(4)	-3(4)	-6(5)
C9A	23(4)	26(5)	56(7)	4(4)	12(4)	-6(4)
Si1L	25.3(10)	10.2(8)	15.0(12)	-0.3(9)	2.8(11)	-2.2(7)
C5L	115(16)	33(10)	37(7)	-5(6)	0(7)	-20(10)
C4L	43(7)	19(8)	66(13)	3(8)	13(7)	4(6)
C6L	49(6)	14(5)	50(6)	0(4)	20(5)	-10(4)
C8L	49(6)	14(5)	50(6)	0(4)	20(5)	-10(4)
C7L	55(10)	30(8)	51(7)	-9(6)	31(6)	-21(7)

C9L	49(6)	14(5)	50(6)	0(4)	20(5)	-10(4)
F1A	26.3(16)	16.2(15)	26.9(17)	-3.6(12)	-4.0(13)	6.1(12)
O1A	47(3)	15.9(18)	27(2)	-3.4(16)	-11.3(19)	-0.9(16)
O2A	40(2)	54(3)	17(2)	-3.7(18)	3.0(18)	-2(2)
O3A	23.4(19)	22.5(19)	25(2)	7.0(15)	-2.4(16)	-1.4(15)
N1A	23(2)	18(2)	13(2)	-0.4(16)	1.5(17)	0.7(17)
C1A	27(3)	21(3)	40(3)	6(2)	-6(2)	1(2)
C2A	19(2)	21(2)	44(3)	1(2)	5(2)	5.0(19)
C10A	15(2)	16(2)	14(2)	0.0(18)	3.1(19)	-1.3(18)
C11A	26(3)	18(3)	20(3)	1(2)	-3(2)	-6(2)
C12A	32(3)	30(3)	21(3)	3(2)	-1(2)	-11(2)
C13A	28(3)	11(2)	19(3)	-0.7(19)	2(2)	0.7(19)
C14A	20(3)	19(3)	25(3)	-3(2)	6(2)	-3(2)
C15A	25(3)	28(3)	22(3)	-2(2)	5(2)	-6(2)
C16A	22(3)	18(2)	24(3)	-1(2)	1(2)	0.4(19)
C17A	24(3)	34(3)	27(3)	-6(2)	3(2)	-5(2)
C18A	36(3)	41(3)	30(3)	-9(3)	-10(3)	6(3)
S1B	35.8(8)	56.9(10)	15.5(7)	-9.9(6)	2.2(6)	-20.9(7)
Si1B	34.3(8)	18.0(7)	24.6(8)	0.7(6)	3.3(7)	2.8(6)
F1B	27.8(17)	17.3(14)	36.0(19)	-0.4(13)	-5.5(14)	6.7(12)
O1B	45(3)	49(3)	53(3)	-25(2)	6(2)	-23(2)
O2B	62(3)	118(5)	18(2)	-12(2)	11(2)	-48(3)
O3B	25(2)	50(2)	27(2)	16.1(18)	-5.4(17)	-13.4(17)
O4B	23.0(18)	15.4(17)	14.5(18)	2.1(14)	6.6(14)	2.2(14)
N1B	21(2)	24(2)	15(2)	-5.6(17)	3.3(17)	-2.3(17)
C1B	20(3)	47(4)	51(4)	20(3)	-8(3)	-5(2)
C2B	16(2)	27(3)	51(4)	16(2)	10(2)	7(2)
C3B	22(2)	16(2)	22(3)	2.7(19)	9(2)	5.6(19)
C4B	32(3)	31(3)	47(4)	12(3)	10(3)	17(2)
C5B	119(7)	34(4)	23(3)	-10(3)	1(4)	-2(4)
C6B	25(3)	18(3)	44(4)	0(2)	-4(3)	-7(2)
C7B	43(4)	18(3)	68(5)	5(3)	-1(4)	-8(3)
C8B	27(3)	33(3)	82(6)	5(3)	-7(3)	-1(3)
C9B	33(3)	40(4)	48(4)	4(3)	14(3)	-1(3)
C10B	19(2)	17(2)	13(2)	1.4(18)	1.4(19)	0.9(18)
C11B	23(3)	23(3)	15(3)	3.7(19)	-6(2)	-0.5(19)
C12B	33(3)	37(3)	21(3)	9(2)	-4(2)	-9(2)
C13B	23(3)	9(2)	21(3)	2.1(18)	-3(2)	1.3(18)
C14B	28(3)	26(3)	17(3)	1(2)	-8(2)	-4(2)
C15B	23(3)	47(3)	23(3)	8(2)	-3(2)	-6(2)
C16B	29(3)	34(3)	30(3)	4(2)	-2(2)	-9(2)

C17B	29(3)	80(5)	27(3)	3(3)	-2(3)	-7(3)
C18B	41(4)	58(4)	36(4)	7(3)	-8(3)	-22(3)
S1C	16.1(6)	22.6(6)	15.9(6)	-6.7(5)	-1.3(5)	-0.2(5)
C3C	21(2)	17(2)	14(2)	0.4(19)	3(2)	0.9(19)
O4C	26.0(18)	11.2(16)	17.5(18)	-1.6(13)	3.2(15)	-0.9(13)
Si1N	20.8(10)	14.3(7)	10.7(10)	1.0(7)	-4.7(7)	-7.3(7)
C4N	51(3)	30(2)	30(3)	-12(2)	15(2)	-11(2)
C5N	34(4)	23(5)	24(3)	3(3)	-9(3)	4(3)
C6N	19(5)	12(5)	36(6)	-5(4)	5(4)	-3(4)
C7N	47(9)	27(7)	30(7)	1(5)	-6(6)	-7(6)
C8N	16(6)	26(6)	34(8)	-5(5)	2(5)	-2(4)
C9N	19(6)	27(6)	51(9)	-14(6)	2(6)	0(5)
Si1C	20.8(10)	14.3(7)	10.7(10)	1.0(7)	-4.7(7)	-7.3(7)
C4C	51(3)	30(2)	30(3)	-12(2)	15(2)	-11(2)
C5C	43(5)	41(5)	63(7)	30(5)	-26(5)	-23(4)
C6C	25(3)	6(3)	16(3)	-1(2)	4(3)	-3(2)
C7C	30(4)	15(3)	27(4)	3(3)	2(3)	-4(3)
C8C	51(3)	30(2)	30(3)	-12(2)	15(2)	-11(2)
C9C	34(4)	23(5)	24(3)	3(3)	-9(3)	4(3)
F1C	19.5(15)	16.9(14)	26.4(18)	-3.9(12)	-4.8(13)	5.7(12)
O1C	22.7(19)	26(2)	28(2)	-7.4(16)	1.2(16)	-4.9(15)
O2C	32(2)	40(2)	10.5(19)	-6.4(16)	1.7(16)	-0.6(17)
O3C	13.8(17)	31(2)	27(2)	-2.7(16)	-3.5(15)	5.2(14)
N1C	13.9(19)	15(2)	12(2)	-3.4(16)	3.8(16)	-2.3(15)
C1C	29(3)	27(3)	28(3)	1(2)	-7(2)	11(2)
C2C	21(2)	19(2)	24(3)	2(2)	-1(2)	10.5(19)
C10C	19(2)	12(2)	9(2)	0.7(18)	0.9(19)	-0.1(18)
C11C	16(2)	12(2)	14(2)	1.1(18)	3.8(19)	-2.8(18)
C12C	21(3)	24(3)	17(3)	-1(2)	-3(2)	-5(2)
C13C	11(2)	12(2)	22(3)	-0.5(19)	4.1(19)	0.0(17)
C14C	16(2)	17(2)	17(3)	2.8(19)	0.8(19)	0.2(18)
C15C	13(2)	35(3)	19(3)	-2(2)	5(2)	-3(2)
C16C	12(2)	24(2)	21(3)	3(2)	-1.4(19)	-3.1(18)
C17C	13(2)	61(4)	24(3)	-4(3)	-1(2)	-14(2)
C18C	32(3)	42(3)	30(3)	2(3)	-15(3)	-14(3)
S1D	29.1(7)	31.3(7)	12.6(6)	-2.6(5)	0.8(5)	-12.1(5)
Si1D	24.6(7)	13.5(6)	19.1(7)	-2.7(5)	1.5(6)	2.1(5)
F1D	19.8(15)	20.7(15)	27.5(17)	-3.7(13)	-1.0(13)	8.0(12)
O1D	41(2)	27(2)	28(2)	-6.3(17)	-3.7(19)	-8.8(17)
O2D	49(3)	64(3)	13(2)	-4.0(18)	3.7(18)	-25(2)
O3D	23(2)	33(2)	24(2)	6.0(16)	-5.1(16)	-11.8(16)

O4D	15.9(16)	15.4(16)	20.8(18)	2.9(13)	-1.0(14)	-0.6(13)
N1D	18(2)	22(2)	17(2)	-1.5(17)	0.6(17)	-7.1(17)
C1D	26(3)	29(3)	37(3)	19(2)	-12(2)	-8(2)
C2D	15(2)	26(3)	40(3)	8(2)	-1(2)	1.4(19)
C3D	15(2)	17(2)	17(2)	2.5(18)	0.1(18)	0.9(17)
C4D	21(3)	25(3)	63(5)	9(3)	3(3)	0(2)
C5D	73(5)	27(3)	31(3)	-9(2)	9(3)	1(3)
C6D	19(2)	18(2)	30(3)	7(2)	-2(2)	2.0(19)
C7D	27(3)	17(3)	62(5)	7(3)	2(3)	-4(2)
C8D	22(3)	27(3)	51(4)	3(3)	-4(3)	-2(2)
C9D	45(3)	36(3)	23(3)	1(2)	19(3)	-3(3)
C10D	18(2)	14(2)	13(2)	-1.9(18)	-1.6(19)	0.1(18)
C11D	14(2)	19(2)	12(2)	-1.4(18)	-1.3(19)	0.3(18)
C12D	23(3)	26(3)	17(3)	6(2)	-4(2)	-11(2)
C13D	8(2)	18(2)	18(3)	0.1(19)	0.7(19)	2.1(17)
C14D	16(2)	18(3)	25(3)	-4(2)	0(2)	2.5(19)
C15D	18(2)	34(3)	21(3)	-3(2)	0(2)	-6(2)
C16D	23(3)	35(3)	17(3)	-1(2)	-4(2)	-3(2)
C17D	23(3)	69(4)	26(3)	-12(3)	3(2)	-15(3)
C18D	37(3)	43(3)	23(3)	-3(2)	1(2)	-11(3)
S1E	20.6(6)	34.0(7)	17.2(6)	1.6(5)	2.3(5)	-9.0(5)
Si1E	38.0(8)	17.8(6)	18.1(7)	0.5(5)	2.2(6)	-9.7(6)
F1E	47(2)	24.0(16)	42(2)	-16.9(14)	-20.8(16)	15.5(14)
O1E	33(2)	32(2)	23(2)	-3.8(16)	5.4(17)	-5.6(17)
O2E	42(2)	77(3)	14.2(19)	2(2)	-0.4(17)	-33(2)
O3E	15.6(18)	28(2)	70(3)	6(2)	-4.2(19)	-2.0(15)
O4E	30.0(19)	14.0(16)	19.7(18)	1.2(13)	4.0(15)	-7.6(14)
N1E	19(2)	21(2)	16(2)	0.2(16)	3.5(17)	-3.4(16)
C1E	31(3)	23(3)	80(5)	9(3)	-17(3)	4(2)
C2E	31(3)	17(3)	78(5)	1(3)	10(3)	10(2)
C3E	24(3)	17(3)	38(3)	3(2)	10(2)	0(2)
C4E	97(6)	30(3)	35(3)	-16(3)	40(4)	-23(3)
C5E	56(4)	44(4)	47(4)	22(3)	-24(3)	-23(3)
C6E	26(3)	12(2)	19(3)	-0.5(19)	1(2)	0.0(19)
C7E	41(3)	19(3)	25(3)	0(2)	4(3)	-4(2)
C8E	36(3)	20(2)	34(3)	-2(2)	14(2)	-2(2)
C9E	26(3)	26(3)	38(4)	7(2)	-2(2)	1(2)
C10E	32(3)	8(2)	19(3)	0.2(18)	6(2)	1.4(19)
C11E	41(3)	15(2)	16(3)	-3.6(19)	9(2)	-8(2)
C12E	63(4)	37(3)	25(3)	-7(2)	17(3)	-22(3)
C13E	36(3)	18(2)	24(3)	-3(2)	-7(2)	2(2)

C14E	59(4)	18(3)	18(3)	-1(2)	-8(2)	-3(2)
C18E	40(4)	71(5)	53(4)	-41(4)	15(3)	-27(3)
C15E	68(6)	30(4)	29(4)	-2(3)	-27(4)	-3(4)
C16E	36(4)	23(3)	30(4)	-4(3)	-14(3)	-1(3)
C17E	19(3)	22(3)	32(4)	-9(3)	3(3)	2(2)
S1F	42.9(8)	21.4(6)	15.6(7)	-0.3(5)	-5.1(6)	-4.8(5)
Si1F	27.4(8)	13.0(7)	44.5(10)	1.7(6)	14.3(7)	-0.3(6)
F1F	30.2(16)	19.3(15)	26.4(18)	-4.6(12)	-2.8(13)	7.9(12)
O1F	64(3)	21(2)	26(2)	-1.6(16)	-12(2)	-8.3(18)
O2F	59(3)	39(2)	18(2)	-5.7(17)	-5(2)	-5(2)
O3F	33(2)	21.5(19)	26(2)	5.7(16)	-5.2(17)	-8.8(15)
O4F	23.9(19)	13.4(17)	23(2)	2.0(14)	7.4(16)	-3.4(14)
N1F	32(3)	18(2)	24(3)	-1.1(18)	0(2)	-0.2(18)
C1F	30(2)	21.5(19)	29(2)	10.8(17)	-2.6(17)	-0.4(16)
C2F	30(2)	21.5(19)	29(2)	10.8(17)	-2.6(17)	-0.4(16)
C3F	23(3)	11(2)	29(3)	1(2)	9(2)	-4.0(19)
C4F	56(4)	26(3)	63(5)	-4(3)	37(4)	2(3)
C5F	50(4)	40(4)	31(4)	7(3)	1(3)	2(3)
C6F	42(3)	22(2)	62(3)	0(2)	8(2)	-12.9(18)
C7F	42(3)	22(2)	62(3)	0(2)	8(2)	-12.9(18)
C8F	28(3)	30(3)	80(6)	3(3)	9(3)	-8(3)
C9F	57(5)	49(4)	41(4)	-3(3)	-13(4)	-10(3)
C10F	26(3)	11(2)	14(3)	-2.0(18)	-1(2)	-1.2(19)
C11F	23(2)	16(2)	13(2)	-0.4(18)	-5(2)	-1.0(19)
C12F	38(3)	30(3)	20(3)	4(2)	-4(2)	-15(2)
C13F	17(2)	12(2)	21(3)	0.9(18)	2.5(19)	3.6(17)
C14F	19(2)	21(3)	10(2)	-2.3(19)	-0.7(19)	-0.7(19)
C15F	16(2)	25(3)	19(3)	-4(2)	0(2)	-1(2)
C16F	29(3)	22(3)	14(3)	-5(2)	5(2)	-2(2)
C17F	26(3)	38(3)	26(3)	-6(3)	-5(2)	-5(2)
C18F	26(3)	39(3)	24(3)	-11(3)	-5(2)	0(2)
S1G	23.8(6)	20.2(6)	15.4(6)	-2.4(5)	1.5(5)	-6.3(5)
Si1G	32.7(8)	13.8(7)	20.5(8)	-2.4(5)	2.3(6)	-2.8(6)
F1G	27.1(16)	24.5(16)	39(2)	-13.7(14)	-0.5(14)	5.2(13)
O1G	33(2)	24(2)	29(2)	1.8(17)	0.3(18)	-10.2(16)
O2G	38(2)	39(2)	15.4(19)	0.9(16)	3.7(16)	-11.5(17)
O3G	17.0(17)	26.6(19)	18.5(19)	3.6(15)	1.1(15)	-5.1(14)
O4G	26.1(19)	16.0(16)	17.1(19)	-0.2(14)	5.0(15)	-4.4(14)
N1G	20(2)	21(2)	16(2)	-1.6(17)	3.1(18)	-7.7(17)
C1G	18(2)	31(3)	24(3)	5(2)	-3(2)	-1(2)
C2G	16(2)	24(3)	27(3)	1(2)	6(2)	0.5(19)

C3G	19(2)	19(2)	17(3)	-2(2)	8(2)	-1.9(19)
C4R	32.7(8)	13.8(7)	20.5(8)	-2.4(5)	2.3(6)	-2.8(6)
C5R	50(30)	10(20)	20(9)	-3(10)	-2(10)	4(18)
C6G	48(3)	21(2)	31(3)	-8(2)	19(2)	-12(2)
C7G	44(3)	20(3)	30(3)	1(2)	12(3)	-7(2)
C8G	65(5)	20(4)	103(7)	-10(4)	53(5)	-12(4)
C9G	75(5)	33(7)	26(3)	-2(3)	3(3)	-30(4)
C10G	23(3)	12(2)	17(3)	-3.3(19)	3(2)	-0.3(19)
C11G	16(2)	22(3)	14(3)	0(2)	-4(2)	-6.4(19)
C12G	32(3)	32(3)	24(3)	7(2)	-3(3)	-6(2)
C13G	16(2)	14(2)	23(3)	-3(2)	2(2)	-3.8(18)
C14G	15(2)	23(3)	18(3)	1(2)	-4(2)	1.0(19)
C15G	27(3)	27(3)	30(3)	-5(2)	-5(2)	6(2)
C16G	22.3(19)	28(2)	26(2)	-4.3(16)	-3.7(16)	0.2(16)
C17G	22.3(19)	28(2)	26(2)	-4.3(16)	-3.7(16)	0.2(16)
C18G	32(3)	48(4)	22(3)	-7(2)	-1(2)	-1(3)
S1H	21.1(6)	19.8(6)	18.5(7)	-1.1(5)	1.1(5)	0.3(5)
Si1H	25.9(7)	11.4(6)	34.7(8)	1.0(5)	15.9(6)	2.1(5)
F1H	27.3(17)	19.9(16)	31(2)	-1.0(14)	-5.5(14)	5.7(13)
O1H	28(2)	17.8(18)	26(2)	-3.2(15)	2.4(16)	-2.8(15)
O2H	35(2)	31(2)	21(2)	-6.3(17)	5.4(18)	-6.6(18)
O3H	26(2)	20.0(19)	25(2)	1.3(15)	-1.9(16)	-1.2(15)
O4H	21.9(18)	18.1(18)	22(2)	2.9(15)	7.6(16)	1.6(14)
N1H	18(2)	19(2)	21(2)	3.1(18)	0.4(18)	0.4(17)
C1H	29(3)	21(3)	24(3)	6(2)	-4(2)	3(2)
C2H	18(2)	22(3)	29(3)	4(2)	1(2)	7(2)
C3H	16(2)	10(2)	22(3)	0.4(19)	6(2)	1.6(18)
C4H	53(4)	15(2)	63(4)	6(3)	43(3)	7(2)
C5H	41(3)	37(3)	24(3)	6(2)	-3(3)	-4(3)
C6H	28(3)	26(3)	34(3)	-6(2)	-2(2)	-2(2)
C7H	40(3)	22(3)	48(4)	-6(3)	7(3)	-7(2)
C8H	25(3)	26(3)	93(6)	-7(3)	12(3)	-5(2)
C9H	57(4)	44(4)	39(4)	6(3)	-24(3)	-10(3)
C10H	13(2)	19(3)	18(3)	-1(2)	0(2)	3.9(19)
C11H	18(2)	19(2)	19(3)	-1(2)	-8(2)	2(2)
C12H	24(3)	30(3)	20(3)	3(2)	5(2)	-6(2)
C13H	22(3)	14(2)	20(3)	2(2)	-6(2)	1(2)
C14H	16(2)	26(3)	15(3)	-1(2)	3(2)	-4(2)
C15H	23(3)	28(3)	21(3)	0(2)	-5(2)	1(2)
C16H	28(3)	23(3)	19(3)	-2(2)	1(2)	-5(2)
C17H	28(3)	34(3)	30(3)	4(3)	-3(3)	-5(2)

C18H	31(3)	29(3)	24(3)	-6(2)	-3(3)	-6(2)
S1I	18.4(6)	22.1(6)	12.3(6)	-1.0(5)	0.3(5)	-9.2(5)
Si1I	27.3(7)	11.9(6)	17.9(7)	-1.3(5)	0.2(6)	-1.4(5)
F1I	14.9(13)	22.9(15)	35.5(18)	-10.2(13)	-1.6(12)	5.1(11)
O1I	29(2)	14.5(18)	29(2)	-8.6(15)	-0.3(16)	-9.0(14)
O2I	26.6(19)	43(2)	13.1(17)	-1.0(16)	0.5(15)	-11.9(16)
O3I	20.9(18)	20.5(18)	21.4(19)	0.7(14)	-3.2(15)	-4.8(14)
O4I	25.8(18)	13.1(16)	20.8(18)	-2.9(13)	4.0(15)	-2.9(13)
N1I	16.0(19)	15(2)	12(2)	-1.9(15)	3.3(16)	-6.8(15)
C1I	21(2)	20(2)	28(3)	0(2)	-4(2)	6.8(19)
C2I	20(2)	23(2)	22(3)	-2(2)	-1(2)	6.3(19)
C3I	21(2)	12(2)	20(3)	-0.7(18)	-4(2)	-0.1(18)
C4I	59(4)	20(3)	55(4)	-4(3)	32(3)	5(3)
C5I	71(5)	35(3)	33(3)	5(3)	-23(3)	-19(3)
C6I	26(3)	13(2)	32(3)	-4(2)	8(2)	-3.1(19)
C7I	70(5)	56(4)	21(3)	9(3)	-7(3)	-29(4)
C8I	41(3)	17(3)	36(4)	1(2)	5(3)	-8(2)
C9I	67(5)	26(3)	80(5)	-1(3)	48(4)	6(3)
C10I	8(2)	18(2)	11(2)	0.9(18)	1.8(17)	-4.8(17)
C11I	17(2)	25(3)	16(3)	1(2)	-2(2)	-0.1(19)
C12I	22(2)	35(3)	15(2)	6(2)	-4(2)	-15(2)
C13I	12(2)	17(2)	18(3)	-0.8(19)	2.7(19)	2.5(17)
C14I	17(2)	17(2)	19(3)	1(2)	1(2)	-1.6(18)
C15I	12(2)	26(3)	28(3)	-9(2)	1(2)	1.8(19)
C16I	20(2)	22(2)	23(3)	5(2)	-7(2)	-3.4(19)
C17I	19(2)	38(3)	23(3)	-2(2)	-2(2)	4(2)
C18I	21(3)	56(4)	26(3)	-15(3)	2(2)	4(3)
S1J	19.2(6)	24.8(6)	19.1(7)	0.2(5)	0.7(5)	-3.9(5)
Si1J	39.5(9)	18.5(7)	20.4(8)	-0.1(5)	4.3(6)	-6.8(6)
F1J	38.9(19)	19.5(15)	33.3(19)	-3.4(13)	-11.2(15)	8.4(13)
O1J	31(2)	21.5(18)	23(2)	-6.5(15)	3.9(16)	-8.0(15)
O2J	36(2)	52(3)	23(2)	-2.1(18)	2.5(18)	-17.1(19)
O3J	19.4(19)	27(2)	44(3)	4.7(17)	-0.6(17)	-1.8(15)
O4J	27.0(19)	20.1(18)	22(2)	0.2(15)	9.2(16)	-4.8(14)
N1J	18(2)	24(2)	17(2)	-2.9(18)	3.8(17)	-0.3(17)
C1J	31(3)	27(3)	56(4)	14(3)	-10(3)	4(2)
C2J	26(3)	25(3)	52(4)	5(3)	18(3)	6(2)
C3J	28(3)	9(2)	23(3)	0.8(19)	12(2)	-2.2(19)
C4J	42(3)	37(3)	46(4)	13(3)	-20(3)	-14(3)
C5J	107(6)	28(3)	39(4)	-15(3)	40(4)	-19(3)
C6J	29(3)	15(2)	24(3)	3(2)	6(2)	2(2)

C7J	48(4)	11(2)	34(3)	1(2)	9(3)	-3(2)
C8J	45(4)	21(3)	33(3)	7(2)	-7(3)	2(2)
C9J	47(4)	20(3)	44(4)	2(2)	25(3)	-2(2)
C10J	19(2)	20(3)	17(3)	-1(2)	4(2)	-1.1(19)
C11J	35(3)	15(2)	19(3)	-3(2)	4(2)	-1(2)
C12J	41(3)	27(3)	25(3)	-2(2)	9(3)	-11(2)
C13J	28(3)	14(2)	20(3)	-1.1(19)	-2(2)	2.2(19)
C14J	53(3)	22(3)	19(3)	-1(2)	-1(2)	-9(2)
C15S	50(3)	45(3)	18(2)	-1.1(18)	-3.3(18)	-18.3(19)
C16S	50(3)	45(3)	18(2)	-1.1(18)	-3.3(18)	-18.3(19)
C17S	50(3)	45(3)	18(2)	-1.1(18)	-3.3(18)	-18.3(19)
C18S	50(3)	45(3)	18(2)	-1.1(18)	-3.3(18)	-18.3(19)
C15J	50(3)	45(3)	18(2)	-1.1(18)	-3.3(18)	-18.3(19)
C16J	50(3)	45(3)	18(2)	-1.1(18)	-3.3(18)	-18.3(19)
C17J	50(3)	45(3)	18(2)	-1.1(18)	-3.3(18)	-18.3(19)
C18J	51(3)	30(2)	30(3)	-12(2)	15(2)	-11(2)
S1K	20.8(6)	18.3(5)	12.7(6)	-1.7(4)	0.2(5)	-8.0(4)
Si1K	34.6(8)	10.1(6)	16.8(7)	-2.4(5)	6.3(6)	2.2(5)
F1K	17.7(15)	18.5(15)	79(3)	-18.1(16)	-15.0(16)	6.7(12)
O1K	31(2)	14.8(17)	34(2)	-6.7(15)	-6.3(17)	-9.3(14)
O2K	43(2)	37(2)	13.7(18)	-1.6(15)	1.7(16)	-12.8(17)
O3K	14.6(16)	19.2(17)	22.1(19)	3.7(14)	-1.6(14)	-4.2(13)
O4K	20.5(17)	13.4(16)	14.8(18)	-2.3(13)	3.2(14)	-4.8(13)
N1K	16.0(19)	14.8(19)	16(2)	-4.6(16)	5.6(16)	-7.2(15)
C1K	20(2)	12(2)	30(3)	5(2)	-3(2)	0.6(18)
C2K	24(3)	24(3)	17(3)	1(2)	6(2)	5(2)
C3K	18(2)	13(2)	9(2)	2.0(17)	0.9(18)	1.7(17)
C4K	42(4)	28(3)	125(7)	25(4)	26(4)	11(3)
C5K	153(8)	37(4)	37(4)	-14(3)	15(5)	-25(4)
C6K	32(3)	14(2)	49(4)	1(2)	12(3)	-9(2)
C7K	37(4)	21(3)	65(5)	2(3)	2(3)	-13(3)
C8K	28(3)	33(3)	116(7)	20(4)	14(4)	2(3)
C9K	93(6)	39(4)	32(4)	-9(3)	39(4)	-28(4)
C10K	13(2)	14(2)	12(2)	-2.0(18)	1.8(18)	-2.8(17)
C11K	22(2)	18(2)	13(3)	0.7(19)	-2(2)	0.5(19)
C12K	29(3)	22(3)	16(3)	7(2)	-3(2)	-11(2)
C13K	14(2)	17(2)	28(3)	-7(2)	-3(2)	0.9(18)
C14K	32(3)	22(2)	28(3)	1.2(19)	-11(2)	-8.6(18)
C15K	32(3)	22(2)	28(3)	1.2(19)	-11(2)	-8.6(18)
C16K	22(4)	24(4)	28(4)	3(3)	-10(3)	-5(3)
C17K	21(4)	33(4)	25(4)	-5(3)	0(3)	0(3)

C18K	29(4)	49(5)	25(4)	-14(4)	6(3)	-9(4)
C4G	53(4)	19(3)	51(4)	-3(3)	26(3)	4(3)
C5G	65(5)	28(3)	38(4)	4(3)	-24(4)	-20(3)
C8R	65(5)	20(4)	103(7)	-10(4)	53(5)	-12(4)
C9R	75(5)	33(7)	26(3)	-2(3)	3(3)	-30(4)
Si1M	25.3(10)	10.2(8)	15.0(12)	-0.3(9)	2.8(11)	-2.2(7)

Table E.12. Bond Lengths for 1 phase II.

Atom	Atom	Length/Å	Atom	Atom	Length/Å	Atom	Atom	Length/Å
S1	O1	1.429(4)	S1F	O1F	1.409(4)	C6G	C8G	1.538(5)
S1	O2	1.433(4)	S1F	O2F	1.427(5)	C6G	C9G	1.542(6)
S1	O3	1.575(4)	S1F	O3F	1.572(5)	C6G	C8R	1.545(6)
S1	N1	1.623(4)	S1F	N1F	1.620(5)	C6G	C9R	1.540(6)
C3	O4	1.406(5)	Si1F	O4F	1.667(4)	C10G	C11G	1.454(7)
C3	C2	1.528(7)	Si1F	C4F	1.868(7)	C10G	C13G	1.548(7)
C3	C10	1.548(7)	Si1F	C5F	1.874(7)	C11G	C12G	1.195(8)
O4	Si1	1.697(3)	Si1F	C6F	1.878(7)	C13G	C14G	1.513(7)
Si1	C4	1.859(5)	F1F	C13F	1.406(6)	C14G	C15G	1.537(7)
Si1	C5	1.860(5)	O3F	C1F	1.467(7)	C15G	C16G	1.521(7)
Si1	C6	1.885(5)	O4F	C3F	1.432(6)	C16G	C17G	1.514(7)
C6	C7	1.546(6)	N1F	C10F	1.490(7)	C17G	C18G	1.523(7)
C6	C8	1.532(6)	C1F	C2F	1.517(9)	S1H	O1H	1.413(4)
C6	C9	1.543(7)	C2F	C3F	1.545(8)	S1H	O2H	1.418(5)
F1	C13	1.407(6)	C3F	C10F	1.565(7)	S1H	O3H	1.573(4)
O3	C1	1.469(6)	C6F	C7F	1.531(8)	S1H	N1H	1.621(5)
N1	C10	1.491(7)	C6F	C8F	1.516(9)	Si1H	O4H	1.664(4)
C1	C2	1.517(8)	C6F	C9F	1.541(10)	Si1H	C4H	1.875(6)
C10	C11	1.476(7)	C10F	C11F	1.468(8)	Si1H	C5H	1.875(6)
C10	C13	1.520(7)	C10F	C13F	1.569(7)	Si1H	C6H	1.872(6)
C11	C12	1.177(8)	C11F	C12F	1.179(8)	F1H	C13H	1.399(6)
C13	C14	1.503(5)	C13F	C14F	1.518(7)	O3H	C1H	1.475(7)
C14	C15	1.524(5)	C14F	C15F	1.531(7)	O4H	C3H	1.430(6)
C15	C16	1.532(5)	C15F	C16F	1.529(7)	N1H	C10H	1.464(7)
C16	C17	1.519(5)	C16F	C17F	1.527(7)	C1H	C2H	1.506(8)
C17	C18	1.530(5)	C17F	C18F	1.517(8)	C2H	C3H	1.542(7)
S1A	O1A	1.417(4)	S1G	O1G	1.412(4)	C3H	C10H	1.565(7)
S1A	O2A	1.428(5)	S1G	O2G	1.430(4)	C6H	C7H	1.538(7)
S1A	O3A	1.574(4)	S1G	O3G	1.577(4)	C6H	C8H	1.533(8)
S1A	N1A	1.615(5)	S1G	N1G	1.621(5)	C6H	C9H	1.524(8)
C3A	O4A	1.405(5)	Si1G	O4G	1.684(4)	C10H	C11H	1.473(8)

C3A	C2A	1.519(7)	Si1G	C4R	1.861(11)	C10H	C13H	1.571(7)
C3A	C10A	1.562(7)	Si1G	C5R	1.856(11)	C11H	C12H	1.179(8)
O4A	Si1A	1.684(3)	Si1G	C6G	1.870(6)	C13H	C14H	1.515(7)
O4A	Si1L	1.741(4)	Si1G	C4G	1.848(6)	C14H	C15H	1.532(7)
O4A	Si1M	1.747(8)	Si1G	C5G	1.862(6)	C15H	C16H	1.518(7)
Si1A	C4A	1.857(6)	F1G	C13G	1.397(6)	C16H	C17H	1.530(7)
Si1A	C5A	1.869(6)	O3G	C1G	1.442(7)	C17H	C18H	1.500(8)
Si1A	C6A	1.886(6)	O4G	C3G	1.426(6)	S1I	O1I	1.432(4)
C6A	C7A	1.548(7)	N1G	C10G	1.494(7)	S1I	O2I	1.427(4)
C6A	C8A	1.528(7)	C1G	C2G	1.519(8)	S1I	O3I	1.565(4)
C6A	C9A	1.546(8)	C2G	C3G	1.520(7)	S1I	N1I	1.619(4)
Si1L	C5L	1.841(7)	C3G	C10G	1.567(7)	Si1I	O4I	1.665(3)
Si1L	C4L	1.860(7)	C6G	C7G	1.540(5)	Si1I	C4I	1.876(6)
Si1L	C6L	1.889(6)	N1D	C10D	1.487(7)	Si1I	C5I	1.851(6)
C6L	C8L	1.551(7)	C1D	C2D	1.515(8)	Si1I	C6I	1.892(6)
C6L	C7L	1.528(8)	C2D	C3D	1.556(7)	F1I	C13I	1.400(5)
C6L	C9L	1.539(8)	C3D	C10D	1.557(7)	O3I	C1I	1.487(6)
F1A	C13A	1.409(6)	C6D	C7D	1.541(7)	O4I	C3I	1.409(6)
O3A	C1A	1.470(7)	C6D	C8D	1.533(7)	N1I	C10I	1.479(7)
N1A	C10A	1.475(7)	C6D	C9D	1.540(8)	C1I	C2I	1.523(7)
C1A	C2A	1.502(8)	C10D	C11D	1.471(7)	C2I	C3I	1.544(7)
C10A	C11A	1.464(7)	C10D	C13D	1.541(7)	C3I	C10I	1.549(7)
C10A	C13A	1.543(7)	C11D	C12D	1.178(8)	C6I	C7I	1.537(8)
C11A	C12A	1.185(8)	C13D	C14D	1.501(7)	C6I	C8I	1.533(7)
C13A	C14A	1.510(7)	C14D	C15D	1.517(7)	C6I	C9I	1.524(7)
C14A	C15A	1.532(7)	C15D	C16D	1.529(8)	C10I	C11I	1.487(7)
C15A	C16A	1.516(8)	C16D	C17D	1.528(8)	C10I	C13I	1.548(6)
C16A	C17A	1.513(7)	C17D	C18D	1.522(8)	C11I	C12I	1.175(8)
C17A	C18A	1.503(8)	S1E	O1E	1.409(4)	C13I	C14I	1.512(7)
S1B	O1B	1.427(5)	S1E	O2E	1.426(4)	C14I	C15I	1.524(6)
S1B	O2B	1.419(5)	S1E	O3E	1.567(5)	C15I	C16I	1.535(7)
S1B	O3B	1.566(5)	S1E	N1E	1.614(5)	C16I	C17I	1.531(8)
S1B	N1B	1.612(5)	Si1E	O4E	1.677(3)	C17I	C18I	1.536(8)
Si1B	O4B	1.686(4)	Si1E	C4E	1.856(6)	S1J	O1J	1.427(4)
Si1B	C4B	1.854(6)	Si1E	C5E	1.873(7)	S1J	O2J	1.428(5)
Si1B	C5B	1.857(7)	Si1E	C6E	1.864(6)	S1J	O3J	1.561(4)
Si1B	C6B	1.874(7)	F1E	C13E	1.408(6)	S1J	N1J	1.622(5)
F1B	C13B	1.411(6)	O3E	C1E	1.464(7)	Si1J	O4J	1.676(4)
O3B	C1B	1.449(8)	O4E	C3E	1.439(6)	Si1J	C4J	1.872(6)
O4B	C3B	1.417(6)	N1E	C10E	1.490(7)	Si1J	C5J	1.851(7)
N1B	C10B	1.491(7)	C1E	C2E	1.525(10)	Si1J	C6J	1.876(5)

C1B	C2B	1.499(9)	C2E	C3E	1.526(8)	F1J	C13J	1.406(6)
C2B	C3B	1.510(8)	C3E	C10E	1.557(7)	O3J	C1J	1.468(7)
C3B	C10B	1.561(7)	C6E	C7E	1.543(7)	O4J	C3J	1.426(6)
C6B	C7B	1.558(8)	C6E	C8E	1.550(7)	N1J	C10J	1.473(7)
C6B	C8B	1.545(8)	C6E	C9E	1.515(8)	C1J	C2J	1.503(10)
C6B	C9B	1.537(9)	C10E	C11E	1.468(8)	C2J	C3J	1.523(8)
C10B	C11B	1.454(8)	C10E	C13E	1.549(8)	C3J	C10J	1.555(7)
C10B	C13B	1.556(7)	C11E	C12E	1.183(8)	C6J	C7J	1.538(7)
C11B	C12B	1.193(9)	C13E	C14E	1.491(7)	C6J	C8J	1.544(8)
C13B	C14B	1.512(7)	C14E	C15P	1.517(11)	C6J	C9J	1.532(7)
C14B	C15B	1.526(7)	C14E	C15E	1.553(8)	C10J	C11J	1.464(8)
C15B	C16B	1.519(8)	C15P	C16P	1.565(12)	C10J	C13J	1.550(7)
C16B	C17B	1.508(8)	C16P	C17P	1.503(12)	C11J	C12J	1.198(8)
C17B	C18B	1.503(9)	C17P	C18E	1.529(12)	C13J	C14J	1.513(5)
S1C	O1C	1.418(4)	C18E	C17E	1.566(8)	C14J	C15S	1.532(7)
S1C	O2C	1.431(4)	C15E	C16E	1.535(8)	C14J	C15J	1.505(6)
S1C	O3C	1.575(4)	C16E	C17E	1.508(7)	C15S	C16S	1.527(7)
S1C	N1C	1.619(4)	S1D	O2D	1.421(5)	C16S	C17S	1.516(6)
C3C	O4C	1.408(5)	S1D	O3D	1.572(5)	C17S	C18S	1.532(6)
C3C	C2C	1.527(7)	S1D	N1D	1.624(5)	C15J	C16J	1.549(6)
C3C	C10C	1.556(7)	Si1D	O4D	1.670(4)	C16J	C17J	1.521(6)
O4C	Si1N	1.681(4)	Si1D	C4D	1.863(6)	C17J	C18J	1.530(6)
O4C	Si1C	1.723(3)	Si1D	C5D	1.859(6)	S1K	O1K	1.424(4)
Si1N	C4N	1.858(6)	Si1D	C6D	1.868(6)	S1K	O2K	1.425(4)
Si1N	C5N	1.863(7)	F1D	C13D	1.394(6)	S1K	O3K	1.567(4)
Si1N	C6N	1.892(6)	O3D	C1D	1.480(7)	S1K	N1K	1.622(4)
C6N	C7N	1.548(7)	O4D	C3D	1.432(6)	Si1K	O4K	1.649(4)
C6N	C8N	1.525(7)	C17T	C18T	1.528(7)	Si1K	C4K	1.875(6)
C6N	C9N	1.541(8)	C15K	C16K	1.533(6)	Si1K	C5K	1.846(7)
Si1C	C4C	1.854(6)	C16K	C17K	1.523(5)	Si1K	C6K	1.869(6)
Si1C	C5C	1.867(6)	C17K	C18K	1.526(5)	F1K	C13K	1.396(6)
Si1C	C6C	1.882(5)	Si1M	C5M	1.8937	O3K	C1K	1.488(6)
C6C	C7C	1.549(6)	Si1M	C4M	1.8933	O4K	C3K	1.428(6)
C6C	C8C	1.529(7)	Si1M	C6M	1.9116	N1K	C10K	1.477(7)
C6C	C9C	1.545(7)	C6M	C8M	1.5454	C1K	C2K	1.518(8)
F1C	C13C	1.406(6)	C6M	C7M	1.5447	C2K	C3K	1.540(7)
O3C	C1C	1.472(7)	C6M	C9M	1.5431	C3K	C10K	1.558(7)
N1C	C10C	1.493(6)	C15C	C16C	1.514(7)	C6K	C7K	1.540(7)
C1C	C2C	1.519(8)	C16C	C17C	1.534(6)	C6K	C8K	1.549(8)
C10C	C11C	1.473(7)	C17C	C18C	1.527(8)	C6K	C9K	1.501(9)
C10C	C13C	1.534(7)	S1D	O1D	1.421(5)	C10K	C11K	1.486(7)

C11C	C12C	1.177(8)	C14K	C15K	1.540(6)	C10K	C13K	1.546(6)
C13C	C14C	1.503(7)	C15T	C16T	1.548(7)	C11K	C12K	1.170(8)
C14C	C15C	1.519(6)	C16T	C17T	1.516(6)	C13K	C14K	1.501(6)
C14K	C15T	1.501(6)						

Table E.13. Bond Angles for 1 phase II.

Atom	Atom	Atom	Angle/°	Atom	Atom	Atom	Angle/°	Atom	Atom	Atom	Angle/°
O1	S1	O2	119.5(3)	O1F	S1F	O2F	119.7(3)	N1I	C10I	C3I	108.7(4)
O1	S1	O3	103.4(2)	O1F	S1F	O3F	103.9(3)	N1I	C10I	C11I	113.1(4)
O1	S1	N1	112.2(2)	O1F	S1F	N1F	111.8(3)	N1I	C10I	C13I	105.1(4)
O2	S1	O3	110.3(3)	O2F	S1F	O3F	110.4(3)	C11I	C10I	C3I	110.2(4)
O2	S1	N1	105.3(2)	O2F	S1F	N1F	104.8(3)	C11I	C10I	C13I	108.9(4)
O3	S1	N1	105.5(2)	O3F	S1F	N1F	105.5(2)	C13I	C10I	C3I	110.7(4)
O4	C3	C2	111.6(4)	O4F	Si1F	C4F	111.2(3)	C12I	C11I	C10I	175.0(6)
O4	C3	C10	106.3(4)	O4F	Si1F	C5F	105.9(3)	F1I	C13I	C10I	107.3(4)
C2	C3	C10	114.8(4)	O4F	Si1F	C6F	108.2(3)	F1I	C13I	C14I	108.6(4)
C3	O4	Si1	128.1(3)	C4F	Si1F	C5F	111.3(4)	C14I	C13I	C10I	116.9(4)
O4	Si1	C4	107.4(2)	C4F	Si1F	C6F	110.1(4)	C13I	C14I	C15I	112.2(4)
O4	Si1	C5	109.4(2)	C5F	Si1F	C6F	110.1(3)	C14I	C15I	C16I	114.6(4)
O4	Si1	C6	107.5(2)	C1F	O3F	S1F	116.1(4)	C17I	C16I	C15I	113.8(4)
C4	Si1	C5	111.6(3)	C3F	O4F	Si1F	126.8(3)	C16I	C17I	C18I	110.7(5)
C4	Si1	C6	111.2(2)	C10F	N1F	S1F	124.3(4)	O1J	S1J	O2J	118.9(3)
C5	Si1	C6	109.7(2)	O3F	C1F	C2F	109.0(5)	O1J	S1J	O3J	103.6(2)
C7	C6	Si1	109.1(3)	C1F	C2F	C3F	116.9(5)	O1J	S1J	N1J	111.0(2)
C8	C6	Si1	110.7(4)	O4F	C3F	C2F	111.7(5)	O2J	S1J	O3J	110.9(3)
C8	C6	C7	108.3(4)	O4F	C3F	C10F	105.5(4)	O2J	S1J	N1J	106.2(3)
C8	C6	C9	109.8(5)	C2F	C3F	C10F	112.1(4)	O3J	S1J	N1J	105.4(2)
C9	C6	Si1	110.4(3)	C7F	C6F	Si1F	109.0(5)	O4J	Si1J	C4J	106.9(2)
C9	C6	C7	108.5(4)	C7F	C6F	C9F	110.7(6)	O4J	Si1J	C5J	110.2(3)
C1	O3	S1	116.5(3)	C8F	C6F	Si1F	111.3(5)	O4J	Si1J	C6J	106.9(2)
C10	N1	S1	124.9(4)	C8F	C6F	C7F	109.6(6)	C4J	Si1J	C6J	109.8(3)
O3	C1	C2	109.7(4)	C8F	C6F	C9F	106.6(6)	C5J	Si1J	C4J	110.9(4)
C1	C2	C3	117.8(5)	C9F	C6F	Si1F	109.7(5)	C5J	Si1J	C6J	111.9(3)
N1	C10	C3	108.7(4)	N1F	C10F	C3F	110.2(4)	C1J	O3J	S1J	117.7(4)
N1	C10	C13	105.2(4)	N1F	C10F	C13F	103.8(4)	C3J	O4J	Si1J	125.9(3)
C11	C10	C3	109.2(4)	C3F	C10F	C13F	110.2(4)	C10J	N1J	S1J	124.4(4)
C11	C10	N1	112.1(4)	C11F	C10F	N1F	112.9(4)	O3J	C1J	C2J	110.5(5)
C11	C10	C13	110.3(4)	C11F	C10F	C3F	109.5(4)	C1J	C2J	C3J	117.9(5)
C13	C10	C3	111.3(4)	C11F	C10F	C13F	110.2(4)	O4J	C3J	C2J	109.5(5)

C12	C11	C10	177.2(6)	C12F	C11F	C10F	175.7(6)	O4J	C3J	C10J	106.6(4)
F1	C13	C10	107.9(4)	F1F	C13F	C10F	106.3(4)	C2J	C3J	C10J	114.4(4)
F1	C13	C14	107.8(4)	F1F	C13F	C14F	108.1(4)	C7J	C6J	Si1J	109.9(4)
C14	C13	C10	116.8(4)	C14F	C13F	C10F	115.5(4)	C7J	C6J	C8J	110.2(5)
C13	C14	C15	112.8(4)	C13F	C14F	C15F	111.5(4)	C8J	C6J	Si1J	109.6(4)
C14	C15	C16	112.8(4)	C16F	C15F	C14F	112.4(4)	C9J	C6J	Si1J	109.1(4)
C17	C16	C15	113.2(4)	C17F	C16F	C15F	113.2(5)	C9J	C6J	C7J	109.2(5)
C16	C17	C18	112.1(4)	C18F	C17F	C16F	112.8(5)	C9J	C6J	C8J	108.9(5)
O1A	S1A	O2A	119.3(3)	O1G	S1G	O2G	118.9(3)	N1J	C10J	C3J	110.7(4)
O1A	S1A	O3A	104.0(3)	O1G	S1G	O3G	104.2(2)	N1J	C10J	C13J	104.0(4)
O1A	S1A	N1A	111.9(2)	O1G	S1G	N1G	110.8(3)	C11J	C10J	N1J	112.3(4)
O2A	S1A	O3A	109.5(3)	O2G	S1G	O3G	110.5(2)	C11J	C10J	C3J	108.3(4)
O2A	S1A	N1A	106.2(3)	O2G	S1G	N1G	105.8(2)	C11J	C10J	C13J	110.8(5)
O3A	S1A	N1A	105.1(2)	O3G	S1G	N1G	106.0(2)	C13J	C10J	C3J	110.7(4)
O4A	C3A	C2A	112.1(4)	O4G	Si1G	C4R	93.9(19)	C12J	C11J	C10J	174.3(6)
O4A	C3A	C10A	106.2(4)	O4G	Si1G	C5R	114(2)	F1J	C13J	C10J	107.0(4)
C2A	C3A	C10A	113.9(4)	O4G	Si1G	C6G	101.8(2)	F1J	C13J	C14J	107.6(4)
C3A	O4A	Si1A	131.7(3)	O4G	Si1G	C4G	111.6(3)	C14J	C13J	C10J	115.4(4)
C3A	O4A	Si1L	118.5(3)	O4G	Si1G	C5G	109.2(2)	C13J	C14J	C15S	107.6(5)
C3A	O4A	Si1M	133.1(4)	C4R	Si1G	C6G	89(2)	C15J	C14J	C13J	116.1(5)
O4A	Si1A	C4A	110.5(3)	C5R	Si1G	C4R	114(3)	C16S	C15S	C14J	116.8(8)
O4A	Si1A	C5A	107.8(3)	C5R	Si1G	C6G	135(3)	C17S	C16S	C15S	113.2(8)
O4A	Si1A	C6A	105.6(3)	C4G	Si1G	C6G	113.5(3)	C16S	C17S	C18S	111.4(7)
C4A	Si1A	C5A	111.4(4)	C4G	Si1G	C5G	108.2(4)	C14J	C15J	C16J	110.9(6)
C4A	Si1A	C6A	111.5(4)	C5G	Si1G	C6G	112.4(3)	C17J	C16J	C15J	109.5(6)
C5A	Si1A	C6A	109.8(3)	C1G	O3G	S1G	118.0(3)	C16J	C17J	C18J	111.8(6)
C7A	C6A	Si1A	109.1(5)	C3G	O4G	Si1G	127.1(3)	O1K	S1K	O2K	120.7(3)
C8A	C6A	Si1A	110.6(5)	C10G	N1G	S1G	123.9(4)	O1K	S1K	O3K	103.0(2)
C8A	C6A	C7A	108.5(6)	O3G	C1G	C2G	111.2(4)	O1K	S1K	N1K	110.9(2)
C8A	C6A	C9A	109.9(6)	C1G	C2G	C3G	117.1(5)	O2K	S1K	O3K	109.8(2)
C9A	C6A	Si1A	110.0(5)	O4G	C3G	C2G	110.7(4)	O2K	S1K	N1K	105.7(2)
C9A	C6A	C7A	108.8(6)	O4G	C3G	C10G	105.2(4)	O3K	S1K	N1K	105.9(2)
O4A	Si1L	C5L	111.6(5)	C2G	C3G	C10G	114.1(4)	O4K	Si1K	C4K	109.5(3)
O4A	Si1L	C4L	107.7(5)	C7G	C6G	Si1G	110.7(3)	O4K	Si1K	C5K	109.9(3)
O4A	Si1L	C6L	101.0(3)	C7G	C6G	C9G	105.3(7)	O4K	Si1K	C6K	104.0(2)
C5L	Si1L	C4L	112.9(6)	C7G	C6G	C8R	96.5(13)	C5K	Si1K	C4K	109.3(5)
C5L	Si1L	C6L	112.5(5)	C7G	C6G	C9R	121.1(12)	C5K	Si1K	C6K	113.6(4)
C4L	Si1L	C6L	110.4(5)	C8G	C6G	Si1G	110.1(4)	C6K	Si1K	C4K	110.5(3)
C8L	C6L	Si1L	107.9(6)	C8G	C6G	C7G	111.7(7)	C1K	O3K	S1K	117.8(3)
C7L	C6L	Si1L	110.0(6)	C8G	C6G	C9G	110.2(7)	C3K	O4K	Si1K	129.0(3)
C7L	C6L	C8L	108.1(7)	C9G	C6G	Si1G	108.8(4)	C10K	N1K	S1K	124.7(3)

C7L	C6L	C9L	110.7(7)	C8R	C6G	Si1G	108.6(6)	O3K	C1K	C2K	109.2(4)
C9L	C6L	Si1L	110.6(6)	C9R	C6G	Si1G	109.8(5)	C1K	C2K	C3K	116.6(4)
C9L	C6L	C8L	109.5(7)	C9R	C6G	C8R	108.8(10)	O4K	C3K	C2K	111.2(4)
C1A	O3A	S1A	117.0(4)	N1G	C10G	C3G	107.5(4)	O4K	C3K	C10K	105.4(4)
C10A	N1A	S1A	125.8(4)	N1G	C10G	C13G	104.8(4)	C2K	C3K	C10K	113.9(4)
O3A	C1A	C2A	110.7(5)	C11G	C10G	N1G	112.9(4)	C7K	C6K	Si1K	110.5(4)
C1A	C2A	C3A	118.0(5)	C11G	C10G	C3G	110.6(5)	C7K	C6K	C8K	109.1(5)
N1A	C10A	C3A	108.8(4)	C11G	C10G	C13G	110.0(4)	C8K	C6K	Si1K	108.5(5)
N1A	C10A	C13A	104.7(4)	C13G	C10G	C3G	110.8(4)	C9K	C6K	Si1K	110.8(4)
C11A	C10A	C3A	109.7(4)	C12G	C11G	C10G	174.3(6)	C9K	C6K	C7K	109.6(5)
C11A	C10A	N1A	112.7(4)	F1G	C13G	C10G	106.7(4)	C9K	C6K	C8K	108.3(6)
C11A	C10A	C13A	109.9(4)	F1G	C13G	C14G	108.1(4)	N1K	C10K	C3K	108.8(4)
C13A	C10A	C3A	111.0(4)	C14G	C13G	C10G	115.8(4)	N1K	C10K	C11K	113.3(4)
C12A	C11A	C10A	173.6(6)	C13G	C14G	C15G	111.2(5)	N1K	C10K	C13K	105.1(4)
F1A	C13A	C10A	106.7(4)	C16G	C15G	C14G	113.6(5)	C11K	C10K	C3K	109.3(4)
F1A	C13A	C14A	108.2(4)	C17G	C16G	C15G	115.2(5)	C11K	C10K	C13K	109.8(4)
C14A	C13A	C10A	116.8(5)	C16G	C17G	C18G	112.6(5)	C13K	C10K	C3K	110.5(4)
C13A	C14A	C15A	111.5(5)	O1H	S1H	O2H	119.5(3)	C12K	C11K	C10K	174.4(6)
C16A	C15A	C14A	112.2(5)	O1H	S1H	O3H	103.4(2)	F1K	C13K	C10K	106.4(4)
C17A	C16A	C15A	114.0(5)	O1H	S1H	N1H	111.5(2)	F1K	C13K	C14K	108.7(4)
C18A	C17A	C16A	115.4(5)	O2H	S1H	O3H	110.5(3)	C14K	C13K	C10K	117.1(4)
O1B	S1B	O3B	104.0(3)	O2H	S1H	N1H	106.1(3)	C13K	C14K	C15K	108.2(4)
O1B	S1B	N1B	111.6(3)	O3H	S1H	N1H	105.0(2)	C15T	C14K	C13K	121.7(6)
O2B	S1B	O1B	119.4(4)	O4H	Si1H	C4H	111.0(2)	C14K	C15T	C16T	111.7(7)
O2B	S1B	O3B	110.2(3)	O4H	Si1H	C5H	106.0(3)	C17T	C16T	C15T	111.6(7)
O2B	S1B	N1B	104.6(3)	O4H	Si1H	C6H	108.0(2)	C16T	C17T	C18T	112.6(7)
O3B	S1B	N1B	106.5(3)	C5H	Si1H	C4H	112.4(3)	C16K	C15K	C14K	114.1(5)
O4B	Si1B	C4B	110.4(3)	C6H	Si1H	C4H	108.5(3)	C17K	C16K	C15K	112.6(5)
O4B	Si1B	C5B	110.0(3)	C6H	Si1H	C5H	110.9(3)	C16K	C17K	C18K	112.3(5)
O4B	Si1B	C6B	103.1(2)	C1H	O3H	S1H	116.7(4)	O4A	Si1M	C5M	113.3(7)
C4B	Si1B	C5B	110.1(4)	C3H	O4H	Si1H	125.1(3)	O4A	Si1M	C4M	105.6(7)
C4B	Si1B	C6B	109.8(3)	C10H	N1H	S1H	124.9(4)	O4A	Si1M	C6M	104.6(6)
C5B	Si1B	C6B	113.2(4)	O3H	C1H	C2H	109.6(5)	C5M	Si1M	C6M	112.3
C1B	O3B	S1B	117.6(4)	C1H	C2H	C3H	117.6(5)	C4M	Si1M	C5M	108.6
C3B	O4B	Si1B	126.0(3)	O4H	C3H	C2H	111.2(4)	C4M	Si1M	C6M	112.3
C10B	N1B	S1B	123.8(4)	O4H	C3H	C10H	106.0(4)	C8M	C6M	Si1M	109.7
O3B	C1B	C2B	111.2(5)	C2H	C3H	C10H	112.6(4)	C7M	C6M	Si1M	109.8
C1B	C2B	C3B	117.8(5)	C7H	C6H	Si1H	108.4(4)	C7M	C6M	C8M	108.8
O4B	C3B	C2B	112.5(4)	C8H	C6H	Si1H	111.5(4)	C9M	C6M	Si1M	110.3
O4B	C3B	C10B	105.8(4)	C8H	C6H	C7H	109.4(5)	C9M	C6M	C8M	109.1
C2B	C3B	C10B	113.4(5)	C9H	C6H	Si1H	110.3(5)	C9M	C6M	C7M	109.2

C7B	C6B	Si1B	110.0(5)	C5D	Si1D	C4D	108.3(3)	C9H	C6H	C7H	109.6(5)
C8B	C6B	Si1B	110.6(5)	C5D	Si1D	C6D	112.5(3)	C9H	C6H	C8H	107.7(6)
C8B	C6B	C7B	109.2(5)	C1D	O3D	S1D	116.7(4)	N1H	C10H	C3H	111.0(4)
C9B	C6B	Si1B	109.5(4)	C3D	O4D	Si1D	125.5(3)	N1H	C10H	C11H	112.3(4)
C9B	C6B	C7B	107.9(6)	C10D	N1D	S1D	124.8(4)	N1H	C10H	C13H	104.5(4)
C9B	C6B	C8B	109.7(6)	O3D	C1D	C2D	109.5(4)	C3H	C10H	C13H	110.1(4)
N1B	C10B	C3B	108.5(4)	C1D	C2D	C3D	116.3(5)	C11H	C10H	C3H	108.6(4)
N1B	C10B	C13B	104.0(4)	O4D	C3D	C2D	111.4(4)	C11H	C10H	C13H	110.3(4)
C11B	C10B	N1B	113.3(5)	O4D	C3D	C10D	105.7(4)	C12H	C11H	C10H	175.8(6)
C11B	C10B	C3B	110.5(5)	C2D	C3D	C10D	113.1(4)	F1H	C13H	C10H	106.4(4)
C11B	C10B	C13B	110.1(4)	C7D	C6D	Si1D	110.0(4)	F1H	C13H	C14H	108.5(4)
C13B	C10B	C3B	110.2(4)	C8D	C6D	Si1D	110.4(4)	C14H	C13H	C10H	115.3(5)
C12B	C11B	C10B	172.4(7)	C8D	C6D	C7D	109.4(4)	C13H	C14H	C15H	111.6(4)
F1B	C13B	C10B	106.1(4)	C8D	C6D	C9D	109.0(5)	C16H	C15H	C14H	112.1(5)
F1B	C13B	C14B	108.2(4)	C9D	C6D	Si1D	109.3(4)	C15H	C16H	C17H	113.7(5)
C14B	C13B	C10B	116.0(5)	C9D	C6D	C7D	108.8(5)	C18H	C17H	C16H	113.9(5)
C13B	C14B	C15B	112.0(5)	N1D	C10D	C3D	109.7(4)	O1I	S1I	O3I	103.0(2)
C16B	C15B	C14B	112.6(5)	N1D	C10D	C13D	103.6(4)	O1I	S1I	N1I	111.2(2)
C17B	C16B	C15B	112.7(5)	C11D	C10D	N1D	112.8(4)	O2I	S1I	O1I	120.1(2)
C18B	C17B	C16B	112.7(6)	C11D	C10D	C3D	108.4(4)	O2I	S1I	O3I	109.6(2)
O1C	S1C	O2C	119.5(3)	C11D	C10D	C13D	111.1(4)	O2I	S1I	N1I	105.9(2)
O1C	S1C	O3C	103.5(2)	C13D	C10D	C3D	111.3(4)	O3I	S1I	N1I	106.2(2)
O1C	S1C	N1C	112.3(2)	C12D	C11D	C10D	173.8(6)	O4I	Si1I	C4I	110.5(2)
O2C	S1C	O3C	110.5(2)	F1D	C13D	C10D	107.2(4)	O4I	Si1I	C5I	110.1(2)
O2C	S1C	N1C	105.5(2)	F1D	C13D	C14D	108.8(4)	O4I	Si1I	C6I	102.8(2)
O3C	S1C	N1C	104.8(2)	C14D	C13D	C10D	116.3(4)	C4I	Si1I	C6I	112.9(3)
O4C	C3C	C2C	111.6(4)	C13D	C14D	C15D	111.8(4)	C5I	Si1I	C4I	107.9(3)
O4C	C3C	C10C	106.9(4)	C14D	C15D	C16D	114.0(5)	C5I	Si1I	C6I	112.6(3)
C2C	C3C	C10C	114.9(4)	C17D	C16D	C15D	113.3(5)	C1I	O3I	S1I	118.0(3)
C3C	O4C	Si1N	122.3(3)	C18D	C17D	C16D	112.9(5)	C3I	O4I	Si1I	127.4(3)
C3C	O4C	Si1C	127.9(3)	O1E	S1E	O2E	118.0(3)	C10I	N1I	S1I	123.9(3)
O4C	Si1N	C4N	111.2(4)	O1E	S1E	O3E	103.8(3)	O3I	C1I	C2I	109.7(4)
O4C	Si1N	C5N	109.5(5)	O1E	S1E	N1E	111.1(3)	C1I	C2I	C3I	116.4(4)
O4C	Si1N	C6N	103.4(3)	O2E	S1E	O3E	112.2(3)	O4I	C3I	C2I	110.5(4)
C4N	Si1N	C5N	111.7(5)	O2E	S1E	N1E	105.8(2)	O4I	C3I	C10I	106.6(4)
C4N	Si1N	C6N	110.3(4)	O3E	S1E	N1E	105.4(2)	C2I	C3I	C10I	113.6(4)
C5N	Si1N	C6N	110.4(5)	O4E	Si1E	C4E	110.6(2)	C7I	C6I	Si1I	107.9(4)
C7N	C6N	Si1N	109.0(6)	O4E	Si1E	C5E	107.3(2)	C8I	C6I	Si1I	111.7(4)
C8N	C6N	Si1N	109.5(5)	O4E	Si1E	C6E	105.8(2)	C8I	C6I	C7I	108.5(5)
C8N	C6N	C7N	109.1(7)	C4E	Si1E	C5E	111.1(4)	C9I	C6I	Si1I	109.8(4)
C8N	C6N	C9N	110.9(7)	C4E	Si1E	C6E	111.2(3)	C9I	C6I	C7I	109.7(6)

C9N	C6N	Si1N	110.6(5)	C6E	Si1E	C5E	110.7(3)	C9I	C6I	C8I	109.2(5)
C9N	C6N	C7N	107.8(7)	C1E	O3E	S1E	115.1(4)	C7E	C6E	Si1E	110.0(4)
O4C	Si1C	C4C	109.4(3)	C3E	O4E	Si1E	125.7(3)	C7E	C6E	C8E	108.5(5)
O4C	Si1C	C5C	107.7(3)	C10E	N1E	S1E	124.8(4)	C8E	C6E	Si1E	109.7(4)
O4C	Si1C	C6C	106.3(2)	O3E	C1E	C2E	107.9(6)	C9E	C6E	Si1E	112.1(4)
C4C	Si1C	C5C	111.6(4)	C1E	C2E	C3E	117.1(5)	C9E	C6E	C7E	109.1(5)
C4C	Si1C	C6C	111.9(3)	O4E	C3E	C2E	109.6(5)	C9E	C6E	C8E	107.3(5)
C5C	Si1C	C6C	109.8(3)	O4E	C3E	C10E	106.0(4)	N1E	C10E	C3E	109.4(4)
C7C	C6C	Si1C	109.3(4)	C2E	C3E	C10E	114.2(5)	N1E	C10E	C13E	105.0(4)
C8C	C6C	Si1C	110.4(4)	F1C	C13C	C10C	107.6(4)	C11E	C10E	N1E	112.3(4)
C8C	C6C	C7C	108.6(5)	F1C	C13C	C14C	108.3(4)	C11E	C10E	C3E	109.5(5)
C8C	C6C	C9C	109.3(5)	C14C	C13C	C10C	116.9(4)	C11E	C10E	C13E	110.2(5)
C9C	C6C	Si1C	110.1(4)	C13C	C14C	C15C	113.0(4)	C13E	C10E	C3E	110.3(4)
C9C	C6C	C7C	109.2(5)	C16C	C15C	C14C	112.3(4)	C12E	C11E	C10E	174.4(6)
C1C	O3C	S1C	116.0(4)	C15C	C16C	C17C	113.5(4)	F1E	C13E	C10E	105.6(4)
C10C	N1C	S1C	124.3(3)	C18C	C17C	C16C	112.0(5)	F1E	C13E	C14E	107.5(4)
O3C	C1C	C2C	109.3(5)	O1D	S1D	O3D	104.0(3)	C14E	C13E	C10E	118.1(5)
C1C	C2C	C3C	116.6(5)	O1D	S1D	N1D	111.0(3)	C13E	C14E	C15P	120.3(9)
N1C	C10C	C3C	109.2(4)	O2D	S1D	O1D	119.0(3)	C13E	C14E	C15E	109.7(5)
N1C	C10C	C13C	105.3(4)	O2D	S1D	O3D	110.8(3)	C14E	C15P	C16P	100.7(11)
C11C	C10C	C3C	109.5(4)	O2D	S1D	N1D	105.4(3)	C17P	C16P	C15P	107.3(12)
C11C	C10C	N1C	112.3(4)	O3D	S1D	N1D	106.0(2)	C16P	C17P	C18E	104.9(11)
C11C	C10C	C13C	109.3(4)	O4D	Si1D	C4D	110.9(2)	C16E	C15E	C14E	115.6(7)
C13C	C10C	C3C	111.2(4)	O4D	Si1D	C5D	111.0(3)	C17E	C16E	C15E	114.0(6)
C12C	C11C	C10C	176.2(6)	O4D	Si1D	C6D	102.7(2)	C16E	C17E	C18E	109.8(5)
C4D	Si1D	C6D	111.4(3)								

Table E.14. Torsion Angles for 1 phase II.

A	B	C	D	Angle/°	A	B	C	D	Angle/°	A	B	C	D	Angle/°
S1	O3	C1	C2	-94.2(5)	C11E	C10E	C13E	F1E	59.2(6)	C2I	C3I	C10I	C13I	173.0(4)
S1	N1	C10	C3	-87.9(5)	C11E	C10E	C13E	C14E	-60.9(6)	C3I	C10I	C13I	F1I	175.3(4)
S1	N1	C10	C11	32.9(6)	C13E	C14E	C15P	C16P	171.6(14)	C3I	C10I	C13I	C14I	-62.6(6)
S1	N1	C10	C13	152.8(4)	C13E	C14E	C15E	C16E	-175.8(6)	C4I	Si1I	O4I	C3I	57.4(5)
C3	O4	Si1	C4	-117.1(5)	C14E	C15P	C16P	C17P	-156(2)	C4I	Si1I	C6I	C7I	56.0(5)
C3	O4	Si1	C5	4.1(5)	C14E	C15E	C16E	C17E	-67.4(9)	C4I	Si1I	C6I	C8I	-63.2(5)
C3	O4	Si1	C6	123.1(4)	C15P	C16P	C17P	C18E	167(2)	C4I	Si1I	C6I	C9I	175.5(5)
C3	C10	C13	F1	-176.5(4)	C15E	C16E	C17E	C18E	-171.0(7)	C5I	Si1I	O4I	C3I	-61.7(5)
C3	C10	C13	C14	61.8(6)	S1F	O3F	C1F	C2F	96.1(5)	C5I	Si1I	C6I	C7I	178.5(4)
O4	C3	C2	C1	64.3(6)	S1F	N1F	C10F	C3F	88.3(5)	C5I	Si1I	C6I	C8I	59.3(5)
O4	C3	C10	N1	-58.6(5)	S1F	N1F	C10F	C11F	-34.5(6)	C5I	Si1I	C6I	C9I	-61.9(5)

O4	C3	C10	C11	178.8(4)	S1F	N1F	C10F	C13F	-153.8(4)	C6I	Si1I	O4I	C3I	178.2(4)
O4	C3	C10	C13	56.9(5)	Si1F	O4F	C3F	C2F	-73.0(6)	C10I	C13I	C14I	C15I	179.7(4)
O4	Si1	C6	C7	165.5(4)	Si1F	O4F	C3F	C10F	164.9(4)	C11I	C10I	C13I	F1I	-63.4(5)
O4	Si1	C6	C8	-75.5(4)	F1F	C13F	C14F	C15F	-65.0(6)	C11I	C10I	C13I	C14I	58.7(6)
O4	Si1	C6	C9	46.3(4)	O1F	S1F	O3F	C1F	-162.7(4)	C13I	C14I	C15I	C16I	178.2(4)
C4	Si1	C6	C7	48.2(4)	O1F	S1F	N1F	C10F	70.8(5)	C14I	C15I	C16I	C17I	66.1(6)
C4	Si1	C6	C8	167.3(4)	O2F	S1F	O3F	C1F	67.8(4)	C15I	C16I	C17I	C18I	172.3(5)
C4	Si1	C6	C9	-70.9(4)	O2F	S1F	N1F	C10F	-158.1(4)	S1J	O3J	C1J	C2J	94.2(6)
C5	Si1	C6	C7	-75.7(4)	O3F	S1F	N1F	C10F	-41.5(5)	S1J	N1J	C10J	C3J	86.8(5)
C5	Si1	C6	C8	43.3(4)	O3F	C1F	C2F	C3F	-80.5(6)	S1J	N1J	C10J	C11J	-34.5(7)
C5	Si1	C6	C9	165.2(4)	O4F	Si1F	C6F	C7F	-160.8(5)	S1J	N1J	C10J	C13J	-154.3(4)
F1	C13	C14	C15	65.5(5)	O4F	Si1F	C6F	C8F	-39.8(6)	Si1J	O4J	C3J	C2J	-96.3(5)
O1	S1	O3	C1	162.8(4)	O4F	Si1F	C6F	C9F	77.9(5)	Si1J	O4J	C3J	C10J	139.6(4)
O1	S1	N1	C10	-69.5(5)	O4F	C3F	C10F	N1F	55.4(6)	F1J	C13J	C14J	C15S	-63.4(11)
O2	S1	O3	C1	-68.3(4)	O4F	C3F	C10F	C11F	-179.8(4)	F1J	C13J	C14J	C15J	-61.8(9)
O2	S1	N1	C10	159.0(4)	O4F	C3F	C10F	C13F	-58.5(6)	O1J	S1J	O3J	C1J	-162.1(5)
O3	S1	N1	C10	42.3(5)	N1F	S1F	O3F	C1F	-44.9(5)	O1J	S1J	N1J	C10J	71.2(5)
O3	C1	C2	C3	77.2(6)	N1F	C10F	C13F	F1F	62.3(5)	O2J	S1J	O3J	C1J	69.1(5)
N1	S1	O3	C1	44.9(4)	N1F	C10F	C13F	C14F	-177.8(4)	O2J	S1J	N1J	C10J	-158.1(4)
N1	C10	C13	F1	-58.9(5)	C1F	C2F	C3F	O4F	-59.8(6)	O3J	S1J	N1J	C10J	-40.4(5)
N1	C10	C13	C14	179.5(4)	C1F	C2F	C3F	C10F	58.4(6)	O3J	C1J	C2J	C3J	-75.7(7)
C2	C3	O4	Si1	69.6(6)	C2F	C3F	C10F	N1F	-66.4(6)	O4J	Si1J	C6J	C7J	-176.3(4)
C2	C3	C10	N1	65.3(5)	C2F	C3F	C10F	C11F	58.4(6)	O4J	Si1J	C6J	C8J	-55.0(4)
C2	C3	C10	C11	-57.2(6)	C2F	C3F	C10F	C13F	179.7(5)	O4J	Si1J	C6J	C9J	64.1(4)
C2	C3	C10	C13	-179.2(4)	C3F	C10F	C13F	F1F	-179.8(4)	O4J	C3J	C10J	N1J	55.8(6)
C10	C3	O4	Si1	-164.4(3)	C3F	C10F	C13F	C14F	-59.9(6)	O4J	C3J	C10J	C11J	179.3(4)
C10	C3	C2	C1	-56.8(6)	C4F	Si1F	O4F	C3F	-2.2(6)	O4J	C3J	C10J	C13J	-59.0(6)
C10	C13	C14	C15	-172.8(4)	C4F	Si1F	C6F	C7F	77.5(6)	N1J	S1J	O3J	C1J	-45.4(5)
C11	C10	C13	F1	62.2(5)	C4F	Si1F	C6F	C8F	-161.5(5)	N1J	C10J	C13J	F1J	62.2(5)
C11	C10	C13	C14	-59.5(6)	C4F	Si1F	C6F	C9F	-43.9(6)	N1J	C10J	C13J	C14J	-178.0(5)
C13	C14	C15	C16	-179.7(4)	C5F	Si1F	O4F	C3F	118.8(5)	C1J	C2J	C3J	O4J	-64.3(6)
C14	C15	C16	C17	-174.9(5)	C5F	Si1F	C6F	C7F	-45.6(6)	C1J	C2J	C3J	C10J	55.2(7)
C15	C16	C17	C18	-177.0(5)	C5F	Si1F	C6F	C8F	75.4(6)	C2J	C3J	C10J	N1J	-65.3(6)
S1A	O3A	C1A	C2A	-93.2(5)	C5F	Si1F	C6F	C9F	-166.9(5)	C2J	C3J	C10J	C11J	58.3(6)
S1A	N1A	C10A	C3A	-88.0(5)	C6F	Si1F	O4F	C3F	-123.2(5)	C2J	C3J	C10J	C13J	179.9(5)
S1A	N1A	C10A	C11A	33.8(6)	C10F	C13F	C14F	C15F	176.2(4)	C3J	C10J	C13J	F1J	-178.8(4)
S1A	N1A	C10A	C13A	153.3(4)	C11F	C10F	C13F	F1F	-58.9(5)	C3J	C10J	C13J	C14J	-59.0(6)
C3A	O4A	Si1A	C4A	-112.9(5)	C11F	C10F	C13F	C14F	61.0(6)	C4J	Si1J	O4J	C3J	-107.8(5)
C3A	O4A	Si1A	C5A	9.1(6)	C13F	C14F	C15F	C16F	176.9(5)	C4J	Si1J	C6J	C7J	68.1(5)
C3A	O4A	Si1A	C6A	126.4(5)	C14F	C15F	C16F	C17F	172.5(5)	C4J	Si1J	C6J	C8J	-170.7(4)
C3A	O4A	Si1L	C5L	56.7(7)	C15F	C16F	C17F	C18F	177.8(5)	C4J	Si1J	C6J	C9J	-51.5(5)

C3A	O4A	Si1L	C4L	-67.8(7)	S1G	O3G	C1G	C2G	-92.9(5)	C5J	Si1J	O4J	C3J	12.8(5)
C3A	O4A	Si1L	C6L	176.4(5)	S1G	N1G	C10G	C3G	-86.9(5)	C5J	Si1J	C6J	C7J	-55.6(5)
C3A	O4A	Si1M	C5M	97.2(7)	S1G	N1G	C10G	C11G	35.5(6)	C5J	Si1J	C6J	C8J	65.6(5)
C3A	O4A	Si1M	C4M	-21.5(7)	S1G	N1G	C10G	C13G	155.1(4)	C5J	Si1J	C6J	C9J	-175.2(4)
C3A	O4A	Si1M	C6M	-140.1(6)	Si1G	O4G	C3G	C2G	93.1(5)	C6J	Si1J	O4J	C3J	134.6(4)
C3A	C10A	C13A	F1A	-179.3(4)	Si1G	O4G	C3G	C10G	-143.2(4)	C10J	C13J	C14J	C15S	177.1(10)
C3A	C10A	C13A	C14A	59.6(6)	F1G	C13G	C14G	C15G	60.5(6)	C10J	C13J	C14J	C15J	178.8(8)
O4A	C3A	C2A	C1A	63.2(6)	O1G	S1G	O3G	C1G	166.1(4)	C11J	C10J	C13J	F1J	-58.6(6)
O4A	C3A	C10A	N1A	-57.7(5)	O1G	S1G	N1G	C10G	-75.9(5)	C11J	C10J	C13J	C14J	61.2(6)
O4A	C3A	C10A	C11A	178.7(4)	O2G	S1G	O3G	C1G	-65.1(4)	C13J	C14J	C15S	C16S	176.3(11)
O4A	C3A	C10A	C13A	57.0(5)	O2G	S1G	N1G	C10G	154.0(4)	C13J	C14J	C15J	C16J	-171.5(8)
O4A	Si1A	C6A	C7A	166.2(6)	O3G	S1G	N1G	C10G	36.6(5)	C14J	C15S	C16S	C17S	79.1(18)
O4A	Si1A	C6A	C8A	-74.6(6)	O3G	C1G	C2G	C3G	73.6(6)	C14J	C15J	C16J	C17J	175.9(10)
O4A	Si1A	C6A	C9A	46.9(6)	O4G	Si1G	C6G	C7G	-175.4(4)	C15S	C16S	C17S	C18S	170.0(13)
O4A	Si1L	C6L	C8L	-73.5(8)	O4G	Si1G	C6G	C8G	-51.4(8)	C15J	C16J	C17J	C18J	179.4(10)
O4A	Si1L	C6L	C7L	44.1(8)	O4G	Si1G	C6G	C9G	69.5(8)	S1K	O3K	C1K	C2K	94.1(5)
O4A	Si1L	C6L	C9L	166.8(8)	O4G	Si1G	C6G	C8R	-70.5(15)	S1K	N1K	C10K	C3K	86.4(5)
C4A	Si1A	C6A	C7A	46.1(7)	O4G	Si1G	C6G	C9R	48.3(15)	S1K	N1K	C10K	C11K	-35.2(6)
C4A	Si1A	C6A	C8A	165.3(6)	O4G	C3G	C10G	N1G	-49.5(5)	S1K	N1K	C10K	C13K	-155.2(4)
C4A	Si1A	C6A	C9A	-73.1(6)	O4G	C3G	C10G	C11G	-173.3(4)	Si1K	O4K	C3K	C2K	-79.9(5)
C5A	Si1A	C6A	C7A	-77.9(7)	O4G	C3G	C10G	C13G	64.5(5)	Si1K	O4K	C3K	C10K	156.3(3)
C5A	Si1A	C6A	C8A	41.4(6)	N1G	S1G	O3G	C1G	49.1(4)	F1K	C13K	C14K	C15T	-49.2(10)
C5A	Si1A	C6A	C9A	162.9(6)	N1G	C10G	C13G	F1G	-60.6(5)	F1K	C13K	C14K	C15K	-58.3(6)
C5L	Si1L	C6L	C8L	45.6(10)	N1G	C10G	C13G	C14G	178.9(4)	O1K	S1K	O3K	C1K	-165.8(4)
C5L	Si1L	C6L	C7L	163.3(9)	C1G	C2G	C3G	O4G	59.1(6)	O1K	S1K	N1K	C10K	74.6(5)
C5L	Si1L	C6L	C9L	-74.1(10)	C1G	C2G	C3G	C10G	-59.4(6)	O2K	S1K	O3K	C1K	64.3(4)
C4L	Si1L	C6L	C8L	172.7(9)	C2G	C3G	C10G	N1G	72.1(6)	O2K	S1K	N1K	C10K	-152.9(4)
C4L	Si1L	C6L	C7L	-69.6(10)	C2G	C3G	C10G	C11G	-51.7(6)	O3K	S1K	N1K	C10K	-36.4(5)
C4L	Si1L	C6L	C9L	53.0(10)	C2G	C3G	C10G	C13G	-173.9(5)	O3K	C1K	C2K	C3K	-75.3(6)
F1A	C13A	C14A	C15A	63.2(6)	C3G	C10G	C13G	F1G	-176.4(4)	O4K	Si1K	C6K	C7K	-172.4(4)
O1A	S1A	O3A	C1A	162.7(4)	C3G	C10G	C13G	C14G	63.2(6)	O4K	Si1K	C6K	C8K	68.1(5)
O1A	S1A	N1A	C10A	-70.8(5)	C4R	Si1G	O4G	C3G	-88(2)	O4K	Si1K	C6K	C9K	-50.7(5)
O2A	S1A	O3A	C1A	-68.7(5)	C4R	Si1G	C6G	C7G	90.9(19)	O4K	C3K	C10K	N1K	51.2(5)
O2A	S1A	N1A	C10A	157.5(4)	C4R	Si1G	C6G	C8R	-164(2)	O4K	C3K	C10K	C11K	175.3(4)
O3A	S1A	N1A	C10A	41.4(5)	C4R	Si1G	C6G	C9R	-45(2)	O4K	C3K	C10K	C13K	-63.7(5)
O3A	C1A	C2A	C3A	76.8(6)	C5R	Si1G	O4G	C3G	31(3)	N1K	S1K	O3K	C1K	-49.3(4)
N1A	S1A	O3A	C1A	45.0(4)	C5R	Si1G	C6G	C7G	-33(3)	N1K	C10K	C13K	F1K	65.9(5)
N1A	C10A	C13A	F1A	-62.1(5)	C5R	Si1G	C6G	C8R	72(4)	N1K	C10K	C13K	C14K	-172.3(4)
N1A	C10A	C13A	C14A	176.7(4)	C5R	Si1G	C6G	C9R	-169(4)	C1K	C2K	C3K	O4K	-58.3(6)
C2A	C3A	O4A	Si1A	64.7(6)	C6G	Si1G	O4G	C3G	-177.5(4)	C1K	C2K	C3K	C10K	60.6(6)
C2A	C3A	O4A	Si1L	88.9(5)	C10G	C13G	C14G	C15G	-179.8(5)	C2K	C3K	C10K	N1K	-71.0(5)

C2A	C3A	O4A	Si1M	111.7(6)	C11G	C10G	C13G	F1G	61.0(6)	C2K	C3K	C10K	C11K	53.1(6)
C2A	C3A	C10A	N1A	66.2(5)	C11G	C10G	C13G	C14G	-59.4(6)	C2K	C3K	C10K	C13K	174.1(4)
C2A	C3A	C10A	C11A	-57.4(6)	C13G	C14G	C15G	C16G	-180.0(5)	C3K	C10K	C13K	F1K	-176.9(4)
C2A	C3A	C10A	C13A	-179.1(5)	C14G	C15G	C16G	C17G	-66.7(7)	C3K	C10K	C13K	C14K	-55.1(6)
C10A	C3A	O4A	Si1A	-170.3(4)	C15G	C16G	C17G	C18G	-170.3(5)	C4K	Si1K	O4K	C3K	75.0(5)
C10A	C3A	O4A	Si1L	-146.1(4)	S1H	O3H	C1H	C2H	95.3(5)	C4K	Si1K	C6K	C7K	-55.0(6)
C10A	C3A	O4A	Si1M	-123.3(6)	S1H	N1H	C10H	C3H	88.2(5)	C4K	Si1K	C6K	C8K	-174.6(5)
C10A	C3A	C2A	C1A	-57.4(6)	S1H	N1H	C10H	C11H	-33.6(6)	C4K	Si1K	C6K	C9K	66.6(6)
C10A	C13A	C14A	C15A	-176.5(4)	S1H	N1H	C10H	C13H	-153.1(4)	C5K	Si1K	O4K	C3K	-45.0(6)
C11A	C10A	C13A	F1A	59.2(6)	Si1H	O4H	C3H	C2H	-72.5(5)	C5K	Si1K	C6K	C7K	68.2(6)
C11A	C10A	C13A	C14A	-62.0(6)	Si1H	O4H	C3H	C10H	164.8(3)	C5K	Si1K	C6K	C8K	-51.3(6)
C13A	C14A	C15A	C16A	179.8(5)	F1H	C13H	C14H	C15H	-66.5(6)	C5K	Si1K	C6K	C9K	-170.1(5)
C14A	C15A	C16A	C17A	-173.7(5)	O1H	S1H	O3H	C1H	-162.1(4)	C6K	Si1K	O4K	C3K	-166.9(4)
C15A	C16A	C17A	C18A	-178.3(5)	O1H	S1H	N1H	C10H	70.0(5)	C10K	C13K	C14K	C15T	-169.8(9)
S1B	O3B	C1B	C2B	-92.4(5)	O2H	S1H	O3H	C1H	68.9(4)	C10K	C13K	C14K	C15K	-178.9(5)
S1B	N1B	C10B	C3B	-87.2(5)	O2H	S1H	N1H	C10H	-158.4(4)	C11K	C10K	C13K	F1K	-56.3(5)
S1B	N1B	C10B	C11B	36.0(6)	O3H	S1H	N1H	C10H	-41.4(5)	C11K	C10K	C13K	C14K	65.5(6)
S1B	N1B	C10B	C13B	155.6(4)	O3H	C1H	C2H	C3H	-78.6(6)	C13K	C14K	C15T	C16T	-162.5(10)
Si1B	O4B	C3B	C2B	78.8(6)	O4H	Si1H	C6H	C7H	-166.0(4)	C13K	C14K	C15K	C16K	176.4(6)
Si1B	O4B	C3B	C10B	-156.9(3)	O4H	Si1H	C6H	C8H	-45.6(5)	C14K	C15T	C16T	C17T	-179.1(13)
F1B	C13B	C14B	C15B	58.6(6)	O4H	Si1H	C6H	C9H	74.0(5)	C14K	C15K	C16K	C17K	65.7(8)
O1B	S1B	O3B	C1B	163.8(4)	O4H	C3H	C10H	N1H	56.5(5)	C15T	C16T	C17T	C18T	-172.8(14)
O1B	S1B	N1B	C10B	-74.0(5)	O4H	C3H	C10H	C11H	-179.5(4)	C15K	C16K	C17K	C18K	170.8(7)
O2B	S1B	O3B	C1B	-67.1(5)	O4H	C3H	C10H	C13H	-58.7(6)	C4G	Si1G	O4G	C3G	-56.0(5)
O2B	S1B	N1B	C10B	155.6(5)	N1H	S1H	O3H	C1H	-45.0(4)	C4G	Si1G	C6G	C7G	64.5(5)
O3B	S1B	N1B	C10B	38.9(5)	N1H	C10H	C13H	F1H	59.4(5)	C4G	Si1G	C6G	C8G	-171.5(8)
O3B	C1B	C2B	C3B	76.2(6)	N1H	C10H	C13H	C14H	179.7(4)	C4G	Si1G	C6G	C9G	-50.6(8)
O4B	Si1B	C6B	C7B	173.2(4)	C1H	C2H	C3H	O4H	-62.5(6)	C5G	Si1G	O4G	C3G	63.6(5)
O4B	Si1B	C6B	C8B	-66.0(5)	C1H	C2H	C3H	C10H	56.4(6)	C5G	Si1G	C6G	C7G	-58.7(5)
O4B	Si1B	C6B	C9B	54.9(4)	C2H	C3H	C10H	N1H	-65.3(6)	C5G	Si1G	C6G	C8G	65.3(9)
O4B	C3B	C10B	N1B	-54.0(5)	C2H	C3H	C10H	C11H	58.6(6)	C5G	Si1G	C6G	C9G	-173.9(8)
O4B	C3B	C10B	C11B	-178.8(4)	C2H	C3H	C10H	C13H	179.5(5)	C4H	Si1H	C6H	C8H	-166.0(5)
O4B	C3B	C10B	C13B	59.3(5)	C3H	C10H	C13H	F1H	178.7(4)	C4H	Si1H	C6H	C9H	-46.4(5)
N1B	S1B	O3B	C1B	45.8(5)	C3H	C10H	C13H	C14H	-61.1(6)	C5H	Si1H	O4H	C3H	115.0(5)
N1B	C10B	C13B	F1B	-68.0(5)	C4H	Si1H	O4H	C3H	-7.3(5)	C5H	Si1H	C6H	C7H	-50.3(5)
N1B	C10B	C13B	C14B	171.8(4)	C4H	Si1H	C6H	C7H	73.6(5)	C5H	Si1H	C6H	C8H	70.1(5)
C1B	C2B	C3B	O4B	60.8(7)	O4E	Si1E	C6E	C8E	-64.0(4)	C5H	Si1H	C6H	C9H	-170.2(4)
C1B	C2B	C3B	C10B	-59.3(7)	O4E	Si1E	C6E	C9E	55.1(4)	C6H	Si1H	O4H	C3H	-126.1(4)
C2B	C3B	C10B	N1B	69.7(6)	O4E	C3E	C10E	N1E	-55.6(6)	C10H	C13H	C14H	C15H	174.4(4)
C2B	C3B	C10B	C11B	-55.1(6)	O4E	C3E	C10E	C11E	-179.1(4)	C11H	C10H	C13H	F1H	-61.5(6)
C2B	C3B	C10B	C13B	-177.0(5)	O4E	C3E	C10E	C13E	59.4(6)	C11H	C10H	C13H	C14H	58.8(6)

C3B	C10B	C13B	F1B	175.9(4)	N1E	Si1E	O3E	C1E	48.4(5)	C13H	C14H	C15H	C16H	-178.5(5)
C3B	C10B	C13B	C14B	55.7(6)	N1E	C10E	C13E	F1E	-62.0(5)	C14H	C15H	C16H	C17H	175.1(5)
C4B	Si1B	O4B	C3B	-73.2(5)	N1E	C10E	C13E	C14E	177.9(5)	C15H	C16H	C17H	C18H	176.9(5)
C4B	Si1B	C6B	C7B	55.6(5)	C1E	C2E	C3E	O4E	61.9(6)	S1I	O3I	C1I	C2I	93.3(5)
C4B	Si1B	C6B	C8B	176.3(5)	C1E	C2E	C3E	C10E	-56.9(7)	S1I	N1I	C10I	C3I	87.6(5)
C4B	Si1B	C6B	C9B	-62.8(5)	C2E	C3E	C10E	N1E	65.2(6)	S1I	N1I	C10I	C11I	-35.1(6)
C5B	Si1B	O4B	C3B	48.5(6)	C2E	C3E	C10E	C11E	-58.3(7)	S1I	N1I	C10I	C13I	-153.9(4)
C5B	Si1B	C6B	C7B	-67.9(6)	C2E	C3E	C10E	C13E	-179.7(5)	Si1I	O4I	C3I	C2I	-94.1(5)
C5B	Si1B	C6B	C8B	52.8(5)	C3E	C10E	C13E	F1E	-179.8(5)	Si1I	O4I	C3I	C10I	142.0(3)
C5B	Si1B	C6B	C9B	173.8(4)	C3E	C10E	C13E	C14E	60.1(7)	F1I	C13I	C14I	C15I	-58.8(6)
C6B	Si1B	O4B	C3B	169.6(4)	C4E	Si1E	O4E	C3E	-16.8(5)	O1I	S1I	O3I	C1I	-165.5(3)
C10B	C13B	C14B	C15B	177.6(4)	C4E	Si1E	C6E	C7E	56.6(5)	O1I	S1I	N1I	C10I	74.4(4)
C11B	C10B	C13B	F1B	53.7(6)	C4E	Si1E	C6E	C8E	175.9(4)	O2I	S1I	O3I	C1I	65.6(4)
C11B	C10B	C13B	C14B	-66.5(6)	C4E	Si1E	C6E	C9E	-65.0(5)	O2I	S1I	N1I	C10I	-153.5(4)
C13B	C14B	C15B	C16B	167.5(5)	C5E	Si1E	O4E	C3E	104.5(5)	O3I	S1I	N1I	C10I	-37.0(4)
C14B	C15B	C16B	C17B	175.3(5)	C5E	Si1E	C6E	C7E	-67.4(5)	O3I	C1I	C2I	C3I	-74.8(6)
C15B	C16B	C17B	C18B	176.2(6)	C5E	Si1E	C6E	C8E	51.9(5)	O4I	Si1I	C6I	C7I	-63.1(4)
S1C	O3C	C1C	C2C	-96.8(5)	C5E	Si1E	C6E	C9E	171.0(4)	O4I	Si1I	C6I	C8I	177.7(4)
S1C	N1C	C10C	C3C	-88.5(5)	C6E	Si1E	O4E	C3E	-137.3(4)	O4I	Si1I	C6I	C9I	56.5(5)
S1C	N1C	C10C	C11C	33.2(6)	C10E	C13E	C14E	C15E	-176.6(6)	O4I	C3I	C10I	N1I	49.9(5)
S1C	N1C	C10C	C13C	152.1(4)	C5D	Si1D	C6D	C9D	-173.5(4)	O4I	C3I	C10I	C11I	174.4(4)
C3C	O4C	Si1N	C4N	16.2(6)	C6D	Si1D	O4D	C3D	-169.5(4)	O4I	C3I	C10I	C13I	-65.0(5)
C3C	O4C	Si1N	C5N	-107.8(6)	C10D	C13D	C14D	C15D	177.5(4)	N1I	S1I	O3I	C1I	-48.5(4)
C3C	O4C	Si1N	C6N	134.6(4)	C11D	C10D	C13D	F1D	-54.9(5)	N1I	C10I	C13I	F1I	58.1(5)
C3C	O4C	Si1C	C4C	-13.4(5)	C11D	C10D	C13D	C14D	67.0(6)	N1I	C10I	C13I	C14I	-179.8(4)
C3C	O4C	Si1C	C5C	108.1(5)	C13D	C14D	C15D	C16D	-173.6(5)	C1I	C2I	C3I	O4I	-59.3(6)
C3C	O4C	Si1C	C6C	-134.4(4)	C14D	C15D	C16D	C17D	179.4(5)	C1I	C2I	C3I	C10I	60.5(6)
C3C	C10C	C13C	F1C	-177.3(4)	C15D	C16D	C17D	C18D	-177.3(6)	C2I	C3I	C10I	N1I	-72.1(5)
C3C	C10C	C13C	C14C	60.7(6)	S1E	O3E	C1E	C2E	-97.9(6)	C2I	C3I	C10I	C11I	52.4(6)
O4C	C3C	C2C	C1C	66.1(6)	S1E	N1E	C10E	C3E	-86.7(5)	C5N	Si1N	C6N	C7N	171.0(8)
O4C	C3C	C10C	N1C	-59.3(5)	S1E	N1E	C10E	C11E	35.1(6)	C5N	Si1N	C6N	C8N	51.7(8)
O4C	C3C	C10C	C11C	177.3(4)	S1E	N1E	C10E	C13E	154.9(4)	C5N	Si1N	C6N	C9N	-70.7(8)
O4C	C3C	C10C	C13C	56.4(5)	Si1E	O4E	C3E	C2E	97.1(5)	C4C	Si1C	C6C	C7C	54.0(5)
O4C	Si1N	C6N	C7N	-72.0(6)	Si1E	O4E	C3E	C10E	-139.2(4)	C4C	Si1C	C6C	C8C	173.3(5)
O4C	Si1N	C6N	C8N	168.8(6)	F1E	C13E	C14E	C15E	64.3(7)	C4C	Si1C	C6C	C9C	-65.9(6)
O4C	Si1N	C6N	C9N	46.3(7)	O1E	S1E	O3E	C1E	165.3(5)	C5C	Si1C	C6C	C7C	-70.5(5)
O4C	Si1C	C6C	C7C	173.4(4)	O1E	S1E	N1E	C10E	-72.1(5)	C5C	Si1C	C6C	C8C	48.8(6)
O4C	Si1C	C6C	C8C	-67.3(5)	O2E	S1E	O3E	C1E	-66.1(5)	C5C	Si1C	C6C	C9C	169.6(5)
O4C	Si1C	C6C	C9C	53.5(5)	O2E	S1E	N1E	C10E	158.7(4)	F1C	C13C	C14C	C15C	62.8(5)
C4N	Si1N	C6N	C7N	47.0(8)	O3E	S1E	N1E	C10E	39.7(5)	O1C	S1C	O3C	C1C	163.3(4)
C4N	Si1N	C6N	C8N	-72.3(8)	O3E	C1E	C2E	C3E	78.8(7)	O1C	S1C	N1C	C10C	-69.1(5)

C4N	Si1N	C6N	C9N	165.3(8)	O4E	Si1E	C6E	C7E	176.8(4)	O2C	S1C	O3C	C1C	-67.6(4)
O2C	S1C	N1C	C10C	159.2(4)	C2C	C3C	C10C	N1C	65.1(5)	S1D	N1D	C10D	C13D	-153.8(4)
O3C	S1C	N1C	C10C	42.5(5)	C2C	C3C	C10C	C11C	-58.3(6)	Si1D	O4D	C3D	C2D	-81.7(5)
O3C	C1C	C2C	C3C	77.9(6)	C2C	C3C	C10C	C13C	-179.1(4)	Si1D	O4D	C3D	C10D	155.0(3)
N1C	S1C	O3C	C1C	45.5(4)	C10C	C3C	O4C	Si1N	-170.4(3)	F1D	C13D	C14D	C15D	-61.4(6)
N1C	C10C	C13C	F1C	-59.1(5)	C10C	C3C	O4C	Si1C	-136.0(4)	O1D	S1D	O3D	C1D	-162.1(4)
N1C	C10C	C13C	C14C	178.8(4)	C10C	C3C	C2C	C1C	-55.8(6)	O1D	S1D	N1D	C10D	71.8(5)
C2C	C3C	O4C	Si1N	63.2(5)	C10C	C13C	C14C	C15C	-175.5(4)	O2D	S1D	O3D	C1D	69.0(4)
C2C	C3C	O4C	Si1C	97.6(5)	C11C	C10C	C13C	F1C	61.7(5)	O2D	S1D	N1D	C10D	-158.1(4)
C11C	C10C	C13C	C14C	-60.3(6)	O4D	C3D	C10D	C13D	-59.4(5)	O3D	S1D	N1D	C10D	-40.6(5)
C13C	C14C	C15C	C16C	176.2(4)	N1D	S1D	O3D	C1D	-44.9(4)	O3D	C1D	C2D	C3D	-79.4(6)
C14C	C15C	C16C	C17C	-175.1(5)	N1D	C10D	C13D	F1D	66.5(5)	O4D	Si1D	C6D	C7D	-173.5(4)
C15C	C16C	C17C	C18C	-177.2(5)	N1D	C10D	C13D	C14D	-171.6(4)	O4D	Si1D	C6D	C8D	65.7(4)
S1D	O3D	C1D	C2D	94.8(5)	C1D	C2D	C3D	O4D	-59.4(6)	O4D	Si1D	C6D	C9D	-54.2(4)
S1D	N1D	C10D	C3D	87.4(5)	C1D	C2D	C3D	C10D	59.6(6)	O4D	C3D	C10D	N1D	54.6(5)
S1D	N1D	C10D	C11D	-33.5(6)	C2D	C3D	C10D	N1D	-67.6(6)	O4D	C3D	C10D	C11D	178.1(4)
C2D	C3D	C10D	C11D	55.9(6)	C3D	C10D	C13D	C14D	-53.9(6)	C4D	Si1D	C6D	C8D	-175.5(4)
C2D	C3D	C10D	C13D	178.4(4)	C4D	Si1D	O4D	C3D	71.3(5)	C4D	Si1D	C6D	C9D	64.6(4)
C3D	C10D	C13D	F1D	-175.8(4)	C4D	Si1D	C6D	C7D	-54.7(5)	C5D	Si1D	O4D	C3D	-49.1(5)
C5D	Si1D	C6D	C7D	67.1(5)	C5D	Si1D	C6D	C8D	-53.7(5)					

Table E.15. Hydrogen Atom Coordinates (Å×10⁴) and Isotropic Displacement Parameters (Å²×10³) for 1 phase II.

Atom	*x*	*y*	*z*	U(eq)	Atom	*x*	*y*	*z*	U(eq)
H3	2176	6047	4205	17	H8DB	6965	6314	4682	51
H4A	2089	6398	1431	39	H8DC	6415	6116	5055	51
H4B	3063	6342	1324	39	H9DA	7961	6295	6223	50
H4C	2794	6591	1565	39	H9DB	8397	6062	6562	50
H5A	1585	6529	3258	47	H9DC	7393	6097	6567	50
H5B	2364	6671	3793	47	H12D	10166	7133	3046	28
H5C	2096	6439	4233	47	H13D	7564	6679	4135	18
H7A	3823	6782	3306	48	H14W	8031	6526	2752	24
H7B	4240	6676	2437	48	H14X	8120	6773	2344	24
H7C	4816	6719	3437	48	H15W	6651	6832	2266	29
H8A	3942	6292	4770	63	H15X	6534	6598	2779	29
H8B	3812	6557	4780	63	H16W	7015	6640	907	31
H8C	4749	6455	4794	63	H16X	6908	6406	1420	31
H9A	4521	6255	2401	49	H17W	5421	6484	1417	47

H9B	4605	6126	3396	49
H9C	5243	6327	3247	49
H1	2740(30)	5726(7)	2360(30)	17
H1B	547	5963	1711	29
H1D	1551	5930	1683	29
H2A	861	5935	3440	25
H2B	1130	6163	2976	25
H12	1028	5438	5014	34
H13	3768	5808	3867	17
H14S	3180	5723	5645	22
H14T	3251	5970	5228	22
H15S	4749	5923	5267	22
H15T	4679	5676	5680	22
H16S	4257	6067	6689	20
H16T	4279	5819	7104	20
H17S	5750	6061	6700	28
H17T	5786	5808	7064	28
H180	6179	6079	8319	44
H181	5437	5913	8540	44
H182	5206	6161	8178	44
H3A	2301	7690	4265	22
H4AA	3051	8024	1330	44
H4AB	2720	8267	1586	44
H4AC	2069	8061	1458	44
H5AA	1556	8176	3304	35
H5AB	2301	8331	3823	35
H5AC	2109	8094	4269	35
H7AA	4101	8370	2405	73
H7AB	4777	8412	3332	73
H7AC	3791	8472	3345	73
H8AA	3773	8246	4766	61
H8AB	4739	8164	4783	61
H8AC	3987	7985	4778	61
H9AA	4649	7822	3408	51
H9AB	5255	8030	3253	51
H9AC	4547	7950	2407	51
H17X	5539	6712	861	47
H0AA	5886	6507	-462	51
HD	4966	6434	-216	51
HE	5779	6278	96	51
H1E	3010(30)	2447(6)	2420(30)	22
H1EA	851	2731	1878	56
H1EB	1837	2677	1812	56
H2EA	1195	2665	3601	51
H2EB	1511	2896	3209	51
H3E	2572	2744	4342	31
H4EA	2422	3239	3941	77
H4EB	3307	3334	4471	77
H4EC	2926	3104	4817	77
H5EA	4712	2945	4642	77
H5EB	5053	3116	3910	77
H5EC	4931	2858	3635	77
H7EA	3566	3514	2830	42
H7EB	3946	3503	1839	42
H7EC	4507	3418	2794	42
H8EA	4704	3061	1923	43
H8EB	4072	3139	1007	43
H8EC	3897	2910	1530	43
H9EA	2450	3058	1560	46
H9EB	2673	3299	1169	46
H9EC	2285	3278	2152	46
H12E	1238	2157	5014	49
H13E	4069	2475	3816	32
H14O	3538	2390	5626	39
H14P	3731	2636	5258	39
H14Q	3423	2420	5566	39
H14R	3835	2641	5208	39
H15O	5213	2458	5448	44
H15P	4760	2254	5940	44
H16O	4403	2706	6523	44
H16P	4374	2483	7150	44
H17O	5954	2650	6646	44

H5LA	2849	8038	5108	94
H5LB	3488	8233	4892	94
H5LC	3810	7979	4955	94
H4LA	1628	8097	2558	63
H4LB	2068	8335	2811	63
H4LC	1624	8202	3596	63
H8LA	4870	8107	3808	55
H8LB	5132	8062	2773	55
H8LC	4632	7874	3283	55
H7LA	3625	7878	1751	65
H7LB	4079	8090	1346	65
H7LC	3080	8097	1431	65
H9LA	3377	8453	2359	55
H9LB	4392	8435	2403	55
H9LC	3968	8449	3366	55
H1A	2980(30)	7419(6)	2390(30)	22
H1AA	693	7600	1778	37
H1AB	1701	7599	1732	37
H2AA	1036	7551	3483	33
H2AB	1207	7793	3073	33
H12A	1353	7059	4974	34
H13A	3989	7491	3861	23
H14A	3406	7390	5637	25
H14B	3466	7639	5240	25
H15A	4914	7348	5678	30
H15B	4974	7597	5277	30
H16A	4454	7733	6691	26
H16B	4504	7483	7095	26
H17A	6002	7485	7076	34
H17B	5943	7737	6702	34
H18A	5423	7834	8182	55
H18B	6407	7763	8275	55
H18C	5709	7589	8544	55
H1BA	3070(30)	9130(6)	2580(40)	24
H1BB	665	9309	2234	49
H1BC	1652	9323	2088	49
H17P	5849	2465	7446	44
H18V	5505	2947	8013	80
H18W	5255	2701	8318	80
H18X	6141	2743	7912	80
H18Y	6113	2823	8183	80
HF	5287	2921	7543	80
HG	5182	2737	8338	80
H15Q	4989	2284	5439	54
H15R	5172	2535	5149	54
H16Q	4788	2413	7000	38
H16R	5740	2448	6762	38
H17Q	4485	2790	6778	29
H17R	5372	2832	6371	29
H1F	8550(30)	8446(8)	5730(40)	30
H1FA	9919	8244	6432	33
H1FB	10934	8229	6439	33
H2FA	10466	8038	5114	33
H2FB	10636	8279	4700	33
H3F	9345	8134	3907	25
H4FA	10074	7681	4767	69
H4FB	9439	7721	3805	69
H4FC	9372	7496	4406	69
H5FA	8479	7782	6767	61
H5FB	9479	7808	6708	61
H5FC	9028	7569	6526	61
H7FA	7562	7472	5745	63
H7FB	7811	7366	4782	63
H7FC	6840	7432	4858	63
H8FA	7046	8019	4747	69
H8FB	6999	7873	5683	69
H8FC	6369	7820	4731	69
H9FA	7878	7607	3347	76
H9FB	7576	7863	3357	76
H9FC	6889	7666	3342	76
H12F	10331	8768	3156	36
H13F	7667	8349	4300	20

H2BA	1145	9222	3883	37	H14Y	8207	8192	2931	20
H2BB	1265	9474	3567	37	HH	8276	8440	2520	20
H3B	2445	9357	4596	24	H15Y	6706	8230	2853	24
H4BA	1574	9855	3420	54	HI	6759	8483	2493	24
H4BB	1858	9813	2392	54	H16Y	7166	8364	1046	26
H4BC	2149	10036	2968	54	HJ	7246	8111	1410	26
H5BA	3217	9963	4958	89	H17Y	5749	8092	1405	37
H5BB	3758	9738	5152	89	HK	5657	8348	1080	37
H5BC	2752	9737	5197	89	H3AA	6101	8256	-393	45
H7BA	4104	10124	3546	65	HL	5291	8107	-231	45
H7BB	3538	10129	2524	65	HM	6228	8001	-67	45
H7BC	4551	10099	2603	65	H1G	2930(30)	857(6)	2460(40)	23
H8BA	4704	9536	3445	73	H1GA	509	1020	2603	30
H8BB	4883	9756	4086	73	H1GB	1433	1051	2270	30
H8BC	5240	9738	3083	73	H2GA	1228	920	4161	26
H9BA	3224	9787	1593	59	H2GB	1302	1177	3878	26
H9BB	3689	9556	1910	59	H3G	2609	1053	4655	21
H9BC	4228	9759	1562	59	H4RA	1775	1434	2775	34
H12B	1517	8705	5102	37	H4RB	2201	1677	2768	34
H13B	4089	9167	3977	22	H4RC	1806	1592	3689	34
H14U	3528	9066	5769	29	H5RA	3037	1420	5297	41
H14V	3682	9313	5401	29	H5RB	3541	1640	5047	41
H15U	4971	8984	5925	38	H5RC	4022	1404	5150	41
H15V	5173	9204	5354	38	H7GA	3533	1857	2737	46
H16U	4883	9431	6624	38	H7GB	4235	1787	2075	46
H16V	4601	9217	7186	38	H7GC	4422	1751	3202	46
H17U	6003	9081	7376	55	H8GA	4455	1386	1686	88
H17V	6298	9284	6758	55	H8GB	3960	1193	2174	88
H18	5952	9535	7959	69	H8GC	4715	1329	2788	88
HB	6709	9367	8338	69	H9GA	2484	1661	1848	68
HC	5765	9323	8589	69	H9GB	2493	1396	1700	68
H3C	2267	4403	4236	21	H9GC	3061	1554	1120	68
H4NA	1677	4873	3485	54	H12G	1735	371	5074	36
H4NB	2489	5014	3946	54	H13G	4093	885	3817	22
H4NC	2275	4778	4397	54	H14E	3774	687	5575	23
H5NA	2912	4694	1336	42	H14F	3828	951	5406	23

H5NB	2771	4948	1632	42	H15E	5230	649	5307	35
H5NC	1998	4773	1579	42	H15F	5283	913	5139	35
H7NA	4000	4872	4790	53	H16E	5007	719	6913	31
H7NB	4929	4780	4662	53	H16F	5922	799	6688	31
H7NC	4146	4610	4658	53	H17E	4509	1082	6908	31
H8NA	4156	5045	2419	38	H17F	5344	1174	6510	31
H8NB	4878	5064	3320	38	H18G	6174	1067	7979	52
H8NC	3911	5128	3421	38	H18H	5311	995	8374	52
H9NA	4624	4473	3172	49	H18I	5473	1252	8134	52
H9NB	5275	4672	3044	49	H1H	8660(20)	10138(8)	5620(30)	24
H9NC	4503	4620	2223	49	H1HA	10002	9894	6396	30
H4CA	2174	4884	3875	54	H1HB	11006	9854	6398	30
H4CB	3035	4992	4401	54	H2HA	10445	9655	5134	28
H4CC	2691	4762	4777	54	H2HB	10723	9882	4667	28
H5CA	4482	4612	4664	78	H3H	9393	9771	3882	19
H5CB	4837	4775	3913	78	H4HA	9942	9307	4654	61
H5CC	4722	4514	3682	78	H4HB	9310	9378	3726	61
H7CA	3338	5162	2827	36	H4HC	9149	9150	4271	61
H7CB	3699	5164	1824	36	H5HA	8522	9460	6772	52
H7CC	4295	5083	2761	36	H5HB	9512	9454	6640	52
H8CA	4574	4721	2005	54	H5HC	8952	9230	6498	52
H8CB	4005	4803	1048	54	H7HA	7476	9141	5705	54
H8CC	3800	4569	1524	54	H7HB	7699	9048	4708	54
H9CA	2316	4696	1470	42	H7HC	6739	9116	4822	54
H9CB	2483	4945	1121	42	H8HA	7018	9707	4910	71
H9CC	2080	4906	2086	42	H8HB	7018	9547	5816	71
H1C	2820(30)	4068(7)	2410(30)	16	H8HC	6322	9513	4900	71
H1CA	699	4338	1691	35	H9HA	7718	9308	3333	74
H1CB	1699	4287	1717	35	H9HB	7440	9563	3423	74
H2CA	945	4314	3433	26	H9HC	6743	9369	3410	74
H2CB	1279	4535	2973	26	H12H	10628	10359	3064	29
H12C	966	3819	4995	25	H13H	7793	10027	4202	23
H13C	3832	4139	3936	18	H14Z	8325	9853	2859	23
H14C	3164	4076	5686	20	HN	8449	10097	2435	23
H14D	3350	4317	5266	20	H15Z	6823	9922	2782	30
H15C	4626	3987	5843	27	HO	6954	10163	2333	30

H15D	4830	4220	5362	27
H16C	4229	4174	7166	24
H16D	4347	4411	6676	24
H17C	5739	4111	7247	39
H17D	5842	4353	6802	39
H18D	5253	4504	8187	54
H18E	6194	4401	8412	54
H18F	5386	4259	8644	54
H1DA	8480(30)	6730(6)	5500(40)	23
H1DB	9899	6538	6114	39
H1DC	10909	6544	6073	39
H2DA	10424	6379	4686	33
H2DB	10542	6632	4373	33
H3D	9242	6486	3575	20
H4DA	9730	6000	5787	55
H4DB	10115	6024	4803	55
H4DC	9562	5808	4997	55
H5DA	8895	6109	2956	66
H5DB	7889	6105	3004	66
H5DC	8440	5882	3205	66
H7DA	8110	5721	5580	53
H7DB	7507	5731	4581	53
H7DC	7102	5753	5553	53
H8DA	6772	6093	4054	51
H9RC	3216	1469	1083	68
H5MA	4572	7904	4657	32
H5MB	4866	8109	4052	32
H5MC	4838	7862	3621	32
H4MA	2212	8165	4127	32
H4MB	3061	8296	4549	32
H4MC	2863	8055	4960	32
H8MA	4308	7978	1921	32
H8MB	4002	8164	1140	32
H8MC	3428	7947	1234	32
H7MA	2144	8058	1717	32
H7MB	2344	8300	1320	32
H16Z	7329	9755	1421	28
HP	7373	9999	967	28
H17Z	5830	9784	1336	37
HQ	5857	10033	934	37
H6AA	6302	9896	-469	43
HR	5415	9784	-300	43
HS	6288	9647	-65	43
H1I	8740(30)	3302(5)	5660(30)	17
H1IA	10197	3106	5895	29
H1IB	11128	3131	5572	29
H2IA	10338	2978	4278	27
H2IB	10417	3235	4003	27
H3I	9016	3103	3509	22
H4IA	9538	2609	3600	64
H4IB	9198	2404	4169	64
H4IC	9857	2579	4711	64
H5IA	7127	2820	3592	73
H5IB	7466	2584	3272	73
H5IC	7856	2810	2910	73
H7IA	9207	2538	6288	75
H7IB	8557	2598	7026	75
H7IC	9012	2793	6510	75
H8IA	7160	2405	5013	47
H8IB	7470	2359	6117	47
H8IC	8089	2303	5341	47
H9IA	7557	2957	5873	82
H9IB	7157	2765	6463	82
H9IC	6839	2794	5351	82
H12I	9923	3776	3027	29
H13I	7555	3276	4335	19
H14	7798	3205	2754	21
HT	7872	3468	2569	21
H15	6427	3513	2853	26
HU	6357	3250	3004	26
H16	5712	3368	1459	27
HV	6627	3448	1227	27

H7MC	2068	8275	2361	32	H17	6271	2989	1613	32
H9MA	3635	8464	3137	32	HW	7124	3079	1243	32
H9MB	3463	8519	2023	32	H0BA	6254	3199	-209	52
H9MC	4345	8406	2468	32	HX	5457	3077	156	52
H8KA	6898	4621	4770	88	HY	6259	2934	-79	52
H8KB	6375	4426	5205	88	H1J	8540(30)	1774(8)	5730(30)	24
H8KC	6650	4399	4164	88	H1JA	9801	1500	6394	47
H9KA	8432	4367	6524	78	H1JB	10790	1447	6347	47
H9KB	7441	4402	6611	78	H2JA	10129	1272	5062	40
H9KC	7977	4599	6209	78	H2JB	10485	1495	4642	40
H12K	9855	5483	3061	27	H3J	9131	1425	3856	23
H13K	7436	4982	4259	24	H4JA	6669	1281	4644	66
H14M	7927	5110	2491	34	H4JB	6654	1051	4062	66
H14N	7659	4866	2783	34	H4JC	6959	1277	3604	66
H14K	7709	4871	2732	34	H5JA	8694	1075	3319	83
H14L	7823	5128	2446	34	H5JB	8373	842	3702	83
H15K	6567	5224	2179	29	H5JC	9250	950	4189	83
H15L	6220	5019	2746	29	H7JA	7153	753	5325	46
H16K	6928	4968	981	29	H7JB	7692	666	6290	46
H16L	6566	4765	1545	29	H7JC	8100	659	5315	46
H17K	5567	5123	645	29	H8JA	9371	887	6003	51
H17L	5182	4943	1307	29	H8JB	9009	887	7006	51
H18P	5826	4833	-432	36	H8JC	9231	1118	6529	51
H18Q	4833	4846	-317	36	H9JA	7762	1255	6647	53
H18R	5422	4655	225	36	H9JB	7526	1024	7112	53
H15M	6271	4941	2973	34	H9JC	6946	1116	6184	53
H15N	6379	5201	2756	34	H12J	10504	1995	3140	36
H16M	5618	5042	1408	31	H13J	7615	1705	4282	25
H16N	6538	5109	1139	31	H14G	8305	1761	2532	38
H17M	6152	4664	1690	32	H14H	8035	1525	2923	38
H17N	6993	4739	1254	32	H14I	8028	1524	2899	38
H18S	6114	4825	-217	51	H14J	8272	1764	2503	38
H18T	5309	4727	225	51	H15G	6601	1642	2913	46
H18U	6078	4565	47	51	H15H	6833	1887	2585	46
H4GA	2465	1752	4080	59	H16G	6146	1742	1240	46
H4GB	1815	1602	3386	59	H16H	7124	1710	1088	46

H4GC	2034	1536	4485	59	H17G	6161	1358	1802	46
H5GA	4184	1579	4856	70	H17H	7082	1333	1457	46
H5GB	3773	1359	5248	70	H18J	6360	1452	-131	57
H5GC	4494	1337	4560	70	H18K	5491	1393	278	57
H8RA	4319	1226	2400	88	H18L	6185	1202	188	57
H8RB	4694	1442	1930	88	H15I	6899	1876	2251	46
H8RC	4827	1412	3061	88	H15J	6587	1659	2773	46
H9RA	2769	1294	1716	68	H16I	7306	1649	999	46
H9RB	2446	1548	1633	68	H16J	7064	1427	1536	46
H3K	8972	4809	3426	16	H17I	5848	1764	838	46
H4KA	9974	4315	4521	95	H17J	5609	1541	1365	46
H4KB	9438	4108	4846	95	H18M	6223	1551	-449	54
H4KC	9716	4308	5575	95	H18N	5263	1493	-290	54
H5KA	7647	4432	2992	113	H18O	6023	1325	82	54
H5KB	8152	4200	3108	113	H1K	8520(30)	4993(5)	5540(40)	18
H5KC	8632	4422	2839	113	H1KA	10027	4795	5864	25
H7KA	7448	4034	4624	63	H1KB	10982	4823	5611	25
H7KB	7053	4059	5602	63	H2KA	10264	4682	4255	26
H7KC	8059	4024	5618	63	H2KB	10348	4941	4030	26

Table E.16. Atomic Occupancy for 1 phase II.

Atom	*Occupancy*	Atom	*Occupancy*	Atom	*Occupancy*	Atom	*Occupancy*
Si1A	0.564(3)	C4A	0.564(3)	C16S	0.389(7)	H4AA	0.564(3)
H4AB	0.564(3)	H4AC	0.564(3)	C17S	0.389(7)	C5A	0.564(3)
H5AA	0.564(3)	H5AB	0.564(3)	C18S	0.389(7)	H5AC	0.564(3)
C6A	0.564(3)	C7A	0.564(3)	H18L	0.389(7)	H7AA	0.564(3)
H7AB	0.564(3)	H7AC	0.564(3)	H15J	0.611(7)	C8A	0.564(3)
H8AA	0.564(3)	H8AB	0.564(3)	H16J	0.611(7)	H8AC	0.564(3)
C9A	0.564(3)	H9AA	0.564(3)	H17G	0.389(7)	H9AB	0.564(3)
H9AC	0.564(3)	Si1L	0.305(3)	H18J	0.389(7)	C5L	0.305(3)
H5LA	0.305(3)	H5LB	0.305(3)	C15J	0.611(7)	H5LC	0.305(3)
C4L	0.305(3)	H4LA	0.305(3)	C16J	0.611(7)	H4LB	0.305(3)
H4LC	0.305(3)	C6L	0.305(3)	C17J	0.611(7)	C8L	0.305(3)
H8LA	0.305(3)	H8LB	0.305(3)	C18J	0.611(7)	H8LC	0.305(3)
C7L	0.305(3)	H7LA	0.305(3)	H18O	0.611(7)	H7LB	0.305(3)

H7LC	0.305(3)	C9L	0.305(3)	H14K	0.670(9)	H9LA	0.305(3)
H9LB	0.305(3)	H9LC	0.305(3)	H15K	0.330(9)	Si1N	0.364(2)
C4N	0.364(2)	H4NA	0.364(2)	H16K	0.330(9)	H4NB	0.364(2)
H4NC	0.364(2)	C5N	0.364(2)	H17K	0.330(9)	H5NA	0.364(2)
H5NB	0.364(2)	H5NC	0.364(2)	H18P	0.330(9)	C6N	0.364(2)
C7N	0.364(2)	H7NA	0.364(2)	C15K	0.670(9)	H7NB	0.364(2)
H7NC	0.364(2)	C8N	0.364(2)	C16K	0.670(9)	H8NA	0.364(2)
H8NB	0.364(2)	H8NC	0.364(2)	C17K	0.670(9)	C9N	0.364(2)
H9NA	0.364(2)	H9NB	0.364(2)	C18K	0.670(9)	H9NC	0.364(2)
Si1C	0.636(2)	C4C	0.636(2)	H18U	0.670(9)	H4CA	0.636(2)
H4CB	0.636(2)	H4CC	0.636(2)	H4GB	0.926(9)	C5C	0.636(2)
H5CA	0.636(2)	H5CB	0.636(2)	H5GA	0.926(9)	H5CC	0.636(2)
C6C	0.636(2)	C7C	0.636(2)	C8R	0.29(3)	H7CA	0.636(2)
H7CB	0.636(2)	H7CC	0.636(2)	H8RC	0.29(3)	C8C	0.636(2)
H8CA	0.636(2)	H8CB	0.636(2)	H9RB	0.29(3)	H8CC	0.636(2)
C9C	0.636(2)	H9CA	0.636(2)	C5M	0.131(2)	H9CB	0.636(2)
H9CC	0.636(2)	H14O	0.776(11)	H5MC	0.131(2)	H14P	0.776(11)
H14Q	0.224(11)	H14R	0.224(11)	H4MB	0.131(2)	C15P	0.224(11)
H15O	0.224(11)	H15P	0.224(11)	C8M	0.131(2)	C16P	0.224(11)
H16O	0.224(11)	H16P	0.224(11)	H8MC	0.131(2)	C17P	0.224(11)
H17O	0.224(11)	H17P	0.224(11)	H7MB	0.131(2)	H18V	0.776(11)
H18W	0.776(11)	H18X	0.776(11)	H9MA	0.131(2)	H18Y	0.224(11)
HF	0.224(11)	HG	0.224(11)	H17J	0.611(7)	C15E	0.776(11)
H15Q	0.776(11)	H15R	0.776(11)	H18N	0.611(7)	C16E	0.776(11)
H16Q	0.776(11)	H16R	0.776(11)	H14N	0.330(9)	C17E	0.776(11)
H17Q	0.776(11)	H17R	0.776(11)	C15T	0.330(9)	C4R	0.074(9)
H4RA	0.074(9)	H4RB	0.074(9)	C16T	0.330(9)	H4RC	0.074(9)
C5R	0.074(9)	H5RA	0.074(9)	C17T	0.330(9)	H5RB	0.074(9)
H5RC	0.074(9)	C8G	0.71(3)	C18T	0.330(9)	H8GA	0.71(3)
H8GB	0.71(3)	H8GC	0.71(3)	H18R	0.330(9)	C9G	0.71(3)
H9GA	0.71(3)	H9GB	0.71(3)	H15N	0.670(9)	H9GC	0.71(3)
H14G	0.611(7)	H14H	0.611(7)	H16N	0.670(9)	H14I	0.389(7)
H14J	0.389(7)	C15S	0.389(7)	H17N	0.670(9)	H15G	0.389(7)
H15H	0.389(7)	H5GB	0.926(9)	H18T	0.670(9)	H16G	0.389(7)
H16H	0.389(7)	H8RA	0.29(3)	H4GA	0.926(9)	H18S	0.670(9)
H17H	0.389(7)	C9R	0.29(3)	C5G	0.926(9)	C4G	0.926(9)

H18K	0.389(7)	H9RC	0.29(3)	H5GC	0.926(9)	H4GC	0.926(9)
H15I	0.611(7)	H5MA	0.131(2)	H8RB	0.29(3)	H7MA	0.131(2)
H16I	0.611(7)	C4M	0.131(2)	H9RA	0.29(3)	C9M	0.131(2)
H17I	0.611(7)	H4MC	0.131(2)	Si1M	0.131(2)	H9MC	0.131(2)
H18M	0.611(7)	H8MA	0.131(2)	H5MB	0.131(2)	H17M	0.670(9)
H14M	0.330(9)	C7M	0.131(2)	H4MA	0.131(2)	H15M	0.670(9)
H14L	0.670(9)	H7MC	0.131(2)	C6M	0.131(2)	H18Q	0.330(9)
H15L	0.330(9)	H9MB	0.131(2)	H8MB	0.131(2)	H16M	0.670(9)
H16L	0.330(9)	H17L	0.330(9)				

Table E.17. Refined atomic coordinates ($\times 10^4$) and equivalent isotropic displacement parameters ($Å^2 \times 10^3$) for 2.

Atom	*x*	*y*	*z*	U(eq)	Atom	*x*	*y*	*z*	U(eq)
S1	7537.7(9)	3215.6(2)	2129.5(7)	31.93(19)	C6	6898(4)	3966.0(11)	6893(3)	39.9(7)
Si1	4634.8(10)	3737.2(2)	5756.8(7)	28.3(2)	C7	8454(5)	3640.1(18)	7047(4)	101.5(18)
F1	3823(2)	4253.1(5)	2673.6(14)	32.2(4)	C8	6804(5)	4071.3(13)	8273(3)	56.0(9)
O1	7333(3)	3155.3(6)	758.5(18)	37.4(5)	C9	7319(6)	4404.4(15)	6305(4)	91.3(16)
O2	9301(2)	3340.6(7)	3063(2)	43.2(5)	C10	4108(3)	3490.3(8)	2028(2)	24.6(6)
O3	6903(3)	2753.0(6)	2526.1(18)	34.7(5)	C11	3258(4)	3180.7(8)	836(2)	27.9(6)
O4	5098(2)	3564.9(6)	4429.3(16)	26.7(4)	C12	1619(4)	2997.5(10)	504(3)	38.1(7)
N1	6090(3)	3582.5(7)	2274(2)	26.9(5)	C13	3079(4)	3941.9(8)	1629(2)	27.2(6)
C1	6629(4)	2729.2(10)	3826(3)	37.1(7)	C14	3241(4)	4151.7(9)	375(2)	30.4(6)
C2	4612(4)	2809.7(9)	3638(3)	32.5(6)	C15	2294(4)	4604.9(9)	-1(3)	30.0(6)
C3	3961(4)	3294.8(8)	3348(2)	26.3(6)	C16	2497(4)	4789.0(9)	-1274(3)	29.5(6)
C4	3862(5)	3252.6(11)	6538(3)	55.6(9)	C17	1529(4)	5232.1(9)	-1766(3)	32.8(6)
C5	2749(5)	4151.4(11)	5267(3)	51.9(9)	C18	1691(4)	5370.5(9)	-3099(3)	36.7(7)

Table E.18. Anisotropic displacement parameters ($Å^2 \times 10^3$) for 2.

Atom	U_{11}	U_{22}	U_{33}	U_{23}	U_{13}	U_{12}
S1	24.2(4)	39.9(4)	36.0(4)	-5.9(3)	16.0(3)	0.9(3)
Si1	29.6(4)	37.4(4)	21.4(4)	-3.2(3)	13.3(3)	1.0(3)
F1	41.1(9)	34.0(8)	24.2(8)	-5.8(6)	14.8(7)	0.4(7)
O1	36.1(11)	48.8(12)	36.4(11)	-8.3(9)	24.2(9)	-1.1(9)
O2	22.9(11)	55.4(13)	50.6(13)	-10.2(10)	11.8(9)	0.6(9)
O3	37.4(11)	36.0(11)	36.8(11)	-4.3(8)	20.6(9)	2.3(9)
O4	26(1)	35.9(10)	20.4(9)	-6.2(7)	11.1(8)	-2.7(8)
N1	21.3(12)	36.6(13)	26.5(12)	-8.1(10)	13.1(10)	-1.4(10)
C1	40.5(17)	43.6(17)	28.8(15)	2.8(12)	14.0(13)	7.3(14)

C2	38.8(16)	34.4(15)	30.2(15)	0.4(11)	19.4(13)	-2.2(12)
C3	24.1(14)	34.8(14)	23.1(14)	-5.1(11)	12.1(11)	-4.0(11)
C4	82(3)	48.2(19)	59(2)	-4.1(16)	53(2)	-10.6(18)
C5	54(2)	67(2)	35.1(18)	-8.8(16)	16.5(16)	17.5(17)
C6	36.0(17)	62(2)	24.0(15)	-9.7(13)	13.8(13)	-6.1(15)
C7	39(2)	167(5)	73(3)	-58(3)	-11(2)	25(3)
C8	54(2)	87(3)	27.4(17)	-18.8(16)	15.0(15)	-13.0(19)
C9	102(3)	114(4)	55(2)	-9(2)	24(2)	-77(3)
C10	19.1(13)	34.1(14)	22.9(13)	-4.2(11)	10.2(11)	-2.8(11)
C11	26.1(15)	37.3(15)	24.1(14)	-6.1(11)	13.7(11)	1.1(12)
C12	30.9(16)	52.5(18)	33.3(16)	-16.7(13)	14.2(13)	-6.6(14)
C13	23.0(14)	36.0(14)	22.5(13)	-6.0(11)	8.1(11)	-1.2(11)
C14	30.5(15)	39.3(15)	24.9(14)	-2.8(12)	14.2(12)	1.3(12)
C15	30.0(15)	37.4(15)	25.5(14)	-3.7(11)	13.6(12)	-0.5(12)
C16	29.2(15)	35.8(15)	27.5(14)	-2.8(11)	15.1(12)	-0.1(12)
C17	34.1(16)	32.9(15)	33.9(16)	-4.6(12)	14.9(13)	-2.9(12)
C18	38.9(17)	38.7(16)	34.3(16)	1.3(13)	15.1(13)	-3.4(13)

Table E.19. Bond Lengths for 2.

Atom	Atom	Length/Å	Atom	Atom	Length/Å
S1	O1	1.424(2)	C2	C3	1.523(4)
S1	O2	1.423(2)	C3	C10	1.563(3)
S1	O3	1.567(2)	C6	C7	1.506(5)
S1	N1	1.607(2)	C6	C8	1.529(4)
Si1	O4	1.6572(18)	C6	C9	1.530(5)
Si1	C4	1.863(3)	C10	C11	1.518(3)
Si1	C5	1.836(3)	C10	C13	1.542(4)
Si1	C6	1.868(3)	C11	C12	1.306(4)
F1	C13	1.406(3)	C13	C14	1.519(3)
O3	C1	1.474(3)	C14	C15	1.518(4)
O4	C3	1.425(3)	C15	C16	1.521(3)
N1	C10	1.482(3)	C16	C17	1.514(4)
C1	C2	1.516(4)	C17	C18	1.525(4)

Table E.20. Bond Angles for 2.

Atom	Atom	Atom	Angle/°	Atom	Atom	Atom	Angle/°

O1	Si1	O3	103.50(11)	C7	C6	Si1	111.3(2)
O1	Si1	N1	110.73(12)	C7	C6	C8	109.4(3)
O2	Si1	O1	118.94(12)	C7	C6	C9	108.5(3)
O2	Si1	O3	110.67(12)	C8	C6	Si1	110.4(2)
O2	Si1	N1	106.30(12)	C8	C6	C9	107.9(3)
O3	Si1	N1	106.07(11)	C9	C6	Si1	109.2(2)
O4	Si1	C4	109.93(12)	N1	C10	C3	107.8(2)
O4	Si1	C5	110.61(12)	N1	C10	C11	112.0(2)
O4	Si1	C6	103.47(11)	N1	C10	C13	106.6(2)
C4	Si1	C6	111.41(16)	C11	C10	C3	112.4(2)
C5	Si1	C4	107.45(17)	C11	C10	C13	105.6(2)
C5	Si1	C6	113.94(15)	C13	C10	C3	112.3(2)
C1	O3	Si1	117.20(16)	C12	C11	C10	124.8(2)
C3	O4	Si1	127.44(15)	F1	C13	C10	109.16(19)
C10	N1	Si1	124.42(18)	F1	C13	C14	106.8(2)
O3	C1	C2	110.4(2)	C14	C13	C10	114.0(2)
C1	C2	C3	115.2(2)	C15	C14	C13	114.6(2)
O4	C3	C2	107.7(2)	C14	C15	C16	111.3(2)
O4	C3	C10	107.41(19)	C17	C16	C15	115.4(2)
C2	C3	C10	114.3(2)	C16	C17	C18	111.4(2)

Table E.21. Torsion Angles for 2.

A	B	C	D	Angle/°	A	B	C	D	Angle/°
Si1	O3	C1	C2	94.8(2)	C1	C2	C3	C10	61.4(3)
Si1	N1	C10	C3	85.2(2)	C2	C3	C10	N1	-74.5(3)
Si1	N1	C10	C11	-39.0(3)	C2	C3	C10	C11	49.5(3)
Si1	N1	C10	C13	-154.07(18)	C2	C3	C10	C13	168.4(2)
Si1	O4	C3	C2	-96.7(2)	C3	C10	C11	C12	48.9(4)
Si1	O4	C3	C10	139.63(17)	C3	C10	C13	F1	58.7(3)
F1	C13	C14	C15	-57.2(3)	C3	C10	C13	C14	178.1(2)
O1	Si1	O3	C1	-169.29(17)	C4	Si1	O4	C3	49.5(2)
O1	Si1	N1	C10	79.5(2)	C4	Si1	C6	C7	69.0(3)
O2	Si1	O3	C1	62.2(2)	C4	Si1	C6	C8	-52.7(3)
O2	Si1	N1	C10	-150.0(2)	C4	Si1	C6	C9	-171.2(3)
O3	Si1	N1	C10	-32.1(2)	C5	Si1	O4	C3	-69.0(2)
O3	C1	C2	C3	-73.7(3)	C5	Si1	C6	C7	-169.2(3)
O4	Si1	C6	C7	-49.1(3)	C5	Si1	C6	C8	69.1(3)
O4	Si1	C6	C8	-170.8(2)	C5	Si1	C6	C9	-49.5(3)
O4	Si1	C6	C9	70.7(3)	C6	Si1	O4	C3	168.6(2)
O4	C3	C10	N1	45.0(2)	C10	C13	C14	C15	-177.8(2)

O4	C3	C10	C11	168.99(19)	C11	C10	C13	F1	-178.48(19)
O4	C3	C10	C13	-72.1(2)	C11	C10	C13	C14	-59.2(3)
N1	S1	O3	C1	-52.7(2)	C13	C10	C11	C12	-73.8(3)
N1	C10	C11	C12	170.5(3)	C13	C14	C15	C16	-179.3(2)
N1	C10	C13	F1	-59.1(2)	C14	C15	C16	C17	177.5(2)
N1	C10	C13	C14	60.2(3)	C15	C16	C17	C18	-175.7(2)
C1	C2	C3	O4	-57.9(3)					

Table E.22. Hydrogen Atom Coordinates (Å×10^4) and Isotropic Displacement Parameters (Å^2×10^3) for 2.

Atom	*x*	*y*	*z*	U(eq)	Atom	*x*	*y*	*z*	U(eq)
H1	6570(40)	3726(8)	2970(20)	34(8)	H9A	7332	4348	5402	137
H1A	7410	2958	4442	45	H9B	8531	4518	6878	137
H1B	7013	2429	4233	45	H9C	6363	4627	6259	137
H2A	4400	2711	4460	39	H12A	865	3055	1026	46
H2B	3836	2619	2890	39	H12B	1180	2807	-258	46
H3	2647	3317	3304	32	H13	1739	3895	1486	33
H4A	2727	3125	5891	83	H14A	4570	4188	509	36
H4B	3617	3356	7333	83	H14B	2702	3942	-385	36
H4C	4834	3023	6799	83	H15A	2844	4820	743	36
H5A	3163	4425	4943	78	H15B	962	4573	-136	36
H5B	2402	4225	6044	78	H16A	3833	4827	-1115	35
H5C	1676	4026	4553	78	H16B	2009	4563	-1994	35
H7A	8182	3353	7391	152	H17A	2083	5468	-1088	39
H7B	9612	3763	7676	152	H17B	204	5204	-1876	39
H7C	8581	3592	6173	152	H18A	1056	5149	-3788	55
H8A	5752	4271	8169	84	H18B	3001	5385	-3002	55
H8B	7954	4219	8828	84	H18C	1119	5666	-3362	55
H8C	6646	3791	8705	84					

E.12. CALCULATED POWDER X-RAY DIFFRACTION PATTERNS FOR PHASE I AND PHASE II

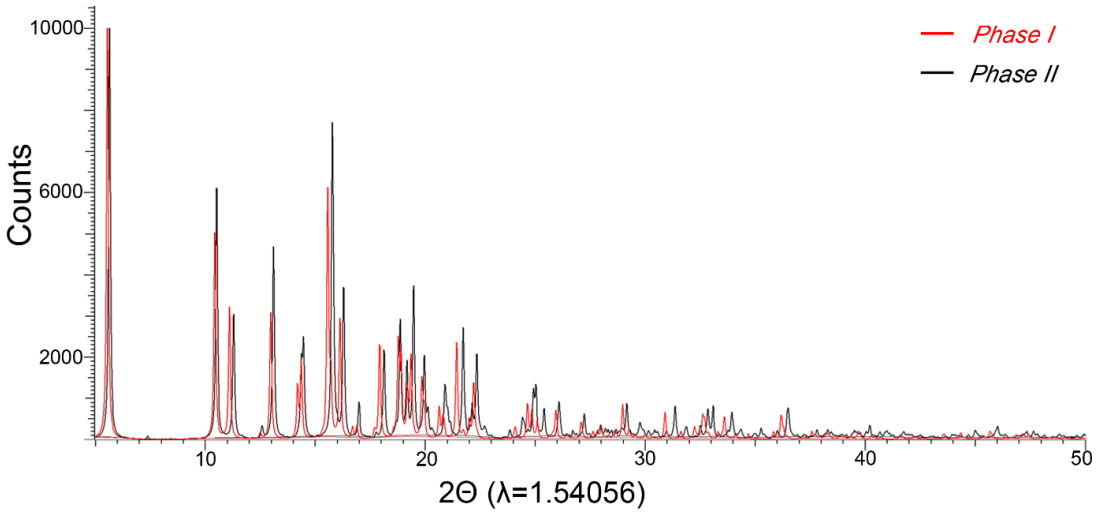

Figure E.9. Overlay of powder X-ray diffraction patterns calculated from the single crystal data. The similarities in the location of the major peaks suggests that the two phases are structurally similar and in fact Phase II can be best described as a superstructure of Phase I.

E.13. DIFFERENTIAL SCANNING CALORIMETRY RESULTS FOR 1

The differential scanning calorimetry measurements were carried out on a TA Q2000 over the range of 263 K to 403 K with step size of 2 K/min.

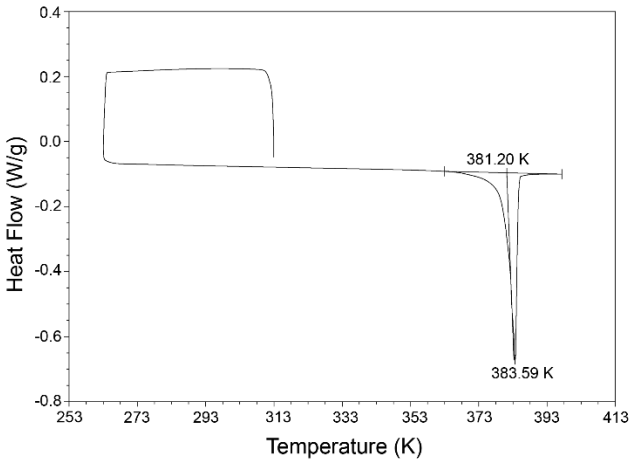

Figure E.10. Differential Scanning calorimetry measurement of **1**. Only a melting event at onset of 381K was observed above I-II phase transition temperature.